APPLICATION OF SACRIFICIAL POLYMERS IN ELECTRONIC AND TRANSIENT DEVICES

A Dissertation
Presented to
The Academic Faculty

by

Jisu Jiang

In Partial Fulfillment
of the Requirements for the Degree
Doctor of Philosophy in the
School of Chemical and Biomolecular Engineering

Georgia Institute of Technology
August 2019

COPYRIGHT © 2019 BY JISU JIANG

APPLICATION OF SACRIFICIAL POLYMERS IN ELECTRONIC AND TRANSIENT DEVICES

Approved by:

Dr. Paul A. Kohl, Advisor
School of Chemical and Biomolecular Engineering
Georgia Institute of Technology

Dr. Meisha Shofner
School of Materials Science and Engineering
Georgia Institute of Technology

Dr. Elsa Reichmanis
School of Chemical and Biomolecular Engineering
Georgia Institute of Technology

Dr. Rosario Gerhardt
School of Materials Science and Engineering
Georgia Institute of Technology

Dr. Ryan P. Lively
School of Chemical and Biomolecular Engineer
Georgia Institute of Technology

Date Approved: [April 10, 2019]

This PhD dissertation is dedicated to my family

ACKNOWLEDGEMENTS

There are many people helped and motivated me to reach to this stage. I would like to thank my advisor, Dr. Paul Kohl, for your guidance in both my research and presentation skills. Your wisdom, humor, patience, and respect made this a memorable experience in my life. I also learned whole a lot outside research from you which I believe will help me in my future career. I would also like to thank my committee members, Dr. Elsa Reichmanis, Dr. Ryan Lively, Dr. Rosario Gerhardt, and Dr. Meisha Shofner, for providing constructive feedback through the process that make this work better.

It is of great honor to work with talented and helpful lab mates in Kohl group. I would like to thank all the current and past graduate students and post-doc fellows in Kohl group, especially Dr. Jared Schwartz, Dr. Dami Phillips, Dr. Lisha Liu, Anthony Engler, Garrett Huang, John Ahlfield for helping me start from scratch with my research and always providing constructive feedback to my research and other aspects of my graduate research career. It has been a lot of fun entertaining with all of you on occasions such as March Madness, dessert competition, white elephant gift exchange, Halloween party, and those are surely highlights in my graduate research career. I would also like to thank all the undergraduate students, Man Hou Vong, Landon Keller, Spencer Temples, Myeongshin Lee, Alexa Espinoza. Your contribution to this thesis is indispensable and I wish all of you a bright future, no matter in academic research or industry. I especially want to acknowledge and show great respect to the ICARUS team, Dami, Anthony, and myself, as well as past members Jared and Jerry, to make a successful prototype in a year that was considered impossible at beginning. I wish all of you have a successful career and wonderful life in the future.

I would like to thank all the IEN staffs for training me and troubleshooting the tools for me to assist the success of my work. Your contribution is important for me to make anything even possible to happen.

I truly value the long-term friendship that I have developed with people I met during middle and high school, as well as people I became very good friend with at college. Most of them already start working in different industries. Their friendship and visions were something that helped me make through the tough time during my graduate research. Special thanks go to my undergraduate research mentor, Yuan Meng, and my best friend, Xiongyi Zhang. Both of them have inspired me along the way to this point and I truly glad to have such firm friendship with you.

There is simply not enough words to describe how grateful and blessed I am to born in the family I was risen. I couldn't get to this stage of my life without the love and support of my parents and grandparents. It is your education methodology, patient, and long-term vision that developed me to be the person I am. It has been the most beautiful thing in my life to meet my wife Mo Shi in my PhD career. You have been and will continuously be a wonderful addition to my life and I look forward to our future endeavors.

TABLE OF CONTENTS

LIST OF TABLES

LIST OF FIGURES

LIST OF SCHEMES

LIST OF SYMBOLS AND ABBREVIATIONS

DCM	Dichloromethane
THF	Tetrahydrofuran
DSC	Differential Scanning Calorimetry
TGA	Thermogravimetric Analysis
ATR	Attenuated Total Reflectance
FT-IR	Fourier Transform Infrared Spectroscopy
UV-Vis	UV-Visible Spectroscopy
NMR	Nuclear Magnetic Resonance
T_g	Glass Transition Temperature
QCM	Quartz Crystal Microbalance
pphr	Part Per Hundred Rubber
APO	Ammonium Pentaborate Octahydrate
AAO	Anodic Aluminum oxide
DI	Deionized
XPS	X-Ray Photoelectron Spectroscopy
V_{BD}	Breakdown Voltage
ppm	Part Per Million
ITRS	International Technology Roadmap for Semiconductors
PWB	Printed Wiring Board
PPC	Poly(propylene carbonate)
$CDCl_3$	Chloroform-d
SMA	Styrene Maleic Anhydride
2E4MI	2-Ethyl-4-Methylimidazole

BPADGE	Bisphenol A Diglycidyl Ether
m-CPBA	3-Chloroperbenzoicacid
MEK	Methyl Ethyl Ketone
ePPC	Epoxide Poly(propylene carbonate)
aPPC	Allyl Poly(propylene carbonate)
SEM	Scanning Electron Microscopy
VAT	Volume Averaging Theory
PPHA	Poly(phthalaldehyde)
PET	Photo-induced Electron Transfer
PAG	Photoacid Generator
DMBA	1,8-Dimethoxy-9,10-bis(phenylehtynyl)anthracene
Đ	Polydispersity Index
BMP TFSI	1-Butyl-1-methylpyrrolidinium bis(trifluoromethylsulfonyl)imide
PEB	Post Exposure Bake
PHA	Phthalaldehyde
E_A	Activation Energy
A	Pre-exponential Factor
BF_3	Boron Trifluoride Etherate
ICP-MS	Inductively Coupled Plasma Mass Spectrometry
Rhodorsil FABA	Tetrakis(pentafluoropenyl)borate-4-methylphenyl[4-(1-methylethyl)phenyl]iodonium
HMP TFSI	1-Hexyl-1-methylpyrrolidinium bis(trifluoromethylsulfonyl)imide
OMP TFSI	1-Methyl-1-octylpyrrolidinium bis(trifluoromethylsulfonyl)imide
PEO	Poly(ethylene glycol) bis(2-ethylhexanoate)
BEHP	Bis(2-ethylhexyl) Phthalate

DMA	Dynamic Mechanical Analysis
P(PHA-co-BA)	Poly(phthalaldehyde-co-butanal)
PEC	Poly(ethylene carbonate)
PCC	Poly(cyclohexane carbonate)
TBD·$HBPh_4$	1,5,7–triaza-bicyclo[4.4.0]dec-5-ene tetraphenylborate
F_A	Adhesion Strength
F_P	Pulling Force
kDa	Kilo-dalton
IC	Integrated Circuit
PNB	Polynorbornene
PNC	Poly(norbornene carbonate)
PCL	Poly(caprolactone)
PEC	Poly(ethylene carbonate)
MEMS	Micro-Electro-Mechanical System
TMSNB	Trimethoxysilyl Norbornene
MSQ	Methylsilsesquioxane
TEM	Transmission Electron Microscope
PVA	polyvinyl alcohol
PLGA	poly(lactic-co-glycolic) acid
POC	Poly(1,8-octanediol-co-citrate)
AgNW	Silver Nanowires
OLED	Organic Light Emitting Diode
VIA	Verticle Interconnect Access
RCC	Resin Coated Copper
CCL	Copper Clad Laminate

SUMMARY

Sacrificial polymers are useful polymers to use in variety of applications. They can be used in microelectronic fabrication process to act as temporary placeholder and create air cavities for different purposes (e.g., porous structure, microelectronic mechanical system (MEMS) device protection, microfluidic channel for drug delivery, temporary adhesive for wafer thinning and integrated-circuit (IC) fabrication etc. More recently, there is interest in using sacrificial polymers as structural materials for transient electronic and other transient devices. Transient devices can be triggered to decompose or distintegrate by forming small monomer unit or dissolving in aqueous solution. The resulting devices can vanish and leave behind little or no traces. This provides great opportunity for disposal of electronic devices, as well as for military application where device discovery after usage is unfavorable. However, challenges are remaining to use the existing materials to achieve the application purpose to be met. In order to make them feasible for actual application, modification of polymer chemical structure and tuning of formulations are needed.

Sacrificial polymers with suitable thermal stability and chemical miscibility with epoxy resin, such as epoxide functionalized poly(propylene carbonate), can act as a temporary placeholder to create nanoporous, low dielectric constant and loss printed circuit boards for faster device switching speed while still maintaining the original mechanical properties. Epoxide functionalized polymers also provide the opportunity to be used as low temperature temporary adhesive with enhanced adhesion strength. Transient polymers can be used to build transient devices where devices can be degraded with little or no trace at end of life to avoid adversary discovery or materials recycling. Photosensitive transient polymers are of interest because they can make use of sunlight to trigger the transient

properties. The transient and mechanical properties of poly(phthalaldehyde) transient polymer were tuned using different types of traditional and ionic liquid plasticizer for possible applications in a variety of conditions. Addition of those plasticizers also improved the transient properties of the film by forming liquid and absorbing into the environment. To extend the application horizon of transient polymers, weakly basic amide and lactam were included in the photosensitive transient films and shown to delay the photo-induced degradation by forming weak conjugate acid in-situ. To make the fabrication process of light sensitive transient device easier, proof-of-concept bilayer photosensitive poly(phthalaldehyde) using photoacid diffusion was explored to make device fabrication more friendly. Based on the transient polymers and formulations developed, prototypes of transient aircraft, transient parachute, and transient triboelectric nanogenerator were successfully demonstrated. The advances in developing transient materials show a pathway forward to apply these technologies in defense and recyclable devices in the future.

CHAPTER 1. BACKGROUND

1.1 Overview of Sacrificial Polymers

Modern electronic devices often require sophisticated 3D fabrication process to achieve desired integrated structures for best performance [1]. In the meantime, there is an emerging request for devices that can be used in one time and triggered to decompose through an external stimulus to avoid adversary reverse-engineering and electronic device recycling [2]. Sacrificial polymer is a category of polymer that is easily adaptable, low-cost potential solutions for building electronic systems described [3]. In many cases, sacrificial polymers can be used as template materials to serve as temporary placeholder before a trigger is applied [3,4]. This intermediate temporary placeholder allows the possibility to do fabrication on top of the sacrificial polymers (e.g., metallization, dielectric deposition etc.). Upon finishing the fabrication process, sacrificial polymer can be selectively removed using a preferred trigger (e.g., heat, photo, chemical etc.) and reverting to its small-unit monomer forms. The formation of volatile monomer units after degradation makes sacrificial polymer an ideal candidate in variety of electronic device applications. Most electronic devices are very sensitive to residuals leftovers. The residual can cause significant change in dielectric properties of materials, resulting in lower operation efficiency and higher loss. The residual can also cause shorter shelf life of devices, resulting in premature failure of integrated devices. Moreover, the formation of volatile byproducts makes sacrificial polymers ideal candidates to be used in transient devices. The degradation can be triggered in the ambient and fully degraded devices can vanish upon completion of physical task. This is especially useful for environmental and

military purpose, as it can significantly reduce the labor cost on recycling the used electronic devices and mitigate the risk of detection by adversaries [2].

Sacrificial polymers can be divided into two categories based on the ceiling temperature of the polymer [3]. Ceiling temperature is the temperature that above which polymer degrades into its monomer form, and below which polymer is thermodynamically stable [5]. Varieties of polycarbonates and poly(norbornene) (PNB) (structures shown in Figure 1.1) are examples of high ceiling temperature sacrificial polymers. Their decomposition temperatures are typically between 200 °C to 300 °C for polycarbonate (e.g., poly(ethylene carbonate) (PEC), poly(norbornene carbonate) (PNC), poly(propylene carbonate) (PPC), etc) and 350 °C to 400 °C for PNB [4,6–8]. The high ceiling temperature nature of these polymers make them compatible with many microelectronic fabrication processes, which typically require processing temperature over 200 °C. These polymers can be functionalized or crosslinked to endure higher processing temperature range [7,9].

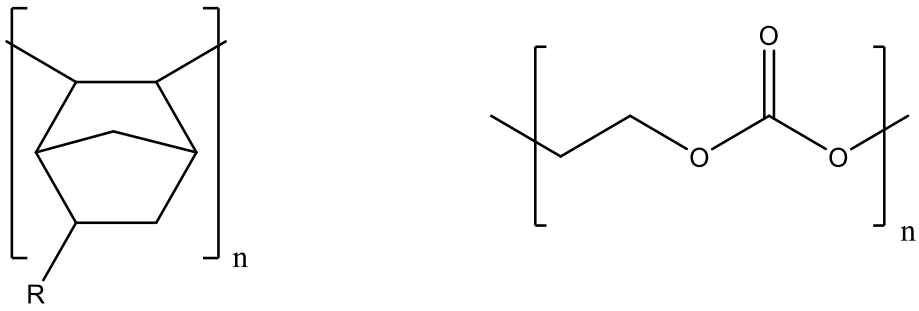

Figure 1.1. Example of poly(norbornene) (left) and polycarbonate (right).

Poly(aldehydes), poly(olefin sulfones), and poly(carbamates) belong to the class of low ceiling temperature polymers (structures shown in Figure 1.2) [10–14]. Their ceiling temperature are typically near or below 70 °C [15]. Some low ceiling temperature polymers

have ceiling temperature near or below room temperature. Therefore they are thermodynamically unstable at ambient temperature and needs to be kinetically stabilized to make them usable. For example, poly(phthalaldehyde) has a ceiling temperature around -42 °C [16]. Poly(olefin sulfones) and poly(carbamates) have relatively slow depolymerization rate, making them unsuitable for device that requires rapid vanishing after depolymerization [17–19]. Typical poly(aldehydes) has a fast depolymerization rate upon triggering, making them ideal materials to be used for transient device application. Poly(aldehydes) are synthesized at low temperatures (below their ceiling temperature) and are unstable at ambient temperatures unless a kinetic end-cap can be added to the polymer to restrict the thermodynamically favorable unzipping reaction from chain ends [20–23]. Another way to make low ceiling temperature poly(aldehydes) stable at ambient or even higher temperature is to form cyclic polymer [5]. The formation of cyclic polymer can remove the reactive chain ends and kinetically stabilize the polymer at the room temperature. The kinetically stabilized poly(aldehyde) polymers can be degraded upon removal of its kinetic trap at the end group or random chain scission in the polymer chain. Both actions reverting the polymer to its thermodynamically unstable state (unless the ambient temperature is below its ceiling temperature). Example of low ceiling temperature poly(aldehydes) include but not limited to, poly(phthalaldehyde) [5], poly(ethyl glyoxylate) [24–27], poly(phthalaldehyde-co-butanal) [28], poly(phthalaldehyde-co-benzaldehydes) [29], etc.

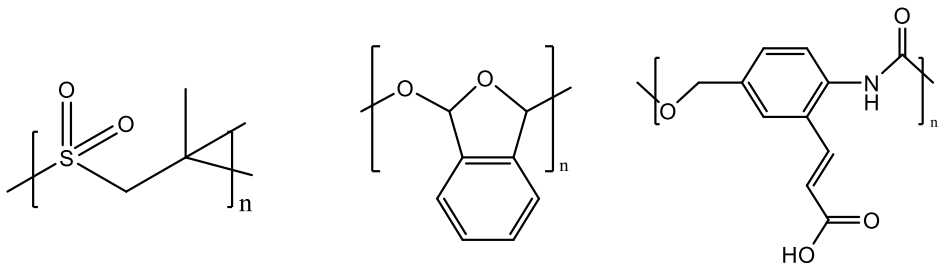

Figure 1.2. Example of poly(sulfone) (left), poly(aldehyde) (middle), poly(carbamate) (right).

1.2 Application of Sacrificial Polymers

There are variety usage of different sacrificial polymers in different situations. Most applications focused on using sacrificial polymers to build electronic devices. The following paragraphs describe some areas where sacrificial polymers have been used or are of interest.

1.2.1 Application in MEMS Packaging

Packaging of MEMS device is a critical step to provide physical protection and electrical connectivity of the device to ensure the proper functioning of the device over a long period [30]. Conventional wafer-level packaging involves bonding MEMS wafer by various bonding method such as anodic bonding, fusion bonding, eutectic bonding [30,31]. Most of these methods require high temperature treatment for packaging to happen and might cause damage to the MEMS device. Moreover, they require careful alignment of capping wafer to the device to avoid position mismatch of the package with the device [32]. Therefore, it is desirable to find an easier, low-temperature method to achieve MEMS packaging process.

Sacrificial polymers provide an excellent alternative to realize packaging of MEMS devices. They can be used as barrier layer to protect devices from exposing to air or other unwanted conditions, and later removed after an overcoat material is applied. Uzunlar et al demonstrated the feasibility of using PPC as sacrificial polymer to achieve low temperature packaging of MEMS devices [4,33]. PPC can be solvent-casted onto a silicon substrate. The casted PPC film can be patterened either through photoexposure steps with the addition of photoacid generator, or by conventional etching techniques (e.g. reactive ion etching). The patterned PPC can then be covered with an overcoat material to achieve the protection purpose. Afterwards, PPC can be selectively removed by subjected to temperature above its onset decomposition temperature. The small molecules formed in its decomposition stage assure the good permeation through the overcoat, leaving air-cavities behind. This method has been demonstrated to be able to package MEMS device such as capacitive resonator [32].

1.2.2 Application in Low-k Porous Materials

Because of its capability of decomposing into small molecules that can be later removed cleanly out of the system, sacrificial polymer can be used as porogenic materials to create micro and nano porous materials. These porogenic materials can be further used in interconnects and insulators in electronic device owing to their low dielectric constant. A critical requirement to apply porous materials in electronic device is to achieve small pore size. Larger pore size can result in inferior thermal/mechanical properties.

Creating porous structure for methylsilsesquioxane (MSQ) was studied extensively owing to its relatively low dielectric constant. Padovani et al used a substituted

polynorbornene (PNB) polymer trimethoxysilyl norbornene (TMSNB) as a temporary placeholder in a crosslinked MSQ glass to create nanoporous substrate [34]. Figure 1.3 (left) shows the cross-sectional TEM images of porous MSQ film with 20% TMSNB. The obtained dielectric constant of porous MSQ decreased from 2.68 to 2.24 for a porous MSQ containing 30% TMSNB initially. Nguyen et al prepared a nanoporous MSQ films by mixing MSQ prepolymer with a star polymer of poly(caprolactone) (PCL) with hydroxyl end group that effectively crosslinked with MSQ (Figure 1.3 right) [35]. PCL was later selectively removed to leave behind porous PMSQ films. Dielectric constant as low as 1.9 was achieved with 30% composition of PCL, with nanometer-sized pore, shown in Figure 1.3 (right).

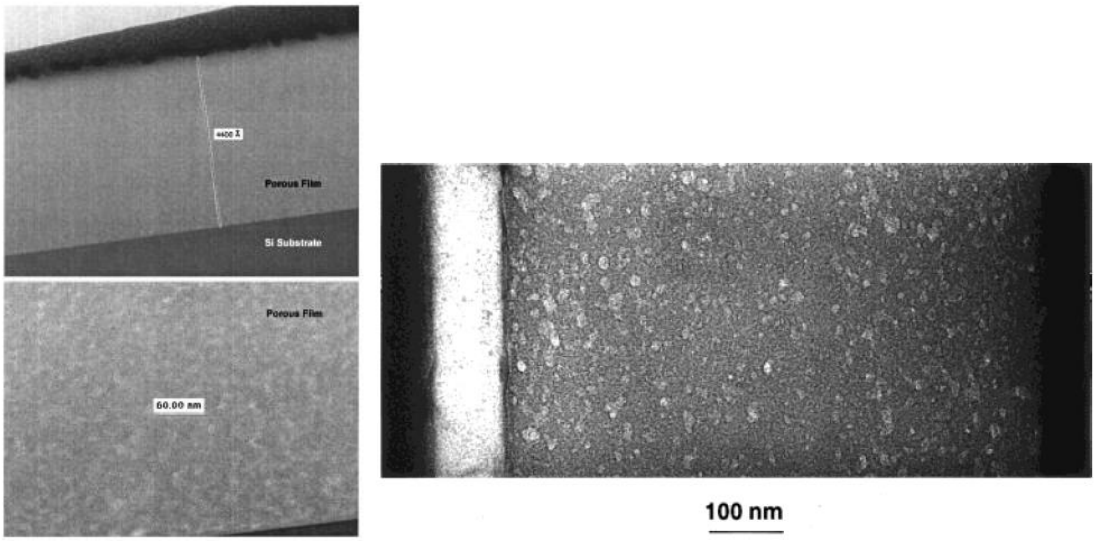

Figure 1.3. Left: TEM images for 20:80 wt% TMSNB:MSQ film after decomposition. Adapted from Padovani et al, Electrochemical and Solid-State Letters, 2001 [34]. Right: TEM image porous PMSQ film with 10 wt% loadings of PCL. Adapted from Nguyen et al, Chemistry of Materials, 1999 [35].

PPC is another ideal material to be used for generating porous structures due to its clean decomposition that leaves little residue. Owing to its relatively low decomposition temperature compare to other known sacrificial polymers (e.g., PCL, PNB etc.), it is more applicable to be used as sacrificial polymer with polymer matrix that can be cured at relatively low temperature, such as epoxy. Li et al has demonstrated the possibility of generating porous epoxy structures using PPC as a temporary placeholder through direct mixing of high molecular weight PPC (100 kDa) into epoxy resin [36]. This resulted in porous structures with micron-size pores, shown in Figure 1.4.

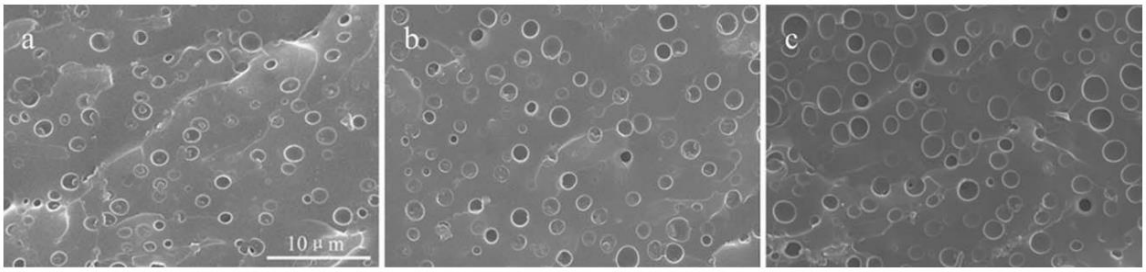

Figure 1.4. Porous epoxy with 5%, 8%, and 12% PPC concentration. Adapted from Li et al, Journal of Polymer Science: Part B: Polymer Physics, 2010 [36].

1.2.3 Application in Temporary Adhesive

Wafer bonding is an importance process in fabrication of MEMS devices. It enables the possibility to create complex 3D structures and enable the possibility of thinning the wafer for 3D-stacking. The temporary placeholder nature of sacrificial polymers makes it possible to create complex 3D structure after wafer bonding process. This feature can be used in field of packaging of electronic components or sensors.

Sacrificial polymer can be used as a temporary adhesive to achieve the wafer thinning purpose. Fritz et al and Xue et al demonstrated feasibility of using polycarbonate as temporary adhesive to successfully achieve temporary bonding of two wafers and thinned the wafer through grinding process [37,38]. The temporary adhesive was later removed through heat with minimal residuals left behind after the entire process. No mechanical forces was required to separate wafers, which ensured the good quality of grinded wafer.

Sacrificial polymers can also be used to transfer device from one substrate to another [39,40], as shown in Figure 1.5. Through the sacrificial polymers, the device from another substrate can be flip-bonded onto a new substrate with designed circuit and structures. The mother substrate can later on be etched, grinded, or polished away to result in the successful transfer of thin films or designed structures.

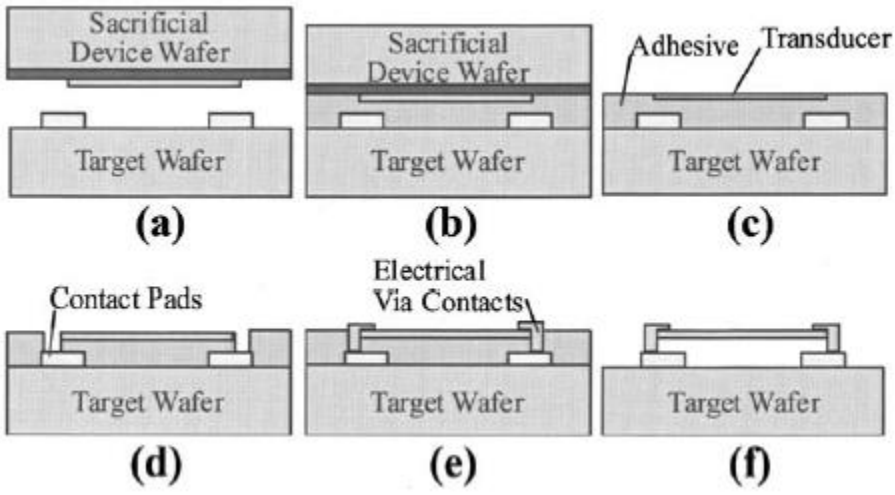

Figure 1.5. Thin film and device transfer using temporary adhesive. Adapted from Niklaus et al, Journal of Applied Physics, 2006 [1].

1.2.4 Application in Transient Electronics and Devices

More recently, interest in designing transient devices using sacrificial polymers has arisen. Different from conventional purpose of using sacrificial polymers as temporary placeholder, the goal is to use sacrificial polymers as structural materials. Transient electronics are devices that can be triggered to decompose/dissolved under a certain stimuli, and device needs to vanish after exposure to trigger to avoid adversary detection, reverse engineering of devices, and electronics recycling. A big part of this research was focused on water-soluble polymers, for example, polyvinyl alcohol (PVA) , poly(lactic-co-glycolic) acid (PLGA), Poly(1,8-octanediol-co-citrate) (POC), poly(caprolactone) (PCL), etc (examples of fabricated devices is shown in Figure 1.6) [41–43].

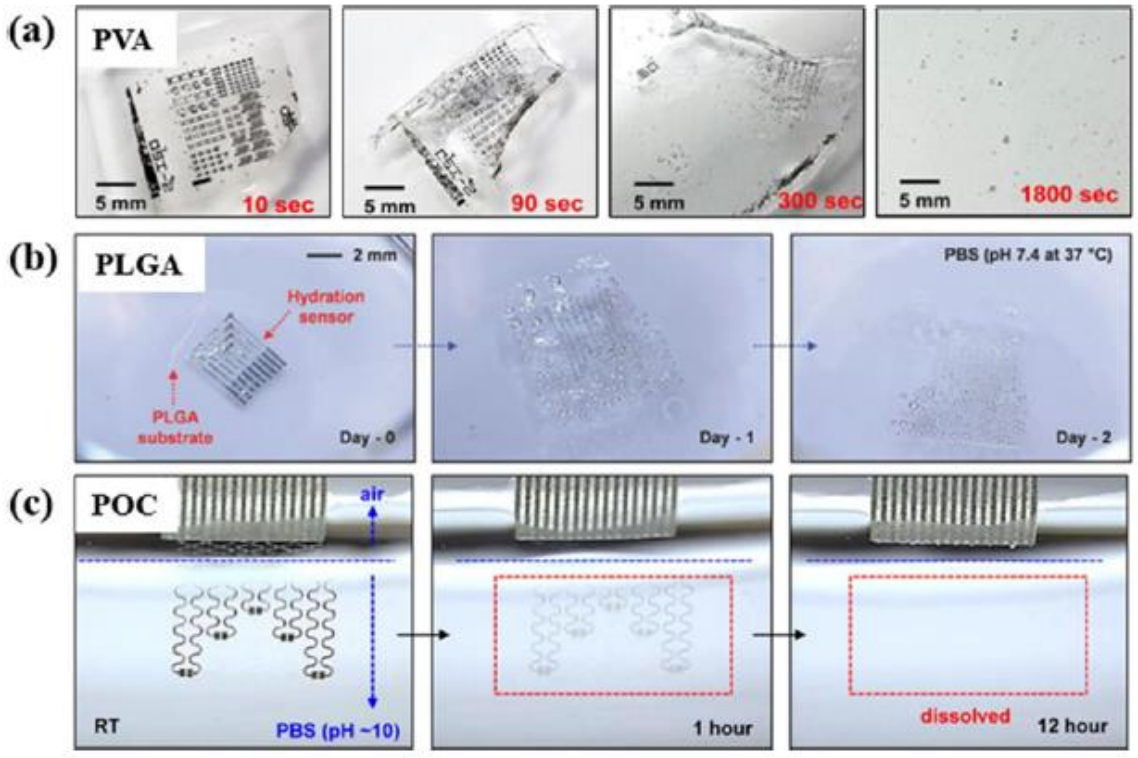

Figure 1.6. Transient devices made from water-soluble polymers. Adapted from Hwang et al, Advanced Materials [42], 2014; Hwang et al, Nano Letters, 2015 [41]; Jin et al, Applied Physics Letter, 2014 [43].

Other triggering mechanisms are desirable for application of transient in different situations. Stimuli responsive polymer that can degrade under different environmental stimuli is highly desirable for their flexibility in variety of application environments [2]. Polysulfone is one of the polymers that can response to relatively low temperature before degradation occurs [44]. However, in many situations, a room temperature, and even low temperature triggered degradation of polymers is desirable for different application scenarios.

The discovery and development of low-ceiling temperature poly(aldehydes) can accommodate this requirement. Owing to their low ceiling temperatures, these kinetically stabilized metastable poly(aldehydes) polymers can rapidly unzip from chain ends and depolymerize to its monomers upon removal of the kinetic trap or exposure of its end-group [45]. Among all poly(aldehydes), cyclic poly(phthalaldehyde) (PPHA) is of the greatest interest. It has the ability to be massive produced with high molecular weight [5]. PPHA was originally proposed to be used as a photoresist material by Ito et al as a dry developing photoresist materials that are highly sensitive to exposure of low doses e-beam with the incorporation of photoacid generator (PAG) [46]. The resulting monomer has a non-negligible vapor pressure that can be removed by moderate heating to result in patterned surface.

Phillips et al. made use of the low-ceiling temperature nature of PPHA to demonstrate visible light sensitive transient films [47]. By incorporating photosensitizer and PAG into the PPHA, the photoacid can be generated after exposing to visible light, resulting in complete degradation of PPHA. Lee et al used this concept to further extend the application into organic light emitting diode (OLED) devices [48], where photosensitizer with longer absorption wavelength was incorporated. The OLED device fabricated can be triggered to failure with accurate timing. Hernandez et al made use of metastable PPHA and built a transient transistor series on PPHA substrate with the incorporation of PAG that was triggered to failure, decompose, and vanish upon exposure to UV light [49].

1.3 **Decomposition Trigger Mechanism of Sacrificial Polymers**

Two sacrificial polymers that are particularly studied in this dissertation are PPC and PPHA. Both polymers are capable of degrade at relatively low temperatures [50,51]. Moreover, both polymers degrade into volatile monomer units, making it easier to clean the residuals left behind after degradation. Different triggers can be used to degrade PPC and PPHA to expand the application horizon of both sacrificial polymers in the field needed. Most interesting ones include heat, photo (UV to visible range), chemical (acid and base), and acoustic/mechanical triggers.

Poly(propylene carbonate) (PPC)

Thermal decomposition of PPC can be achieved through two different pathways, as described in Figure 1.7 [9]. At lower temperature (between 180 °C and 200 °C), PPC can decompose via hydroxyl end-group unzipping that leads to cascading degradation of

PPC into monomer units. At higher temperature, PPC backbone can undergo random chain scission of polymer backbone that also results in degradation into small molecule units.

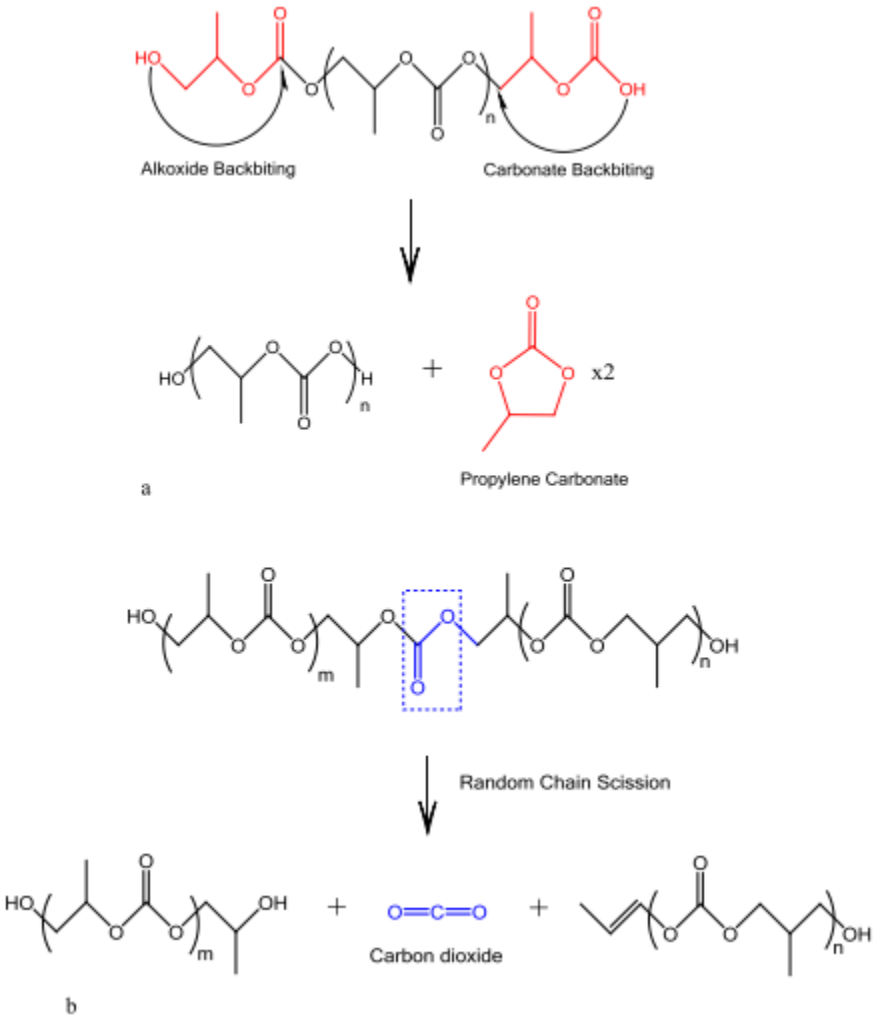

Figure 1.7. PPC decomposition mechanism. Adapted from Phillips et al, Polymer Degradation and Stability, 2016 [9].

Thermal degradation of PPC can be tuned by addition of PAG and photobase generator (PBG) into the polymer film [52,53]. PAG and PBG can be UV activated to create strong acid/base. The resulting PPC can degrade at a significantly lower temperature,

as shown in Figure 1.8. The lowering of the degradation temperature is due to the sensitivity of PPC backbone to acid and base at elevated temperatures [9].

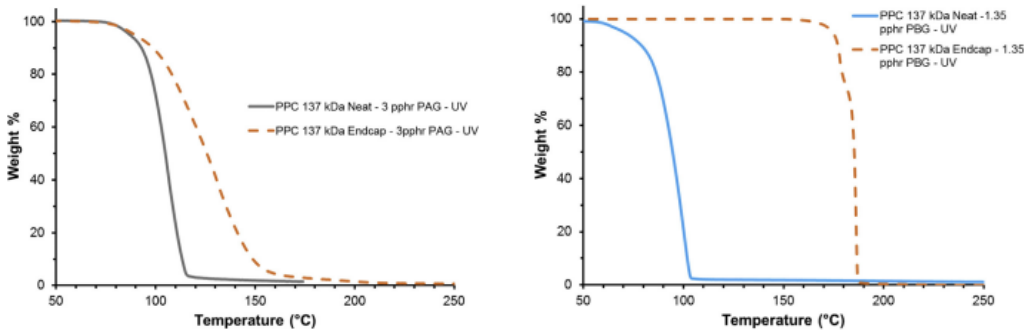

Figure 1.8. Thermal decomposition of PPC with addition of PAG (left) and PBG (right). Adapted from Phillips et al, Polymer Degradation and Stability, 2016 [9].

Thermal stability of PPC can be tuned by using end-caps to stabilize the hydroxyl chain ends [9]. End capping using different agents result in elimination of unzipping reaction from reactive chain ends, leaving random chain scission the only possible mechanism for degradation. Therefore, the stability of the PPC can be improved. Through these chemical tuning of PPC backbone structures and addition of photosensitive package, the process window and application of PPC are significantly broadened.

Poly(phthalaldehyde) (PPHA)

Cyclic PPHA (synthesized cationically using boron trifluoride etherate (BF_3OEt_2)) can degrade thermally through random cleavage of the polymer backbone at its relatively weak ether linkage [22]. The most stable PPHA synthesized so far can be stable thermally up to around 150 °C. Thermal stability of PPHA can be improved through further purification of BF_3OEt_2 [5,54].

Addition of PAG into PPHA can tune the decomposition temperature at ambient temperature due to the formation of strong photoacid after UV exposure [49]. Further addition of sensitizer (e.g., anthracene) can resulted in photoinduced electron transfer (PET) reaction (Scheme 1.1) between sensitizer and PAG to result in degradation of PPHA after exposure to visible light/LED light [47]. Mechanism of acid induced degradation of PPHA is shown in Scheme 1.1. The photosensitizer can be excited upon exposure to its absorption wavelength. The resulting excited photosensitizer transfer its electron to a lower-energy state of PAG to result in heterolytic cleavage of chemical bonds that later generate strong photoacid.

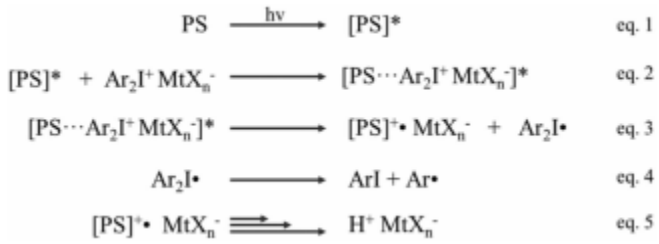

Scheme 1.1. PET reaction mechanism of onium salts. Adapted from Phillips et al, Journal of Applied Polymer Science, 2019 [47].

Diesendruck et al also demonstrated a mechanically triggered unzipping of PPHA that resulted in heterolytic bond scission [55]. This further widens the application of transient devices in different scenarios where acoustic and mechanical energy can be used to trigger decomposition of transient devices.

In the following chapters of this dissertation, chemical functionality and sacrificial polymer formulations were modified to achieve desired properties of relevant materials/devices. Expansion of usage of sacrificial polymers were also demonstrated.

CHAPTER 2.

GRAFTED EPOXIDE FUNCTIONALIZED POLY(PROPYLENE CARBONATE) POROGEN FOR LOW DIELECTRIC CONSTANT EPOXY FILMS

2.1 Introduction

Epoxy resins are commercially used in the fabrication of printed wiring board (PWB) and integrated circuit package substrates because they have an acceptable dielectric constant, good adhesive strength, high modulus, high thermal stability, and are solvent resistant [56]. However, advanced polymers are used in applications where lower dielectric constant is needed for higher speed substrates and packages [57–60]. High parasitic capacitance can cause interconnect delay for electronic devices and increase energy consumption [61,62]. The tradeoff in improving electrical performance through the use of non-epoxy materials comes with high cost and more difficult process conditions. Thus, improved epoxy formulations are desired because they combine existing market acceptance, low cost and simple processing. The primary objective of this chapter is to modify existing epoxy resin formulations to achieve lower dielectric constant in off-chip interconnect pathways (i.e. the PWB and chip substrate).

Different methods have been investigated to lower the dielectric constant of epoxy polymer films. A hyperbranched epoxy thermoset has been synthesized and cast into film to reduce the dielectric constant by increasing the free volume in the hyperbranched polymer network [63]. Silica/epoxy resin nanocomposites have been formulated to produce organic-inorganic hybrid PWBs with reduced dielectric constant based on mesoporous

silica [64]. Oligomeric silsesquioxane has been used to crosslink with the epoxy resin to reduce the dielectric constant due to the organic functional groups on the cage corners that can reduce the polarization of the molecular structure [65]. The epoxy resin backbone has been perfluorinated to lower the dielectric constant by reducing the dipole of the backbone using fluorine as the electron-withdrawing group, however, perfluorinated compounds are expensive and dangerous to produce [66].

The incorporation of air in the epoxy resin through the creation of porous regions is another viable approach to reduce the dielectric constant of polymer films, because air has a dielectric constant of about one. There are several reported techniques to form porous films, including gas expansion by using gas-blowing agent such as nitrogen [67], concentrated emulsion by polymerizing one phase and selectively removing the dispersed liquid phase [68], thermally induced phase separation by freeze-drying the solvent below the glass transition temperature (T_g) of the polymer [69], and chemically induced phase separation by crosslinking the polymer to form two phases followed by removal of the solvent to create pores [70,71]. Despite the large pore volume created using these methods, the pores are either large or open-pores, leading to the formation contiguous pathways through the polymer film. This can significantly deteriorate the mechanical property of the film, making them undesirable in preparation for PWB substrate.

The formation of large pores from phase segregation can be mitigated by covalently bonding the porogen materials to the polymer matrix, resulting in a nanoporous structure inside the cured polymer film. Thermal decomposition of the labile sacrificial polymer could lead to creation of nanoporous regions inside the film. Various ways have been used to introduce a sacrificial polymer into the polymer matrix, including synthesis of block

copolymers that have one phase consisting of a sacrificial polymer [72–76], direct crosslinking of the sacrificial polymer with the polymer matrix in a solvent where both components are miscible with each other [35,77,78], and grafting the sacrificial polymer to the polymer matrix before crosslinking of the film [34,79–81]. In those studies, sacrificial polymers such as poly(propylene oxide), valerolactone, polycaprolactone, polylactide and polyacrylic were used. However, these polymers have high decomposition temperature (> 250 °C) that exceed the process window for epoxy resin.

Polypropylene carbonate (PPC) polyol is an attractive porogen material for epoxy resins because of its relatively low decomposition temperature (about 180 °C) and generation of small volatile molecules upon decomposition that can diffuse through the crosslinked polymer matrix [4,9]. In this chapter, it has been shown that nanoporous epoxy resins can be formed by first grafting the epoxide functionalized PPC polyol to a polymer backbone before thermal curing with the epoxy resin. Selective decomposition of the functionalized PPC polyol leads to the formation of low dielectric constant nanoporous epoxy films.

2.2 Experimental

Materials. PPC polyol with molecular weight of 2 kDa was supplied by Novomer Inc. Catalyst 2-ethyl-4-methylimidazole (2E4MI) was obtained from Momentive Specialty Chemicals. Styrene Maleic Anhydride (SMA, M_w=9090 g/mol), with styrene to maleic anhydride ratio of 4:1, was provided by Yuan Hong Corporation. Poly(bisphenol A diglycidyl ether) (pBPADGE, M_w=1750 g/mol), allyl chloroformate and 3-chloroperbenzoic acid (m-CPBA, ≤ 77%) were purchased from Sigma-Aldrich.

Tetrahydrofuran (THF), dichloromethane (DCM) and methanol solvent were all purchased from BDH, at purity level >99%. Methyl ethyl ketone solvent (MEK, >99%) was purchased from Fisher Scientific. Pyridine (>99%) and Chloroform-d ($CDCl_3$, >99.8%) were purchased from Alfa Aesar. All chemicals were used as received.

Epoxidation of PPC Polyol. Scheme 2.1 shows the reaction procedure that yields the desired grafting product. The epoxide form of PPC (ePPC) was synthesized by dissolving 20 wt% PPC polyol in THF. 5 eq. of end capping reagent, allyl chloroformate and 5 eq. of pyridine were added dropwise to the dissolved PPC polyol at 5 °C and stirred for 2 hr. The mixture was brought to room temperature and stirred for 3 days to complete the reaction. The byproduct pyridinium-chloride salt was filtered and the resulting functionalized polymer allyl PPC (aPPC) was precipitated in the cold methanol, followed by drying in vacuum oven at 100 °C for 3 hr.

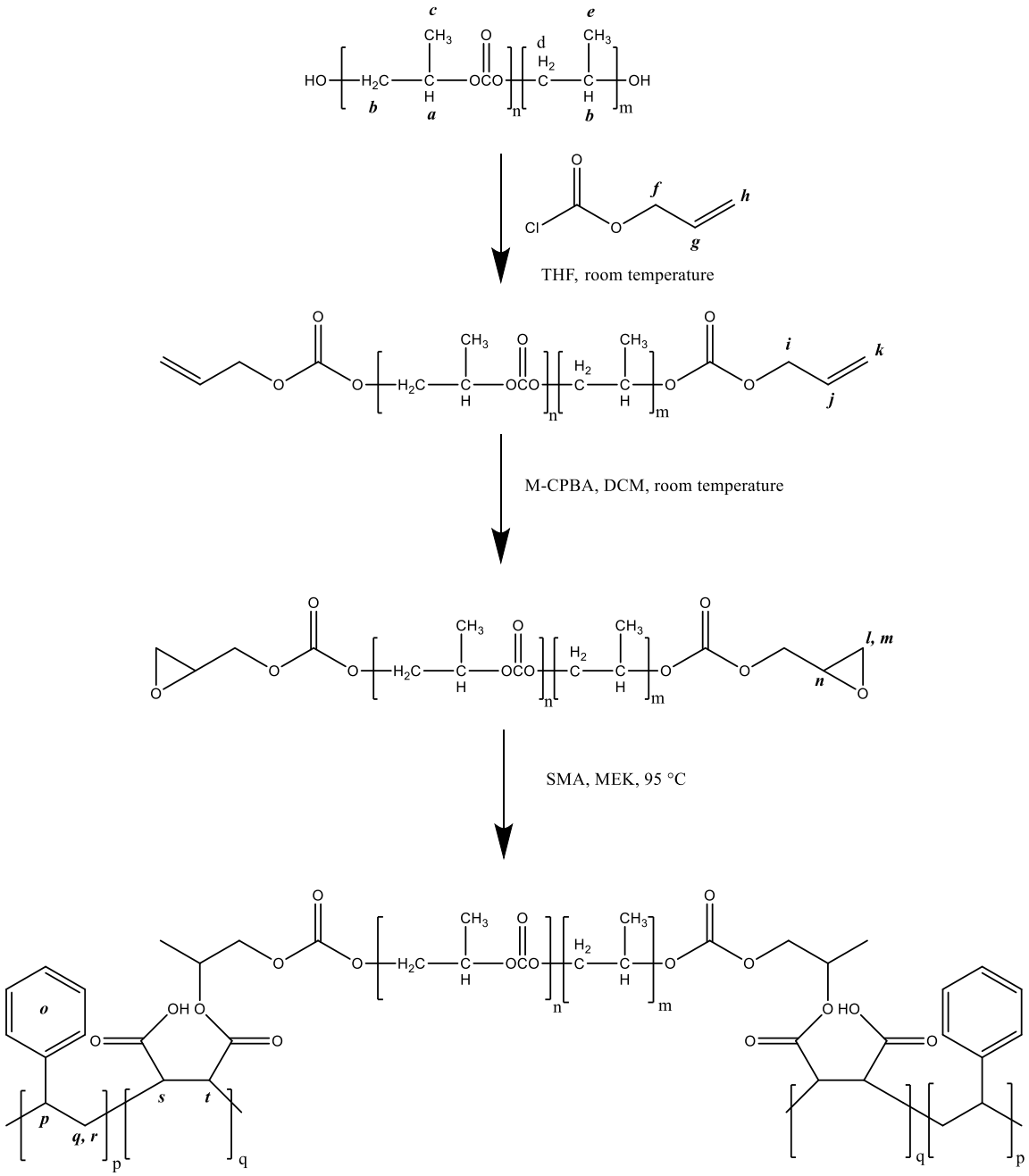

Scheme 2.1. Synthesis route for epoxidized PPC and SMA-grafted PPC

Epoxidation is finished by dissolving 20 wt% aPPC in DCM. 10 eq. of m-CPBA was added to the dissolved aPPC and mixed. Continuous stirring was performed for four days at 25 °C to form ePPC. The ePPC was precipitated in cold methanol, and air dried.

Grafting Copolymerization. The ePPC was grafted onto the SMA by ring opening the SMA maleic anhydride catalyzed by a tertiary amine 2E4MI. 10%, 20%, 30% and 50% weight fractions of grafted ePPC were prepared. The SMA was dissolved in the MEK and 1 wt% 2E4MI catalyst with respect to ePPC was added. The reaction was then refluxed at 95 °C for 6 days. The resulting product SMA-g-PPC_x was precipitated at room temperature in the methanol and the product was separated by filtration and air-dried. The x in SMA-g-PPC_x is the weight fraction of ePPC in the copolymer (e.g., 10% weight ePPC in SMA-g-PPC_x is SMA-g-$PPC_{0.1}$).

Preparation of Epoxy Resin Solution. The porous epoxy resin mixture was made by mixing 0.3 g of pBPADGE with SMA-g-PPC_x, where the amount of SMA corresponded to 0.4 g within the SMA-g-PPC_x. Mixtures where made corresponding to weight fractions of 0%, 5%, 13% and 20% ePPC within the total mass. MEK was used as the solvent. The mixture was sonicated at room temperature.

Film Formulation. Silicon wafers were cleaned using acetone and dried in a nitrogen stream. CHA Modified Mark-40 E-beam evaporator was used to deposit metal films at a pressure below 10^{-5} torr. Titanium was deposited at the rate of 1 Å/s to a thickness of 30 nm followed by aluminum (99.99% pure), 800 nm thick, at a rate of 2 Å/s. The pBPADGE/SMA-g-PPC_x solution was spin coated onto the silicon at a ramp rate of 1500 rpm to a speed of 1500 rpm for 10 seconds. The films were cured by first soft baking at 50 °C for 1 min, followed by 75 °C for 18 hr to begin the pBPADGE-SMA reaction and 180 °C for 6 hr to decompose the PPC. Finally, the pBPADGE was fully cured at 220 °C for 10 min to ensure complete PPC decomposition and to complete the epoxy curing. A 300

nm top layer of aluminum was deposited at 2 Å/s by evaporation on the cured polymer film for capacitance measurements.

Characterization. The ePPC synthesis (i.e. aPPC, ePPC, and SMA-g-PPC_x) was characterized by ^1H NMR using a Varian Mercury Vx 400 (400 MHz) spectrometer before and after the functionalization PPC polyol using chloroform-D as the solvent. 0.5 mg of polymer was dissolved in 0.75 ml of chloroform-D for the ^1H NMR analysis using 32 scans with relaxation time of 1 s. The $CDCl_3$ peak was calibrated at 7.26 ppm.

Differential scanning calorimetry (DSC) was performed (TA Instruments Q20) to examine the T_g of the crosslinked polymer film. The film was sealed in a platinum pan and ramped at a rate of 10 °C/min to 200 °C. Thermogravimetric analysis (TGA) was performed (TA Instruments Q50) to investigate the PPC decomposition temperature and weight fraction in the formulation. The platinum pan was cleaned in acetone and re-zeroed before each run. PPC polyol, aPPC and ePPC were ramped at rate of 5°C/min to 400°C. The SMA-g-PPC_x and formulated polymer films were ramped at 5 °C/min to 500 °C.

The capacitance and tangent loss of the epoxy films were measured with a GWinstek LCR-821 meter. At least five capacitors with an electrode area of 0.065 cm^2 were measured for each data point. The frequency was controlled at 200 kHz and bias was set to 1.275 V. The dielectric constant was calculated based on $\varepsilon = Cd/(A\varepsilon_0)$, where C is the capacitance, ε_0 is the vacuum permittivity ($8.85*10^{-12}$ F/m), A is the area of the smaller electrode, and d is the dielectric thickness.

A Hitachi SU8230 scanning electron microscope (SEM) was used to image cross-sections of the polymer film. The SEM was operated at 1 kV with emission current of 5

mA. Nitrogen absorption isotherms of the films were measured at 77 K on a Quadrasorb system from Quantachrome Instruments.

The reduced modulus and hardness of the spin-casted films were determined using a Hysitron Triboindenter with a 1 μm diameter conical tip. The indent depth was less than 10% of the film thickness. The indent depth for the 0%, 5%, 13% and 20% porogen samples was 67 nm, 79 nm, 98 nm, and 56 nm, respectively. A polycarbonate sample was used as the reference to calibrate the projected area coefficient. 4-point data were obtained between 50 μN to 200 μN with an interval of 50 μN to avoid substrate effects. The reduced modulus of the film can be determined using Equation 1.

$$\boldsymbol{E_r = \frac{\sqrt{\pi}}{2\beta}\frac{dP/dh}{\sqrt{A}}} \quad [1]$$

In Eq. 1, E_r is the reduced modulus of the material tested, β is a geometric constant on the order of unity, dP/dh is the slope of the linear portion of the unloading curve, and A is the projected area of the indentation.

2.3 Results and Discussion

Functionalization of PPC polyol. The first step in the modification of PPC was to react the hydroxyl free-ends with the allyl chloroformate via S_N2 nucleophilic substitution forming aPPC. The aPPC was then functionalized to ePPC by Prilezhaev epoxidation as described in the experimental section. The ^{1}H NMR spectrum for the PPC polyol and its subsequent functionalized products are shown in the Figure 2.1. Figure 2.1a shows the ^{1}H NMR of PPC polyol. The major PPC polyol peaks were identified as follows: ^{1}H NMR ($CDCl_3$, δ, ppm), 4.92 – 5.02 (1H: CH, peak *a*), 4.1 – 4.5 (2H: CH_2, peak *b*), 1.35 – 1.4 (3H: CH_3, peak *c*), 3.95 – 4.05 (2H: CH_2, 1H: CH, peak *d*), 1.0 (3H: CH_3, peak *e*). The

ratio of peak a: peak b: peak c is 1:2:3. This proton ratio on the PPC polyol backbone matches with the integration of the peak in the PPC polyol ^{1}H NMR spectrum and is consistent with previous results [9].

Figure 2.1b shows the ^{1}H NMR of allyl chloroformate. The peaks for allyl chloroformate shown in Figure 2.1b were identified as follows: ^{1}H NMR ($CDCl_3$, δ, ppm), 4.77 – 4.83 (2H: –CH_2–, peak *f*), 5.9 – 6.02 (1H: CH, peak *g*), 5.35 – 5.5 (2H: =CH_2, peak *h*). The ratio of peak a: peak b: peak c is 2:1:2. This ratio matches the proton ratio on the molecule. Fig. 2.1c shows the ^{1}H NMR spectrum of aPPC. Major PPC backbone spectrum still matches the PPC polyol spectrum with the correct ratio and all the protons identified on the NMR spectrum are the same as Figure 2.1a. Proton peaks' position for the end-capped allyl chloroformate were identified as follows: ^{1}H NMR ($CDCl_3$, δ, ppm), 4.57 – 4.63 (2H: –CH_2–, peak *i*), 5.85 – 5.95 (1H: CH, peak *j*), 5.22 – 5.37 (2H: ═CH_2, peak *k*). Comparison of peaks of allyl chloroformate before and after reaction show a slight upfield shift of the protons on the allyl group. The shift in the allyl protons is due to the substitution of hydroxyl for chlorine on the PPC bonded to the carbonyl group on allyl chloroformate. Oxygen is less electron withdrawing than chlorine, leading to the upfield shift of the allyl protons. Moreover, the formation of water-soluble pyridinium-chloride solid caused by the S_N2 reaction indicates that the reaction has occurred. Thus, the proton shift of the allyl group and formation of the water-soluble salt confirm that PPC polyol have been converted to aPPC. The molecular weight of the aPPC was calculated using end-group analysis based on ^{1}H NMR spectrum. Integration of peaks at 4.92 ppm – 5.02 ppm and 5.22 ppm – 5.37 ppm gives a ratio of 19.64 of PPC repeat units to a single allyl proton. The molecular weight of aPPC is determined to be 2,205 Da. This value matches the expected molecular weight

of aPPC based on the starting weight of PPC polyol of 2 kDa. Thus, there appears to be a complete conversion of PPC polyol to aPPC.

The aPPC was then converted to ePPC by oxidation of the allyl double bond with m-CPBA. Figure 2.1d shows the ^{1}H NMR spectrum of ePPC. The major peaks for the PPC backbone remain with the correct peak area ratio and all the protons identified on the spectrum is the same as Figure 2.1a. Peaks position for the epoxide ring were identified as follows: ^{1}H NMR ($CDCl_3$, δ, ppm), 2.65 – 2.70 (1H, CH, peak *l*), 2.85 – 2.9 (1H, CH, peak *m*), 3.23 – 3.28 (1H, CH, peak *n*). The ratio of peak a: peak b: peak c is 1:1:1 matches with the proton ratio on the epoxide ring. The complete disappearance of allyl proton peaks at 4.57 ppm – 4.63 ppm, 5.85 ppm – 5.95 ppm and 5.22 ppm – 5.37 ppm, and appearance of epoxide ring peaks at 2.65 ppm – 2.70 ppm, 2.85 ppm – 2.90 ppm and 3.23 ppm – 3.28 ppm show that the conversion of aPPC to ePPC was completed. The molecular weight of ePPC was calculated using end group analysis based on ^{1}H NMR spectrum. Integration of peaks at 4.92 – 5.02 ppm and peaks at 2.65 ppm – 2.70 ppm gives a ratio of 27.16 of PPC repeat units to the epoxide ring on both ends, which corresponds to a molecular weight of 3 kDa for ePPC.

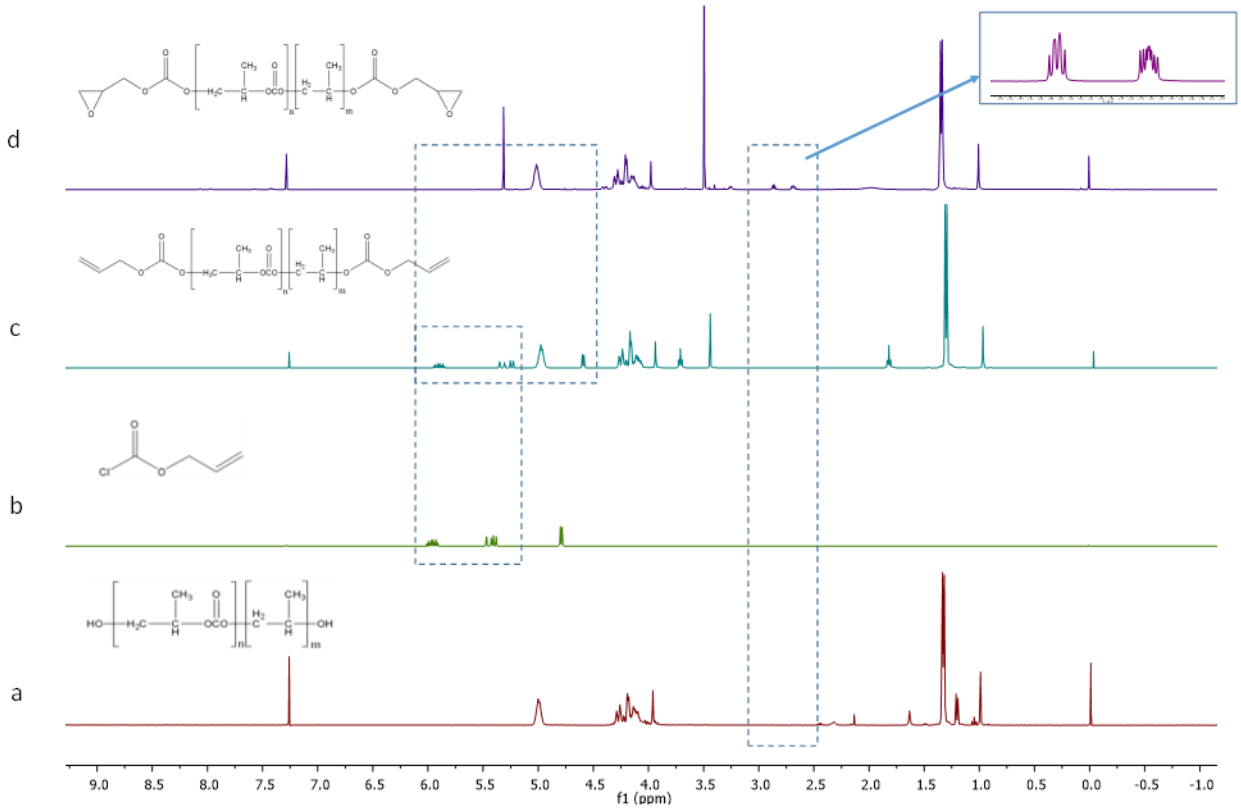

Figure 2.1. ^{1}H NMR spectrum for a) PPC polyol, b) allyl chloroformate, c) aPPC, d) ePPC

The TGA of PPC polyol, aPPC and ePPC are shown in Figure 2.2. PPC polyol decomposes by two mechanisms, end-unzipping (or sometimes called backbiting) which occurs first at a lower temperature, and random chain scission which usually occurs at a higher temperature [9]. The onset of thermal degradation of aPPC was similar to that of PPC polyol. However, the degradation process was completed at a slightly higher temperature because the allyl chloroformate stabilized the ends of the PPC polyol. This forced the reaction to occur more through random chain scission, leading to a higher temperature process. The thermal degradation of ePPC also occurred at a slightly higher

temperature than PPC polyol because of the suppression of the end-group unzipping reaction. Complete decomposition of ePPC occurred at a higher temperature than PPC polyol due to the stabilization of the end group, forcing the random chain scission to dominate.

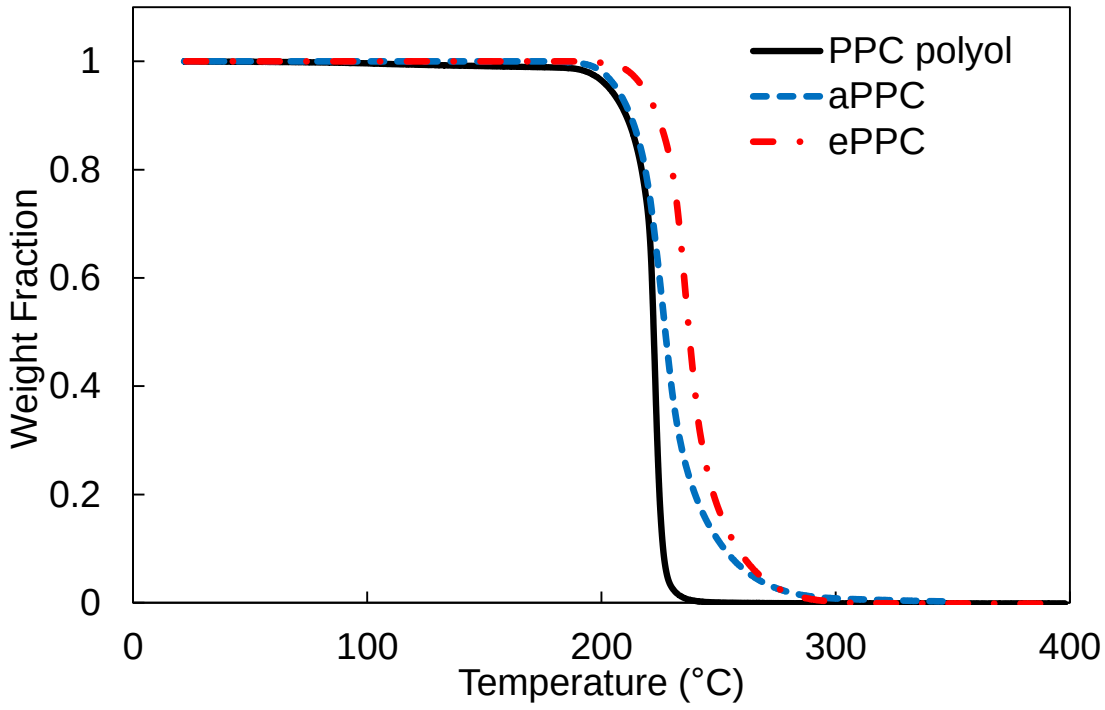

Figure 2.2. Thermal decomposition profile for PPC polyol, aPPC, ePPC

Synthesis and Characterization of SMA-g-PPC$_x$. SMA is known to improve the properties of epoxy resin formulations, including raising the T_g and lowering the dielectric constant [82]. The anhydride monomers within SMA provide sites for epoxy crosslinking. PPC has been shown to be a porogen within epoxy polymer films by decomposing during or after polymer gelation [36]. However, the immiscibility of PPC with epoxy leads to phase segregation of the PPC, resulting in large pores up to several micrometers [36]. In this chapter, ePPC was grafted onto SMA before crosslinking with pBPADGE. Grafting

PPC onto SMA can help to mitigate phase segregation since ePPC is stabilized by covalent bonding to the SMA copolymer. The ratio of styrene to maleic anhydride in the SMA was evaluated by ^{1}H NMR shown in Figure 2.3a. The broad peak in the range 5.75 ppm – 8 ppm represents five aromatic protons (annotated as *o* in the chemical formula of SMA) on styrene. The broad peak in the range 0.75 ppm – 3 ppm represents the remainder of the SMA protons, including three protons on a single styrene molecule (annotated as *p*, *q*, *r* in the chemical formula of SMA) and two protons on a single maleic anhydride molecule (annotated as *s* and *t* in the chemical formula of SMA). The ratio between the two peaks was determined to be 10:7 based on ^{1}H NMR spectrum. Assuming there are x moles of styrene and y moles of maleic anhydride in 1 mole of SMA, the ratio of the two peaks can be represented by 5x/(3x+2y). Since 5x/(3x+2y) is equal to 10/7, the ratio between x and y, i.e., the ratio between styrene and maleic anhydride, was determined to be 4:1.

Figure 2.3b – 2.3d show the ^{1}H NMR for the final product of SMA-g-PPC$_x$ with loadings of 10 wt%, 20 wt% and 30 wt% ePPC. The styrene to ePPC ratio before the reaction was determined by calculating number of moles of styrene and ePPC that were added into the reaction flask. The ratio between styrene and ePPC after the reaction was determined by ^{1}H NMR using the ratio between styrene aromatic peak *o* at 5.75 ppm – 8 ppm and ePPC peak *a* at 4.92 ppm – 5.02 ppm. Each styrene contains 5 aromatic protons, therefore number of moles of styrene can be calculated by dividing its integral by 5. Similarly, ePPC peak at 4.92 ppm – 5.02 ppm represents 19 repeat units for the ePPC backbone. Thus, the number of moles of ePPC can be determined by dividing its integral by 19. Table 2.1 summarizes the ratio of styrene to ePPC before and after the reaction.

Similar ratios of styrene to ePPC was obtained for each of the three grafting reactions. This shows that most of the ePPC added was grafted onto the SMA.

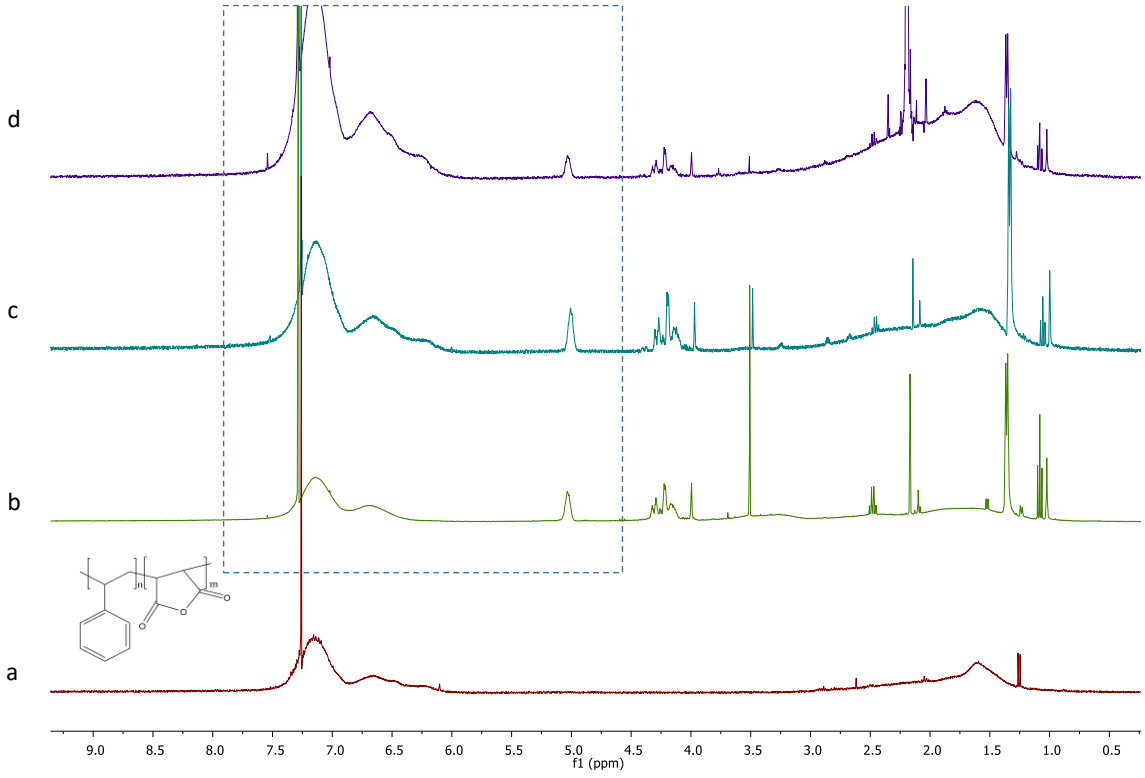

Figure 2.3. ^{1}H NMR spectrum for a) SMA, b) SMA-g-PPC$_{0.1}$, c) SMA-g-PPC$_{0.2}$, d) SMA-g-PPC$_{0.3}$

Table 2.1. Molar ratio of styrene to ePPC before and after the reaction.

ePPC added for reaction (g)	SMA added for reaction (g)	Expected mole ratio of Styrene : ePPC in the final product	Actual mole ratio of Styrene : ePPC in the final product
2.48	4.68	45:1	50:1
1.36	4.68	70:1	86:1
0.486	4.68	195:1	200:1

Figure 2.4 shows the TGA result for the decomposition of SMA-g-PPC_x products. For SMA-g-$PPC_{0.1}$, SMA-g-$PPC_{0.2}$ and SMA-g-$PPC_{0.3}$, 10%, 20% and 30% weight loss was observed between 150 °C and 300 °C, while pure SMA showed no weight loss in that temperature range. The ePPC decomposition started at a lower temperature than before it was grafted onto SMA due to the addition of the amine catalyst that catalyzed the decomposition reaction. The ePPC also decomposed at a much slower rate due to the protection of the bulky end group that restrict end-unzipping. For SMA-g-$PPC_{0.5}$, only 32% weight loss was observed between 150 °C and 300 °C. This shows that only 64 wt% of ePPC added to the SMA for reaction resulted in SMA-g-$PPC_{0.5}$ formation. The result suggests that a maximum loading of about 32 wt% PPC can be grafted onto SMA with 4:1 styrene maleic anhydride copolymer. This limitation to further grafting ePPC onto other vacant anhydride sites on SMA may be due to the steric hindrance of the grafted ePPC on the SMA.

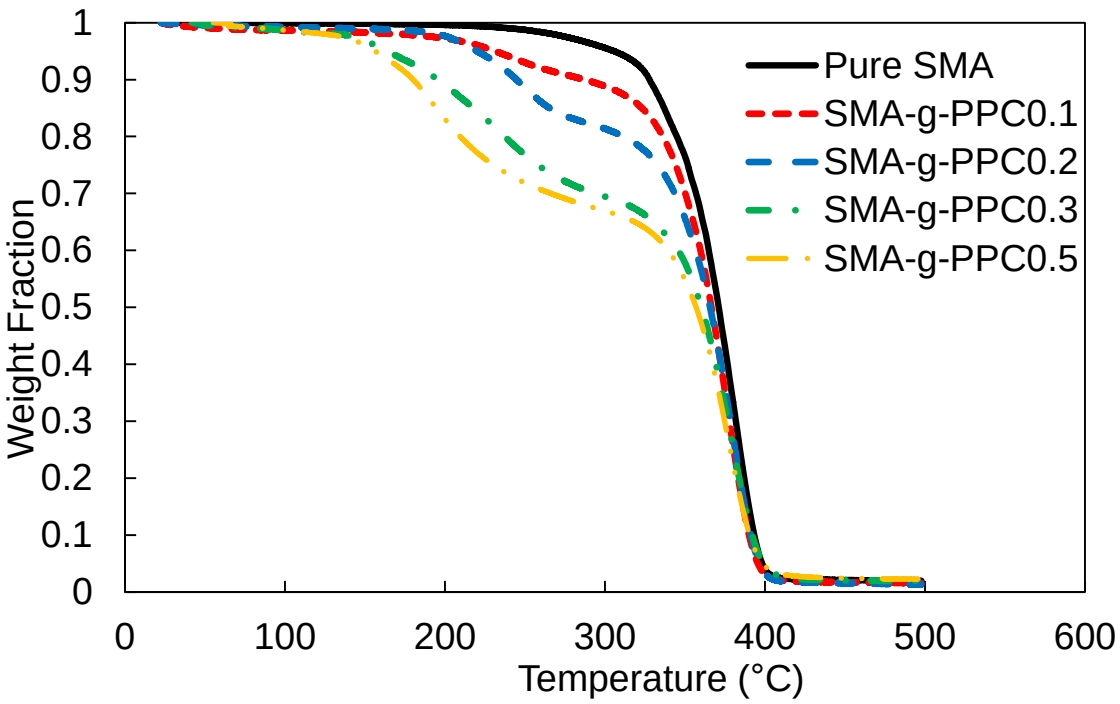

Figure 2.4. Thermal decomposition profile for SMA-g-PPC$_x$

Film Properties and Characterization. Curing of the epoxy resin film is desirable before ePPC decomposition to ensure the formation of closed pores. Thus, confirmation of crosslinking before decomposition is important. Park et.al. demonstrated the cure behavior of an epoxy-anhydride-imidazole system, where a tertiary amine could initiate the crosslinking between epoxy and anhydride molecules at 75 °C for 18 hours [83]. Crosslinking was confirmed by observing the increasing of T_g due to the addition of anhydride molecules in the resin formulation [83]. For the first stage, the film was each cured at 75 °C for 18 hours to ensure that crosslinking occurred. Figure 2.5a shows the TGA for the film after the first stage curing. About 5 wt% residual solvent evaporated before the decomposition of ePPC. For SMA-g-PPC$_{0.1}$, SMA-g-PPC$_{0.2}$ and SMA-g-PPC$_{0.3}$ crosslinked films, 5%, 13% and 20% weight loss was observed between 150 °C and 300

°C. The pure SMA showed no weight loss in the same temperature range. This shows that ePPC decomposition did indeed occur. These films were subsequently brought to 180 °C for 6 hr and finally to 220 °C to complete the ePPC decomposition. Figure 2.5b shows the TGA spectrum for the film after the decomposition of ePPC. No weight loss occurred until 320 °C, suggesting that all the ePPC were removed after the 220 °C step. The density of different starting materials was similar: pBPADGE 1.17 g/cm^3, SMA 1.08 g/cm^3, and PPC 1.2 g/cm^3. Thus, the mass fraction of ePPC could be used to estimate the pore volume fraction inside the film, assuming the components did not change density when mixed. This results in pore volumes of 5%, 13% and 20% pore volume in the films SMA-g-PPC$_{0.1}$, SMA-g-PPC$_{0.2}$ and SMA-g-PPC$_{0.3}$, respectively.

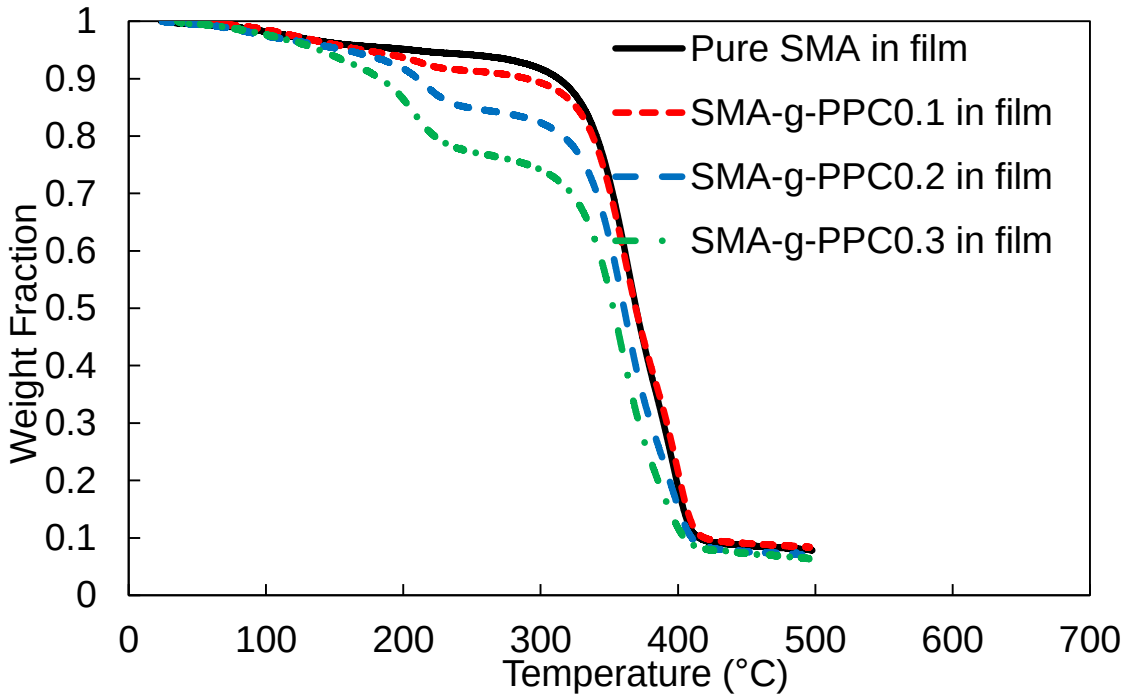

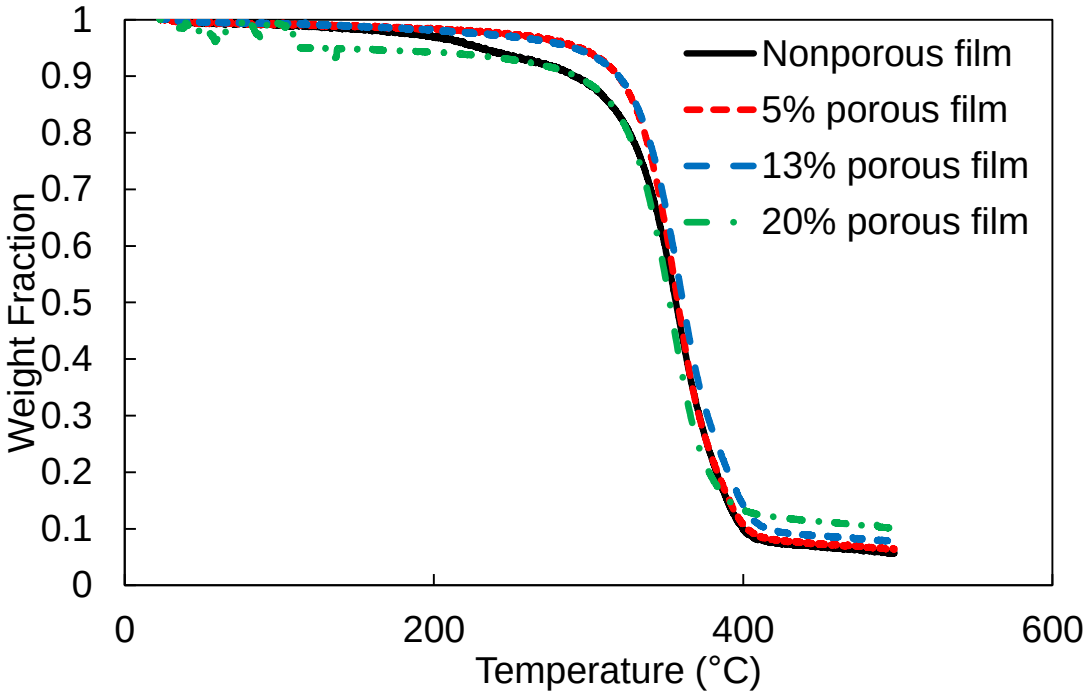

Figure 2.5. Thermal decomposition profile for SMA-g-PPC$_x$ crosslinked films a) before removal of porogen, b) after removal of porogen

Cross-sectional SEM images of the polymer films spin-coated on aluminum coated silicon wafers are shown in Figure 2.6. Spin speed of 1500 rpm/s resulted in similar thickness of 1.05 µm, 1.11 µm, 1.04 µm, and 1.08 µm, for films with 0%, 5%, 13%, and 20% volume fraction ePPC. Figure 2.7 is a high magnification image to examine if the pores are large enough to be observed. Figure 2.7a shows the cross section of a nonporous film where no pores were observed. Figure 2.7b and 2.7c show the 5% and 13% porous epoxy films where there were also no pores observed. However, in Figure 2.7e, where the 10 wt% ePPC was directly mixed with SMA and pBPADGE without grafting the ePPC onto SMA before curing, large pores up to 90 nm are observed. This shows that the pores inside Figure 2.7b and 2.7c are small enough that using SEM to observe the pore size is

difficult. Figure 2.7d shows the 20% porous epoxy film where some small pores are observed.

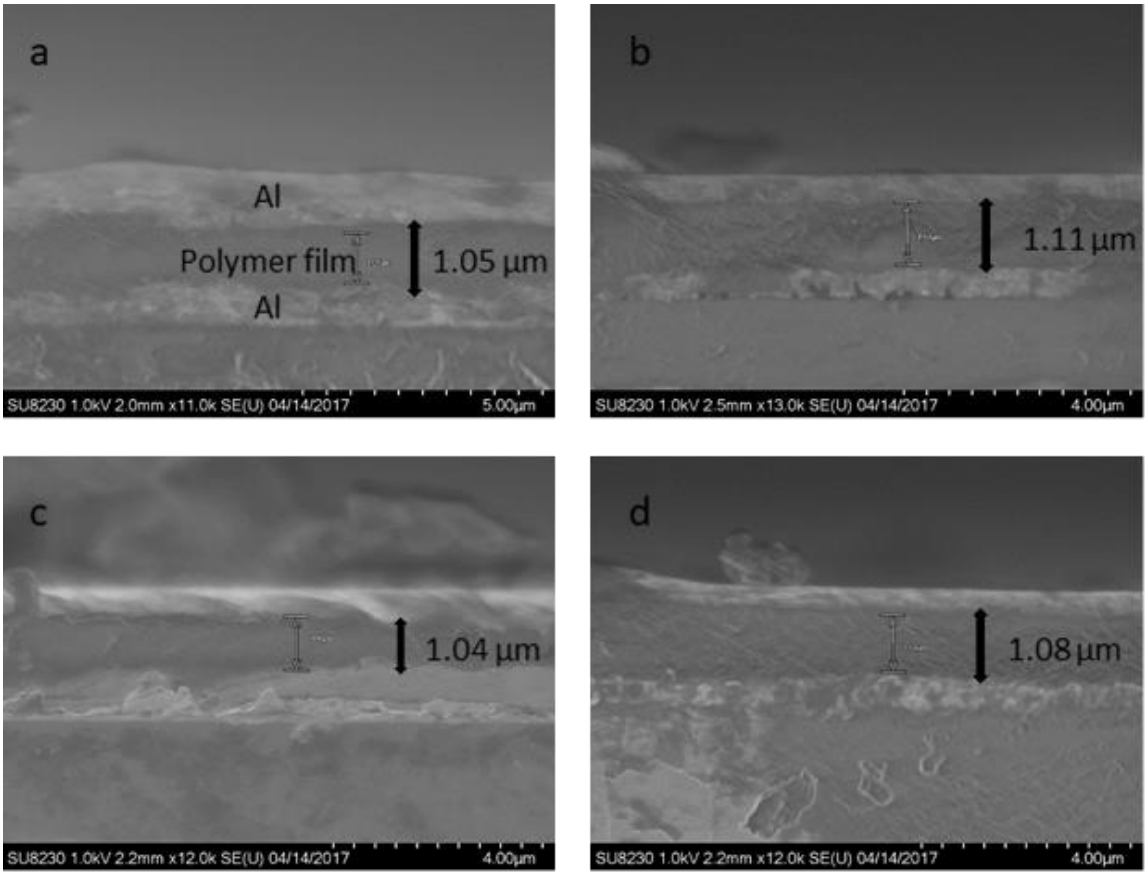

Figure 2.6. SEM image of cross-section thickness for a) nonporous film, b) 5% porous film, c) 13% porous film, d) 20% porous film, e) 10% porous film without grafting ePPC

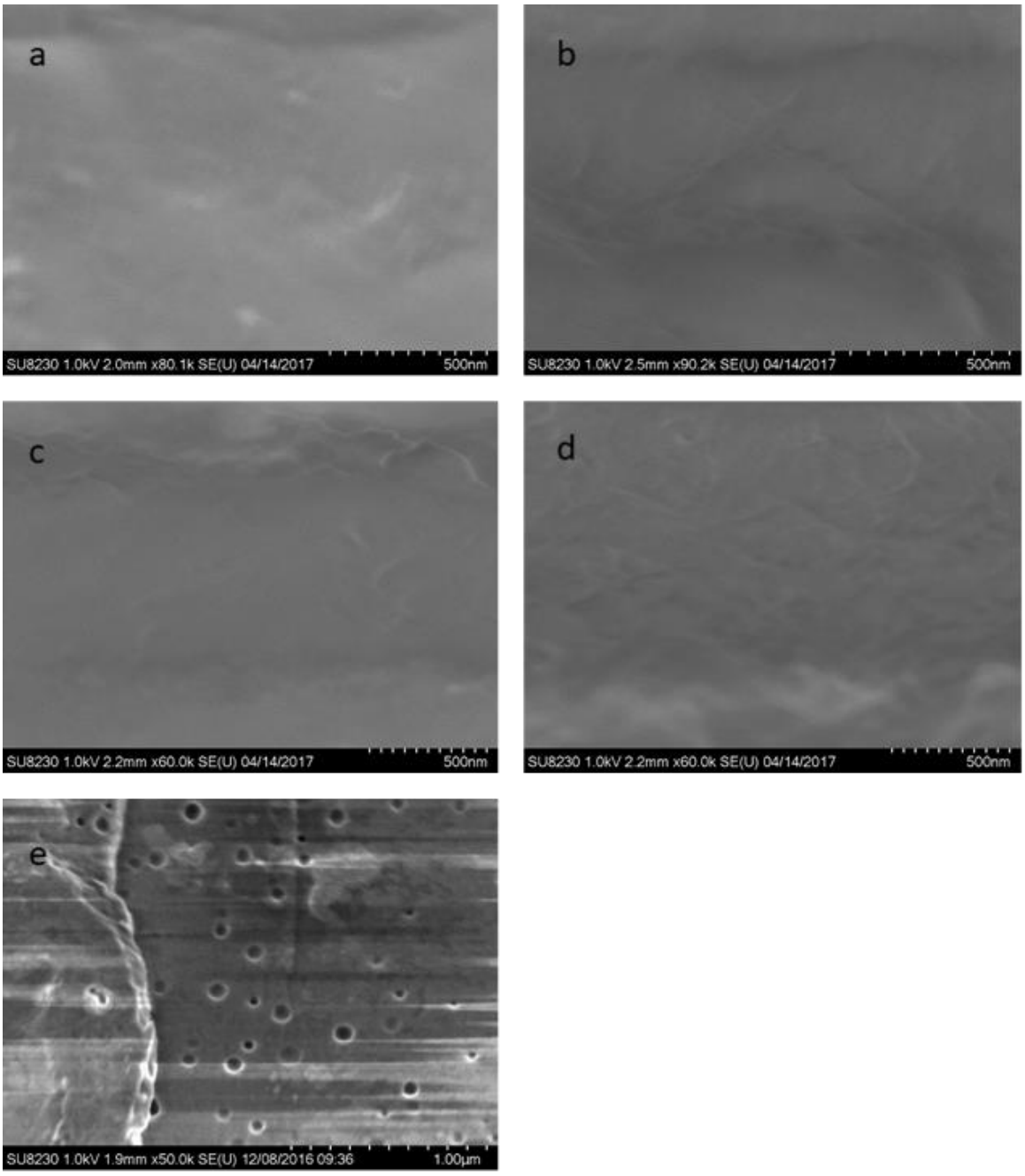

Figure 2.7. SEM image of pore size for a) nonporous film, b) 5% porous film, c) 13% porous film, d) 20% porous film, e) 10% porogen mixed into epoxy without chemical grafting

Nitrogen absorption measurements were performed to further investigate the pore size in the films. Figure 2.8 shows the nitrogen absorption result for films with 0%, 5%, 13% and 20% pore volume. Pore volume in the range of 3 to 5 nm was observed within all the epoxy films, including the non-porous film. This is likely due to the pore volume within the crosslinked polymer chains. Pores in the range of 6 to 8 nm were found in the films with 5%, 13% and 20% porogen. The molecular size of the 2000 g/mol porogen is about 3 nm^3, which is in the range of the pores found within the epoxy matrix. For the 20% porous epoxy film, larger pores between 15 to 20 nm were observed. This pore size distribution from the nitrogen absorption experiment agrees with the SEM image, where larger pores could only be observed for 20% porous epoxy film by SEM. This increase in pore size for the 20% porous epoxy film may be caused by the reaction of ePPC with other ePPC sites during the curing stage, leading to the increase of pore size upon decomposition. The densely grafted SMA-g-$PPC_{0.3}$ has ePPC chains that are more likely to interact with each other, thus leading to an increase in the pore size.

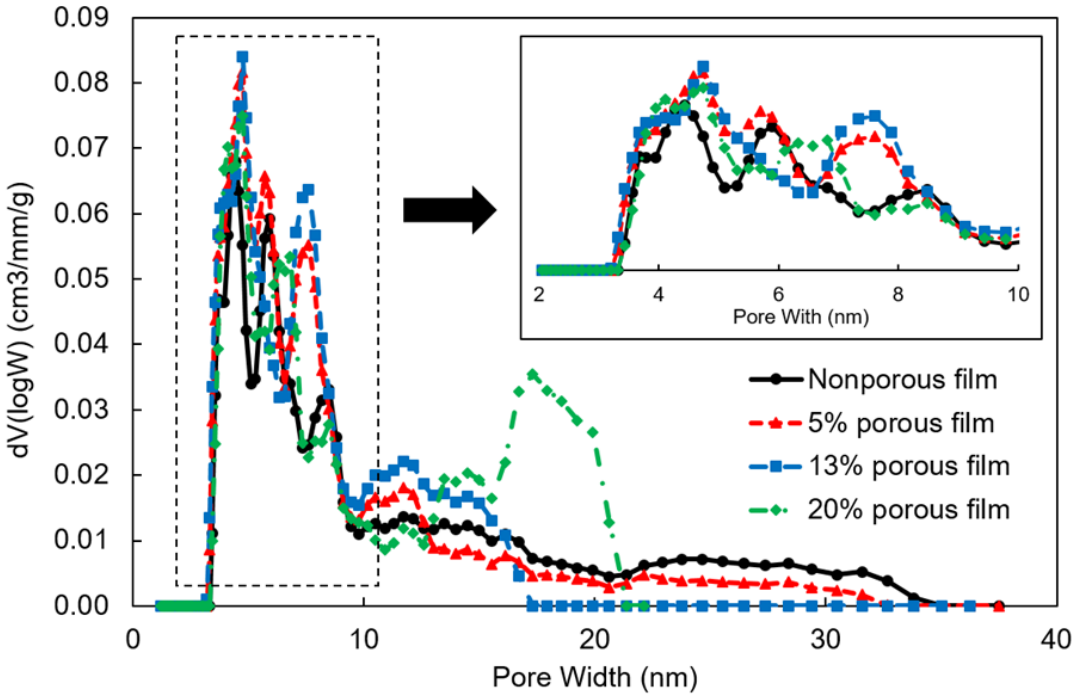

Figure 2.8. Nitrogen absorption for films with different pore density

To examine the effect of the pore volume fraction on the dielectric constant, capacitance values for different capacitor structures were measured. Figure 2.9 shows the dielectric constant and loss of the formulations with the error bars set a one standard deviation. At least five capacitors were measured for each data point. For the nonporous epoxy film, the dielectric constant was 3.22 and the tangent loss was 0.0185. 5% porosity into the film lowered the dielectric constant to 3.17 and the loss tangent dropped to 0.0146. Increasing the porosity to 13% lead to a film with 2.91 dielectric constant and 0.0141 loss tangent. The loss tangent may not be dropping as rapidly as the dielectric constant because of water or hydroxyl coverage of the pore walls. This will be addressed in a chapter 3. When the porosity was increased to 20%, dielectric constant dropped to 2.77, however the loss tangent remained about the same at 0.0150. The mixing rule based on two different

models, Maxwell equation of volume averaging theory (VAT), which is expressed in Equation 2 and Lichtenecker's rule, Equation 3, are shown below.

$$\boldsymbol{\varepsilon_{eff} = (1 - P)\varepsilon_m + P\varepsilon_i} \quad [2]$$

$$\boldsymbol{ln\varepsilon_{eff} = P * ln\varepsilon_i + (1 - P) * ln\varepsilon_m} \quad [3]$$

In Eq. 2 and 3, ε_m is the dielectric constant of the epoxy film, ε_i is the dielectric constant of the air, and P is the porosity of the film [84]. In these two models, the porosity of the epoxy films was modelled as a two-component system, consisting of air and epoxy. The experimental results agree with predicted values based on the VAT model, where the measured dielectric constant decreased linearly. The experimental data also gave less than a 2.2% deviation from the VAT model and an 8.3% deviation from the Lichtenecker model.

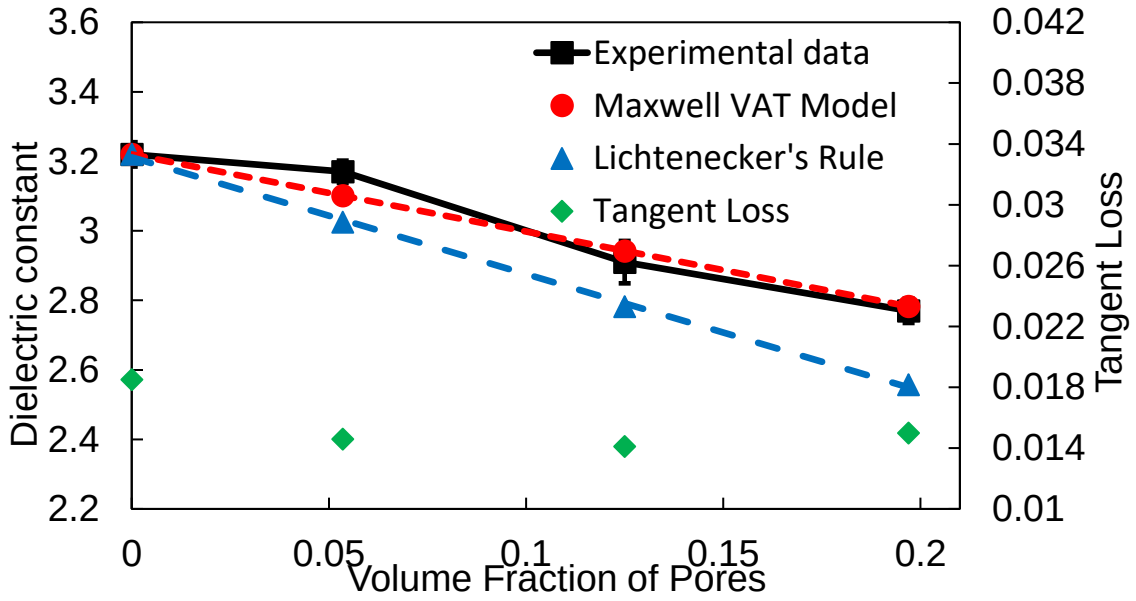

Figure 2.9. Dielectric constant and tangent loss of the films

T_g of the crosslinked films was studied using DSC. Figure 2.10 shows the DSC curve for samples containing 0%, 5%, 13% and 20% porosity. All the films have a T_g between 140 °C and 160 °C. The non-porous epoxy/SMA crosslinked film had a T_g of 157 °C. The T_g of porous films was somewhat lower at 142 °C due to the decrease of crosslink density after the decomposition of the ePPC leaving pore volume for polymer chain to move in a less hindered environment.

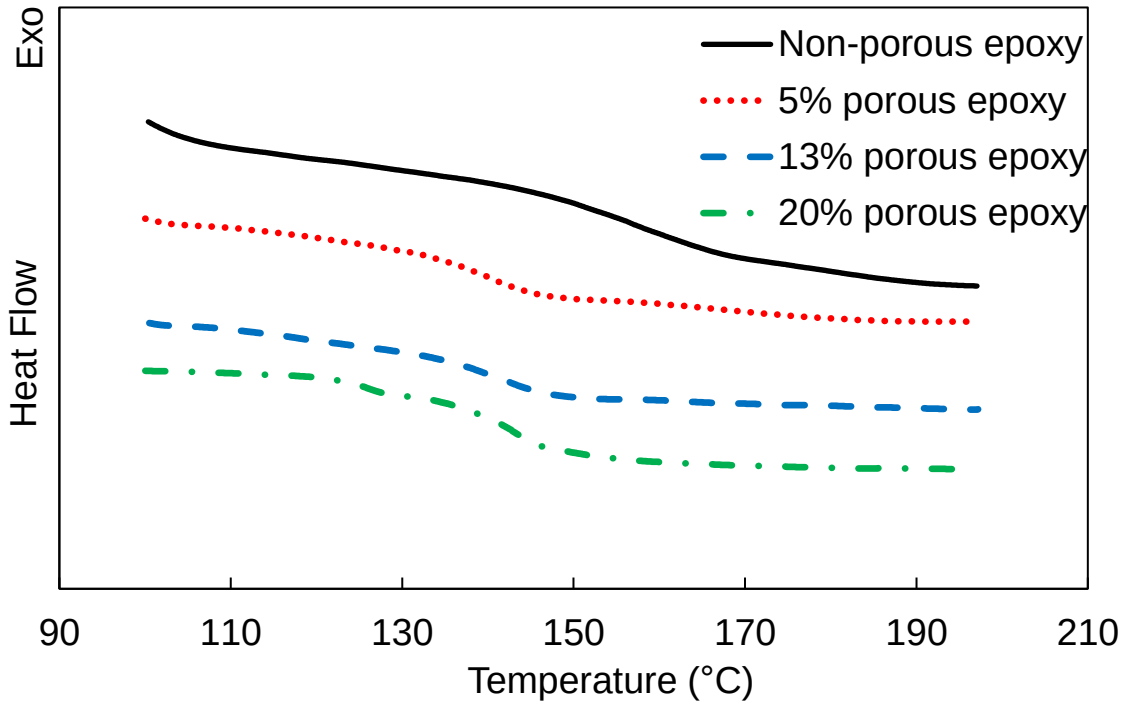

Figure 2.10. Glass transition temperature for films with different porosity

Mechanical properties of the crosslinked films, including reduced modulus and hardness, were studied using nanoindentation, Figure 2.11. For the nonporous epoxy film, the reduced modulus based was 10.4 GPa. The reduced modulus dropped slightly to 10.3 GPa for film with 5% porosity. The reduced modulus was 8.13 GPa for film with 20% porosity. The reduction in reduced modulus with increase in porosity of the epoxy film is

caused by the decrease in crosslink density of the film. The decrease in crosslink density happens due to the decomposition ePPC, which was previously crosslinked to the SMA and pBPADGE. This may be corrected by changing the styrene to maleic anhydride ratio. The hardness of the film also decreased from 0.44 for nonporous epoxy film to 0.36 for the 20% porous epoxy film, due to the decrease in crosslink density caused by the increasing pore volume.

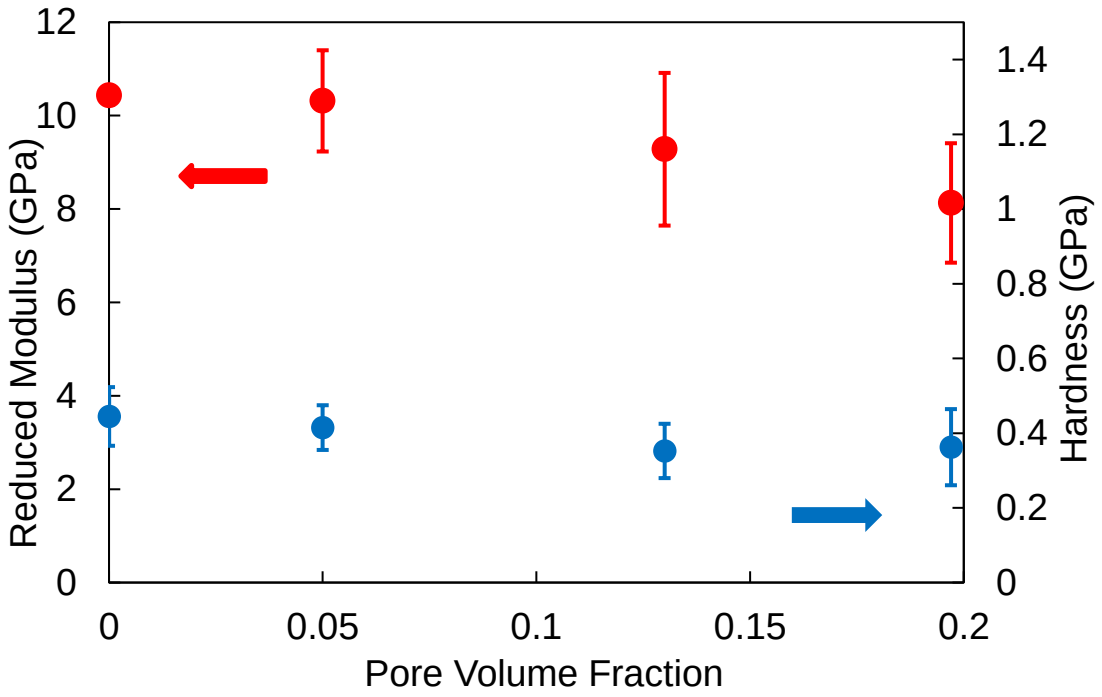

Figure 2.11. Reduced modulus and hardness for films with different porosity

2.4 Summary

In this work, we described the synthesis of SMA-grafted PPC copolymer, and used this grafting copolymer for preparation of nanoporous epoxy films. Nanoporous thin films were obtained by thermal decomposition of a PPC porogen crosslinked to the

pBPADGE/SMA system. The chemical crosslinking of PPC with SMA prevented the aggregation of PPC molecules and restricted the formation of large pores inside the epoxy film. Pore size lower than 10 nm was observed inside the epoxy film with the PPC-grafted formulation. The electrical and mechanical properties of the film based on different percent pore volume was studied. The dielectric constant of the epoxy film was lowered with increasing the pore volume without significantly sacrificing the mechanical properties of the films. A new functionalized porogen materials was demonstrated in this chapter that could be incorporated into the epoxy film without degrading the mechanical and electrical properties of the film. The ease of processing of this low dielectric constant epoxy film makes it potentially useful for electronic applications involving advanced devices.

CHAPTER 3.

LOW DIELECTRIC CONSTANT AND LOSS, NANOPOROUS EPOXY THIN FILM FOR ELECTRONIC PACKAGING

3.1 Introduction

In the previous chapter, we demonstrated a nanoporous epoxy film by grafting porogenic materials onto the crosslinker to immobilize it from aggregation. In this chapter, a direct mixing of all formulation into one pot, followed by conventional curing stages, is demonstrated to show similar effect on improving dielectric properties without hurting extensively thermal-mechanical properties. Moreover, a hydrophobic treatment is demonstrated to further improve the dielectric properties described in chapter 2.

Epoxy resins are the dominant insulator for printed wiring board (PWB) and interconnect owing to their good electrical, thermal, and mechanical properties [3,56,85,86]. Cured epoxy resin has several advantages over other dielectric materials. It has better adhesion strength compared to other polymers (e.g., polytetrafluoroethylene (PTFE) [87]), which allows laminated metal layers and sputtered metal contacts to be easily fabricated into a substrate [85,88]. In addition, epoxy resin has competitive coefficient of thermal expansion (CTE) compared to other materials [56]. Moreover, epoxy resins are relatively low-cost compare to other low-k materials, making them cost-effective [89]. However, it is difficult to lower dielectric constant of epoxies, which is needed for higher speed electronic components, because of the polarity of the resulting hydroxyl, ether and ester moieties that form upon curing [62,90–93]. Thus, methods to lower the dielectric constant of epoxy-based materials without sacrificing mechanical or chemical properties

are needed so that the same basic set of materials can be used to meet the need of advanced packaging while maintaining current fabrication processes.

Various methods have been investigated to reduce the dielectric constant of epoxy-based polymers. These methods include synthesizing hyperbranched epoxy thermosets to increase the free volume in the crosslinked network [63], addition of mesoporous silica nanoparticles [64,94], reducing polarization of the molecular structures by incorporating low polarity molecules such as oligometric silsesquioxane and dicyclopentadiene [65,95], and fluorination of the epoxy backbone [66,96,97]. Previously, we demonstrated a method of bonding a functionalized sacrificial polymer, epoxide functionalized poly(propylene carbonate) (ePPC), onto the epoxy crosslinker, styrene maleic anhydride (SMA), to immobilize the ePPC [98]. The resulting ePPC grafted copolymers were included in the epoxy resin formulation and thermally cured, followed by removal of the ePPC porogen at higher temperature resulting in a nanoporous epoxy resin. While this approach resulted in lowering in dielectric constant, the grafting reaction added an additional step to the manufacturing process.

In this chapter, electrical, mechanical and thermal properties of nanoporous epoxy films were studied for films crosslinked via mixing of epoxy resin, SMA, and ePPC into a formulation and cured by following a conventional curing process. Two types of SMA crosslinker, SMA2000 and SMA4000, were investigated to see how the styrene to maleic anhydride ratio in the SMA affected the thermal, mechanical, and dielectric properties of the nanoporous epoxy resin. The index of refraction was used to show pore formation within the epoxy resin. Nanometer size pore structures observed using scanning electron microscopy. Dielectric properties were measured to quantify the decrease in dielectric

constant with porosity. Furthermore, the hydrophobicity was increased by post-pore formation treatment to improve the dielectric loss of the porous epoxy resins.

3.2 Experimental

PPC polyol with molecular weight of 2 kDa was supplied by Novomer Inc. Epoxy resin EPON 1134 and Epikote Resin 523 and catalyst 2-ethyl-4-methylimidazole (2E4MI) were obtained from Momentive Specialty Chemicals. Styrene maleic anhydride 4000 (SMA4000, with styrene to maleic anhydride ratio of 4:1) was provided by Yuan Hong Corporation. Styrene maleic anhydride 2000 (SMA2000, with styrene to maleic anhydride ratio of 2:1) was purchased from Sigma Aldrich. Methyl ethyl ketone solvent (MEK, >99%) was purchased from Fisher Scientific. Hexamethyldisilazane (HMDS) was purchased from Alfa Aesar. All chemicals were used as received.

Epoxide functionalized PPC (ePPC) was synthesized using a previously reported method, as shown in Scheme 3.1 [98]. NMR of the resulting ePPC is shown in Figure C.2 of the Appendix. All polymer formulations were prepared with epoxy:anhydride ratio of 1:1 which is intended to give optimum mechanical properties because there is one epoxy for each anhydride [99]. Various weight loadings of ePPC were added into the epoxy formulations to produce different levels of porosity (e.g., 10% ePPC added to achieve 10% porosity, assuming the density of polymers are about the same). A weight fraction of 0.48% catalyst to the total solids weight was added into each formulation to accelerate the curing process, as suggested in a previous study [99]. Epoxy resin and SMA mixtures were added to a clean scintillation vial and MEK was used as the solvent. A separate vial was used to dissolve the ePPC in MEK. The vials were sonicated to homogenize the mixture before the

epoxy resin, SMA and ePPC were mixed together. Catalyst 2E4MI was added last after mixtures were homogenized.

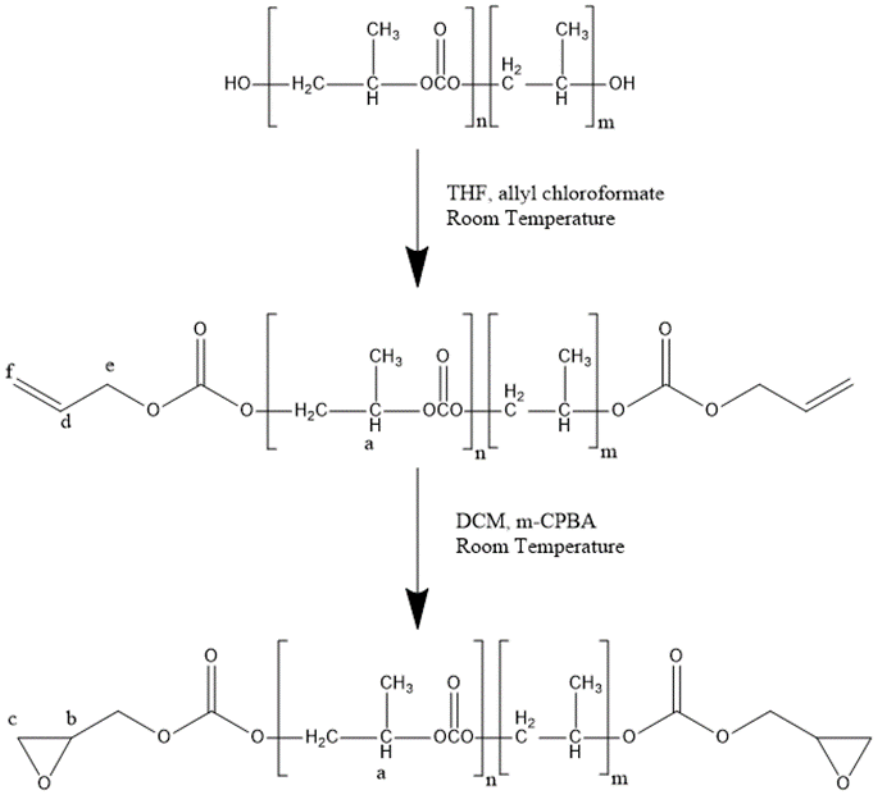

Scheme 3.1. Synthesis of epoxide functionalized poly(propylene carbonate)

CHA Modified Mark-40 E-beam evaporator was used to deposit metal films onto a silicon wafer at a pressure below 10^{-5} torr. Titanium was deposited at the rate of 1 Å/s to a thickness of 30 nm followed by 800 nm of aluminum (99.99% pure) at a rate of 2 Å/s. The epoxy formulations were then spin coated onto an aluminum coated silicon wafer at a spin speed of 1500 rpm for 40 seconds. The spin coated samples were then put into a tube oven for curing using the following steps: (1) ramping at 1 ºC/min to 35 ºC, and isothermal

hold for 1 hr; (2) ramping at 0.5 ºC/min to 150 ºC, and isothermal hold for 3 hr; (3) ramping at 1 ºC/ min to 180 ºC, and isothermal hold for 6 h; and (4) ramping at 0.6 ºC/min to 230 ºC, and isothermal hold for 1 h.

The cured samples were sealed in a closed jar with 0.5 mL of HMDS. The jar was heated to 80 ºC and held for 4 h to complete the post-cure treatment. A 500 nm top layer of aluminum was deposited at 2 Å/s by evaporation using a shadow mask to fabricate the parallel-plate capacitor structure for capacitance measurements. Top metal layer was comprised of 0.065 cm^2 circles.

The capacitance and loss tangent values for the epoxy films were measured with a GWinstek LCR-821 meter. Each sample was measured 6 times at a frequency of 200 kHz and bias of 1.275 V. The dielectric constant was calculated using $\varepsilon = Cd/(A\varepsilon_o)$, where C is the capacitance, ε_o is the permittivity of free space ($8.85*10^{-12}$ F/m), A is the area of the smaller electrode (i.e., 0.065 cm^2), and d is the dielectric thickness. The refractive index of the films was measured using a Woollam Ellipsometer 2000.

A Hitachi SU8230 scanning electron microscope (SEM) was used to image the cross-sectional thickness of the polymer films for dielectric constant calculations and pore size measurements. The SEM was operated at 1 kV with emission current of 7 mA. Thickness measurement is shown in Figure C.1 of Appendix.

The coefficient of thermal expansion (CTE) values were measured on samples prepared following the procedures described above on a silicon wafer. The in-plane CTE values were calculated based on the silicon substrate radius of curvature measured with a Flexus Tencor F2320 (equipped with a He-Ne laser) at various temperatures (120 °C, 130

°C, 140 °C, 150 °C, and 160 °C). CTE of the resulting epoxy films was calculated using the equations 1 to 3.

$$\frac{1}{R} = \frac{1}{R_2} - \frac{1}{R_1} \quad [1]$$

$$\sigma = \left(\frac{E_s}{1 - v_s}\right)\frac{t_s^2}{6Rt_f} \quad [2]$$

$$\frac{\partial \sigma}{\partial T} = \left(\frac{E_f}{1 - v_f}\right)[\alpha_{xy} - \alpha_x] \quad [3]$$

In Eq. 1, 2 and 3, R_2 is the radius of curvature of the substrate after film processing, R_1 is the radius of curvature for the bare substrate, σ is the thin film stress, E_s is the elastic modulus of the substrate, v_s is poisson's ratio, t_s is the thickness of the substrate, t_f is the thickness of the thin film, E_f is the elastic modulus of the thin film, v_f is the Poisson's ratio of the thin film, α_{xy} is the in-plane CTE of the thin film, and α_x is the CTE of the substrate. For the silicon wafer, E_s = 180.5 GPa, v_s = 0.22, α_x = 2.6 ppm/K. The v_f of the epoxy thin films were taken as 0.3.

Differential scanning calorimetry (DSC) was performed using a TA Instrument Q20 to examine the glass transition temperature (T_g) of the crosslinked porous epoxy film. Each film was sealed in an aluminum pan and ramped to high temperature at a rate of 10 °C/min.

The reduced modulus and hardness of the spin-coated films was determined using a Hysitron Triboindenter with a 1 μm conical tip. A polycarbonate sample was used as the reference to calibrate the projected area coefficient. Four data points were obtained for each

sample between 100 µN to 250 µN with an interval of 50 µN. The indentation depth was less than 10% of thin film thickness to avoid substrate effects on the measurements. The nano-indentation depth for each film is summarized in Table C.1 and C.2 in the Appendix. The reduced modulus of the film was determined using Equation 4.

$$E_r = \frac{\sqrt{\pi}}{2\beta}\frac{dP/dh}{\sqrt{A}} \tag{4}$$

In Eq. 4, E_r is the reduced modulus of the material tested, β is a geometric constant on the order of unity, dP/dh is the slope of the linear portion of the unloading curve, and A is the projected area of the indentation.

3.3 **Result and Discussion**

The introduction of air-filled pores within the polymer film lowers the index of refraction of the film because the index of refractive index of air is about one [34]. Figure 3.1 shows the refractive index for films with different degrees of porosity and crosslinked using SMA4000. The index of refractive was lowered from 1.6 to 1.54 when porosity was increased from 0% to 30%, show the effect of porosity within the epoxy thin film. Figure 3.2 shows SEM cross-section images of the epoxy films with 0%, 20% and 30% porosity. For film with 0% porosity, the SEM image is smooth with no observed pores. The average pore size was 30 nm for the 20% porous film. The pore size increased to 100 nm for the 30% porous film due to the aggregation of the ePPC within the epoxy film.

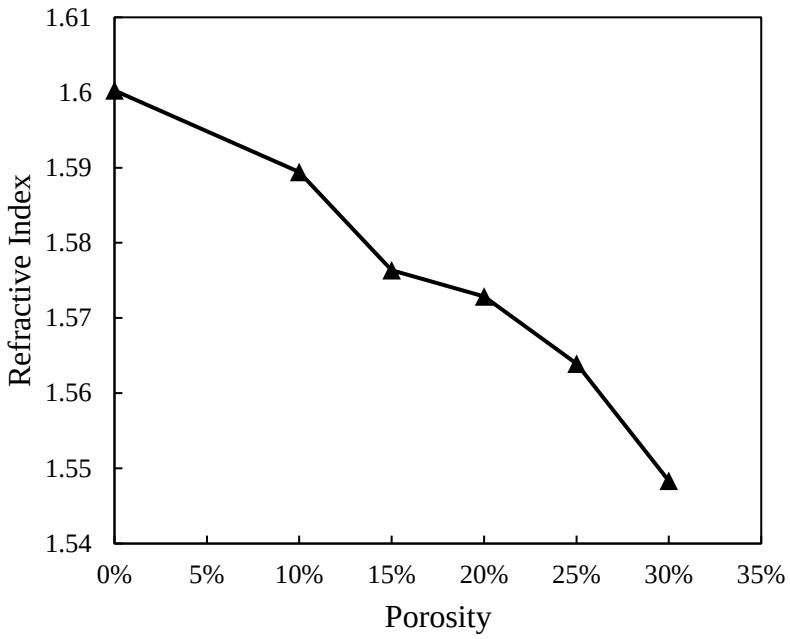

Figure 3.1. Refractive index of epoxy films crosslinked using SMA4000 with different porosity

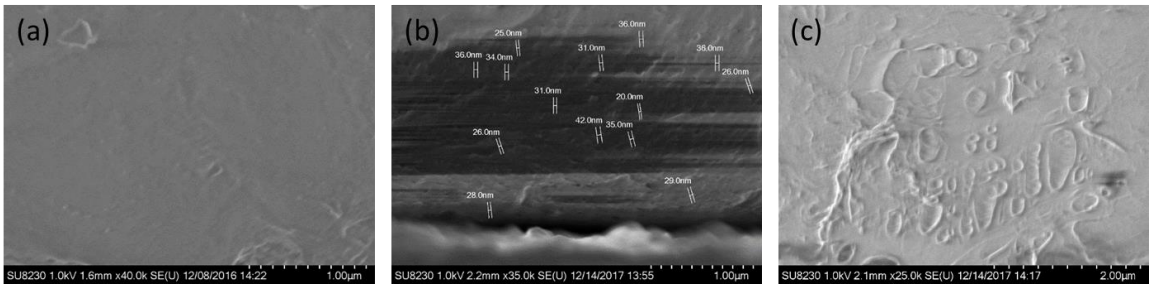

Figure 3.2. SEM cross-sectional image of epoxy films using SMA4000 as crosslinker with different porosity. a) 0%; b) 20%; c) 30%

Figure 3.3 shows the dielectric constant and tangent loss (tanδ) of the epoxy films at various porosity levels using SMA4000 as the crosslinker before and after the HMDS hydrophobic treatment. The dielectric constant was lowered from a value of 3.78 with no pores to 2.76 with 30% porosity prior to HMDS treatment. The drop in dielectric constant

is due to the incorporation of pores ($\varepsilon' = 1$ for air). The $\tan\delta$ dropped from 0.0227 to 0.0209 for the 10% porous film. At higher porosity, the loss tangent increased to 0.248 with 30% porosity. This increase in loss tangent with porosity indicates that hydrophobic groups are formed at the pore walls (e.g., hydroxyl group) with the ePPC removed. The hydrophilic pore walls left after ePPC decomposition (e.g., hydroxyl group) has a relatively high polarization resulting in an increase in loss. Various silane couplers were studied previously to create a hydrophobic interface [100]. In this case, the HMDS treatment resulted in a drop in the dielectric constant. For example, the dielectric constant of the epoxy film with 10% porosity dropped from 3.597 to 3.238 and the dielectric constant of the epoxy film with 20% porosity dropped from 3.321 to 2.946. The drop in dielectric constant was accompanied by a drop in loss tangent for each porous epoxy sample. The loss tangent of the 10% porous epoxy film dropped from 0.0209 to 0.0149, and the loss tangent of the 20% porous epoxy film dropped from 0.0248 to 0.0192. The reduction of both dielectric constant and tangent loss with HMDS treatment shows the effectiveness of a hydrophobic pore wall termination.

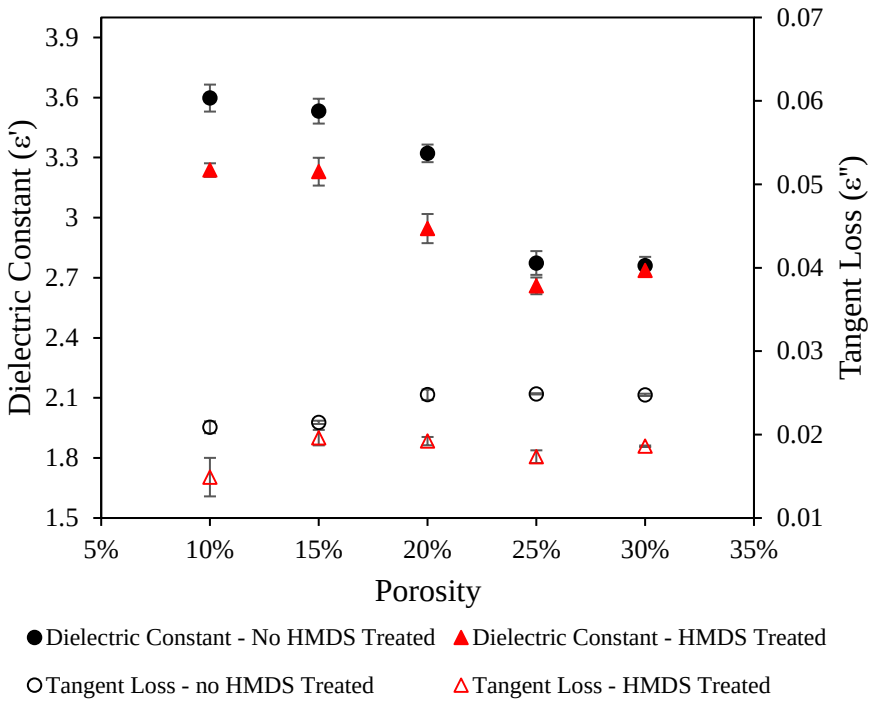

Figure 3.3. Dielectric constant and tangent loss measurement for epoxy films crosslinked using SMA4000 with different porosity before and after treatment of HMDS

The effect of styrene-to-maleic anhydride ratio within the SMA cross-linker was studied using SMA2000 and SMA4000. Figure 3.4 shows the dielectric constant and tanδ of epoxy films with various porosity using SMA2000 without HMDS treatment. The dielectric constant decreased from 4.091 for non-porous epoxy to 2.998 for 30% porous epoxy. The dielectric constant and tanδ for epoxy films crosslinked using SMA2000 were slightly higher than the films crosslinked using SMA4000 at equal porosity. This is due to the higher concentration of maleic anhydride in SMA2000. Maleic anhydride is more

hydrophilic than styrene due to the polarizable carbonyl bond. Moreover, maleic anhydride has a larger affinity for water absorption, which has a very high dielectric constant [101].

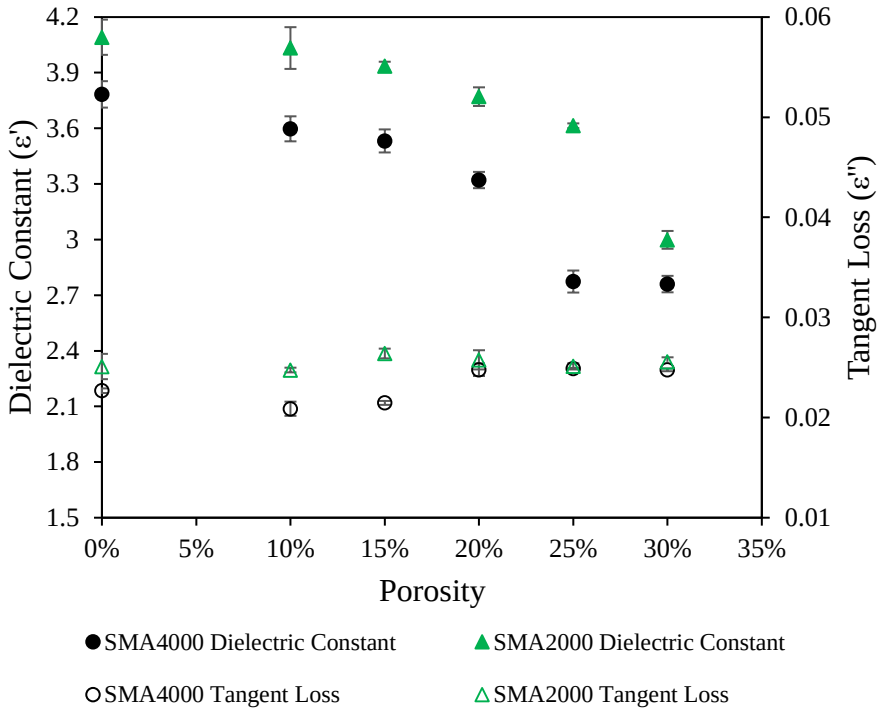

Figure 3.4. Comparison of dielectric constant and tangent loss for epoxy films crosslinked using SMA2000 and SMA4000 without HMDS treatment

A volume average theory (VAT) model was used to estimate the theoretical dielectric constant for porous films cross-linked using SMA4000 and SMA2000. Films were modelled as a two-component system: air and epoxy [98]. Figure 3.5 shows the experimental data and the VAT model data. There was a good fit between the experimental data and VAT modeling result for both SMA4000 and SMA2000 with an average of 5.6% deviation between the two for the SMA4000 cross-linked films and 7.1% deviation for the SMA2000 cross-linked films.

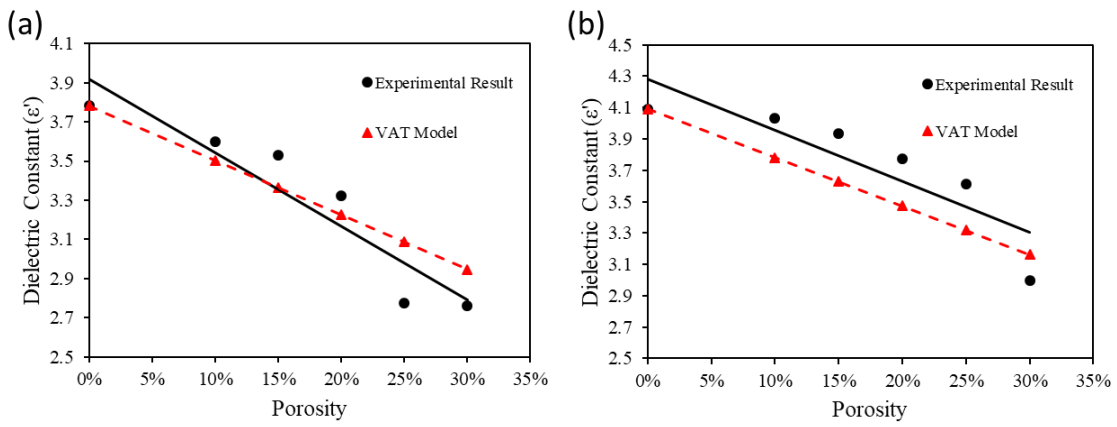

Figure 3.5. Comparison of dielectric constant estimation using VAT model and experimental data for porous epoxy films crosslinked using different crosslinker. a) SMA4000; b) SMA2000

The mechanical properties of the porous epoxy films crosslinked with SMA2000 and SMA4000 were measured using nanoindentation and are shown in Figure 3.6. Both reduced modulus and hardness of epoxy films crosslinked using SMA2000 were about 1.5 times greater than those with SMA4000. Films with higher maleic anhydride content are known to have higher mechanical strength [101]. The higher maleic anhydride content of SMA2000 results in a higher cross-link density within the epoxy. The reduced modulus decreased by 12% for SMA4000 films with 20% porosity. The reduced modulus was 4.23 GPa at 0% porosity and 3.71 GPa at 20% porosity. The further increase in porosity to 30% resulted in a 47% decrease of reduced modulus; the reduced modulus dropped to 2.24 GPa at 30% porosity. This is due to the larger pore size of the 30% porous epoxy films. The reduced modulus of films cross-linked using SMA2000 were less affected by porosity as it only dropped by 18% with 30% porosity; the reduced modulus dropped from 6.83 GPa at 0% porosity to 5.63 GPa at 30% porosity. The enhanced mechanical properties using

SMA2000 is due to the higher crosslink density of polymer chains. Table 3.1 shows the Young's modulus of the epoxy films crosslinked using SMA2000 and SMA4000 at different porosity. Young's modulus can be derived from reduced modulus using Equation 5.

$$\frac{1}{E_r} = \frac{1-\nu_i^2}{E_i} + \frac{1-\nu_s^2}{E_s} \qquad [5]$$

In Eq. 5, ν_i is the Poisson ratio of the indenter, which is a diamond tip with Poisson ratio is 0.07; ν_s is the Poisson ratio of the testing material, which is about 0.3; E_r is the reduced modulus of the porous epoxy film; E_s is Young's modulus of the porous epoxy film; and E_i is Young's modulus of the diamond tip, 1140 GPa.

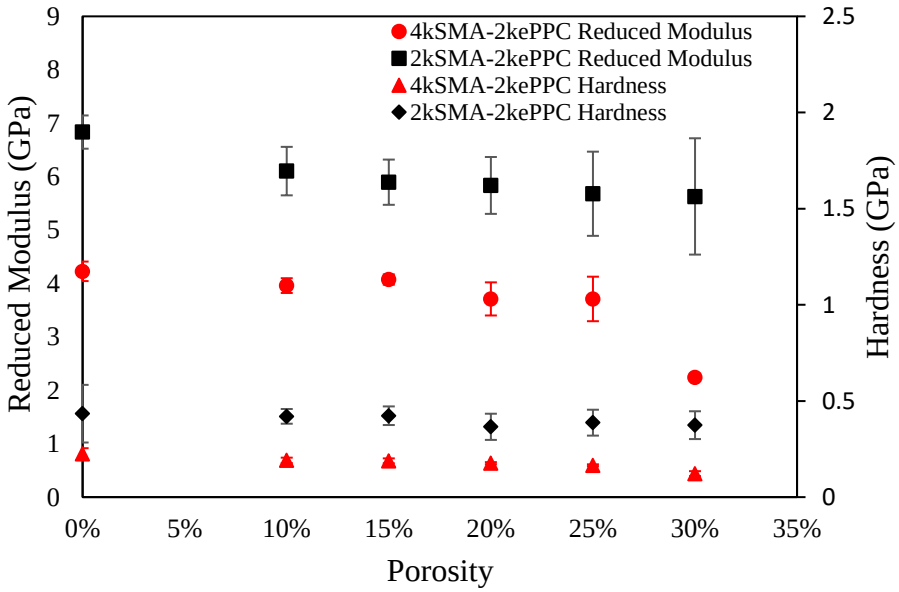

Figure 3.6. Reduced modulus and hardness of epoxy films with different porosity using SMA2000 and SMA4000 as crosslinker

Table 3.1. Young's modulus of epoxy films with different porosity using SMA2000/SMA4000 as crosslinker

Porosity	SMA4000 Young's Modulus (GPa)	SMA2000 Young's Modulus (GPa)
0%	8.05	13.0
10%	7.54	11.6
15%	7.76	11.2
20%	7.07	11.1
25%	7.07	10.8
30%	4.27	10.7

Thermal strain is induced in the thin film upon cooling which results in a change in the radius of curvature of the substrate due to the mismatch in CTE between the silicon wafer substrate and the epoxy film. The in-plane CTE for films containing 0%, 20%, and 30% porosity using SMA2000 and SMA4000 were calculated using Eq. 1 to 3. The parameters used in the CTE calculation are shown in Table C.3 and C.4 in Appendix. A linear regression line was fit to the residual stress vs temperatures for each film and plotted in Figure 3.7. The CTE for films with different porosity levels using the two SMA cross-linkers are shown in Figure 3.8. The epoxy films crosslinked using SMA4000 have a larger

CTE compared to the SMA2000 films due to the higher cross-link density with SMA2000 [102]. Increasing the porosity also resulted in an increase in CTE. For example, the CTE increased from 19.991 ppm/K to 68.174 ppm/K with a porosity increase from 0% to 30% using SMA4000. The CTE increased from 18.729 ppm/K to 35.249 ppm/K using SMA2000 as the crosslinker. The higher porosity lowers the cross-link density [102].

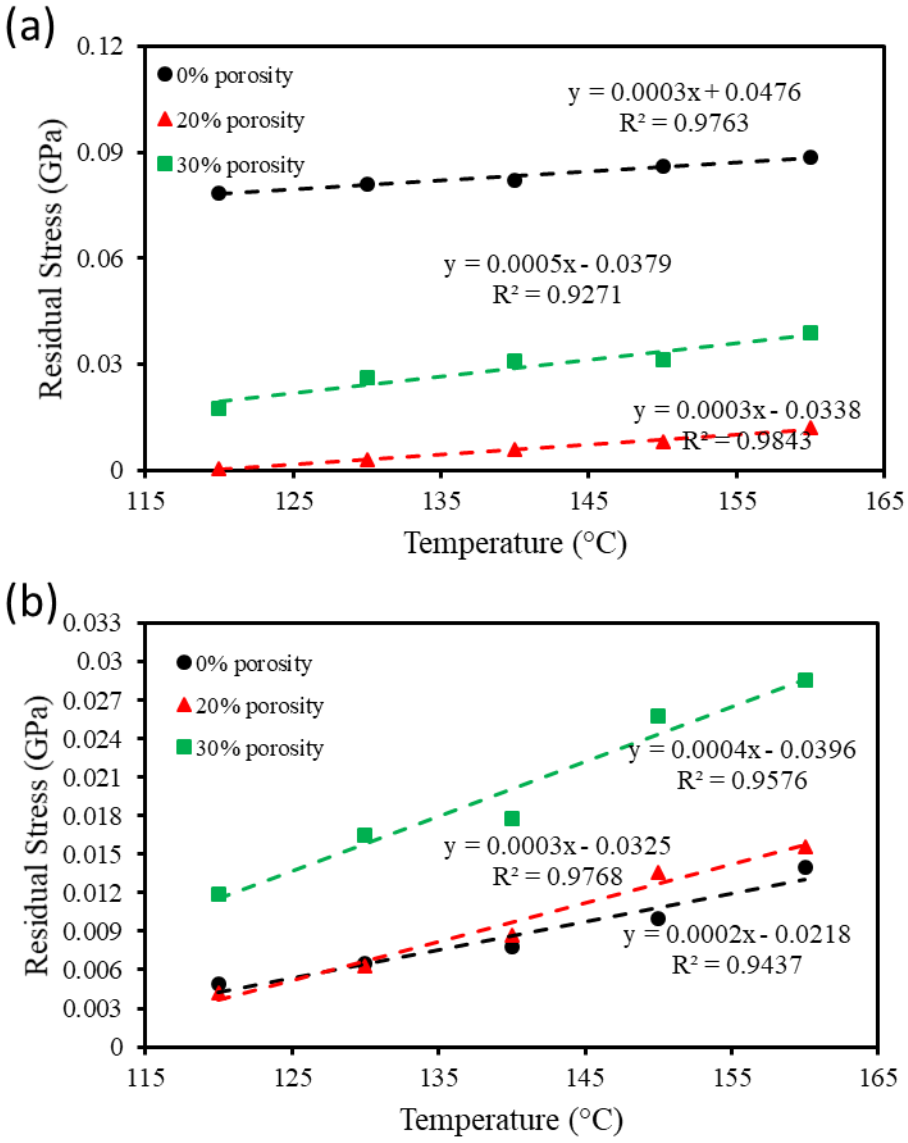

Figure 3.7. Linear regression fitting of residual stress between epoxy film and silicon wafer substrate vs temperature for film with different porosity using different crosslinker. a) SMA2000; b) SMA4000

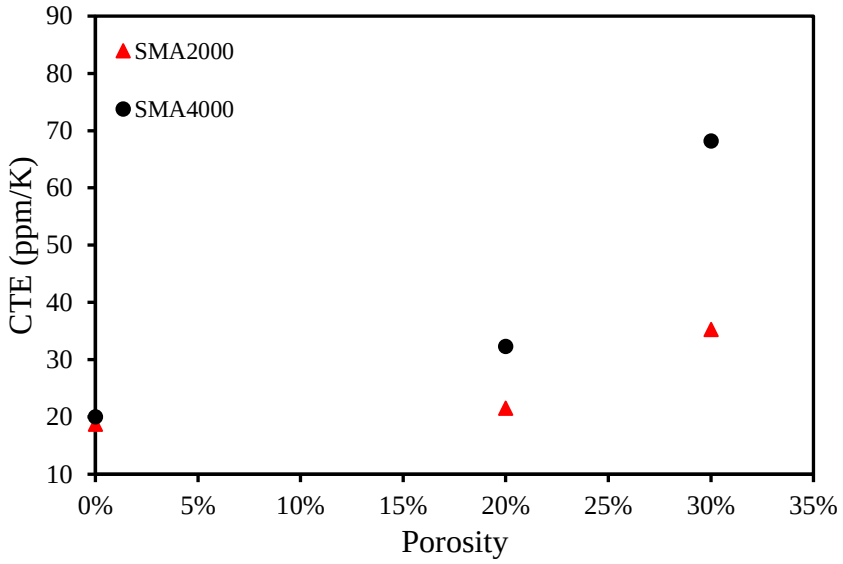

Figure 3.8. CTE of epoxy films with different porosity using SMA2000 and SMA4000 as crosslinker

DSC measurement of T_g for the epoxy films with different porosity and cross-linker are shown in Figure 3.9. The glass transition temperature of films crosslinked using SMA2000 decreased from 155 °C to 143 °C by the addition of 30% porosity, while films crosslinked using SMA4000 decreased from 155 °C to 130 °C. T_g decreased with porosity due to lower crosslink density of porous epoxy films and greater pore volume. This allows greater chain segment mobility for the polymer chains [98]. Epoxy films crosslinked using SMA2000 had a higher T_g compared to those with SMA4000 at equal porosity due to the effect of higher crosslink density [103].

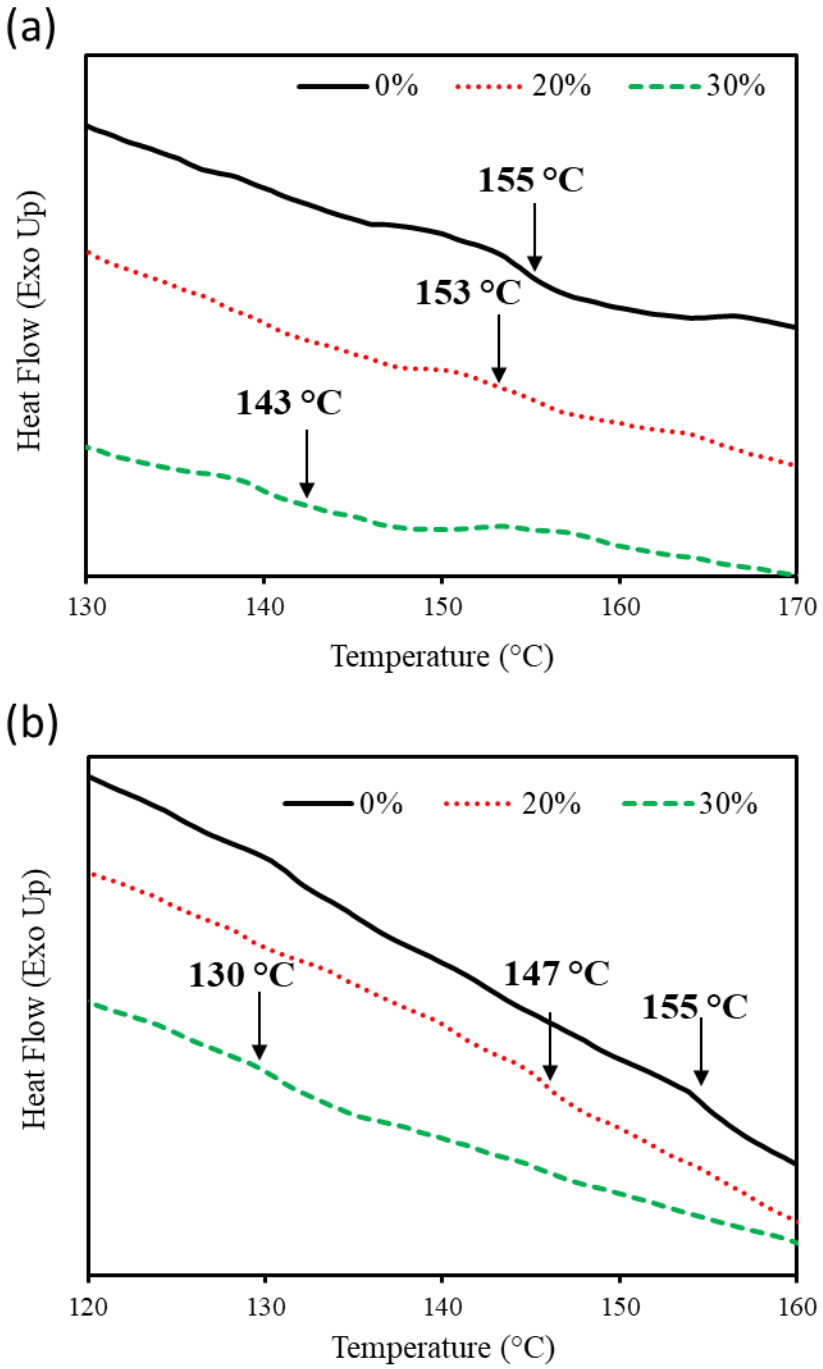

Figure 3.9. Glass transition temperature measurement of epoxy films with different porosity using different crosslinker. a) SMA2000; b) SMA4000

3.4 **Summary**

In this work, the feasibility of mixing of epoxide functionalized poly(propylene carbonate) into epoxy resin formulations to create nano-porous epoxy films to reduce dielectric constant of cured epoxy film was demonstrated. By treating cured porous epoxy film with hydrophobic HMDS, a further reduction in dielectric constant and tangent loss were observed. SMA4000 had better electrical properties compare to SMA2000, however, SMA2000 had better thermal and mechanical properties. The resulting porous, low dielectric constant epoxy films provided a pathway for developing insulating layer for future electronic devices.

CHAPTER 4.

TUNABLE TRANSIENT AND MECHANICAL PROPERTIES OF PHOTODEGRADABLE POLY(PHTHALALDEHYDE)

4.1 Introduction

Previous two chapters focused on high ceiling temperature, PPC based sacrificial polymers and its application in dielectric materials. In this chapter, the focus is on low ceiling temperature poly(aldehydes) materials and their application in transient devices.

Self-immolative polymers, such as poly(phthalaldehyde), are of interest for use in transient devices where device self-destruction avoids the need for component retrieval from the field and prevents reverse-engineering [44,51,104]. Anionically polymerized, linear poly(phthalaldehyde) (PPHA) is a low ceiling temperature polymer which is thermodynamically unstable above its ceiling temperature, -43 °C. The rapid unzipping of the polymer backbone at temperatures above -43 °C can be kinetically suppressed by end-capping the polymer chains or by synthesizing cyclic polymer chains. PPHA with thermal stability up to 160 ºC has been achieved [5,16,22–24,29,105,106]. The acetal bonds of the backbone in PPHA are sensitive to electrophilic attack from protons which initiate rapid cationic unzipping [45]. Previous studies have demonstrated thermal or photo activated triggers to initiate depolymerization of PPHA. Photo acid generators (PAG) have been used to produce acids that can catalyze the depolymerization at or below room temperature [49,107,108]. Photosensitizers have been used to expand the spectral range of PAGs into the visible region [47].

Important metrics for the transient properties of PPHA include photoresponse time (i.e. time to create the photo-acid), poly(aldehyde) depolymerization rate, and evaporation time of newly created monomer products. Copolymerization of phthalaldehyde (PHA) with higher vapor pressure monomers, such as butanal (BA), has been shown to increase the evaporation rate of the depolymerized products by a factor of 12 for micrometer-thick films [28]. However, the evaporation rate decreases for depolymerized thick films because of the limited surface area. An alternative pathway for device transience is the liquification of the depolymerized device followed by absorption of the liquid products into the environment. The acid-catalyzed depolymerization of PPHA is known to form liquid or solid products followed by evaporation or sublimation of the monomers. Liquification of the depolymerized products is assisted by heat from the exothermic depolymerization reaction and incorporation of low melting point additives in the PPHA mixture [109]. The depolymerization of PPHA or poly(aldehyde) copolymers is rapid and has been recorded to be as fast as 33 s by quartz crystal microbalance (QCM) [28].

Pure PPHA or P(PHA-co-aldehyde) copolymers by themselves are brittle because of the fused ring backbone structure. Thus, additives can be used to improve the ductility and toughness or adjust the elastic modulus of poly(aldehyde) structures. Once the photo-acid trigger is initiated, PPHA can achieve rapid transience via liquification and absorb into the environment as opposed to evaporation of PHA monomer over a long period of time. The liquid-state can potentially absorb into the surrounding environment where visible detection is impaired. Crystallization of the PHA monomer can occur because its freezing point, ca. 55 ºC, is often above the ambient temperature. In addition to improving

the mechanical properties, additives can lower the freezing point of the depolymerized poly(aldehyde) mixture.

In this chapter, additives are used to improve the mechanical properties and maintain transient properties of poly(aldehyde) films. The effect of liquid plasticizers on the mechanical properties of poly(aldehyde) films, physical state of the depolymerized products and photo-transience speed is assessed. PPHA has a high elastic modulus that is desirable for forming rigid structure, however, its brittle nature makes it unfavorable for broader range of applications. Recently, a diamine and diethyl phthalate were used as plasticizers to improve film flexibility and to thermally stabilize the polymer for use at higher temperatures including hot-press molding of PPHA [54]. Plasticizers [110] can improve the flexibility of brittle poly(aldehyde) films and suppress the freezing point of the depolymerized polymer because they disrupt the intermolecular interactions of PPHA. The chemical structure, specific functional groups, molecular weight and ionic charge on the plasticizer contribute to their overall effectiveness. However, many studies have also shown that phase segregation is a primary concern with the addition of excessive plasticizers [110–113]. Here, two classes of plasticizers (non-ionic ether-ester, and ionic liquid) are evaluated [114]. Ether-ester plasticizers are expected to have the best miscibility with the PPHA backbone in films as well as with the PHA monomer to significantly improve the range of mechanical capability. Alternative plasticizers, such as ionic liquids, have previously been investigated in poly(methacrylate) and poly(vinyl chlorides) to improve the mechanical properties and lower the glass transition temperature (T_g) [110,111,113]. In this work, both ionic liquid and ether-ester plasticizers were evaluated. A polyethylene oxide and a phthalate-based ether-ester plasticizers were chosen to evaluate

the traditional plasticizer effects on PPHA. The pyrrolidinium-bis(trifluoromethylsulfonyl)imide based ionic liquid plasticizers were specifically used here because of their low freezing point that favours the transience application of absorbing into environment. Structures of selected plasticizers and their freezing point are shown in Table 4.1 [115,116]. Combination of these two plasticizers in PPHA films enable a wider mechanical feasibility for variety of structural application with enhanced transience properties.

Table 4.1. Name of plasticizers used, their chemical structures, and their freezing point

Plasticizer	Chemical Structure	Freezing Point (ºC)
Poly(ethylene glycol) bis(2-ethylhexanoate)	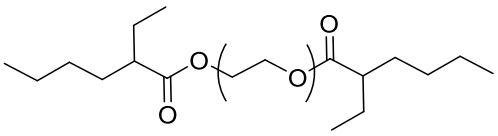	-48
Bis(2-ethylhexyl) phthalate	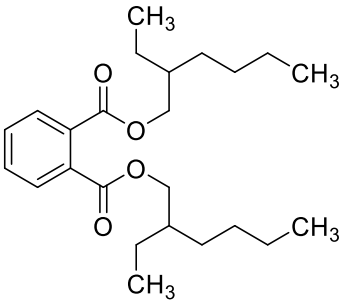	-58

1-Butyl-1-Methylpyrrolidinium Bis(trifluoromethylsulfonyl)imide	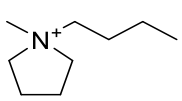	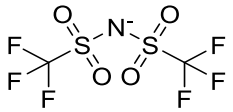	-17
1-Hexyl-1-Methylpyrrolidinium Bis(trifluoromethylsulfonyl)imide	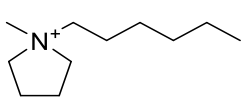	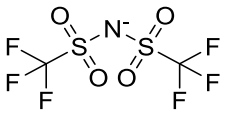	-24
1-Methyl-1-Octylpyrrolidinium Bis(trifluoromethylsulfonyl)imide	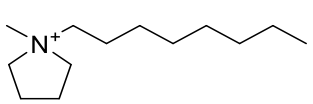	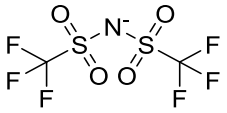	-12

4.2 **Experimental**

Materials: Tetrakis(pentafluoropenyl)borate-4-methylphenyl[4-(1-methylethyl)phenyl]iodonium (Rhodorsil FABA) was purchased from TCI Chemicals. Anthracene was purchased from Alfa Aesar. 1-Butyl-1-methylpyrrolidinium bis(trifluoromethylsulfonyl)imide (BMP TFSI), 1-Hexyl-1-methylpyrrolidinium bis(trifluoromethylsulfonyl)imide (HMP TFSI), and 1-Methyl-1-octylpyrrolidinium bis(trifluoromethylsulfonyl)imide (OMP TFSI) were purchased from Iolitec. Tetrahydrofuran (THF) was purchased from BDH. Poly(ethylene glycol) bis(2-ethylhexanoate) (PEO) with a number-average molecular weight (M_n) of 650 g/mole and bis(2-ethylhexyl) phthalate (BEHP) were purchased and used as received from Sigma Aldrich. Poly(phthalaldehyde) (PPHA) was cationically polymerized using boron trifluoride etherate (BF_3) below its ceiling temperature (-42 ºC) following the procedure of Schwartz et al. [5]. M_n of the synthesized polymer is 340 kDa with a dispersity (Đ) of 1.27. Poly(phthalaldehyde-co-Butanal) (P(PHA-co-BA)) was synthesized following the procedure of Schwartz et al. with detailed NMR analysis provided for butanal incorporation

ratio [28]. The number average molecular weight of the used P(PHA-co-BA) is 53 kDa with a molar incorporation of 10% butanal.

All polymer films casted for mechanical property measurement contained 10 pphr Rhodorsil FABA photoacid generator (PAG) as the photocatalyst, 2 pphr anthracene as the photosensitizer. The weight percentage of each additive is with respect to the weight of polymer. Polymer mixtures were formulated by dissolving all components in THF in a clean glass vial in a weight ratio of 12:1 THF:PPHA. Formulations were roll-mixed on a roller until homogeneous. The formulations were then dried under 15 psig nitrogen for 2 days. The nitrogen overpressure slowed the THF evaporation rate and produced good quality films. The dry films were peeled off the substrate and allowed to dry for two additional days in ambient.

Characterization: QCM experiments were performed with a Stanford Research Systems QCM 200 to quantify the solid-state kinetics of depolymerization of poly(aldehyde). The Butterworth-van Dyke model was used to describe the mechanical changes of the polymer coating on the quartz crystal. Polymer formulations were made with 9.1 wt% polymer solids in cyclopentanone with 5 parts per hundred resin (pphr) of PAG and 1.05 pphr anthracene. Thin film samples were spin-coated onto a 2.54 cm QCM with 5 MHz unloaded resonant frequency and an active surface area of 0.4 cm^2. An open-faced holder was used to allow exposure of the polymer films with an Oriel Instruments flood exposure source with a 1000 W Hg(Xe) lamp filtered to 365 nm light. An exposure dose of 730 mJ/cm^2 is used for all samples.

Thermal gravimetric analysis (TGA) was performed on a TA TGA Q50 instrument at a ramp rate of 5 ºC/min. A nitrogen atmosphere was used at a flow rate of 40 ml/min.

Dynamic mechanical analysis (DMA) of films were performed on TA Q800 DMA instrument. Operation environment was controlled at 30 ºC with 0.1% strain at 1 Hz in a closed chamber. Cryogenic DMA was performed by ramping temperature at a rate of 5 ºC/min from -50 ºC to 30 ºC. The samples were 8 mm wide, 30 mm long and about 250 μm thick. Tensile tests were performed with an Instron 5843 at a strain rate of 10% per minute at 21°C. Each sample has a tested length of 10 mm, width between 5.5 and 7.5 mm, and thickness between 0.16 and 0.22 mm.

4.3 **Results and Discussion**

The effect of additives on the thermal stability of PPHA is important because stability of PPHA is sensitive to additives and premature degradation of PPHA is undesirable. The thermal stability of PPHA with addition of 20 pphr plasticizer (both ionic liquid and ether-ester plasticizers) were investigated individually by thermogravimetric analysis (TGA) and shown in Figure 4.1. The mass of some of the mixtures did not go to zero at high temperature because of the presence of ionic liquids with very small vapor pressures. Table 4.2 summarizes the onset and endset decomposition temperature of PPHA containing different plasticizers. The rapid degradation of PPHA film with no additives happened at an onset temperature of 158 ºC, which matches a previous report [54]. Most of the ionic liquids had no significant effect on the thermal stability of the PPHA, as shown by the similar onset decomposition temperature and rate of mass change. This shows that PPHA is stable with these ionic liquids. PEO lowered the onset by 32 ºC, showing that it

made PPHA less thermally stable. A qualitative test for pH of PEO using pH test paper show a range between 2 and 3 when mixed in water. The acidic nature of PEO catalyzes the degradation of PPHA. Nevertheless, all PPHA films containing 20 pphr of each additive were all stable at room temperature for months.

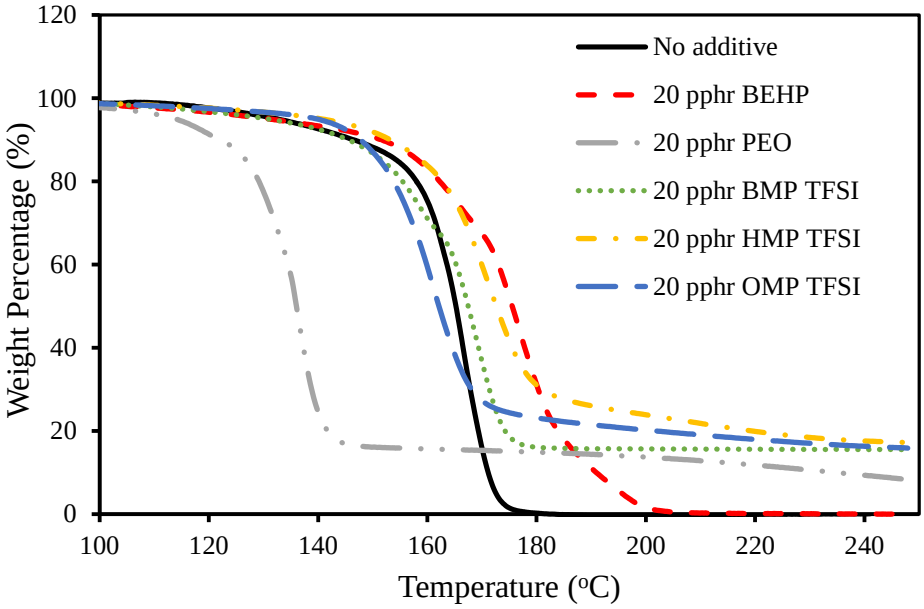

Figure 4.1. TGA plot of PPHA with 20 pphr loadings of various plasticizers ((part of these data were also in Oluwadamilola Phillips Thesis Dissertation. The data present here just to ensure the completeness of analysis.)

Table 4.2. TGA results for the onset and endset of depolymerization of PPHA with 20 pphr loadings of different plasticizers (part of these data were also in Oluwadamilola Phillips Thesis Dissertation. The data present here just to ensure the completeness of analysis.)

Plasticizer	Onset (ºC)	Endset (ºC)	Difference (ºC)
None	158	172	14
BEHP	165	187	22
PEO	126	140	14
BMP TFSI	153	174	21
HMP TFSI	161	179	18
OMP TFSI	152	168	16

The onset photo-induced depolymerization of PPHA was monitored using a quartz crystal microbalance (QCM), as described previously [28], to investigate the photoresponse time for PPHA using different plasticizers. The increase of resistance in the Butterworth-van Dyke equivalent circuit model corresponds to energy loss and softening of the solid polymer film. Table II summarizes the photoresponse time for PPHA to degrade after being exposed. PEO show longer photoresponse time compared to other plasticizers. This is likely due to ether linkages of PEO that compete with PPHA backbone for bonding with

photoacid. Other plasticizers show a photoresponse time at similar range to the pure PPHA film, indicating they didn't affect the photoresponse of PPHA. It was also observed that ionic liquid plasticizers kept the depolymerized PPHA in liquid state longer than ether-ester ionic liquid after being exposed. This indicates that ionic liquid has better transient properties compared to the ether-ester plasticizer by forming liquid products that can be absorbed into environment.

Table 4.3. Photoresponse time for PPHA with various plasticizers at loadings of 20 pphr after UV exposure from QCM (part of these data were also in Oluwadamilola Phillips Thesis Dissertation. The data present here just to ensure the completeness of analysis.)

Type of Plasticizer	Photoresponse Time (seconds)
None	14 ± 1
BEHP	19.9 ± 2.90
PEO	1436 ± 73.5
BMP TFSI	23.2 ± 0.122
HMP TFSI	25.7 ± 7.6
OMP TFSI	12.6 ± 1.4

The plasticizing effect of individual commercial plasticizers on PPHA, including BEHP, PEO, BMP TFSI, HMP TFSI, and OMP TFSI, were investigated separately. Storage modulus with addition of various amount of each plasticizer were measured using DMA and are shown in Figure. A linear regression line was fitted for each plasticizer to estimate the rate of change of storage modulus with amount of plasticizers added. PEO and BEHP plasticizers show a faster storage modulus change rate compared to ionic liquid plasticizers. PEO and BEHP have better plasticizing effect likely due to their favorable interaction of PPHA polymer chain. However, addition of over 20 pphr PEO and BEHP plasticizer led to significant phase segregation, as films started turning cloudy, opaque and brittle. Lesser degree of phase segregation happened when high loadings of ionic liquid were mixed with PPHA, as the dried films were still transparent. The ionic liquids of interest show similar effect on plasticizing the PPHA film. HMP TFSI has a slightly better plasticizing effect, followed by OMP TFSI, then BMP TFSI. The superior plasticizing effect from HMP TFSI is likely due to its lowest melting point among these ionic liquids (at -24 °C). While OMP TFSI has a higher melting point than BMP TFSI, it has a slightly better plasticizing effect when compared to BMP TFSI is likely due to its increased alkyl chain length on the pyrrolidinium cation. The longer alkyl chain enabled OMP TFSI to undergo more molecular conformations than HMP TFSI and BMP TFSI, leading to a better plasticizing effect to high molecular weight PPHA.

Table 4.4 shows the elastic modulus for five polymer batches (four repetitions each). Repetitions where made because it is possible to have false negative values in modulus testing, but false positive values are rare. Thus, it is probably more valid to view the highest modulus for each polymer lot. Lots 82 and 68 had the highest modulus and lot 72 had the

lowest modulus. Lot PA 45 is suspect due to the poor polymer quality for PA lots, as discussed in the next section. Two conclusions can be drawn from these results. First, high quality PPHA with molecular weight above 200 kDa with 50 wt% BMP TFSI has a modulus above 1 GPa. Second, there is a slight trend that higher molecular weight is produces a higher modulus film.

Table 4.4. Elastic modulus (MPa) for PPHA film with 50 pphr BMP TFSI plasticizer. RM – Rieke Metals Inc. produced batches. PA – PharmAgra Inc. produced batch.

Lot #	Molecular weight, kDa	Sample #1	Sample #2	Sample #3	Sample #4	Average Modulus, MPa
RM 82	331	1257.0	1174.9	1019.1	1094.9	1136.5
RM 77	258	1121.8	1078.4	1101.1	1044.6	1086.5
RM 72	195	1015.6	770.17	882.56	812.92	870.32
RM 68	237	1290.1	1334.9	1081.1	1352.8	1264.7
PA 45	251	1011.5	903.25	783.96	864.63	890.84

Figure 4.2 shows the change in storage modulus vs. BMP TFSI concentration with 20 pphr BEHP loading. The polymer matrix used for these films contained a mass ratio of 1:1 for P(PHA-co-BA) to PPHA. A near-linear decrease in storage modulus with BMP TFSI content was observed. This shows that adding BMP TFSI has a positive influence on

making softer PPHA films. The addition of both plasticizers also resulted in fully transient films, as it formed liquid that absorbed into ground. Figure 4.3 compares the film with both additive (above) and without additive (below). The yellow residuals corresponded to the monomer. Tensile test was also performed on the film with 100 pphr BMP TFSI and 20 pphr BEHP, as shown in Figure 4.4. The addition of plasticizers significantly reduce the brittleness nature of PPHA and improve its ability to be plastically deformed. Low temperature performance of this specific film was also performed using DMA, as shown in Figure 4.5. Temperature of the DMA instrument was ramped at 3 °C/min for this specific measurement.

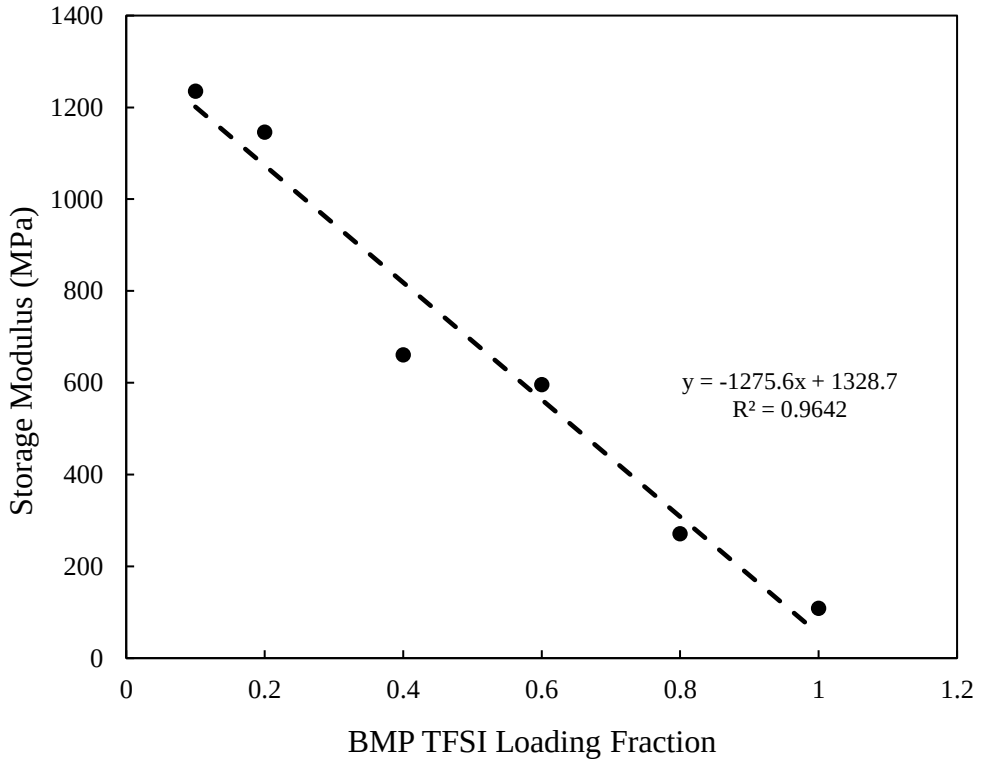

Figure 4.2. Storage modulus of PPHA films with varying loadings of BMP TFSI

Figure 4.3. Sunlight-induced depolymerization of anthracene sensitized PPHA films with no additives (bottom) and 100 pphr BMP TFSI + 20 pphr BEHP (top) at 11 am at 15 °C. Both films contained 10 pphr PAG and 2.1 pphr anthracene.

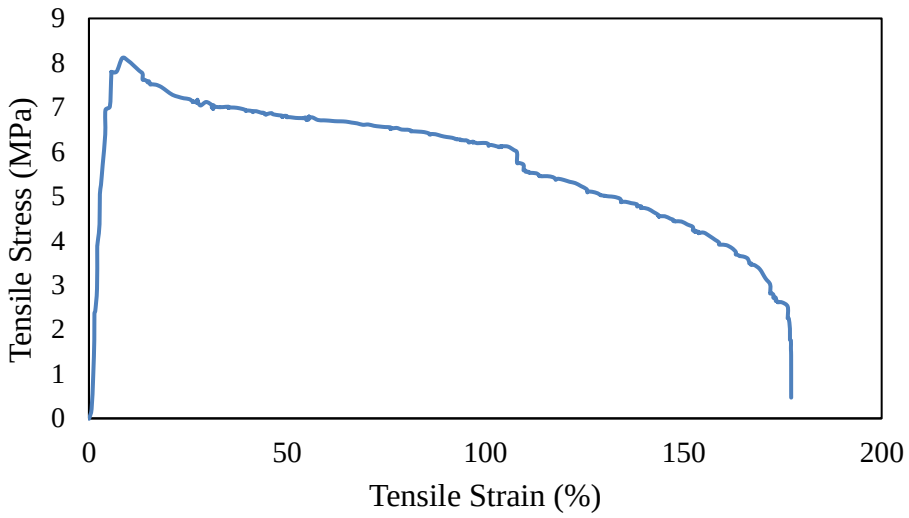

Figure 4.4. Tensile test of a PPHA film with 100 pphr BMP TFSI + 20 pphr BEHP

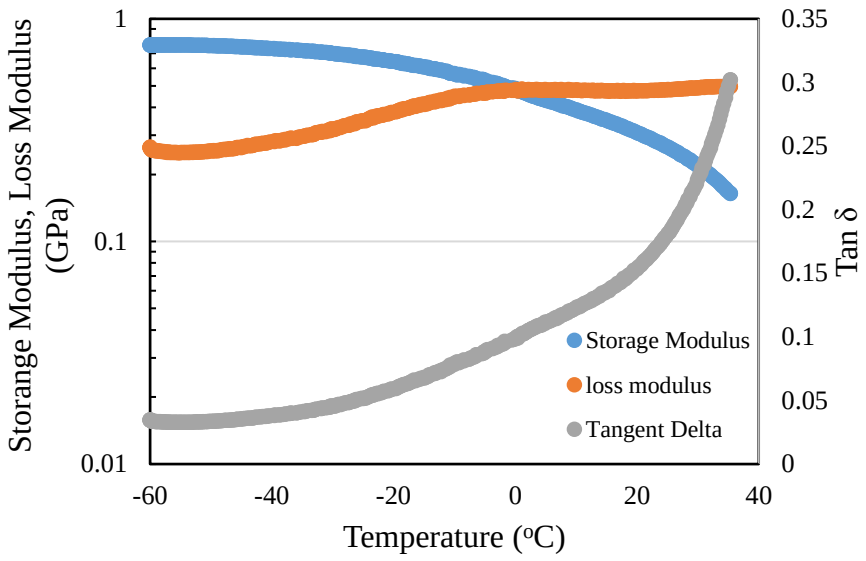

Figure 4.5. Cryogenic DMA test of PPHA film with 100 pphr BMP TFSI and 20 pphr BEHP

Aliphatic aldehyde PPHA copolymer has been demonstrated to have better transient properties compared to PPHA homopolymer, due to the incorporation of higher vapor pressure aldehyde comonomer that increases the evaporation rate of depolymerized products [28]. However it has the tradeoff of lower mechanical modulus. Figure 4.6 shows the storage modulus comparison for polymer film blended with 1:1 and 2:1 weight ratio of P(PHA-co-BA):PPHA, each containing 10% PEO as plasticizer and various loadings of BMP TFSI. Polymer film made with 1:1 blend ratio of P(PHA-co-BA):PPHA had a higher modulus than the 2:1 blend. The reducing modulus of increasing copolymer blend ratio is due to the lower molecular weights of copolymer [28].

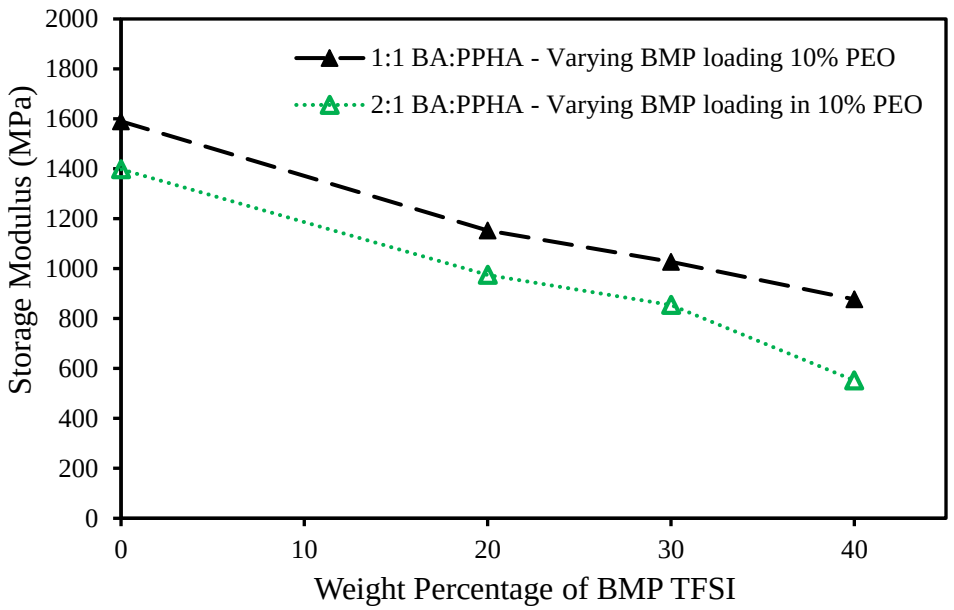

Figure 4.6. Storage modulus of PPHA/P(PHA-co-BA) blended films with 10 pphr PEO and various loadings of BMP TFSI

Addition of extra plasticizers helps to achieve the degree of flexibility of PPHA film. However, extra addition of plasticizers hurts the elastic modulus of PPHA film as it cause more segmentation of polymer chains. This led to the premature inelastic deformation of transient films under stress. Glass fibers with extreme high modulus have been shown in literature to enhance the elastic modulus of other polymer matrices [117]. Figure 4.7 shows the effect of adding 120 μm long glass fiber (20 pphr) to PPHA/(PHA-co-BA) blended films containing 20 pphr, 30 pphr and 40 pphr BMP TFSI and 10 pphr PEO. Samples with glass fibers all have a higher modulus, indicating high modulus of glass fibers compensated to some degree for the elastic modulus loss from plasticizers.

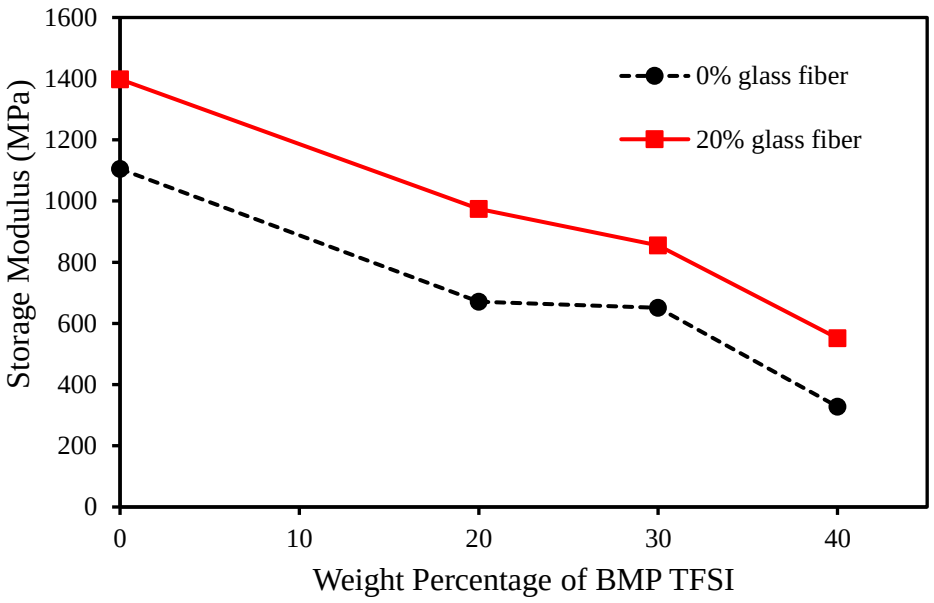

Figure 4.7. Storage modulus of 1:1 P(PHA-co-BA):PPHA films containing 20 pphr, 30 pphr, and 40 pphr BMP TFSI and 10 pphr PEO with various loadings of glass fibers

4.4 Conclusion

The thermal, mechanical, and transient properties of PPHA were assessed with a variety of non-ionic and ionic plasticizers. The storage modulus was found to decrease substantially by the addition of the plasticizers. BEHP was found to have the greatest effect on lowering the storage modulus and maintaining the liquid state of PHA and achieving fast depolymerization rates. The pyrroldinium and ammonium ionic liquids were found to not undergo phase separation at high loadings, up to 100 pphr, and had the least effect on the modulus of elasticity. Addition of ionic liquid plasticizer resulted in liquid byproducts that can be absorbed into environment to achieve transient purpose.

CHAPTER 5.

TIME-DELAYED PHOTO-INDUCED DEPOLYMERIZATION OF POLY(PHTHALALDEHYDE) SELF-IMMOLATIVE POLYMER VIA IN-SITU FORMATION OF WEAK CONJUGATE ACID

5.1 Introduction

While photosensitive poly(aldehydes) is the main goal for this dissertation, it is ideal if the photoinduced depolymerization can be controlled/delayed under normal lighting conditions to expand the time-frame for transient device usage. In this work, a time-delayed mechanism for our transient system is explored.

Polymer-based transient devices and materials are an emerging field of research where the triggered disposal of the device is required so as to avoid reverse-engineering, retrieval or detection [2,51]. Some transient concepts involve the dissolution of the device in an aqueous solvent, however, solution-based resources may not be available [42,43,118,119]. Moore et al. introduced the concept of stimuli-responsive polymers such as poly(phthalaldehyde) (PPHA) as a metastable material that can be used for a variety of transient device applications [49,107]. Low ceiling temperature polymers, such as PPHA, are thermodynamically unstable above their ceiling temperature and can be kinetically stabilized by end-capping or cyclization of the chains for use above their ceiling temperature [16,104,105]. The removal of the kinetic-trap can induce rapid, unzipping depolymerization at room-temperature [106,120]. The PPHA backbone is susceptible to

cleavage via free-acid protonation of the acetal linkage [45]. A recent study used polymeric thermal acid generators, such as poly(vinyl t-butyl carbonate sulfone), to increase the depolymerization kinetics at low temperature [108]. A specific-ion coactivation effect at the surface of cyclic PPHA microcapsules has been shown to accelerate depolymerization in acidic methanol solution [121]. Photo-acid generators (PAG) have also been used to trigger PPHA depolymerization via sunlight and other radiation sources [28,49,51,122]. The PAG spectral response has been extended to include the entire visible spectrum for sunlight or targeted wavelength exposure [47,48,123]. The use of a photo-induced electron transfer (PET) reaction between a chemical sensitizer and photo-acid generator (PAG) to create a strong acid in-situ upon exposure to visible light is of particular interest because it opens up device applications where visible light is available upon mission completion.

The mechanism of triggering PPHA depolymerization using visible light has been discussed [47], however, the time-delayed, controlled depolymerization of PPHA remains largely unexplored. One limitation of the immediate, photo-initiated depolymerization of PPHA is that abundant radiant energy may not be available at the end of the device mission. Either low or uneven light radiant energy across the device can cause problems for device destruction. Also, inadvertent predeployment or in-use photo-exposure of the PAG can cause premature device destruction. Thus, it is desirable to activate the PAG just prior to deployment or during the mission where reliable exposure conditions can be guaranteed, followed by time-delayed PPHA depolymerization. This allows the one-time use of transient devices during daytime hours, if the delay time can be made to match the mission lifetime. It would be especially valuable for the delay time to be predetermined by the user.

It has been found that certain amide and lactam-based compounds delay PPHA depolymerization after exposure of the PAG-loaded mixtures. The chemical interaction of the amide or lactam with the in-situ, photo-generated strong acid has been explored. The depolymerization rate vs. temperature shows that the delay follows first-order kinetics and an Arrhenius relationship for the activation energy. It has also been shown that the mechanical properties of the PPHA film can be maintained during the post-exposure delay period.

5.2 Experimental

Materials: The PAG, tetrakis(pentafluorophenyl)borate-4-methylphenyl[4-(1-methylethyl)phenyl]iodonium (Rhodorsil FABA), was purchased from TCI Chemicals. Anthracene and dimethylacetamide (DMAc) were purchased from Alfa Aesar. 1-Butyl-1-methylpyrrolidinium bis(trifluoromethylsulfonyl)imide (BMP TFSI) was purchased from Iolitec. N-methyl-pyrrolidone (NMP), 1-phenyl-2-pyrrolidinone, N-isopropylacrylamide, 1,5-dimethyl-2-pyrrolidinone, and bromothymol blue were purchased from Sigma Aldrich. Tetrahydrofuran (THF) was purchased from BDH. Cyclopentanone was purchased from EMD Millipore Corporation. All chemicals were used as received. PPHA was cationically polymerized using boron trifluoride etherate (BF_3) at -80 ºC following the procedure of Schwartz et al. [9]. The PPHA number average molecular weight of the polymer used in this chapter was 352 kDa with a dispersity (Đ) of 1.27.

Sample Preparation: PPHA films were formulated in a clean scintillation vial by dissolving the solid contents and BMP TFSI in THF. A weight ratio of 12:1 for THF-to-PPHA was used in all formulations in this chapter. PAG and anthracene were added with

a molar ratio of 1:1.2 in all formulations. Anthracene was present in all films containing PAG at the mole ratio in order to make the films sensitive to near-UV radiation. Films were cast in a PTFE petri dish and dried at room temperature at 17 psig nitrogen atmosphere for 18 h, followed by 30 h at 15 psig with slow bleeding of THF vapor. The films were peeled off the PTFE petri dish and allowed to dry at ambient temperature and pressure for 2 days in the dark before characterization.

Characterization: Quartz crystal microbalance (QCM) experiments were performed at 23 °C using a Stanford Research Systems QCM 200 to quantify the solid-state kinetics of PPHA depolymerization. Polymer formulations were made with 9.1 wt% polymer solids in cyclopentanone with 5 parts per hundred resin (pphr) of PAG and 1.05 pphr anthracene. The PAG and anthracene loadings were with respect to the PPHA weight. The QCM films were 1.2 µm thick and made by spin-coating onto a 2.54 cm diameter QCM substrate. The disks had a resonant frequency of 5 MHz unloaded and an active surface area of 0.4 cm^2. An open-faced holder was used to expose the polymer film to the output of a 1000 W Hg(Xe) Oriel Instruments flood exposure lamp with 365 nm bandpass filter. The exposure dose was 730 mJ/cm^2 for all samples. QCM experiments were also performed at different temperatures using a Q-Sense E4 QCM to quantify the PPHA depolymerization time vs. temperature.

The PPHA depolymerization kinetics were studied using the QCM. The Butterworth-van Dyke equivalent circuit model for the QCM electrical response provided information on PPHA degradation, especially as the solid converted into a viscous liquid. The change in resonance frequency is related to the mass change of thin film, as shown in Equation 1.

$$\Delta f = -C_f m \quad (1)$$

In Eq. 1, C_f is a calibration constant, m is the mass of the film, and Δf is the change in resonance frequency. The decrease in mass resulting from evaporation of the PPHA monomer results in an increase in resonance frequency. An increase in motional resistance for the QCM in the Butterworth-van Dyke model occurs when the solid PPHA film softens or liquefies on the QCM resulting in QCM vibrational energy loss. The increase in resistance, visual inspection of the QCM and detection of PHA odor are direct evidence of PPHA depolymerization.

Dynamic mechanical analysis (DMA) of films was performed on a TA Q800 DMA instrument. All DMA samples were 30 x 8 x 0.1 mm (length-width-thickness). The measurements were performed at 23 °C with 0.075% strain at 1 Hz. The samples were measured at constant temperature for 3 min before being exposed to a dose of 730 mJ/cm^2. This dose was chosen because it is greater than the minimum dose needed to fully expose the PAG. The storage modulus of the films was continuously measured to track the mechanical degradation of PPHA after photo-exposure.

UV-visible (UV-Vis) absorption spectroscopy was performed using Hewlett Packard 8543 UV-Vis spectrophotometer in THF solution. Attenuated total reflectance (ATR) infra-red spectroscopy experiments were performed using a Nicolet iS50 FT-IR instrument. Duplicate samples prepared for DMA were examined by ATR-IR. The ATR-IR spectra were recorded before and after 730 mJ/cm^2 optical exposure. A total of 32 FT-IR scans were obtained for each sample.

5.3 **Results and Discussion**

The PET reaction between anthracene and PAG was used to create a strong acid within the PPHA film to catalyze PPHA depolymerization after UV exposure. Figure 5.1 shows the QCM resistance (from the Butterworth-van Dyke model) versus time after exposure of a series of PPHA films containing different concentrations of NMP. The rapid increase in resistance in Figure 1 represents QCM energy loss due to viscoelastic damping caused by depolymerization and liquification of the PPHA film. PPHA films with no NMP had a QCM photoresponse delay of 34 s. This corresponds to the time needed for the strong acid to be formed and catalyze PPHA depolymerization to the point where the solid film liquefied. The addition of 0.25 pphr and 0.5 pphr NMP in the PPHA film delayed the photoresponse by 48 s and 59 s, respectively. Higher levels of NMP, 1 pphr, 5 pphr and 10 pphr, delayed the photoresponse further to 195 s, 4034 s and 6292 s, respectively. The mole ratio of NMP-to-PAG is 0.5:1, 1:1, 2:1, 10:1, 20:1 for films containing 0.25, 0.5, 1, 5, 10 pphr NMP and 5 pphr PAG (i.e. the films giving the above mentioned delay times). Photographs of 150 μm thick PPHA films with and without 5 pphr NMP as a function of time after photo-exposure are shown in Figure 5.2. The photoresponse delay is due to the moderating effect of NMP on the acidity of the acid produced by the PET reaction.

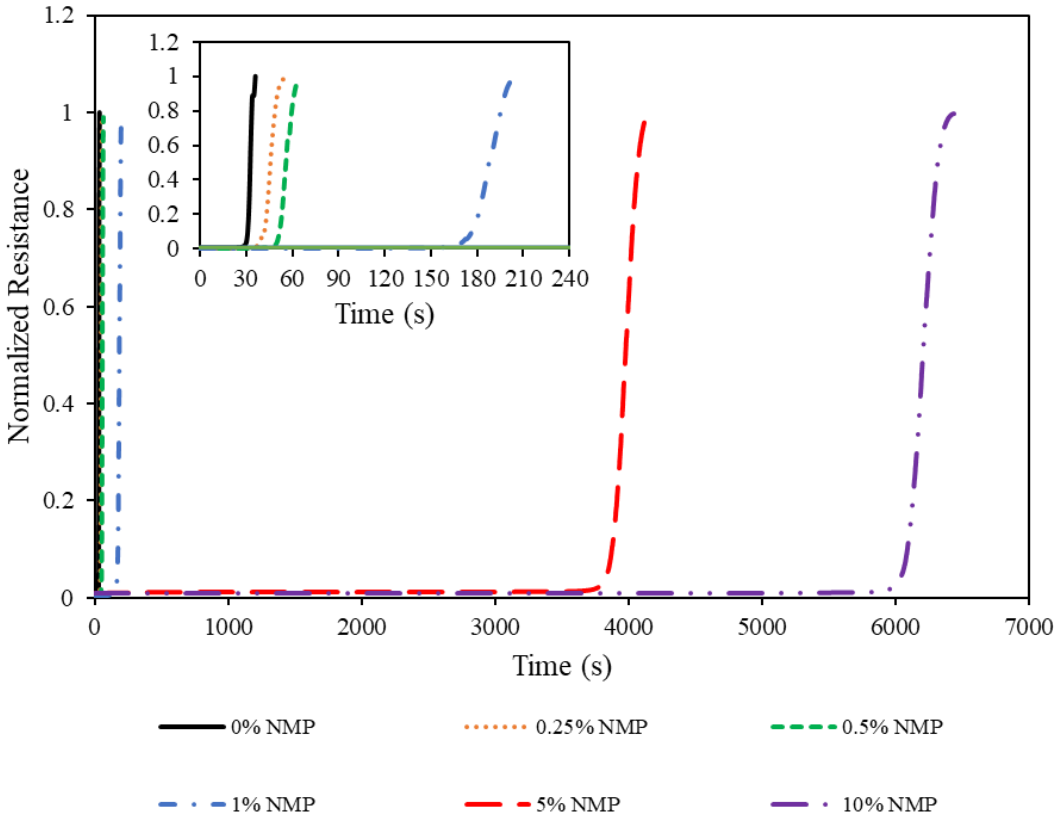

Figure 5.1. QCM experiments for PPHA films containing various loadings of NMP. From left to right are the films containing 0%, 0.25%, 0.5%, 1%, 5%, 10% loadings of NMP respectively

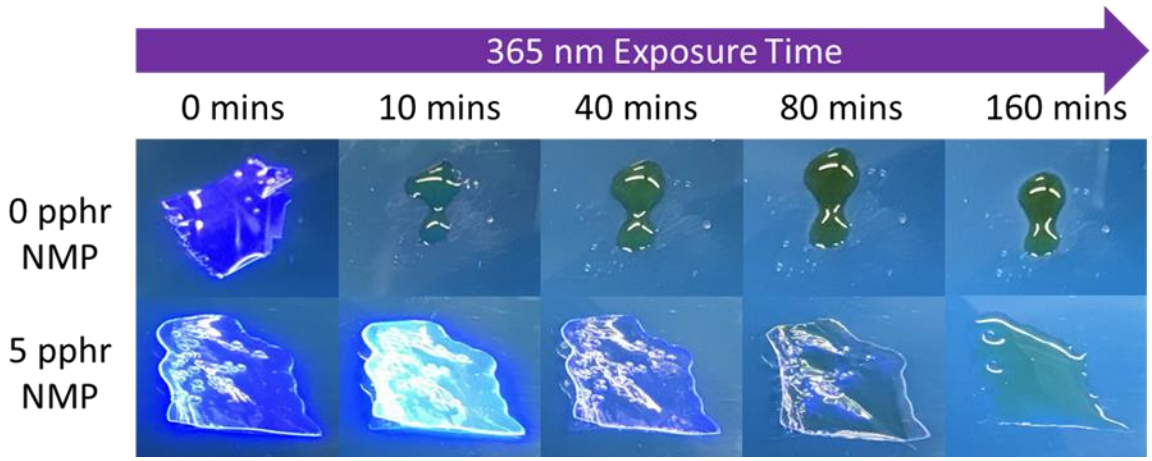

Figure 5.2. Time lapse photo comparison for depolymerizing PPHA films containing 0 pphr and 5 pphr NMP

NMP is a polar, basic solvent. Its conjugate acid has a $pK_a = -0.92$ (i.e. $pK_b = 14.92$), as measured in aqueous sulfuric acid [124]. The photo-generated acid and NMP are in acid-base equilibrium, as shown in Scheme 5.1. In this context, the products resulting from the reaction of the superacid and weak base (NMP) is a conjugate acid ($NMP\text{-}H^+$) where the acidity of the conjugate acid ($NMP\text{-}H^+$) is less than that of the original superacid. The acid-base complex formed between NMP and the PAG-generated acid depolymerizes the PPHA polymer more slowly than the photo-generated free acid due to the higher activation energy required to depolymerize PPHA using a weak acid ($NMP\text{-}H^+$). Lactam and lactim tautomers formed with the $NMP\text{-}H^+$ protonated additive were previously investigated by FT-IR and shown to be stabilized by a resonance structure created through the organic amide functionality (i.e. carbonyl adjacent to amine) [125]. The acidity of the conjugate acid created by reaction of photo-generated strong acid and lactam is less than that of other photo-generated acid because of the resonance stabilization of the protonated organic amide.

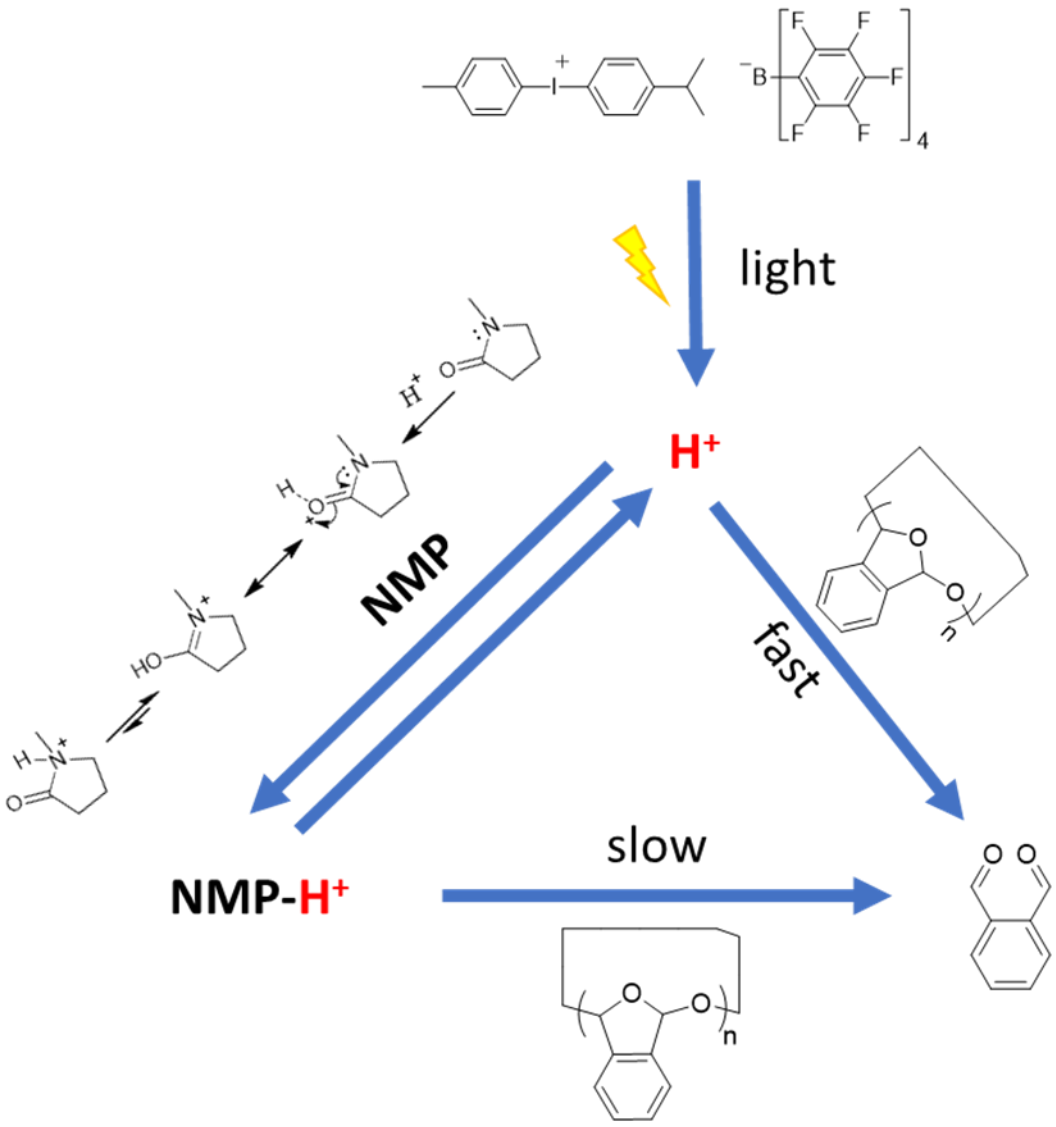

Scheme 5.1. Schematic for competitive reaction of H^+ and NMP-H^+ react with PPHA

The effect of conjugate acid acidity on the PPHA depolymerization delay time was investigated by using various amides and lactams with different basicity. Scheme 5.2 shows the chemical structures of additives (i.e. amides and lactams) used. Figure 5.3 shows the UV-Vis spectrum for several of the compounds shown in Scheme 5.2 and anthracene, the photo-sensitizer used to activate the PAG. Anthracene has near-UV absorption from

365 nm to 390 nm. This is the radiation used to induce electron transfer to the PAG and create the photo-acid. The amide and lactam additives do not interfere with photo-acid creation because they do not absorb UV radiation between 365 nm to 390 nm, the spectral region where anthracene absorbs. Thus, the time-delay in PPHA depolymerization was not due to attenuation of UV radiation in the activation of the PAG.

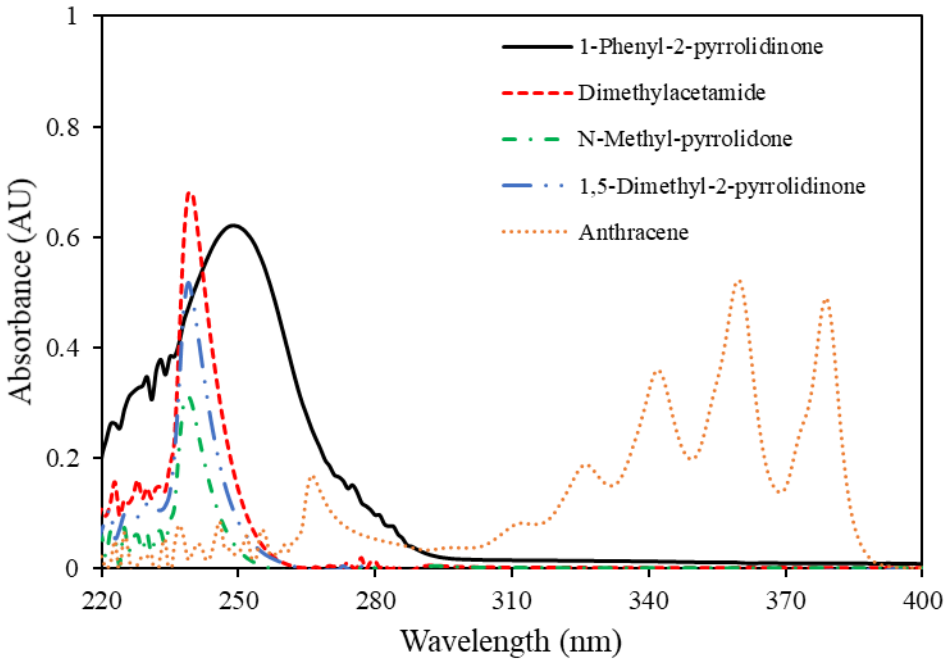

Figure 5.3. UV-Vis spectrum for anthracene and additive used for time-delayed photo-depolymerization of PPHA

Additive	Chemical Structure
1-Phenyl-2-pyrrolidinone	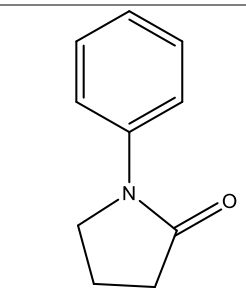
N-Isopropylacrylamide	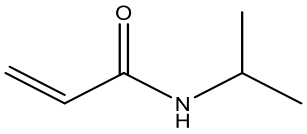
Dimethylacetamide (DMAc)	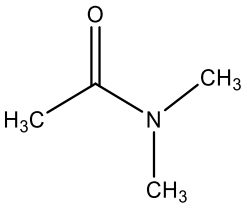
N-Methyl-pyrrolidone (NMP)	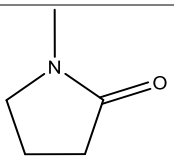
1,5-Dimethyl-2-pyrrolidinone	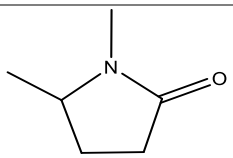

Scheme 5.2. Chemical structures of weakly basic additives used for time-delayed photo-depolymerization of PPHA

Figure 5.4 shows the QCM resistance change after exposure of PPHA films with the five different amides and lactams (Scheme 5.2) in the PPHA at a 10:1 base-to-PAG mole ratio. A 10:1 mole ratio of base-to-PAG corresponds to the 5 pphr NMP experiment described above. All samples were exposed to a 730 mJ/cm^2 radiation dose, which is above

the threshold needed to activate the anthracene-sensitized PAG. The PPHA depolymerization time increased with the basicity of the amide or lactam additive. As the basicity of the amide/lactam additive increased, the acidity of the resulting conjugate acid decreased, thus increasing the activation energy for the conjugate acid to depolymerize PPHA. It is noted that the shift in PPHA depolymerization time shown in Fig. 5.4 corresponds to the case of excess base with respect to the PAG-generated acid. The PPHA film containing 1-phenyl-2-pyrrolidinone resulted in the most rapid PPHA depolymerization after exposure among five amide or lactams shown in Fig. 5.4. 1-Phenyl-2-pyrrolidinone is a weaker base than NMP due to the strong electron withdrawing nature of the aromatic ring on the nitrogen. The weaker base results in the formation of a stronger conjugate acid. Thus, the depolymerization of PPHA occurred faster than the film containing NMP. N-isopropylacrylamide had a slightly longer delay time than 1-phenyl-2-pyrrolidone due to the absence of the strong electron withdrawing phenyl ring, making it a stronger base or better electron pair donor. N-isopropylacrylamide is less effective in delaying depolymerization than DMAc due to its less basic secondary amine compared to the tertiary amine of DMAc in a non-aqueous PPHA film. Moreover, the disappearance of the electron withdrawing acryloyl group in N-isopropylacrylamide also led to higher basicity for the nitrogen atom in DMAc. DMAc has less affinity for H^+ (less basic) compared to NMP, making it a weaker base than NMP in an acidic environment [126]. Therefore, the conjugate acid of DMAc is more acidic than NMP-H^+, leading to a shorter delay time. The inductive effect of alkyl chain length increases the basicity of the compound (creates a weaker conjugate acid), as can be seen in the longer delay time with 1,5-dimethyl-2-pyrrolidinone compared to NMP. 1,5-Dimethyl-2-pyrrolidone has an

additional methyl group resulting in greater electron donating, compared to NMP. This makes 1,5-Dimethyl-2-pyrrolidone a stronger base than NMP (i.e. weaker conjugate acid), resulting in longer PPHA depolymerization delay time. It is also noted that strong bases inhibit any PPHA depolymerization and weaker bases have no effect on PPHA depolymerization time, as described below.

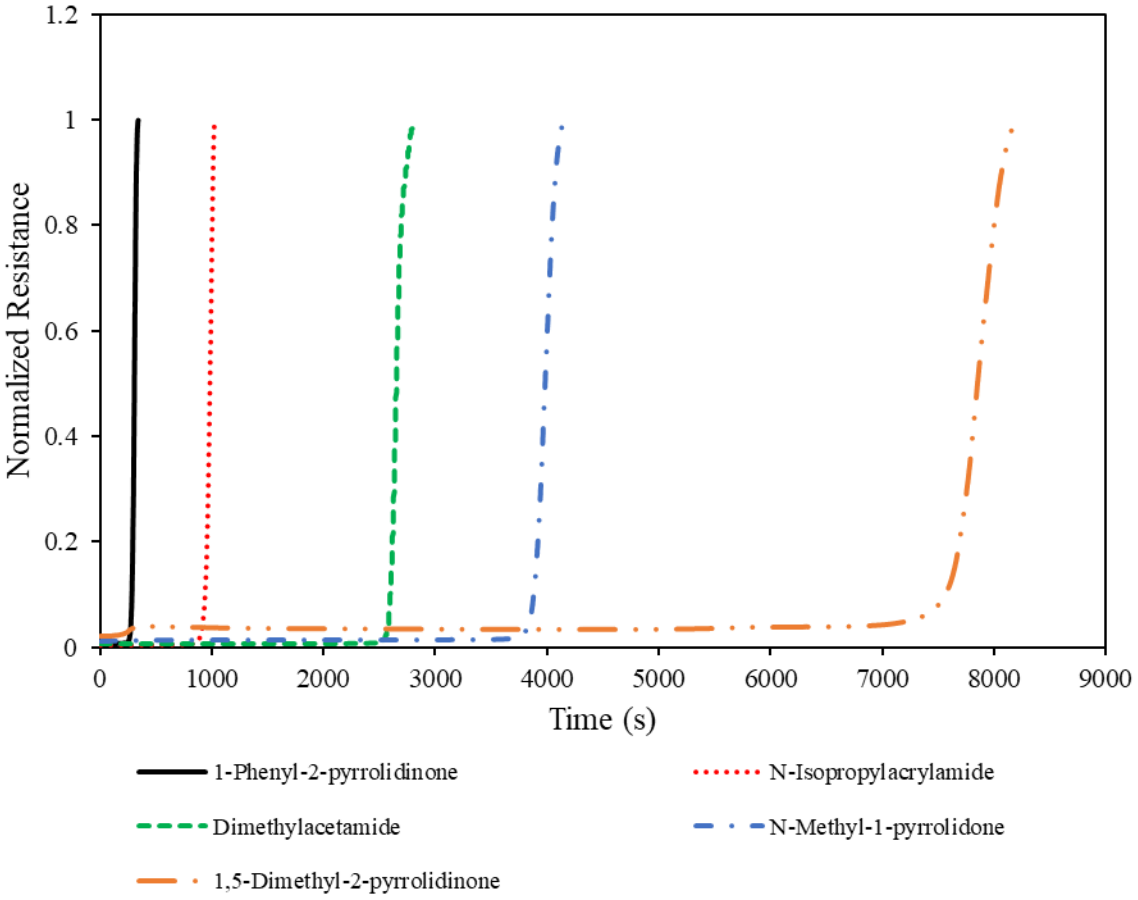

Figure 5.4. QCM experiments for PPHA films containing equal molar of different lactam/amide additives to 5 pphr NMP

The shift in acidity of the photo-generated acid by use of a lactam or amide additive was confirmed by incorporation of an acid/base color indictor in the PPHA film. Bromothymol blue is magenta at pH<0 and progressively more yellow as the pH is increased from zero to 6 [127]. Figure 5.5 shows the color change of PPHA films containing bromothymol blue, PAG and anthracene. The three samples on the left side of Fig. 5 contained 0.5 wt% (with respect to PPHA) bromothymol blue and also contained (left to right): (i) no amide/lactam additive, (ii) NMP, and (iii) 1,5-dimethyl-2-pyrrolidinone. After UV exposure (picture on the right side of Fig. 5), all three samples were liquid due to PPHA depolymerization. The time to depolymerize the PPHA was longer for the samples containing NMP and 1,5-dimethyl-2-pyrrolidinone, as described above. The liquid remnant of film with no additive turned magenta upon UV exposure showing that the bromothymol blue was in its most acidic state. The remnant of the films with NMP and 1,5-dimethyl-2-pyrrolidinone were orange after UV exposure with the NMP appearing more orange than the 1,5-dimethyl-2-pyrrolidinone-containing sample. This test proves that the pH is lower in the sample containing no lactam/amide additive and the conjugate acid formed by reaction of the photo-acid with the NMP or 1,5-dimethyl-2-pyrrolidinone is less acidic. It also shows that the conjugate acid formed from NMP is more acidic than the formed from 1,5-dimethyl-2-pyrrolidinone.

Figure 5.5. pH test for in-situ generated acid strength inside PPHA films with and without addition of 5 pphr NMP using bromothymol blue as indicator

Bases which were either stronger or weaker than the lactams and amides discussed above had a more extreme effect on depolymerization time than the ones shown in Scheme 5.2. Bases weaker than NMP had little or no effect on PPHA depolymerization time because the conjugate acid was effectively not different from the photo-generated acid. For example, bis(2-ethylhexyl) phthalate had no effect on PPHA depolymerization delay time [123]. Bases which were stronger than the ones listed in Scheme 5.2, such as 1-octyl-2-pyrrolidone, had extremely long delay times because the conjugate acid was weaker. It is noted that 1-octyl-pyrrolidone is a stronger base because of the electron donating effect of the long alkyl chain attached to the nitrogen atom. Similarly, the addition of tetramethyl-1,6-hexanediamine also resulted in a near-infinite delay time due to its higher basicity. The tertiary amine structures on each end of the molecule and its long alkyl group in the middle makes it a stronger base than NMP.

The activation energy for the NMP-H^+ catalyzed PPHA depolymerization was determined in order to estimate the delay time for PPHA after UV exposure at different temperatures. Figure 5.6 shows the depolymerization time, as determined by the rise in

QCM resistance, for the PAG (5 pphr) and NMP (5 pphr) loaded films at different temperatures. At 28 °C, it took 2700 s for the film to start depolymerizing. At 33 °C and 38 °C, the onset of depolymerization was only 1920 s and 1200 s, respectively. First-order reaction kinetic and an Arrhenius relationship for the rate were used, Equations 1 and 2.

$$k(T) = Aexp(-\frac{E_A}{RT}) \quad (1)$$

In Eq. 1, k(T) is the reaction rate (s^{-1}) at a specific temperature, A is the pre-exponential factor, E_A is the activation energy, R is the gas constant (8.314 J/mol-K), and T is the reaction temperature (K). The equation can be linearized, as shown in Equation 2.

$$\ln(k) = -\frac{E_A}{R}\frac{1}{T} + \ln(A) \quad (2)$$

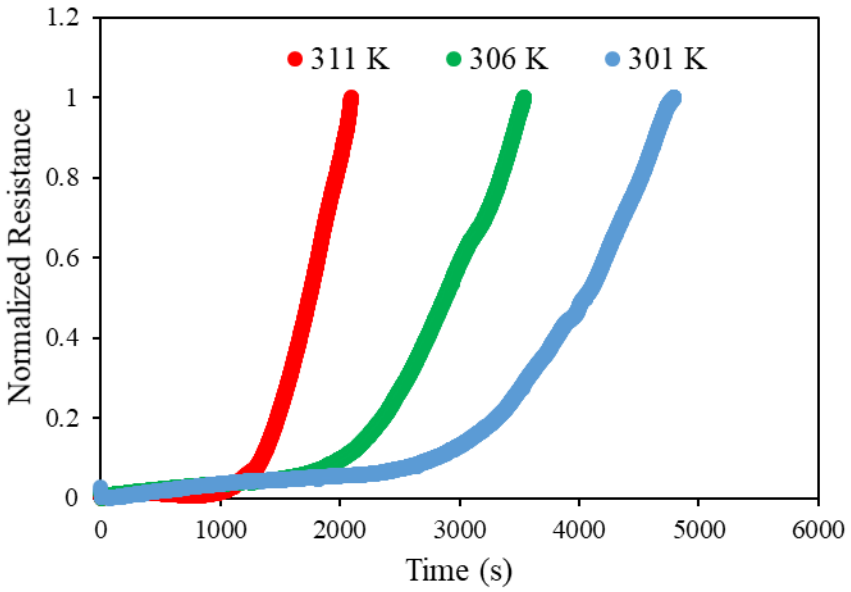

Figure 5.6. QCM experiments at different temperatures for PPHA films containing 5 pphr NMP

Figure 5.7 shows the linearized plot of ln(k) vs. 1/T for PPHA films containing 5 pphr NMP and 5 pphr PAG (in addition to anthracene). The value of k(T) for each sample was taken as the inverse of onset time for depolymerization in the QCM. The resulting E_A for the reaction is 61 kJ/mol and A is $1.3*10^7$ s^{-1}.

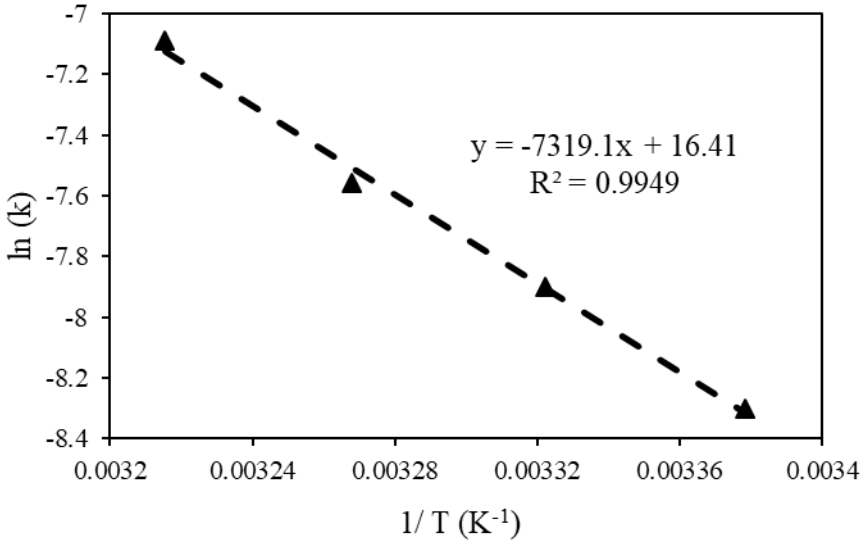

Figure 5.7. Plot of ln(k) vs 1/T for PPHA films containing 5 pphr NMP. Arrhenius type response was assumed and linear fitting was used to extrapolate activation energy and pre-exponential factor

Depolymerization of PPHA leads to the formation of phthalaldehyde (PHA) monomers, which can be monitored by following the carbonyl peak height in infrared spectroscopy. The carbonyl peak height was monitored for films containing 0 pphr, 1 pphr and 5 pphr NMP (i.e. mole ratio of NMP-to-PAG of 0:1, 2:1, and 10:1) using the C-F stretch at 1352 cm^{-1} from BMP TFSI as the reference peak for total internal reflectance FTIR after photo-exposure. Figure 5.8 shows the absorbance of PHA monomers vs time after PPHA film exposure. The rate of formation of the carbonyl peak, corresponding to

PPHA depolymerization (i.e. PHA monomer formation), was slower for films containing higher NMP content, which confirms slower PPHA depolymerization rate when more NMP is present in the film.

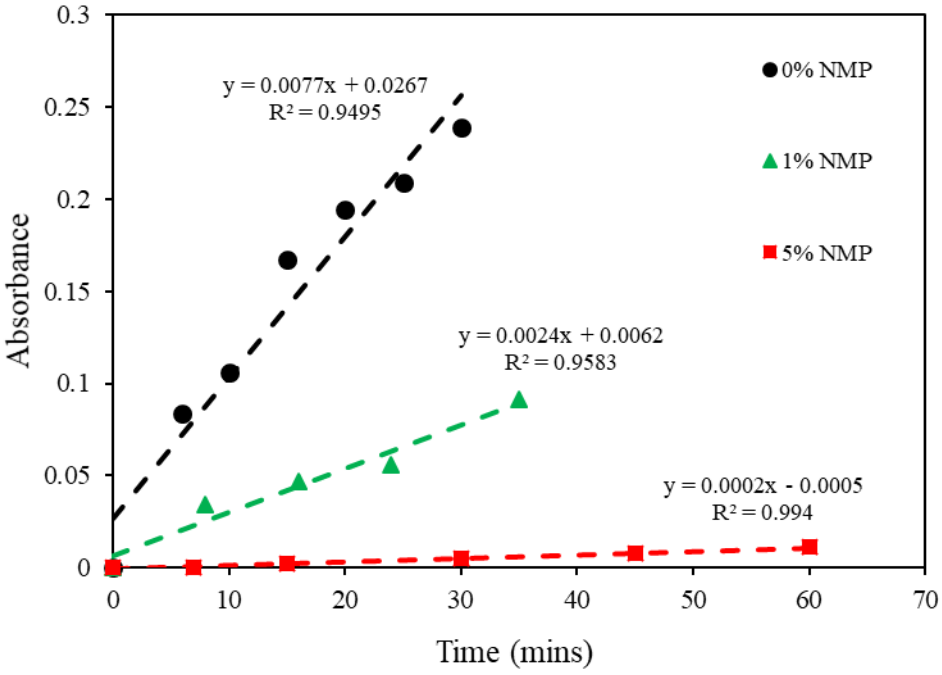

Figure 5.8. ATR absorbance of PHA monomer peak after periods of time for films containing 0 pphr, 1 pphr, and 5 pphr NMP

The mechanical properties of the films containing NMP after exposure were investigated. Figure 5.9 shows the storage modulus for films with different NMP loadings after photo-exposure. The PAG in the PPHA films was fully exposed to ensure complete PET activation. With the addition of 5 pphr NMP in PPHA, no significant loss of mechanical stiffness before UV exposure was observed. The average storage modulus was 1600 MPa. Upon UV exposure, the immediate mechanical degradation was observed for

films without NMP. Films containing higher loadings of NMP maintained mechanical integrity longer. Films with 5 pphr NMP and 5 pphr PAG had similar mechanical stiffness for the first 80 min after exposure. The delay time for a significant drop in modulus approximately matched the QCM liquefaction time. Therefore, the addition of 5 pphr NMP helped delay the photoresponse of PAG loaded PPHA films while can still maintaining similar mechanical properties during the transition period.

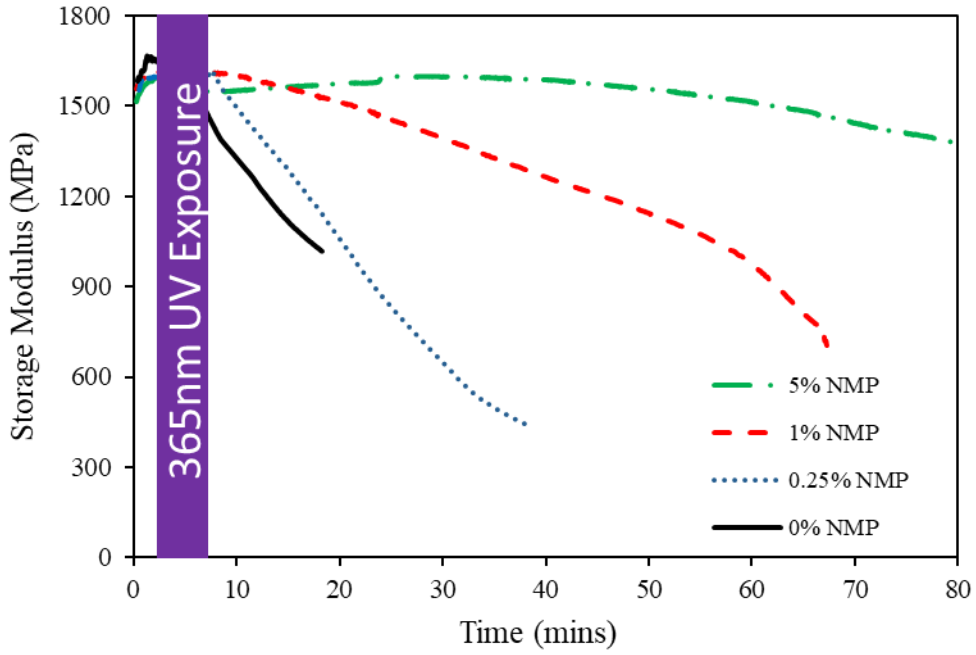

Figure 5.9. In-situ DMA measurement of films storage modulus change over time with different loadings of NMP after UV exposure

5.4 Conclusion

A class of lactam and amide based additives was found to effectively delay the photo-depolarization of PAG loaded PPHA photo-transient materials. The fundamental

cause of the delayed depolymerization was attributed to the formation of a weaker conjugate acid when the lactam/amide additive was present. The delay time was related to the basicity of the additive. By incorporating a suitable amount of lactam or amide additive into the PPHA film (molar excess compared to the photo-generated acid), the mechanical property integrity could be maintained for more than 80 min at room temperature without sacrificing the initial mechanical stiffness. The delay time was considerably longer at lower temperature. By tuning the amount of additive in the film, the depolymerization time of PPHA-based transient devices can be tuned to specific mission lifetimes.

CHAPTER 6.

PHOTODEGRADABLE TRANSIENT BILAYERED POLY(PHTHALALDEHYDE) WITH IMPROVED SHELF-LIFE

6.1 Introduction

Fabrication of photosensitive transient device requires extra caution with fabrication environment, as accidental light exposure could result in irreversible damage to transient device that is in fabrication process. In this chapter, the goal is to show the feasibility of fabricating bilayer transient device where the fabrication can be safely done at ambient lights while still be able to achieve transient purpose in the end.

The emerging field of research into transient devices has attracted attention due to the need for disappearing electronics and other applications where device discovery, recovery or retrieval is undesirable. The goal is to create devices that degrade and can be incorporated into the surrounding environment with little or no environmental impact [2,128]. To meet the transient device goals, the material needs to degrade quickly under local stimuli and disappear completely after degradation. Cyclic poly(phthalaldehyde) (PPHA), a cationically polymerized rigid polymer, is a potential candidate material for the emerging transient device applications [5,49,129]. PPHA is a self-immolative polymer where breaking an acetal linkage in the cyclic PPHA polymer backbone leads to cascading chain unzipping resulting in the polymer reverting back to its monomer form at temperatures above its ceiling temperature, ca. -42 $^{\circ}$C [45,46].

PPHA degradation can be triggered by different types of stimuli. These include photo-chemical (e.g., visible light, light emitting diode, ultraviolet) [46–49], chemical [54,121], thermal [54,108], and mechanical stimulus [55,130]. Visible light stimulus is particularly attractive because of the availability of ambient light. Phillips et al. demonstrated the use of a photo-induced electron transfer (PET) reaction between a fused-aromatic-ring sensitizer and photoacid generator (PAG) to create a strong acid that led to PPHA degradation using visible light [47]. Anthracene (λ_{max} = 370 nm) was modified to form 1,8-dimethoxy-9,10-bis(phenylethynyl)anthracene (DMBA, λ_{max} = 476 nm and 504 nm) allowing a broader wavelength of light to be harvested, resulting in a faster rate of degradation in sunlight [47].

However, the direct addition of photosensitive compounds into PPHA presents a risk of inadvertent photo or thermal triggering of PPHA during device fabrication. Also, photo-active compounds are known to have a limited shelf-life at elevated temperatures [131]. The free acid created by PAG activation limits the ultimate shelf-life of the PPHA-containing component. Therefore, it is desirable to avoid adding the photosensitive compounds when fabricating transient devices until the last possible moment before use.

The use of a photosensitive/non-photosensitive bilayer structure to study photoacid diffusion in photoresists has been previously reported [132–137]. The rate of photoacid diffusion in photoresist can be quantified by allowing the photoacid to diffuse from a photosensitive layer to a non-photosensitive layer. Specifically, diffusion occurs through a ‘reaction front’ mechanism. This occurs in photoresist when the temperature is below the glass transition temperature of the non-photosensitive material. The reaction front propagates stepwise from the photosensitive layer to the non-photosensitive layer

following a layer-by-layer mechanism. Here, the acid diffuses into the non-photosensitive layer initiating its depolymerization. A transient, bilayer structure can be made by first fabricating a non-photosensitive PPHA structure under visible light followed by the formation of a thin, photosensitive PPHA layer on the existing structure using lamination or spray coating. When triggered, the photoacid propagates into the non-photosensitive layer and catalyzes PPHA depolymerization.

In this chapter, a quantitative determination of the activation energy for the thermally induced depolymerization of PPHA powder, and PPHA films (with and without photosensitive compounds) were compared. The activation energy provided the basis for estimating the shelf-life of the transient PPHA device based on the storage temperature. Bilayer PPHA structures were fabricated and the diffusivity of the acid was studied to determine the PPHA degradation rate based on acid diffusion.

6.2 **Experimental**

Materials: 1-Butyl-1-methylpyrrolidinium bis(trifluoromethylsulfonyl)imide (BMP TFSI) was purchased from Iolitec. The PAG, Tetrakis(pentafluorophenyl)borate-4-methylphenyl[4-(1-methylethyl)phenyl]iodonium (Rhodorsil FABA), was purchased from TCI Chemicals. Anthracene was purchased from Alfa Aesar and tetrahydrofuran (THF) was purchased from BDH. All chemicals bought were used as received. Cyclic PPHA was cationically polymerized below its ceiling temperature (-42 ^{o}C) following previous synthesis procedure [5]. The resulting PPHA has a number average molecular weight of 397 kDa with a dispersity (Đ) of 1.18.

All PPHA films were solvent cast with 60 part per hundred (pphr) BMP TFSI (with respect to the weight of PPHA) in order for the depolymerized products of PPHA to remain liquid. Polymer formulations were prepared in a clean glass vial with addition of all solid contents (PPHA, PAG, and anthracene) and BMP TFSI dissolved in THF, with a 12:1 weight ratio for THF:PPHA. The films were cast onto PTFE-lined petri dishes and dried at room temperature with a 15 psig nitrogen overpressure for 18 h, followed by 12 h at 15 psig nitrogen with a slow THF vapor bleed rate. The films were peeled off the PTFE substrates and allowed to dry in the dark for two days.

Thermogravimetric analysis (TGA) was performed with a TA Q50 Instrument. All samples prepared were dried for over a month to ensure low solvent content. All samples tested were isothermally aged in a nitrogen rich environment for 24 h. TGA pan was cleaned by ramping to 900 ºC to remove organic residue. The time for 2% weight change for each sample was recorded as an indication of the onset of decomposition of the polymer and film.

To study the photoacid diffusivity from the photosensitive layer to the non-photosensitive layer, the films were held in-place using double-sided tape on a quartz substrate and flattened using 300 kPa hydraulic pressure to ensure sample flatness for later thickness measurement. Bilayer PPHA films were prepared by laminating two PPHA film layers using solvent bonding. Bilayer PPHA films were then exposed at a total dose of 3.6 J/cm^2 from a Xe lamp to ensure complete activation of the PAGs [47]. This dose was chosen because it is greater than the minimum dose needed for full PAG activation. Scheme 6.1 describes the preparation of a bilayer PPHA film. Films were post-exposure baked (PEB) at various temperatures for different times. The depolymerization product,

phthalaldehyde (PHA), was removed by dissolution in methanol. The resulting films were again dried under nitrogen. A Veeco Dektak 150 Profilometer was used to measure the depth of the pit formed. The profilometer was operated at a scan rate of 1.11 µm/s with a stylus tip force of 1 g.

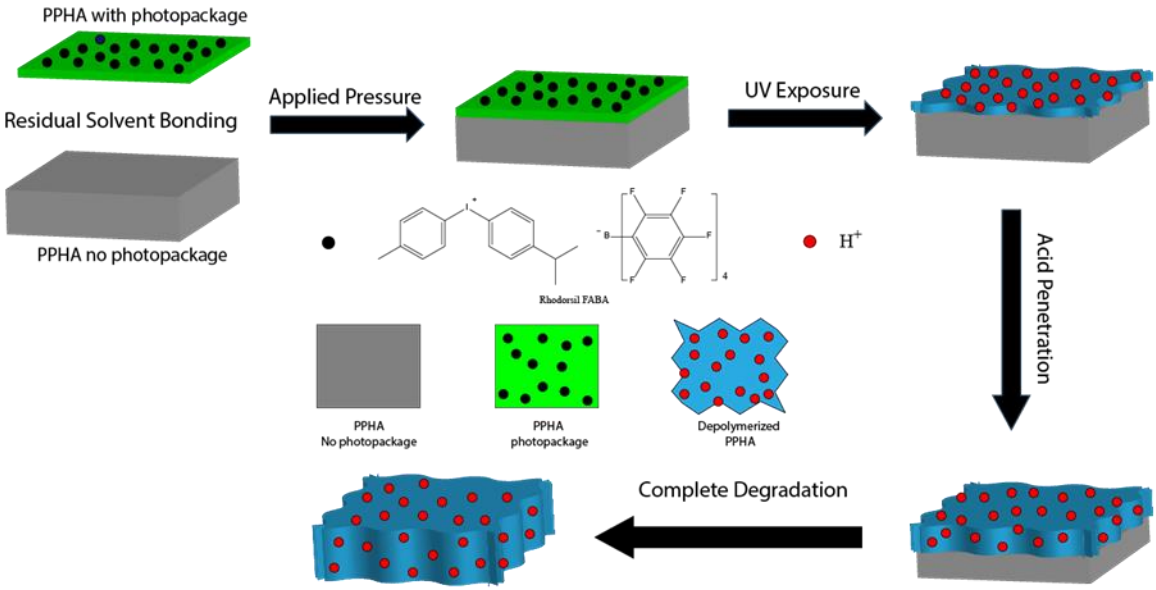

Scheme 6.1. Preparation of bilayer photosensitive PPHA film using solvent bonding

6.3 Results and Discussion

The rate limiting step is PPHA depolymerization after the initial chain scission ring opening reaction [45]. Chain scission ring-opens the cyclic polymer and activates (deprotects) the newly created chain ends, initiating the rapid depolymerization of PPHA back to monomer [54]. First order reaction kinetics and an Arrhenius relationship for the rate constant was used to describe the PPHA degradation rate, Equation 1.

$$k(T) = Aexp(-\frac{E_A}{RT}) \qquad (1)$$

In Eq. 1, k(T) is the reaction rate at a specific temperature T, A is a pre-exponential factor for the reaction, E_A is the activation energy for the reaction, and R is the gas constant. Eq. 1 can be linearized to obtain E_A and A from gradient and interception, Equation 2.

$$\ln(\mathrm{k}) = -\frac{E_A}{R}\frac{1}{T} + \ln(\mathrm{A}) \qquad (2)$$

The stability of PPHA polymer powder, PPHA polymer film without photosensitive compounds, and PPHA polymer film with photosensitive compounds (10 pphr PAG, 2.1 pphr anthracene) were evaluated. The fractional weight change under isothermal conditions for each sample at a specific temperature was recorded, shown in Figure 6.1. Figure 6.2 shows a plot of natural logarithm of reaction rate versus inverse temperature. Table 6.1 summarizes E_A and A values from the linear data fit for each sample, Eq. 2. The pre-exponential factor has been used to express the collision frequency of molecules at different temperatures. It was calculated from the y-intercept in Figure 6.2. No specific physical interpretation was given to the pre-exponential factor. The results show that high-purity, high molecular weight PPHA polymer is extremely stable with a high activation energy, $3.32*10^5$ J/mol. The PPHA polymer was cationically polymerized using boron trifluoride etherate as the catalyst. A strong Lewis acid can catalyze the depolymerization of PPHA at room temperature through attack of the PPHA ether linkage in the polymer backbone. Purification of the PPHA after synthesis is critical to achieving stable polymer. This includes removing the BF_3 catalyst to a level below 1 part per million, as measured by inductively coupled plasma mass spectrometry (ICP-MS). It is noted that this concentration is lower than the previously documented safe BF_3 level [123]. Inclusion of 60 pphr BMP

TFSI into the PPHA film lowered the activation energy slightly to $2.23*10^5$ J/mol. The decrease in activation energy may be due to the higher chain segment and impurity (e.g. BF_3) mobility within the mixture caused by the BMP TFSI plasticizing effect on the polymer film. Nevertheless, the expected stability of PPHA films with no photosensitive compounds should be about 400 days at 50 °C, based on extrapolation of the Arrhenius data.

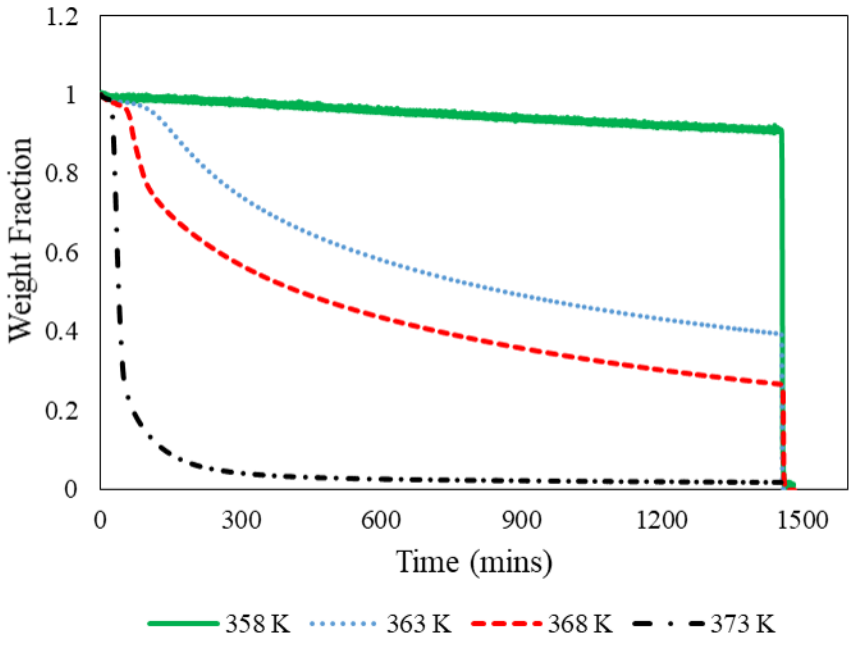

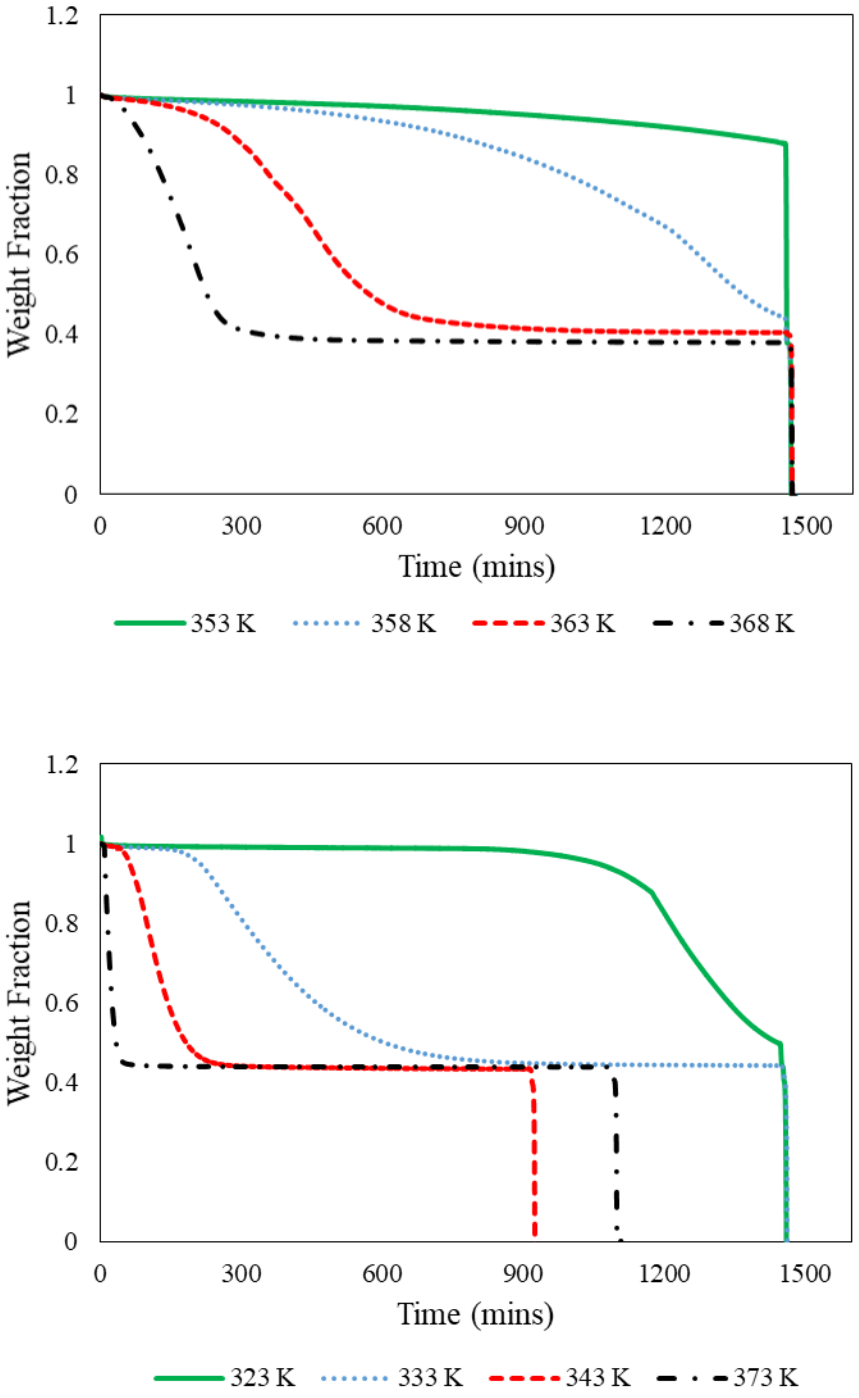

Figure 6.1. TGA result for weight fraction versus time at several isothermal temperatures for a) PPHA polymer powder thermally stressed at 358 K, 363 K, 368 K, and 373 K; b) PPHA film with 60 pphr BMP TFSI was thermally stressed at 353

K, 358 K, 363 K, and 368 K; c) PPHA film with 60 pphr BMP TFSI and photosensitive compounds was thermally stressed at 323 K, 333 K, 343 K, and 373 K

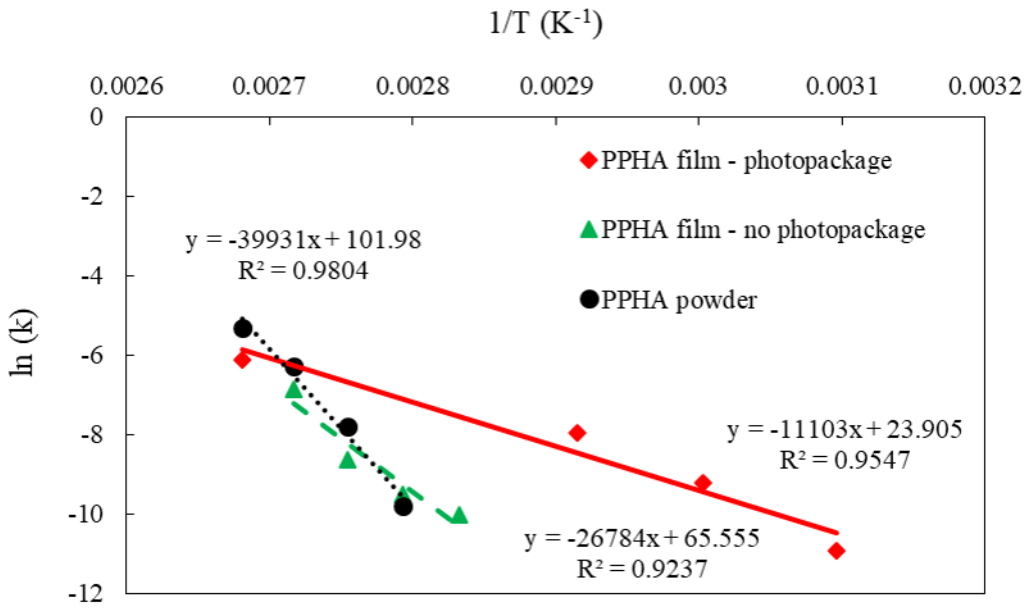

Figure 6.2. Natural logarithm of reaction rate versus isothermal temperature of as-synthesized PPHA polymer powder, PPHA polymer films without photosensitive compounds, and PPHA polymer films with photosensitive compounds at various temperatures

The addition of 10 pphr Rhodorsil FABA and 2.1 pphr anthracene caused the activation energy to drop to $9.23*10^4$ J/mol. The expected shelf life dropped to as low as 15 hr at 50 °C. This is due to the acid impurities in Rhodorsil FABA caused by prior thermal degradation or in-situ degradation. Cold storage greatly extends the shelf life of all samples. PPHA structures without photosensitive compounds are clearly easier to store and handle compared to Rhodorsil FABA containing polymer. This creates the opportunity for fabricating non-photosensitive PPHA structures in any ambient lighting conditions

followed by long term storage and addition of a photo-sensitive layer at a time near the point of deployment.

Table 6.1. Activation energy and Pre-expoenential factor extrapolated from Arrhenius equation for PPHA polymer powder, PPHA film with and without photosensitive compounds

Sample	Activation Energy (J/mol)	Pre-Exponential Factor (s^{-1})
PPHA Powder	$3.32*10^5$	$1.95*10^{44}$
PPHA Film – No Photosensitive Compounds	$2.23*10^5$	$2.95*10^{28}$
PPHA Film – Photosensitive Compounds	$9.23*10^4$	$2.41*10^{10}$

The bilayer structure composed of a non-photosensitive core and (later added) photosensitive layer was investigated. Various thicknesses of photosensitive PPHA films with different PAG and anthracene loadings were laminated onto 600 µm thick non-photosensitive PPHA films using the solvent in the polymer film as the bonding agent. No additional adhesive was applied to bond the films together. The PPHA depolymerization mechanism in the non-photosensitive layer is by acid diffusion from the PAG-containing layer into the 600 µm thick non-photosensitive PPHA films. Sufficient BMP TFSI was added to photosensitive layer to keep the depolymerized PPHA liquid so that acid diffusion

was high during the whole depolymerization process [134]. Figure 6.3 shows the photoacid penetration depth of the 100 μm thick PAG-containing film into the 600 μm thick non-photosensitive PPHA layer at different temperatures. A clear trend showing an increase in the rate of penetration by the photoacid with PEB temperature can be seen. Both the rate of acid reaction with the PPHA and increase in diffusion rate occurred at higher temperature. Glassy PPHA decomposes below its glass transition temperature (T_g). Therefore, the resulting penetration of acid into a non-photosensitive PPHA occurred through a liquid reaction front propagation mechanism [133], as explained in Scheme 6.2. The PAG was uniformly distributed in the photosensitive film prior to photo-exposure. Once the PAG was photo-activated, PPHA depolymerization occurred and the photo-active layer liquefied. The photoacid-containing depolymerized liquid front moved into the fresh (non-photosensitive) PPHA material on a layer-by-layer basis. The reaction front continued to move until all the PPHA was mixed with the acid-loaded material, the PAG was consumed, or the PAG was diluted to such extent that it was no longer able to depolymerize PPHA. Although the PAG is a catalyst, impurities in the film, such as water and residual solvent, can consume a fraction of the in-situ created photoacid.

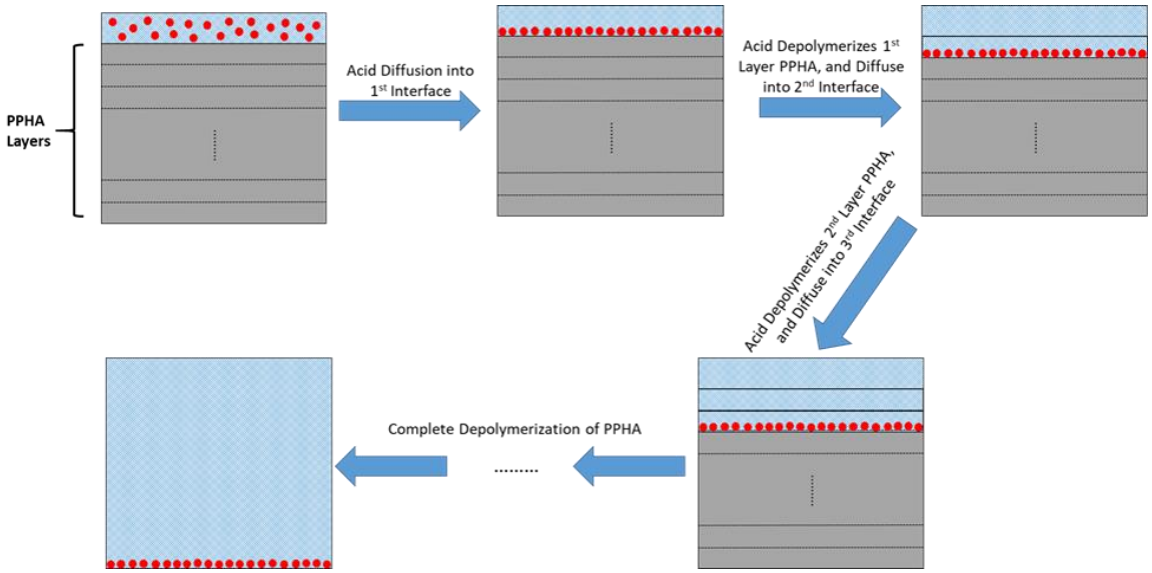

Scheme 6.2. Explanation of reaction front propagation mechanism for photoacid diffusion in depolymerized PPHA medium into reaction interface

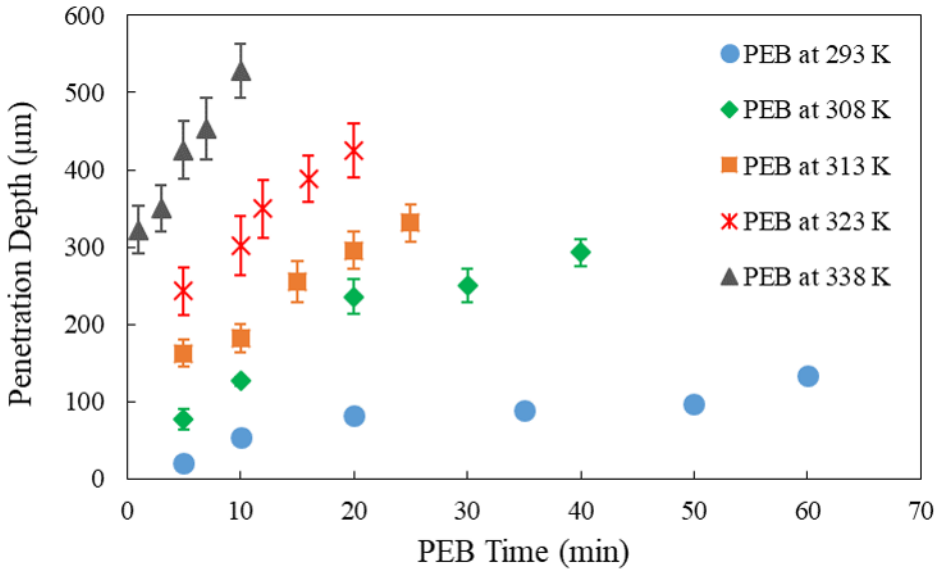

Figure 6.3. Photoacid penetration depth for exposed 100 µm PPHA film with 10 pphr PAG, 2.1 pphr anthracene and 60 pphr BMP against increasing PEB time under various PEB temperatures

The rate of photoacid diffusion and degradation of the PPHA is dominated by four factors: (i) rate of photoacid generation, (ii) rate of PPHA depolymerization and liquification, (iii) rate of photoacid quenching (i.e. consumption), and (iv) rate of photoacid diffusion into the solid PPHA [28]. Here, a high exposure dose was used to activate the PAG in a short time eliminating photoacid generation from being the rate limiting step. Moreover, the photoacid is known to be a very strong acid (pK_a < -14) that will depolymerize PPHA rapidly [109]. The only consumption of acid that would occur is from trace alkaline impurities or side reactions, of which none have been identified. Since there are no alkaline additives in the PPHA films, photoacid quenching can be assumed negligible. Therefore, the rate limiting step for depolymerization of non-photosensitive PPHA using the two-layer structure is the rate of photoacid diffusion into the solid PPHA medium. Figure 6.4a shows the square of the penetration thickness versus PEB time at various temperatures. A linear relationship is expected for Fickian diffusion, assuming a constant diffusion coefficient vs. concentration. Linear regression lines were fitted to estimate diffusion coefficient of the photoacid into PPHA, following classical Fickian diffusion. Table 6.2 summarizes the photoacid diffusivity into depolymerized PPHA vs temperature. Higher temperature led to an increase in the diffusion coefficient. The relationship of the diffusion coefficient and temperature was assumed to follow the usual Arrhenius relationship. The activation energy and pre-exponential factor for acid diffusion was calculated. Figure 6.4b shows the plot of the temperature dependence of the photoacid diffusion coefficient into depolymerized PPHA medium. The activation energy for the photoacid diffusion was found to be 79 kJ/mol with a pre-exponential factor of $7.6*10^{14}$ s^{-}

[1]. By knowing these two parameters, an amount of time for complete degradation of a PPHA film using a 100 µm photosensitive film with 5 pphr PAG can be estimated.

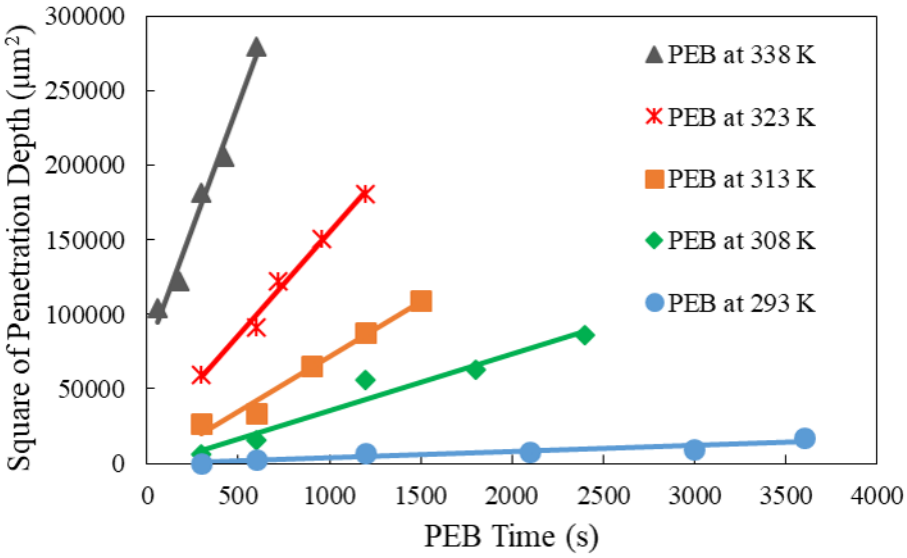

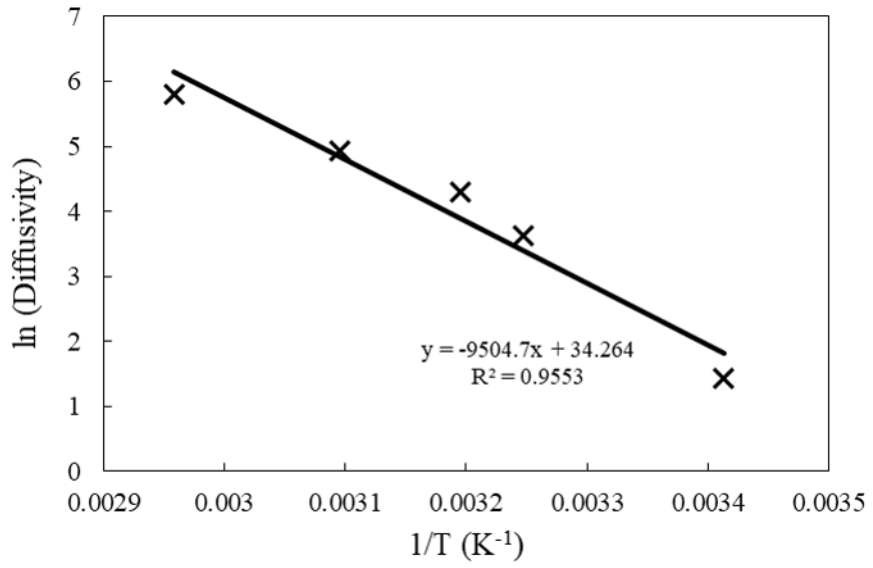

Figure 6.4. a) Square of penetration depth of photoacid versus time for exposed 100 µm PPHA film with 10 pphr PAG under various PEB temperatures for different

length. Linear regression line was fit for data points at each temperature, assuming a Fickian diffusion model. b) Natural log of diffusion constant at various temperatures

Table 6.2. Diffusion coefficient of photoacid from a fully exposed 100 μm PPHA film containing 5 pphr PAG at various temperatures into depolymerized PPHA

	PEB Temperature				
	293 K	308 K	313 K	323 K	338 K
Photoacid Diffusion Coefficient ($\mu m^2/s$)	4.23	38.0	73.5	139	331

The PAG concentration in the photo-active layer and photosensitive layer thickness were varied to see their influence on acid diffusion. The penetration depth and standard deviation are summarized in Figure 6.5. Figure 6.6a compares the square of the penetration thickness vs. PEB time at room temperature for 5 pphr PAG and 10 pphr PAG. A higher diffusivity, 8.9 $\mu m^2/s$, was observed for the film containing 10 pphr PAG, compared to 4.2 $\mu m^2/s$ for the film containing 5 pphr PAG. Figure 6.6b compares the square of penetration thickness versus PEB time at room temperature for films containing 5 pphr of PAG at various thicknesses. The diffusivity was also evaluated with a thicker photo-active film. The diffusivity increased from 4.2 $\mu m^2/s$ to 8.6 $\mu m^2/s$ when the photo-active film thickness increased from 100 μm to 167 μm. In both cases, acid diffusivity increased with the thickness of the photosensitive layer or PAG concentration. Acid-catalyzed degradation of PPHA is known to be an exothermic reaction [47]. The addition of more polymer and more PAG resulted in greater local heating to facilitate acid diffusion. In addition, a higher concentration of PAG or greater thickness of the photosensitive layer produced a higher

local concentration of acid during liquification of the underlying layers. Thus, the diffusivity increased for both cases, concentration and thickness.

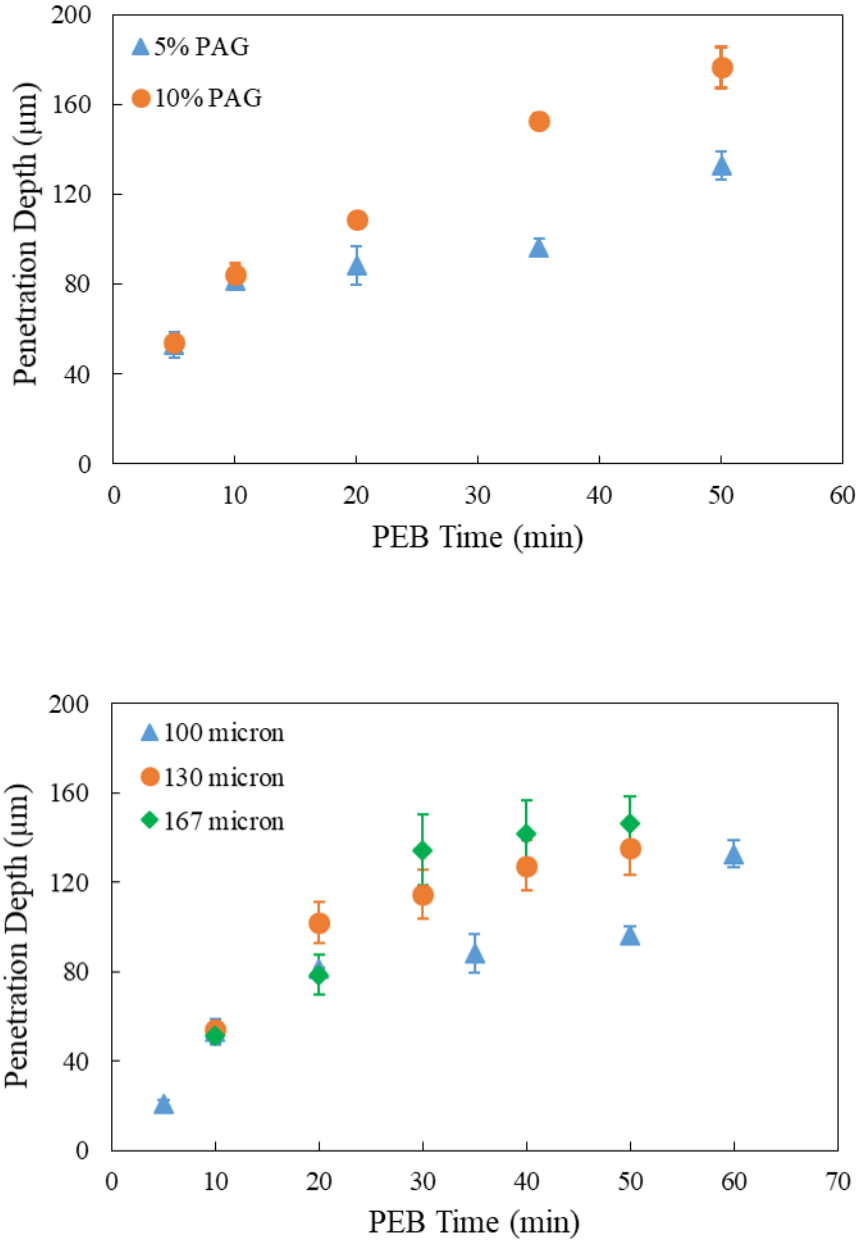

Figure 6.5. Penetration depth of photoacid in PPHA film versus PEB time at room temperature for (a) PPHA films containing 5 pphr and 10 pphr PAG; (b) PPHA films containing 5 pphr PAG with thickness of 100 µm, 130 µm, 167 µm

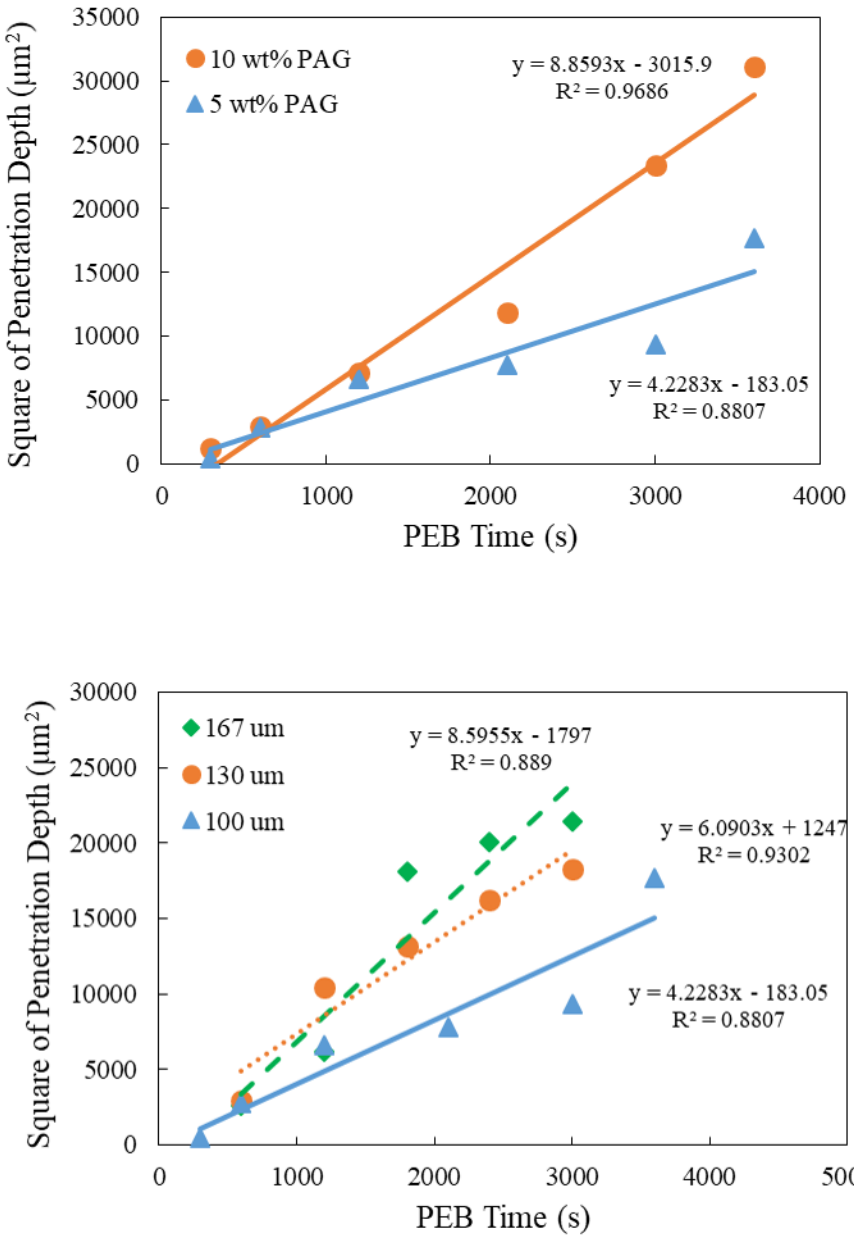

Figure 6.6. a) Comparison of square of penetration depth of photoacid versus PEB time for exposed 100 μm PPHA film with 5 pphr and 10 pphr PAG. b) Comparison of square of penetration depth of photoacid versus PEB time for exposed PPHA films containing 5 pphr PAG with various thickness of 100 μm, 130 μm, and 167 μm

To demonstrate the utility of a bilayer transient PPHA film, a formulation of 0.3 g PPHA containing 60 pphr BMP, 10 pphr PAG and 2.1 pphr anthracene was prepared and spray coated onto a 150 µm thick PPHA film. Figure 6.7 shows time lapse pictures of exposed bilayer PPHA transient films at room temperature. The transient bilayer PPHA film completely disappeared after 1 h and soaked into the surrounding environment.

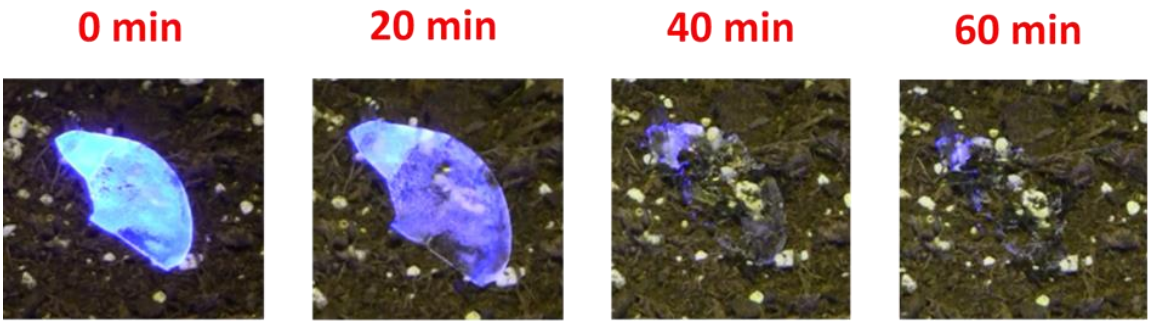

Figure 6.7. Time lapse photos of acid diffusion through a bilayer PPHA films prepared by spray-coating

6.4 Summary

The need for and advantages of using a photo-active/non-photoactive bilayer structure in the fabrication of PPHA-based transient devices is described. Non-photosensitive PPHA films have a long shelf-life at room temperature and can be safely handled in any lighting condition. By addition of a photosensitive layer near the time of deployment, the risk of accidental device triggering can be lowered. Once irradiated, the photoacid propagates following a Fickian diffusion mechanism and a layer-by-layer liquid reaction front. The designed bilayer fabrication of transient devices allow the fabrication to be done under normal lighting condition, regardless of the type of photosensitizer that is

going to be used. This can tremendously makes the device characterization easier and cost of fabrication lower.

CHAPTER 7.

EPOXIDE FUNCTIONALIZED POLY(PROPYLENE CARBONATE) AS TEMPORARY ADHESIVE

7.1 Introduction

Temporary adhesive is attractive because of its capability of temporarily adhere to another materials and debond from one another upon triggering of a stimulus. It requires the material to breakdown into their surrounding environment leaving behind little or no chemical footprint. This breakdown can be accomplished through a variety of mechanisms such as liquefaction, volatilization or dissolution. Temporary adhesives have variety of applications in material products and manufacturing processing [1]. Emerging technology in transient electronics requires the materials that can vanish once the device finishes its product cycle [2]. This functionality can potentially reduce the demand for landfill space, improve recyclability, and decrease environmental burdens. Temporary adhesives are needed to package transient electronic components onto transient substrate, as shown in Scheme 7.1. Some transient devices were made using metastable polymer (e.g., poly(phthalaldehyde)) that are heat sensitive [28,51,54]. Therefore, low temperature (especially room temperature) processing is preferred to protect the bulk transient electronic devices from stressful conditions.

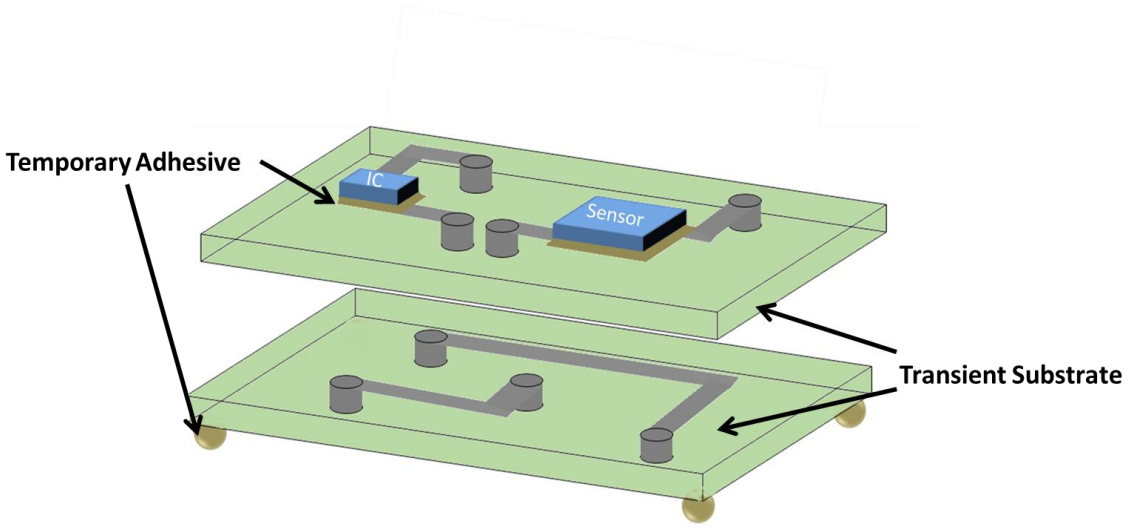

Scheme 7.1. Application of temporary adhesive in transient device

A good candidate of temporary adhesive needs to have durable adhesive strength that can match with the requirement of the application, low contents of decomposition residuals and fast vanishing upon stimulus, and desirable thermal and chemical stability compatible with the application. Previous research have been done on different types of polycarbonates [37,38], including high molecular weight polypropylene carbonate (PPC), polyethylene carbonate (PEC), polycyclohexane carbonate (PCC) and PPC/PCC copolymer. Among these polycarbonates, PPC/PCC show the highest adhesive strength but left behind the highest amount of residuals. PEC show the lowest decomposition temperature with low residuals but had minimum adhesive strength. PPC was of the most interest among these polycarbonates because of its moderate adhesive strength, as well as low chemical footprint left behind after decomposition. Despite its good transient behavior, PPC still show in lack of adhesive strength.

To accommodate issues with the adhesive strength, chemical footprint upon debonding, and processing temperature range, an epoxide functionalized PPC is introduced

in this chapter. Generally, improvement of the adhesive properties of a material can be achieved by increasing the level of entanglement using larger molecular weight polymers, increasing the physical interaction such as hydrogen bonding, and improving interface interaction by modifying chemical functionality. Based on these concepts, a chemically modified PPC oligomer is introduced to make it a good temporary adhesive for transient electronic application at low temperature range.

7.2 Experimental

PPC polyol with molecular weight of 2 kDa was supplied by Novomer Inc. and 1 kDa was supplied by Aramco Services Company. The photoacid generator (PAG) used was 4-methylphenyl [4-(1-methylethyl) phenyl] tetrakis(pentafluorophenyl) borate iodonium salt (referred to as Rhodorsil-Faba) from Solvay Inc A polymercaptan type hardener was directly used from commercial 5-minute epoxy adhesive. Allyl chloroformate and 3-chloroperbenzoic acid (m-CPBA, ≤ 77%) were purchased from Sigma-Aldrich. Tetrahydrofuran (THF), dichloromethane (DCM) and methanol solvent were all purchased from BDH, at purity level >99%. Pyridine (>99%) and Chloroform-d ($CDCl_3$, >99.8%) were purchased from Alfa Aesar. All chemicals were used as received.

Epoxidation reaction of both 1 kDa and 2 kDa PPC polyol follows the previous report where the PPC polyol was first converted to allyl-ended PPC (aPPC), and then oxidized to form epoxide-ended PPC (ePPC) [98].

Preparation of 1 kDa and 2 kDa ePPC adhesive at room temperature. Thin layer adhesive material, either 1 kDa or 2 kDa epoxyPPC, was doctor bladed onto the FR-4 substrate using razor blade at room temperature. Aluminum foil was pressed onto the adhesive at 300 kPa. Ten sets of samples with different chemical moieties and processing

condition were added and applied to the adhesive material to tune its adhesive properties and stability. All samples containing PAG or hardener were added with 5 wt% and 25 wt% respectively. List of samples prepared are shown in Table 7.1. For the preheated samples, the samples was heated and cooled before it was used. For the PAG/PBG loaded samples, 248 nm UV light was irradiated at a dosage of 2 J/cm^2 before aluminum foil was adhered.

Table 7.1. Samples made for adhesive strength and stability test

Sample	1 kDa PPC polyol	1 kDa epoxyPPC	2 kDa epoxyPPC	PAG/PBG	Hardener	Preheated
1	✓	✗	✗	✗	✗	✗
2	✓	✗	✗	✓	✗	✗
3	✗	✓	✗	✗	✗	✗
4	✗	✓	✗	✗	✗	✓
5	✗	✓	✗	✓	✗	✗
6	✗	✓	✗	✓	✓	✗
7	✗	✗	✓	✗	✗	✗
8	✗	✗	✓	✗	✗	✓
9	✗	✗	✓	✓	✗	✗
10	✗	✗	✓	✓	✓	✗

Thermogravimetric analysis (TGA) was performed using a TGA Q50 from TA instruments to investigate the decomposition temperature of adhesive materials. Nitrogen rich environment was supplied in the TGA chamber with a constant nitrogen flowrate of 40 ml/min. Samples were heated at a ramp rate of 1 ºC/min to temperature at either 300 ºC or 350 ºC.

Adhesive strength measurement was done using an Instron model 5842 based on an ASTM D429 Rubber-90 peel test. Aluminum foil was pulled in a direction normal to the rigid substrate. Adhesion strength at each point was calculated using $F_A = F_P/w$, where F_A is the adhesion strength at a specific point, F_P is the pull force on the aluminum foil at that point, and w is the width of the rectangular substrate. Note initial and end data of F_P were not counted to avoid the ramp up pulling force at beginning and detachment of aluminum foil from the substrate in the end. Recorded adhesion strength for each sample was then calculated by taking the average of all eligible F_A on the testing sample. Standard deviations were also calculated based on all eligible data.

7.3 Result and Discussion

Adhesive Strength

Figure 7.1 shows the adhesion strength of different samples. The 1 kDa PPC polyol (sample 1) shows an average adhesive strength of 0.03 N/mm, similar to the reported high molecular weight PPC samples by Fritz et al [37]. Although the molecular weight of PPC decreased, concentration of the hydroxyl group increased for 1 kDa PPC polyol. The increased hydrogen bonding balanced the decrease in physical entanglement, resulting in a similar adhesive strength. A cohesive failure was observed upon debonding.

2 kDa ePPC (sample 7) show a three-fold increase to an average of 0.096 N/mm in adhesive strength. This happens likely due to the increased in interfacial interaction of hydroxyl group of FR-4 substrate with epoxide group. Similar to the 1 kDa PPC polyol, cohesive failure was observed after debonding the aluminum foil from the substrate.

Average adhesion strength of 0.13 N/mm was obtained for partially crosslinked 2 kDa ePPC (sample 10) and 0.068 N/mm for crosslinked 1 kDa ePPC (sample 6), both using

polymercaptan commercial hardener. The adhesive strength increases because of the higher degree of chemical interaction between adhesive molecules and interfaces. Cohesive failures was observed after debonding were observed for both samples.

The adhesive strength for the preheated 2 kDa ePPC increased to an average of 0.18 N/mm (sample 8). The increase in adhesive strength after heat treatment of 2 kDa ePPC was due to the further removal of solvent from the reaction and increased physical entanglement of the polymer. The increased in entanglement of heated 2 kDa ePPC was also supported by the observation of adhesive failure upon debonding. The observation of adhesive failure also indicates that the actual adhesive strength with the heat treated 2 kDa ePPC is larger than the value measured using attached aluminum foil. 1 kDa ePPC shows an adhesion strength of 0.058 N/mm after heat treatment (sample 4). The adhesive strength of heat treated 1 kDa ePPC is three times smaller than heat-treated 2 kDa ePPC because of the less effective chain entanglement caused by the shorter polymer chain length. Observation of cohesive failure after heat treatment also indicates the less degree of entanglement in 1 kDa ePPC.

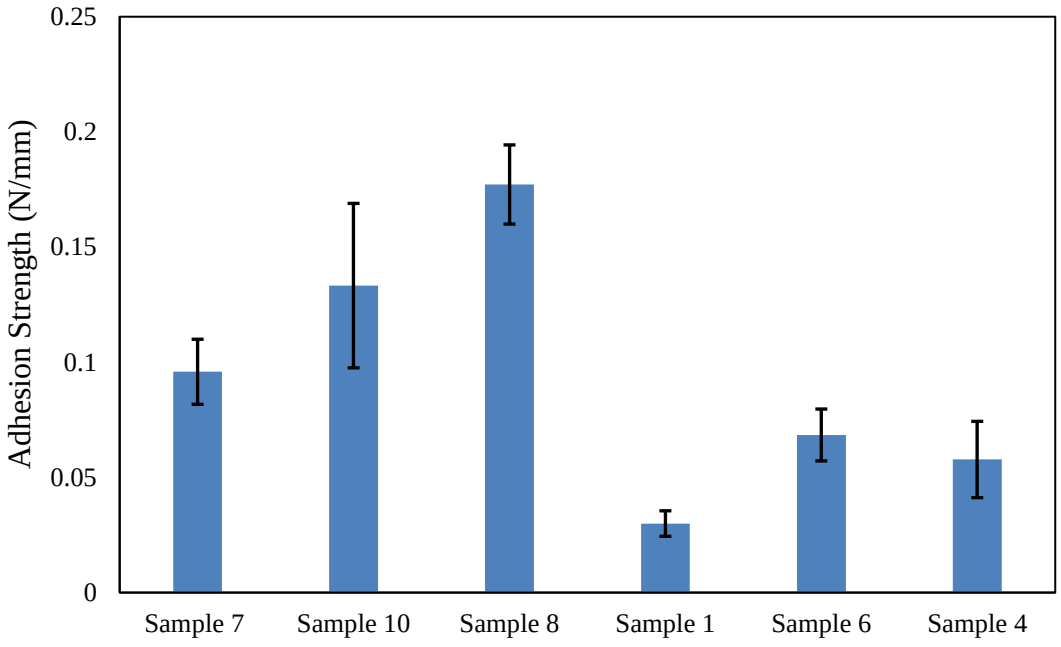

Figure 7.1. Adhesion strength of PPC-based adhesives

Thermal Stability Analysis of Adhesive Materials

TGA of untreated 1 kDa PPC polyol were done with and without addition of PAG (sample 1 and sample 2) and is shown in Figure 7.2. 1 kDa PPC polyol without addition of photoactivated PAG shows an onset decomposition temperature at around 180 ºC. With the addition of photoactivated PAG, the onset decomposition temperature significantly dropped to around 90 ºC. The generation of superacids accelerated the chain scission of PPC backbone and led to the faster degradation of PPC polyol [9,50].

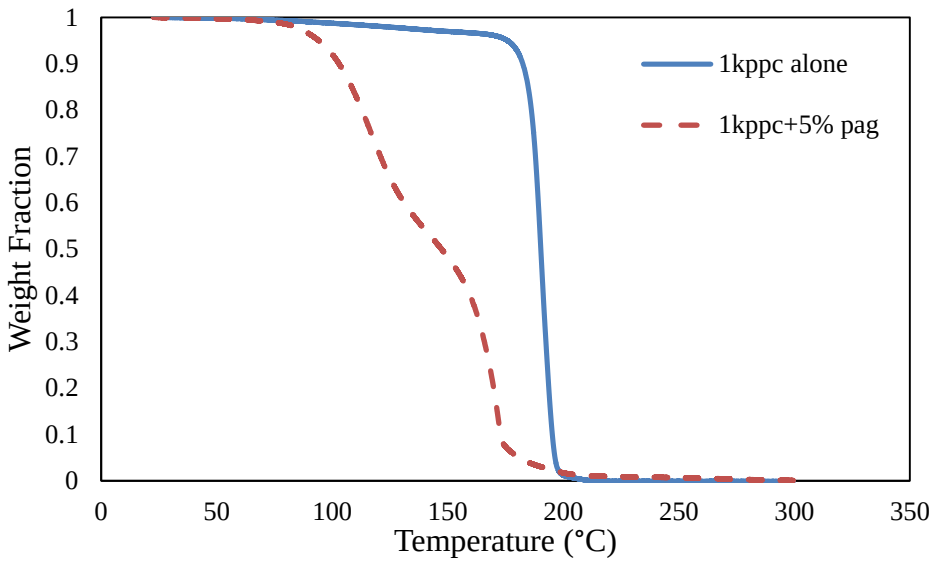

Figure 7.2. Decomposition of 1 kDa PPC with and without addition of PAG

Figure 7.3 shows the TGA of 1 kDa ePPC alone (sample 7), 1 kDa ePPC with PAG (sample 9) and 1 kDa ePPC with both PAG and hardener (sample 10). For the 1 kDa ePPC, onset decomposition temperature of the polymer happened at around 206 ºC due to the epoxide end caps of the PPC that slowed the backbiting decomposition mechanism. With the addition of photoactivated PAG, onset decomposition temperature drop to around 90 ºC due to the super-acid assisted chain scission of PPC backbone. With the addition of both photoactivated PAG and hardener, the onset decomposition temperature increased to 150 ºC due to the neutralization of superacids by weakly basic polymercaptan hardener. Similar result for 2 kDa ePPC was observed, as the onset decomposition temperature decreased to 90 ºC with the addition of photoactivated PAG. The addition of both PAG and hardener increased the onset decomposition temperature to 150 ºC due to the neutralization of weakly basic hardener.

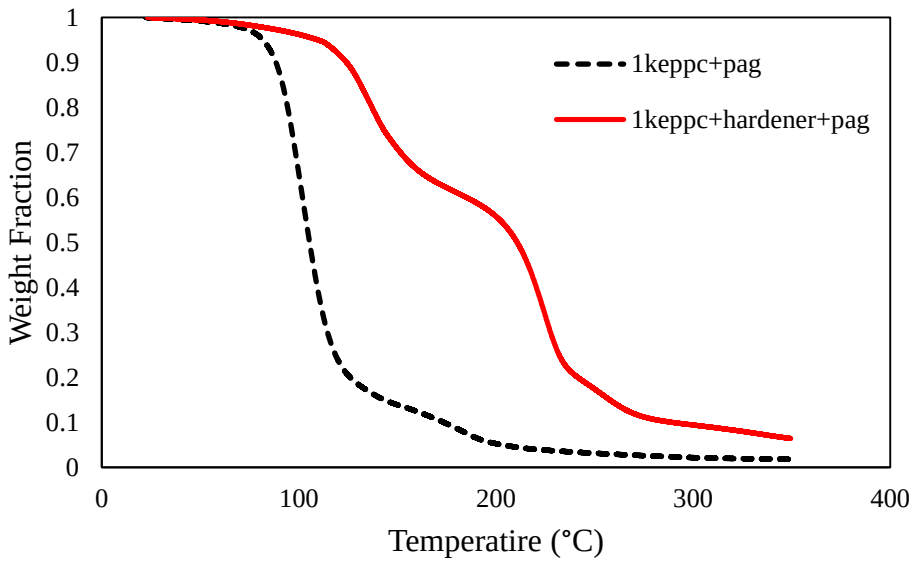

Figure 7.3. Decomposition of 1 kDa ePPC with addition of PAG and hardener

Residual analysis based on the TGA results show that with addition of PAG, residual less than 5 wt% was left after ramping up to 200 ºC. Addition of hardener resulted in higher residual left over, which corresponds to around 10 wt% at 250 ºC and 7 wt% at 300 ºC. The left over residuals were mainly residaul of photoactivated compound and hardener. Both residuals could be easily washed away with common organic solvents such as THF, acetone etc.

7.4 **Summary**

An epoxide functionalized poly(propylene carbonate) was found to achieve an adhesion peel strength 6 times higher than the high molecular PPC previously reported. The increased adhesion peel strength happened due to the increased interfacial interaction of epoxide group with the substrate. Addition of a commercial hardener further improved the adhesion strength. By subjecting the polymer to heating, the increased entanglement of polymer chain also helped to improve the adhesion peel strength. Low level of residuals

were left over upon thermal decomposition, making it easier to clean up the substrate after debonding.

CHAPTER 8

CONCLUSION AND FUTURE PERSPECTIVE

The main goal of this dissertation is to modify sacrificial polymer and its formulation to expand the application into a broader application area. Two types of sacrificial polymers, a high ceiling temperature PPC and a low ceiling temperature PPHA, are studied for their applications in electronic and transient devices in this dissertation. In chapter 2 and chapter 3, an epoxide functionalized PPC was shown to be able to create nanoporous epoxy film with enhanced dielectric properties. In chapter 7, the same epoxide functionalized PPC was shown to be an effective temporary adhesive with improved adhesion peel strength compare to its non-functionalized form. In chapter 4, modification of mechanical and transient properties for low ceiling temperature PPHA via addition of additives were shown to broader its application versatility. In chapter 5, a delayed-photoresponse of transient PPHA was demonstrated using weakly basic additives so that the application of photosensitive transient devices at normal lighting condition is feasible. In chapter 6, a fabrication-friendly, bilayered transient PPHA structures was demonstrated to make the scale-up production and storage of transient devices easier and cheaper.

While the technology development and application of sacrificial polymers in electronic and transient devices demonstrated in this dissertation provide a positive start for future prototyping, rooms are still open for improvement from materials and formulations aspects, as well as the integration of technology into actual devices.

Recommendation for Application of Nanoporous Epoxy

The demonstration of nanoporous, low dielectric constant and tangent loss epoxy film provides a way forward to create a better quality PWB. However, it requires further investigation of whether it is compatible with the metal lamination process. The creation of porous structure via removing the porogenic materials at its B-stage results in creation gases that can lead to blistering effects, which is destructive to the quality of the PWB. Instead of using traditional copper clad laminate (CCL) process for metal lamination (requires lamination of metal layer onto a B-staged material), a resin coated copper (RCC) structure has been proposed where a C-staged layer can be added between metal foil and B-staged epoxy resin, as shown in Figure 8.1 [138]. This C-staged layer can act as a better insulating layer, while still providing the required adhesion between B-stage material and metal layer. Exploration into application of porous epoxy into this RCC structure is an alternative way forward to make a better quality epoxy-based PWB with enhanced dielectric properties.

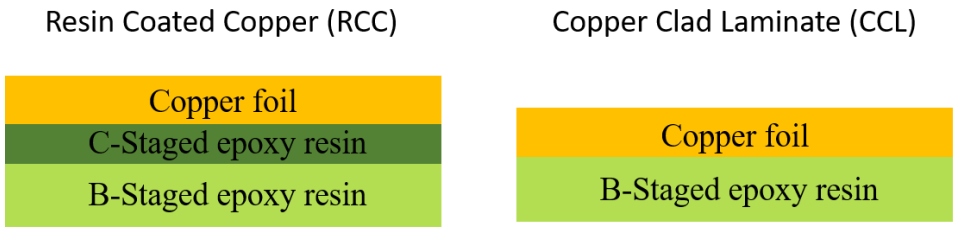

Figure 8.1. Resin coated copper structure (left) and copper clad laminate structure (right)

Vertical interconnect access (VIA) is an electrical connection between layers that goes through the plane of layers for PWB. With the creation of nanoporous epoxy film, the sidewall of VIA can be rough and result in poor quality of sputtered metal on the inner wall. Moreover, no warpage study for porous epoxy film is done in this dissertation. Both

of these are necessary investigations need to be conducted to ensure the feasibility of applying nanoporous epoxy in PWB or interconnect materials.

There are other emerging substrate and interconnects materials that have been developed over years. With the demonstration of feasibility to reduce dielectric constant via incorporation of functionalized porogenic materials into epoxy resin that can be later selectively removed, it will be interesting to see how the similar types of ideas can be used for other substrate materials by creating nanoporous substrates and interconnects.

Recommendation for Transient Polymer and Devices

The major breakthrough of tuning mechanical and transient properties of PPHA shown in this dissertation provide a pathway forward for making transient devices with broader range of properties and feasibility, depending on the application scenarios. Improvements with respect to materials and formulations can further strengthen the application horizon of PPHA. Moreover, integration of transient technology developed based on PPHA into a fully transient, self-powering devices, will be attractive for future transient devices.

Following the work described in this dissertation, a flexible and foldable transient films can be fabricated. However, limitation with respect to its foldability and crack resistance at extreme environment (e.g., -20 °C or lower) still needs to be explored. This is important for application where flexible parachute-type materials is needed and requires deployment/usage at high altitude and latitude. Research needs to be done with respect to type of materials that can provide the flexibility and toughness to PPHA at low temperature while still maintaining the low residuals level after degradation. Particularly, materials with low T_g are of great interest as it can maintain its chain mobility at low temperature. One

category of additive materials that could be explored further is elastomer (good mechanical flexibility, low T_g). Main issue that was faced in this dissertation with addition of extra additive is phase separation of polymers with other additives. To get more insight of phase behavior between additives, Hansen solubility parameter of PPHA and other additives used should be investigated to provide a prediction of types of materials to be added into current PPHA formulation.

Alternatively, instead of physically adding low T_g materials into current PPHA formulation, chemically tuning T_g of PPHA by grafting or copolymerizing PHA monomer with other known low T_g material (e.g., polydimethylsiloxane) can also tune the thermal-mechanical properties of the resulting poly(aldehydes). Furthermore, an interpenetrated network of second network consisting of low T_g material can also be investigated. This second network can provide a mechanical toughness for the relatively brittle PPHA backbone and result in good flexibility of composite structure.

In terms of low ceiling temperature poly(aldehydes), further investigation of polymer composition, where a high vapor pressure, second or third comonomer, that can be incorporated into the polymer backbone with high molar ratio needs to be investigated. These high vapor pressure components provide advantages for transient properties of the decomposed devices/materials, resulting in lower residual contents in faster time span after usage. The second or third comonomer could also provide crosslinkable sites for poly(aldehydes) backbone that can further improving the mechanically properties.

Variety of transient devices using PPHA as based materials have been demonstrated at this point, including transient structures (PWB, drones, and parachute), transient resistor, and transient OLED. In the appendix of this dissertation, we demonstrated the feasibility

of a transient energy source and sensor using the idea of triboelectric nanogenerator. However, at this point, no demonstration of fully transient, self-powered device has been shown. To expand the usage of transient technologies, the demonstration of fully transient, self-powered device via integration of different transient parts will be a critical milestone for pushing development of transient technologies into next level.

Besides its application in transient electronics and devices, poly(aldehydes) have other potential application. For example, owing to its hydrophobic backbone, it can be used as a temporary protecting layer to protect a delicate surface or materials (e.g., silicon/germanium substrate, metal and dielectric layer) from water and oxygen diffusion. Moreover, owing to its sensitivity to variety of triggers, it can be used to control the release of chemicals to avoid disastrous event. For example, in the case where high temperature may cause combustion, poly(aldehyde) can be used as a capsule to release flame retardant materials once the safety limit is triggered. This can be useful in field such as battery.

While the main focus of this dissertation is on PPC and poly(aldehydes) based sacrificial polymers, there are many different types of sacrificial polymers that are of research interest. The advancement of sacrificial polymers described are not limited to only PPC and poly(aldehydes) based materials. The idea in chemically tuning functionality and formulation can be used as a reference for other types of sacrificial polymers for different applications in which different purposes need to be achieved. While technological progress is made in transient devices and electronics, attentions needs to be paid towards environmental impact of degradation residuals to see the possibility of both transient and green polymeric transient devices.

APPENDIX A.

FABRICATION OF PRECISION INTEGRATED CAPACITOR

A.1 Introduction

Integrated, mass formed, passive components in electronic package substrates or printed wiring boards allow for denser electronic systems [139]. Among the most common passive components, capacitors are of high interest because of the number of components used on the substrate for power-ground decoupling, filtering and noise suppression [140–142]. Directly incorporating the capacitor into the substrate, compared to surface mounting, can free-up surface area for other components and decrease the parasitic properties caused by the mounting technology [143].

The capacitor dielectric material can be divided into paraelectric and ferroelectric materials. Both types of dielectric materials experience electronic, ionic and atomic polarization [144]. Ferroelectric materials retain their polarization when the external field is removed, because atoms cannot move within the lattice [144]. However, the dielectric properties of ferroelectric materials depend strongly on temperature and frequency, which is a disadvantage at high frequency application. Paraelectric materials such as SiO_2 [145], Si_3N_4 [145], TiO_2 [145,146], Al_2O_3 [145,147], Ta_2O_5 [145,148], and many polymers and polymer nanocomposite [139,149,150] have relatively low dielectric constant compared to ferroelectric materials, however, they can operate consistently over a wide range of temperatures and frequencies, which make them useful for capacitors. Among all the paraelectric materials, inorganic thin-film oxides made from valve metals (e.g. aluminum, vanadium, zirconium, hafnium, tantalum, tungsten, etc.) stand out because they can be

formed at low temperature with consistent performance using a variety of techniques. Aluminum oxide is often chosen as the dielectric because aluminum metal is inexpensive, relatively malleable, and is easy to deposit by evaporation or sputtering, which is compatible with different applications.

Many techniques have been used to produce aluminum oxide thin films, including plasma oxidation [151], ozone oxidation [152–154], reactive ion beam sputtering [155], e-beam evaporation [156], and atomic layer deposition of the oxide itself [157,158], etc. Among these, anodic oxidation is attractive because the processing can be done at low cost and low temperature. Further, the processing conditions can be easily controlled.

There have been numerous studies of the process conditions and quality of anodic aluminum oxide (AAO) films produced from different electrolytes. Nelms et al. used tartaric acid neutralized with ammonium hydroxide to achieve low leakage current and low defect density, with specific capacitance <100 nF/cm^2 [147]. Diesing et al. used an acetic acid buffer to create capacitors with specific capacitance of 1260 nF/cm^2 with low breakdown voltage and high leakage current [159]. Kaltenbrunner et al. used citric acid electrolyte to acheive 420 nF/cm^2 specific capacitance [160], but resulted in high leakage current [161]. Mardare et al. used a neutral electrolyte to achieve 850 nF/cm^2, but with high leakage current [162]. Oh et al. used ammonium adipate to achieve low leakage current, with low specific capacitance, <65 nF/cm^2 [163]. Ban et al. demonstrated the fabrication of capacitors using boric and citric acid, with 580 nF/cm^2 and breakdown voltage of 530 V [164]. Dickey et al. performed a two-step anodization by using sulfuric acid and boric acid to demonstrate high breakdown voltage, but low specific capacitance of 20.8 nF/cm^2 [165].

Hourdakis et al. also performed a two-step anodization using sulfuric acid and citric acid to achieve low leakage current but with low specific capacitance, 7.2 nF/cm^2 [166].

Studies on usage of ammonium pentaborate octahydrate (APO) as the anodizing electrolyte have shown a better balance between leakage current, specific capacitance, operating voltage and capacitance accuracy. An aqueous solution of APO has a near-neutral pH so that the dissolution of the oxide is minimized during anodization. Ajit et al. used APO as the electrolyte for anodization at relatively high voltage and demonstrated high specific capacitance with low leakage current [167]. Rao et al. used an APO electrolyte to obtain specific capacitance up to 3000 nF/cm^2, with low dielectric loss, and consistent capacitance up to 1 MHz [168]. More recently, Kanadassan et al. used APO as the electrolyte and achieved a specific capacitance of 600 nF/cm^2 that was not sensitive to operating temperature and frequency [169]. Although specific results have shown promise, a comprehensive study of the fabrication parameters including anodization solvent, anodization time, anodization temperature, capacitance accuracy and precision, and electrolyte concentration, have not been fully studied in the previous reports.

Here, the focus is on balancing the specific capacitance and leakage current to achieve integrated capacitors with high precision and accuracy using APO as the aluminum anodization electrolyte. Metal-insulator-metal type capacitors with relatively high specific capacitance and reproducibility have been fabricated using low anodization voltage, without sacrificing leakage current. A detailed and comprehensive parametric study of the solvent system, anodization voltage, anodization temperature and time, and electrolyte concentration effects on the specific capacitance and leakage current is reported.

A.2 Experimental

Anhydrous ethylene glycol and APO were purchased from Sigma Aldrich and used as received. The silicon wafers were cleaned using acetone to remove organic residues. A CHA Modified Mark-40 E-beam evaporator was used to deposit metal films at$1.33*10^{-4}$ Pa. Titanium, 30 nm, was first deposited at the rate of 1 Å/s as the adhesion layer for the subsequent metal layers on the silicon wafer surface. Aluminum, 99.99% pure, was evaporated at a rate of 2 Å/s to a thickness of 800 nm.

The anodization electrolytes were prepared using either deionized (DI) water or ethylene glycol. Aluminum foil was used to form a metal contact to the aluminum deposited on the wafer. The aluminum was anodized under potentiostatic control. Four main anodization process parameters, anodization voltage, anodization time, anodization temperature and electrolyte concentration were varied in the APO parametric study. The anodization was carried out from 8 V to 30 V in each electrolyte. The anodization time was varied between 5 mins and 60 mins. The temperature during anodization was controlled between 5°C and 60°C. Finally, the APO electrolyte concentration was prepared from 0.01 M to 0.05 M. The aluminum oxide films were rinsed in DI water to remove the residual electrolyte salt from the surface, followed by drying with dry N_2 gas. A shadow mask was used to deposit 500 nm of evaporated aluminum to form the top electrode of the capacitor with an area of 0.18 cm^2 at a rate of 3 Å/s.

Capacitance was measured using a GW Instek LCR 821 meter, with voltage ranging from 0 V to 1.275 V at 200 kHz, on a Carl Süss MicroTec probe station. A Microscope was used to place the probe without scratching the surface of the capacitor. The values

from at least five different capacitors of each variety were averaged. The leakage current was measured using a Keithley 2636B sourcemeter on a Cascade Microtech probe station. The voltage was swept from 0 V up to 20 V at intervals of 1 V, to evaluate the leakage current and breakdown voltage of the fabricated capacitors. The maximum leakage current was set at 1 □A, which was taken as the signal for breakdown of the capacitor. A Woollam M2000 Ellipsometer, with incident light wavelength of 632.8 nm, was used to measure the thickness of the aluminum oxide films. A three layer Cauchy film model with five-point measurement was used to analyze the average thickness of the oxide films. A thermo K-Alpha X-Ray photoelectron spectroscopy (XPS) was used to identify the percentage atomic content of aluminum and oxygen in the formed AAO films.

A.3 Results and Discussion

Anodization current vs. time profile: The anodization current was recorded during the electrochemical oxidation of the aluminum surface for the formation of the aluminum oxide dielectric in either DI water or ethylene glycol electrolyte, as shown in Figure A.1. The current decreased with time in both electrolytes as the passivating aluminum oxide was formed. The rapid decrease in anodization current in both solvents is consistent with the formation-dissolution characteristics of the barrier type oxide film [170]. The effective resistances at the end of the 60-minute growth period of the film in the electrolyte were calculated based on Ohm's law, and the values are shown in Figure A.2. In general, the effective electrochemical resistance increased with anodization time in both electrolytes as the film matured. The effective electrochemical resistance was higher for fabrication in ethylene glycol compared to DI water, indicating a more passivating AAO film formed using ethylene glycol as the anodization solvent.

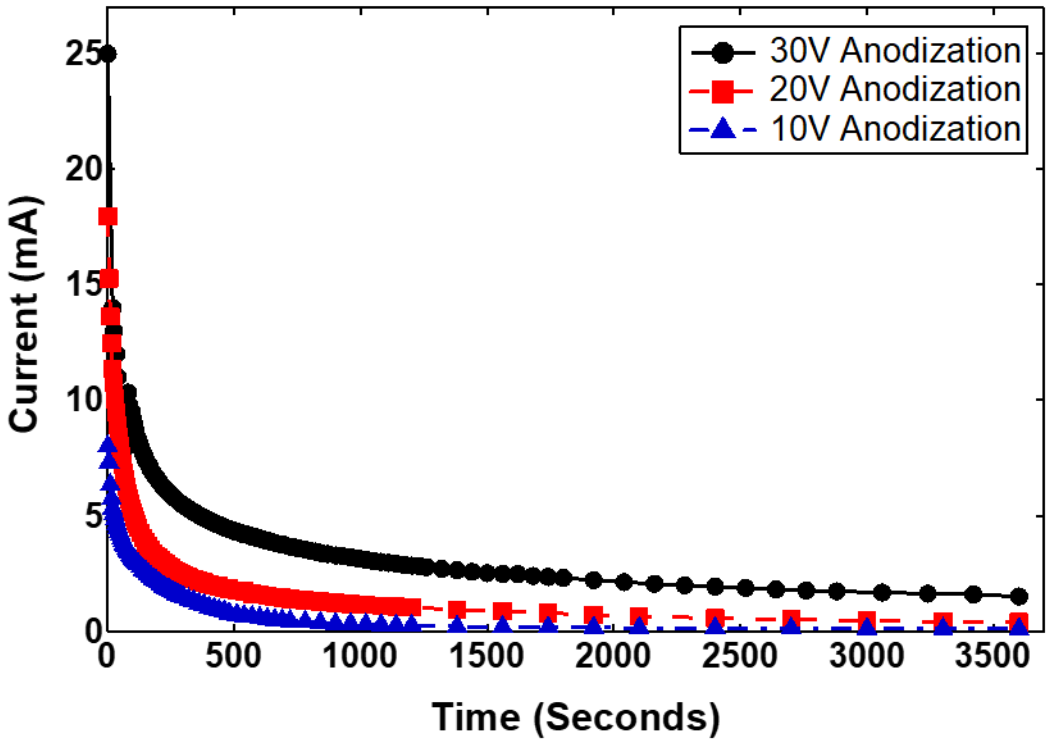
30V Anodization
20V Anodization
10V Anodization
Current (mA)
Time (Seconds)
0
5
10
15
20
25
0
500
1000
1500
2000
2500
3000
3500

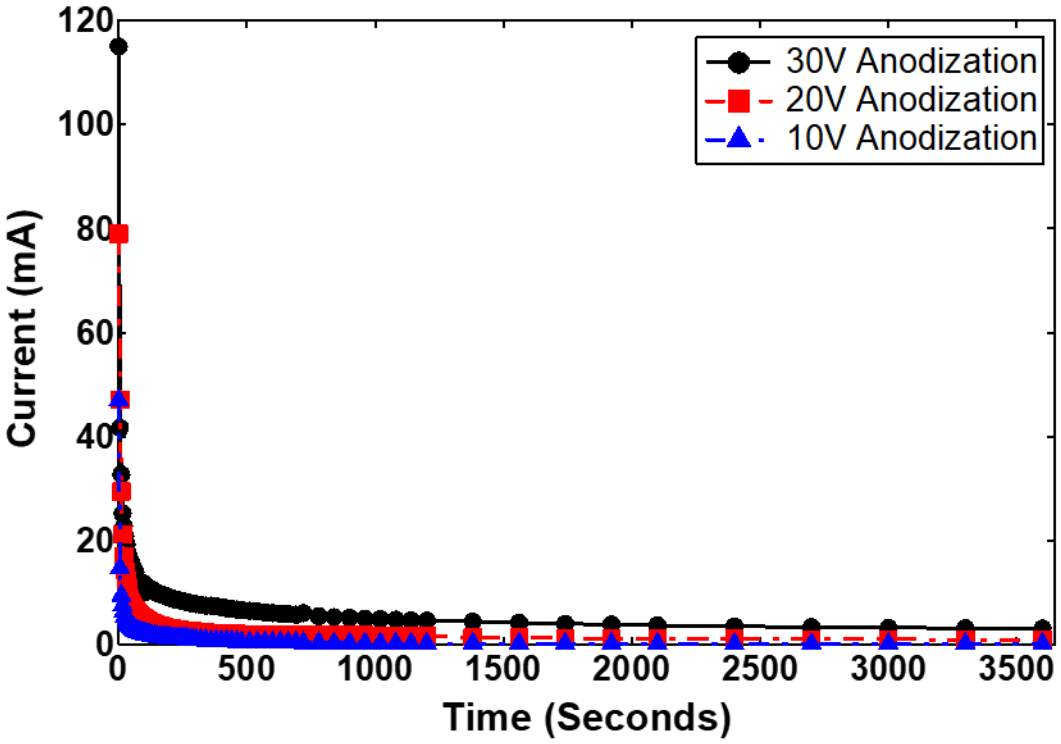

Figure A.1. Current vs time profile for anodization at 10 V, 20 V and 30 V in (a) ethylene glycol, (b) DI water

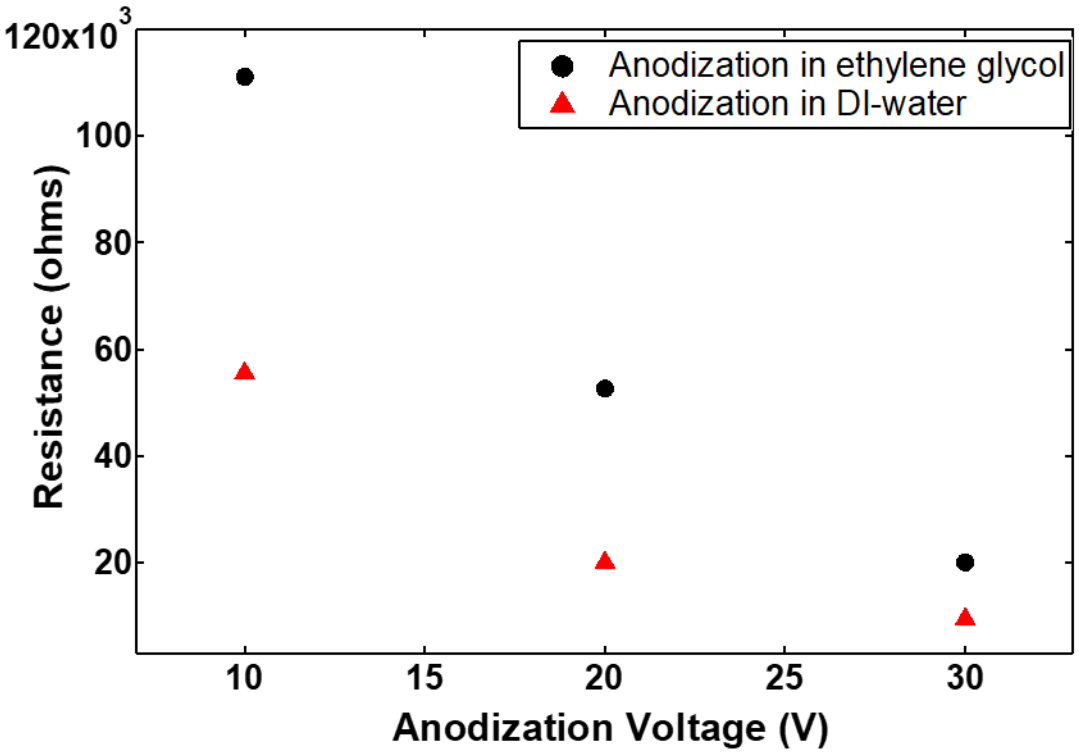

Figure A.2. Film resistance vs. Anodization voltage in ethylene glycol and DI water

Effect of anodization voltage on specific capacitance: The effect of anodization voltage on the specific capacitance of the capacitors fabricated in DI water and ethylene glycol at an APO concentration of 0.05 M is shown in the Figure A.3. The fringing effect was neglected because the anodized aluminum oxide was thin and the perimeter-to-area ratio was small. In general, the specific capacitance increased linearly with a decrease in the anodization voltage, because the oxide is thinner at lower anodization voltage [171]. Moreover, capacitors fabricated in ethylene glycol had about 30 nF/cm^2 higher specific capacitance than those fabricated in DI water under the same anodization conditions. To

examine the cause of the difference in specific capacitance fabricated in the two electrolytes, the thickness of the dielectric film was measured using an ellipsometer. The dielectric constant of the AAO was calculated using Equation 1.

$$\varepsilon_r = \frac{C_s * t}{\varepsilon_0} \quad (1)$$

In Eq. 1, C_s is the specific capacitance of the capacitor, t is the thickness of the dielectric film, and ε_0 is the vacuum permittivity, $8.85*10^{-12}$ F/m. Figure A.4 shows the thickness and dielectric constant of the AAO films fabricated in ethylene glycol and DI water. The linear growth of the dielectric film thickness with the anodization voltage in each electrolyte matches the linear decrease of the specific capacitance with the anodization voltage. Furthermore, the AAO films formed in DI water were slightly thicker than the films formed in ethylene glycol at each anodizing voltage. It was noted that the pH of the ethylene glycol electrolyte was 8.13 while the DI water pH was 6.37. The slightly higher pH for the ethylene glycol electrolyte increased the solubility and dissolution rate of the AAO film. Thus, the steady state anodization-dissolution condition in ethylene glycol resulted in a thinner AAO film compared to that in DI water. Based on the gradient of the thickness vs. voltage shown in Figure A.4, the growth rate of AAO film anodized in ethylene glycol was 1.05 nm/V, and 1.02 nm/V in DI water, which are comparable to

previous values [160,163,172,173].

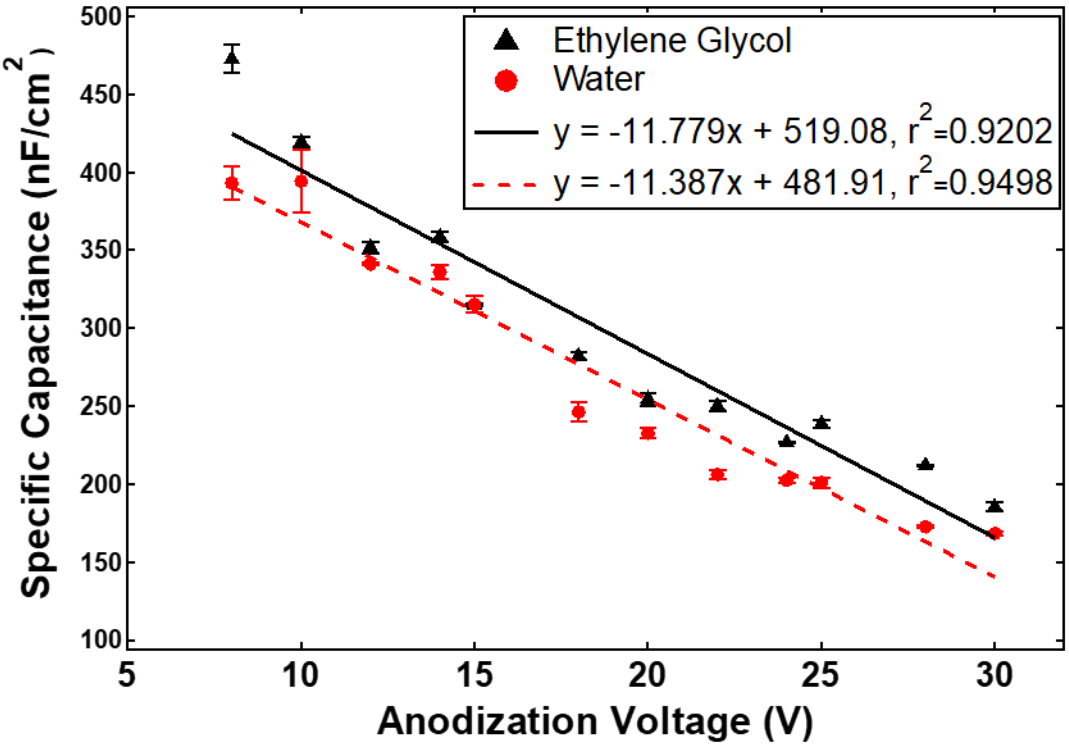

Figure A.3. Specific capacitance of capacitors fabricated in DI water and ethylene glycol vs. anodization voltage

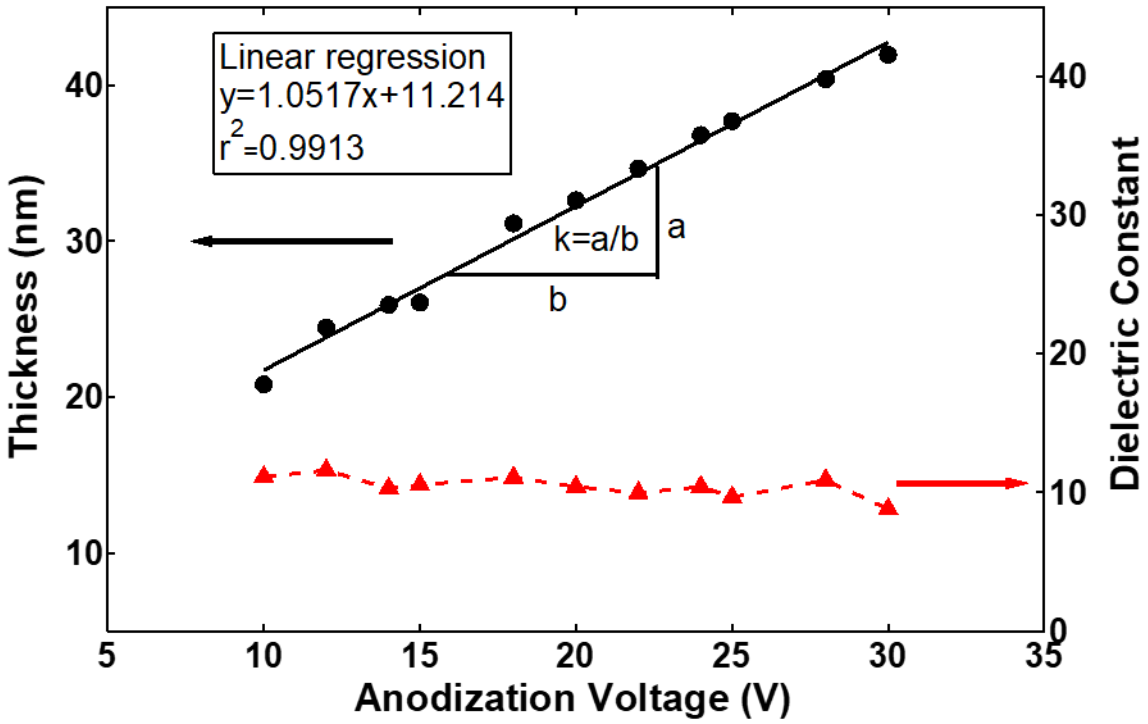
Linear regression
y=1.0517x+11.214
r2=0.9913
k=a/b
a
b
Thickness (nm)
Dielectric Constant
Anodization Voltage (V)
10
20
30
40
0
5
15
25
35

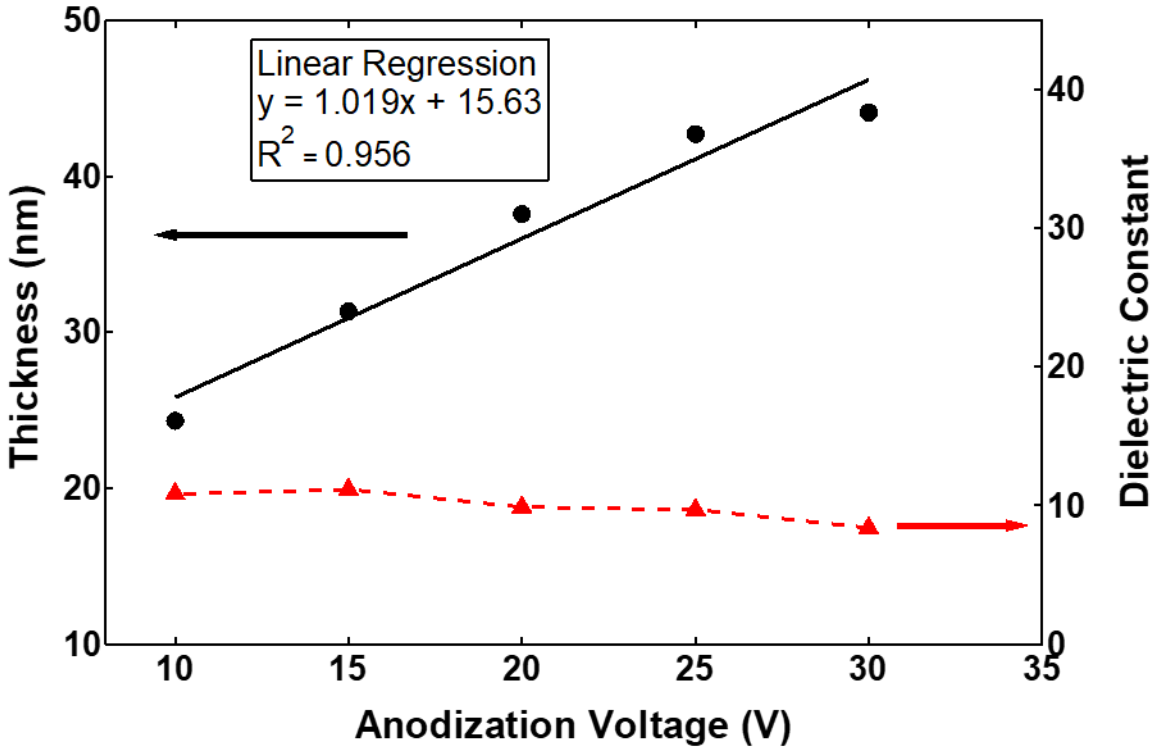

Figure A.4. Thickness and dielectric constant of AAO films anodized in (a) ethylene glycol, (b) DI water

The leakage current for capacitors fabricated in ethylene glycol at different anodization voltages are shown in Figure A.5. An increase in the breakdown voltage (V_{BD}) with increase of anodization voltage was observed, due to the thicker AAO film formed at high anodization voltage. To show how the quality of the film was influenced by the anodization voltage, the breakdown strength was calculated by dividing the measured breakdown voltage by the film thickness. The breakdown strength is plotted in Figure A.6. The breakdown strength was between 2 MV/cm and 5 MV/cm at all anodization voltages,

which were within the expected range of the dielectric strength of aluminum oxide [144,152,153,155,156,158,165]. The quality of the dielectric film can also be seen in the low leakage current shown in Figure A.5, where it was below 1 nA prior to capacitor breakdown.

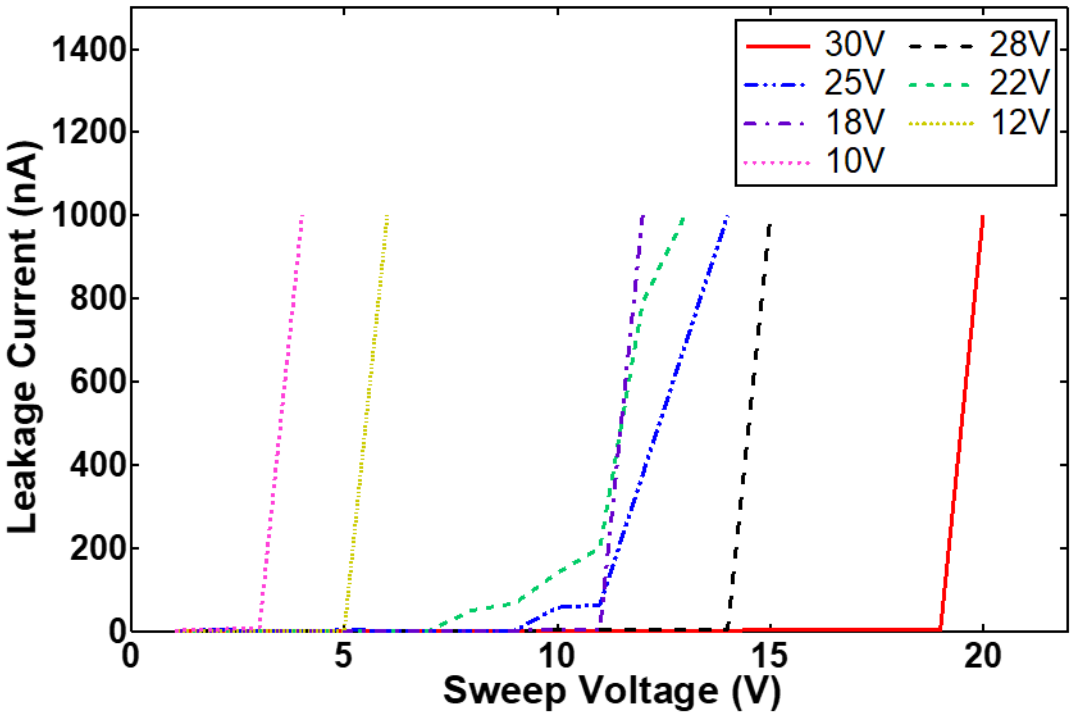

Figure A.5. Leakage current for capacitors fabricated at different anodization voltage in ethylene glycol

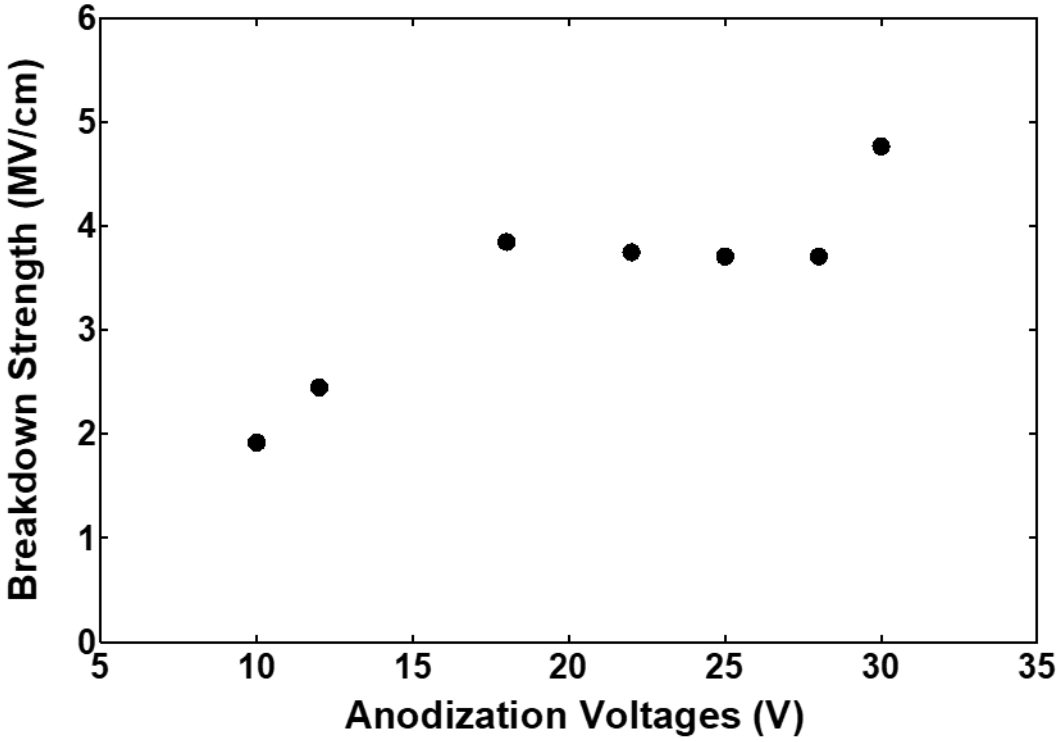

Figure A.6. Breakdown strength of AAO film at different anodization voltage in ethylene glycol

The standard deviation in capacitance for a set of capacitors fabricated in ethylene glycol at different anodization voltages was calculated and used to examine the reproducibility of the fabricated capacitors. Figure A.7 shows that the percentage error (i.e. standard deviation) of capacitors fabricated in ethylene glycol can be controlled below 2% when the anodization voltage is above 10 V.

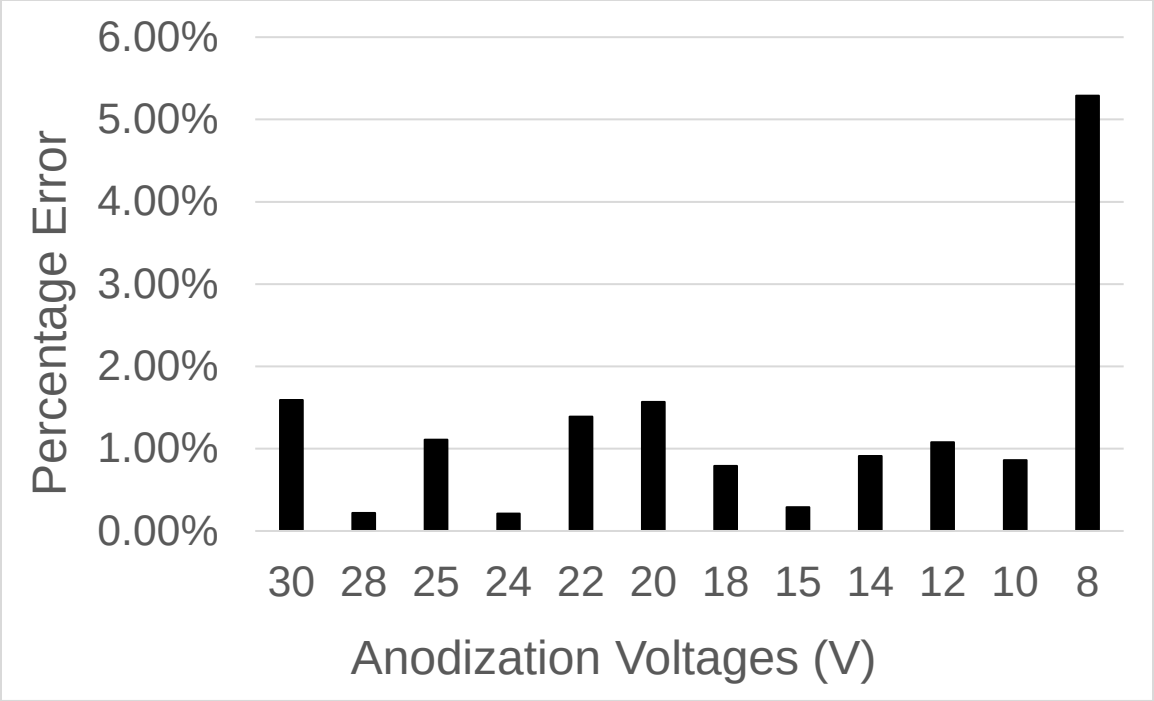

Figure A.7. Percentage error of capacitors fabricated in ethylene glycol at different anodization voltage

Effect of anodization time on specific capacitance: The effect of anodization time on the specific capacitance of the capacitors formed in DI water and ethylene glycol with an APO concentration of 0.05 M is shown in the Figure A.8. The specific capacitance varied slightly with anodization time in both electrolytes. This result is consistent with the measured film thickness and dielectric constant of AAO, shown in Figure A.9. These results show that the AAO film rapidly formed at a particular voltage in the first few minutes of anodization, followed by a steady state film thickness and maturing period. The fast anodization kinetics in the first few minutes is also supported by Figure A.1, where the anodization current quickly dropped to a plateau when dissolution and formation equilibrium occurred. The maturing of the AAO film (i.e. formation of a higher quality AAO film) can be seen in Figure A.10 where the breakdown strength improved with

anodization time with only a slight variation of the AAO film thickness. The improvement in film quality with anodization time may be due to a reduction in the number of defects. The leakage current for the AAO films, regardless of electrolyte, was mostly less than 1 nA, as shown in Figure A.11.

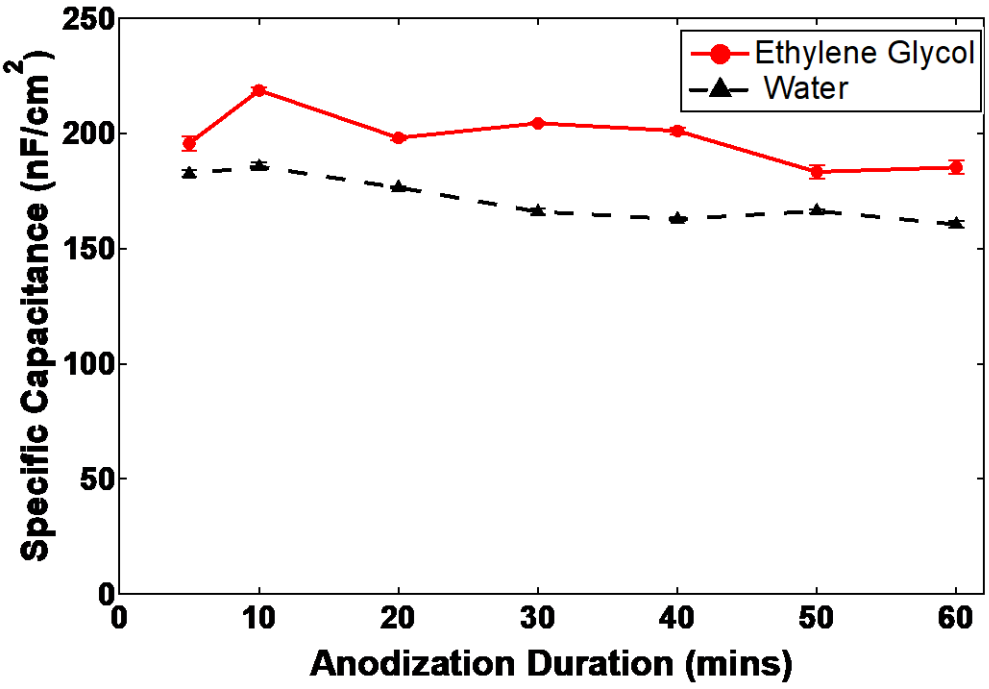

Figure A.8. Specific capacitance at different anodization time in ethylene glycol and DI water

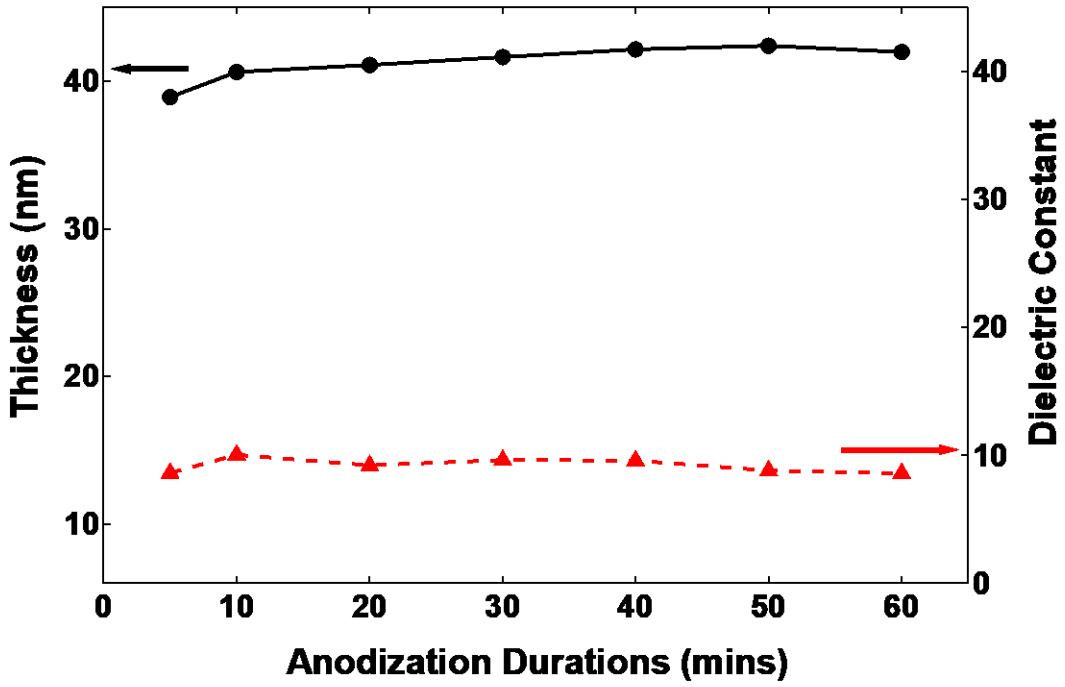

Figure A.9. Thickness and dielectric constant of the AAO film anodized at different time in ethylene glycol

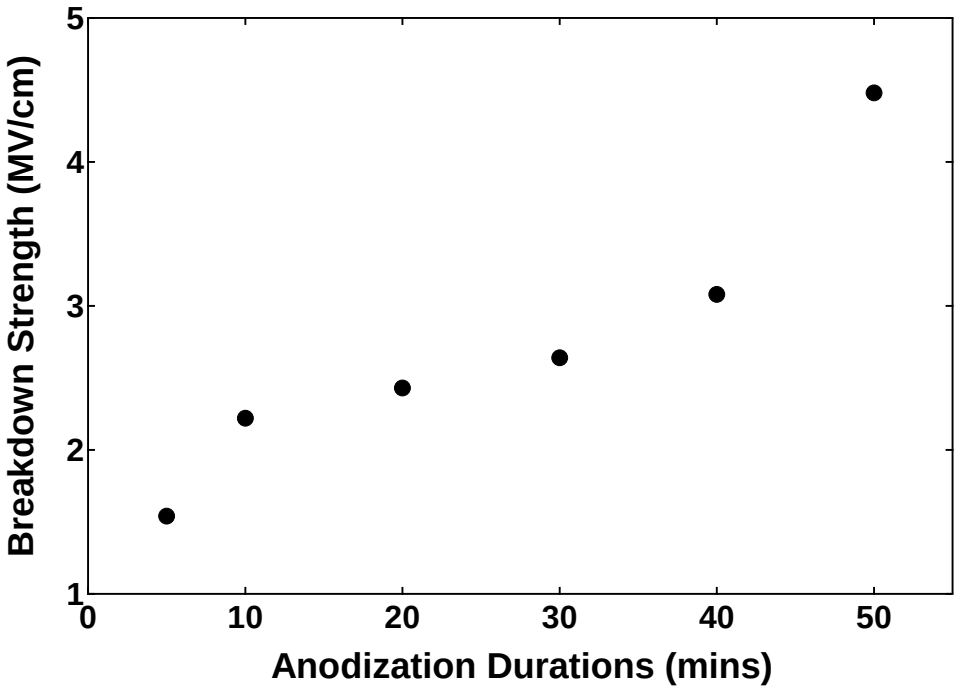

Figure A.10. Breakdown strength at different anodization time in ethylene glycol

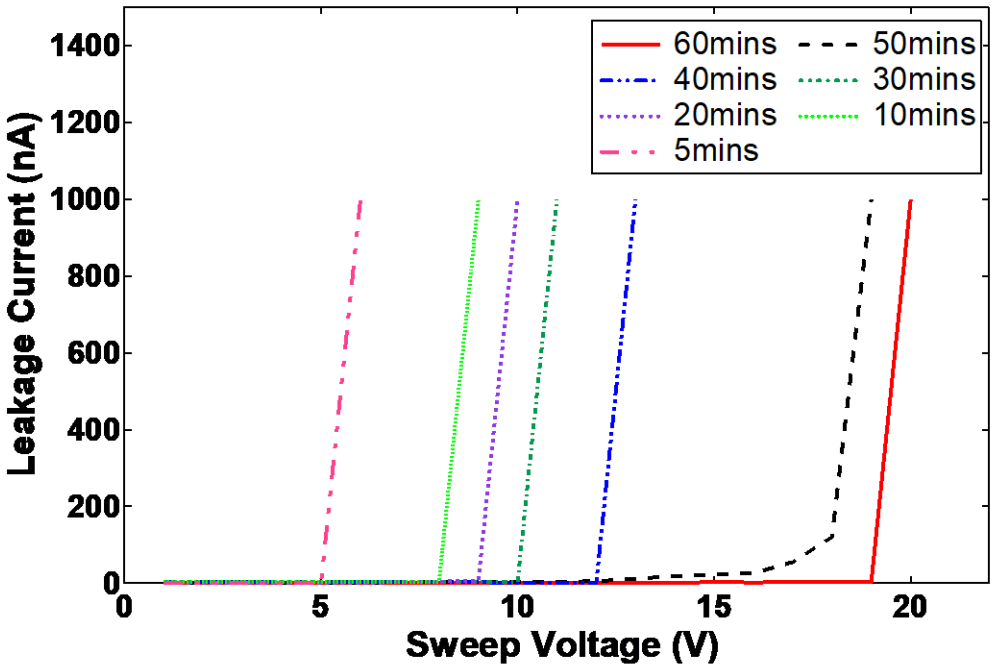
60mins
50mins
40mins
30mins
20mins
10mins
5mins
Leakage Current (nA)
Sweep Voltage (V)
0
200
400
600
800
1000
1200
1400
0
5
10
15
20

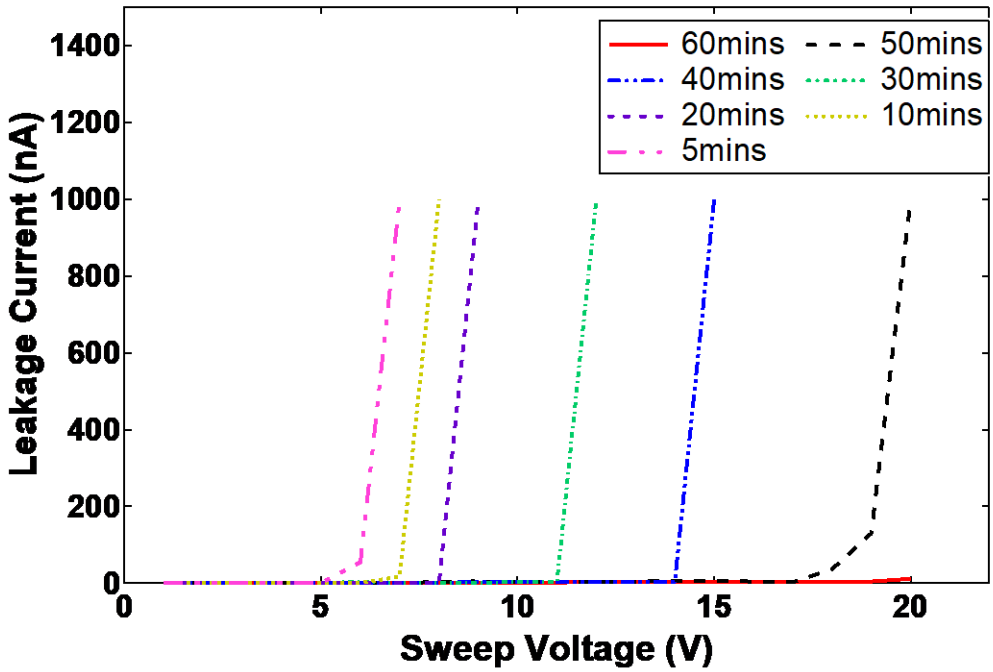

Figure A.11. Leakage current for capacitors fabricated at different time in (a) ethylene glycol, (b) DI water

The elemental composition of the AAO films formed in ethylene glycol was examined using XPS. The ratio of oxygen-to-aluminum atoms is shown in Figure A.12. The atomic ratio was within experimental error of the expected value of 1.5 for Al_2O_3.

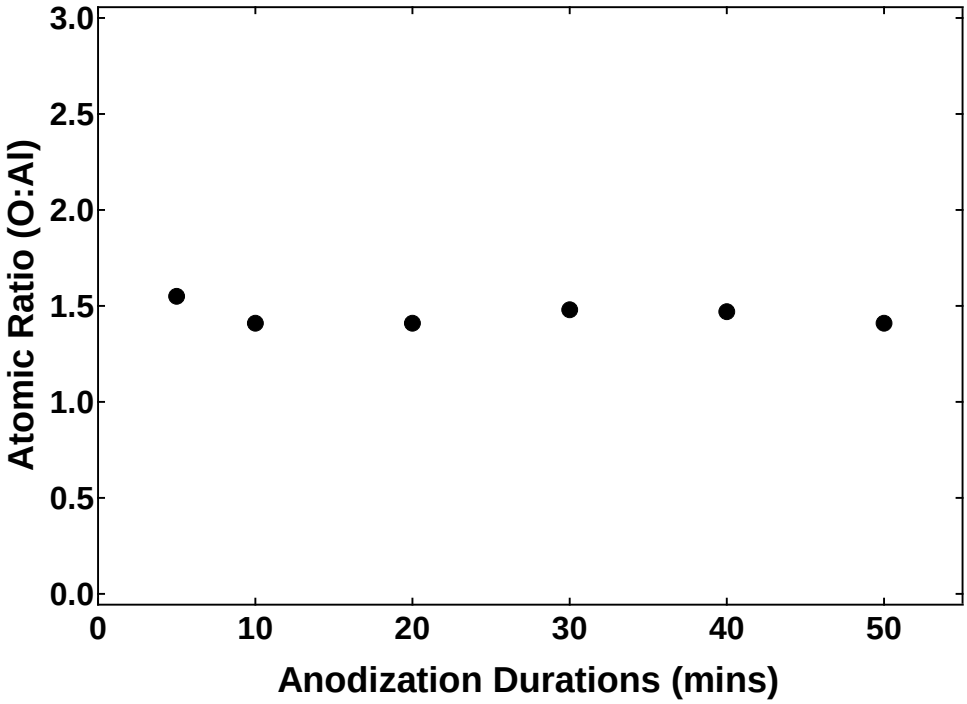

Figure A.12. Atomic ratio between oxygen and aluminum at different anodization time in ethylene glycol

Effect of anodization temperature on specific capacitance: The influence of anodization temperature on the specific capacitance of the capacitors fabricated in DI water and ethylene glycol at an APO concentration of 0.05 M is shown in the Figure A.13. In DI water, the drop of the capacitance with the increase of temperature indicated a strong temperature dependence for fabrication. In contrast, AAO film fabrication in ethylene glycol resulted in a uniform specific capacitance across a wide temperature range. The thickness of the AAO films in the two electrolytes at different temperatures is shown in Table A.1. The AAO film thickness in ethylene glycol was uniform across the temperature

range, in consistent with the specific capacitance in Figure A.13, while film thickness in DI water increased significantly for fabrication above room temperature [174]. Thus, ethylene glycol is the preferred electrolyte for AAO fabrication in this application.

Table A.1. Thickness of AAO films fabricated in ethylene glycol and DI water at different temperatures.

Temperature (°C)	Thickness in ethylene glycol (nm)	Thickness in DI water (nm)
5	39.35	42.24
25	41.97	44.1
40	40.54	200.3
60	41.58	624.7

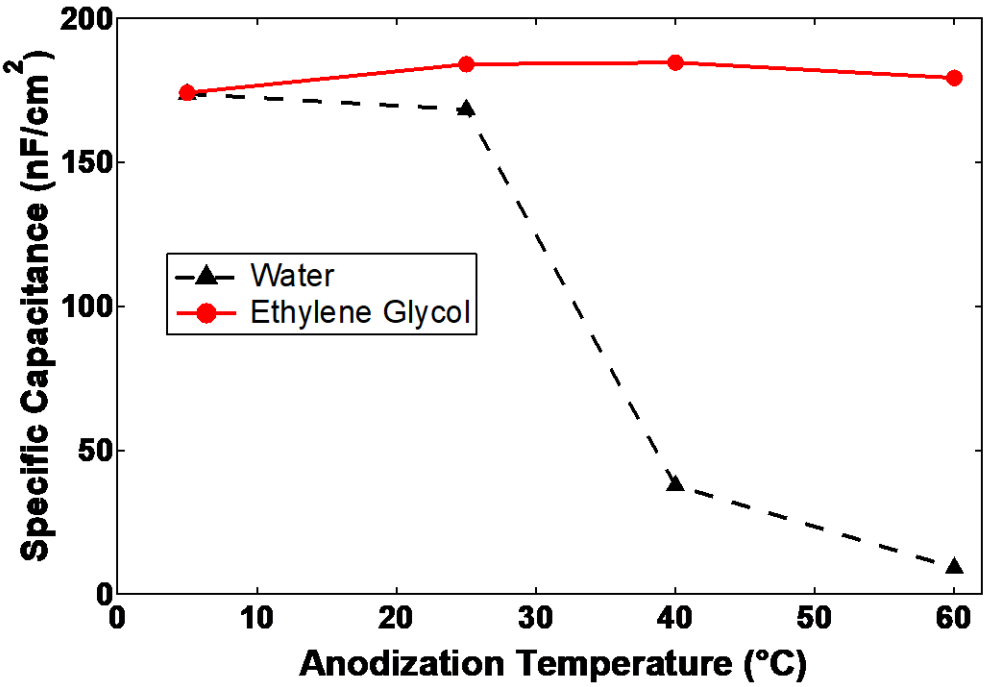

Figure A.13. Specific capacitance at different anodization temperature in ethylene glycol and DI water

The leakage current and breakdown voltage was measured for each of the capacitor formed in DI water and ethylene glycol at different process temperatures, as shown in Figure A.14. Fig. A.14(a) shows that the breakdown voltage for AAO formed at room temperature in ethylene glycol was the highest. The leakage current and breakdown voltage did not change appreciably when the AAO film was formed in water at different temperatures, shown in Figure A.14(b). Thus, it appears that in order to achieve highest specific capacitance with low leakage current and high breakdown strength, room

temperature formation of the AAO film in ethylene glycol is preferred, while low temperature forming of the AAO film in DI water is preferred.

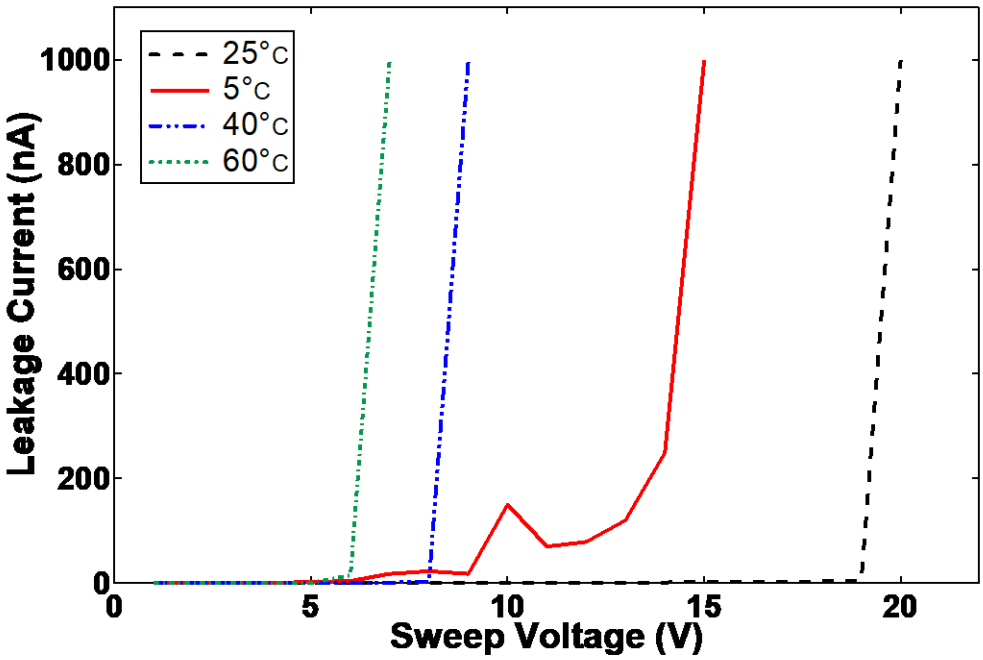

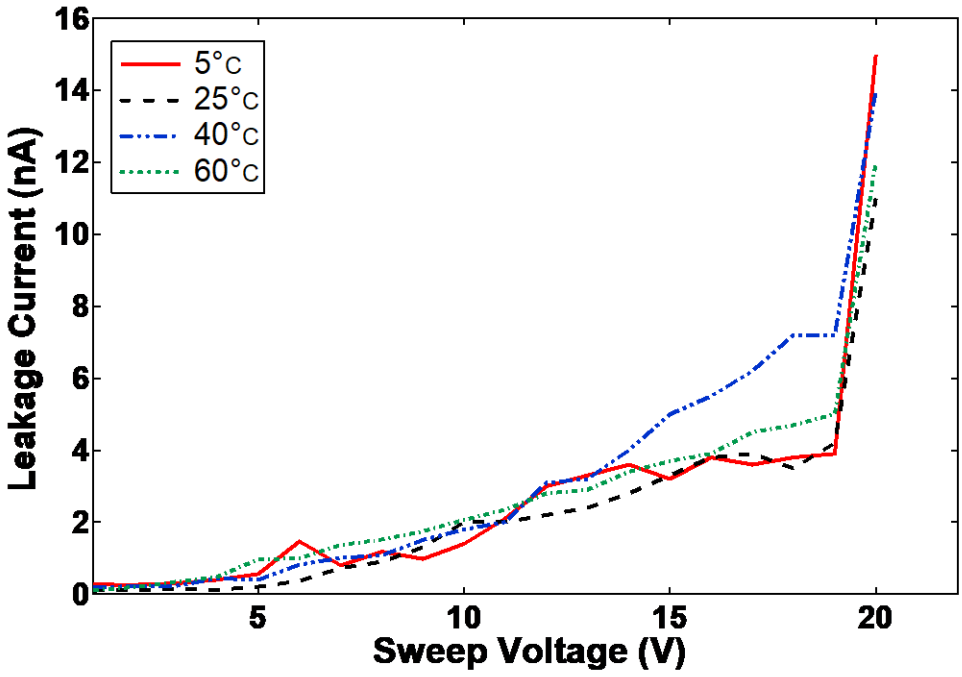

Figure A.14. Leakage current for capacitors fabricated at different temperature in (a) ethylene glycol, (b) DI water

Effect of electrolyte concentration on specific capacitance: The influence of APO concentration on the specific capacitance of the capacitors fabricated in ethylene glycol is shown in Figure A.15. The specific capacitance decreased with increasing APO concentration. The increased APO concentration increased the electrolyte conductivity leading to a higher current at constant potential. However the oxide dissolution rate of dielectric film also increased due to the increase in APO concentration. The equilibrium between anodic film growth and dissolution led to an overall decrease in film growth rate due to faster dissolution caused by higher APO concentration. That is, the current

efficiency (fraction of current resulting is oxide growth) decreased. Thus, the dielectric film growth approached a plateau upon increasing the electrolyte concentration in Figure A.16 [174]. The measured film thickness and dielectric constant at each electrolyte concentration are shown in Figure A.16. The film became slightly thicker when anodized in a more concentrated electrolyte, with the dielectric constant remained between 9 and 10. The breakdown voltage for each of the capacitors formed in the electrolytes with different APO concentrations is shown in Figure A.17. The leakage current density at voltages below breakdown was less than 10 nA/cm^2 for each of the capacitors. The AAO breakdown strength was the highest when the electrolyte concentration was 0.05 M. This indicates that higher quality AAO can be formed at higher APO concentration within the studied concentration range.

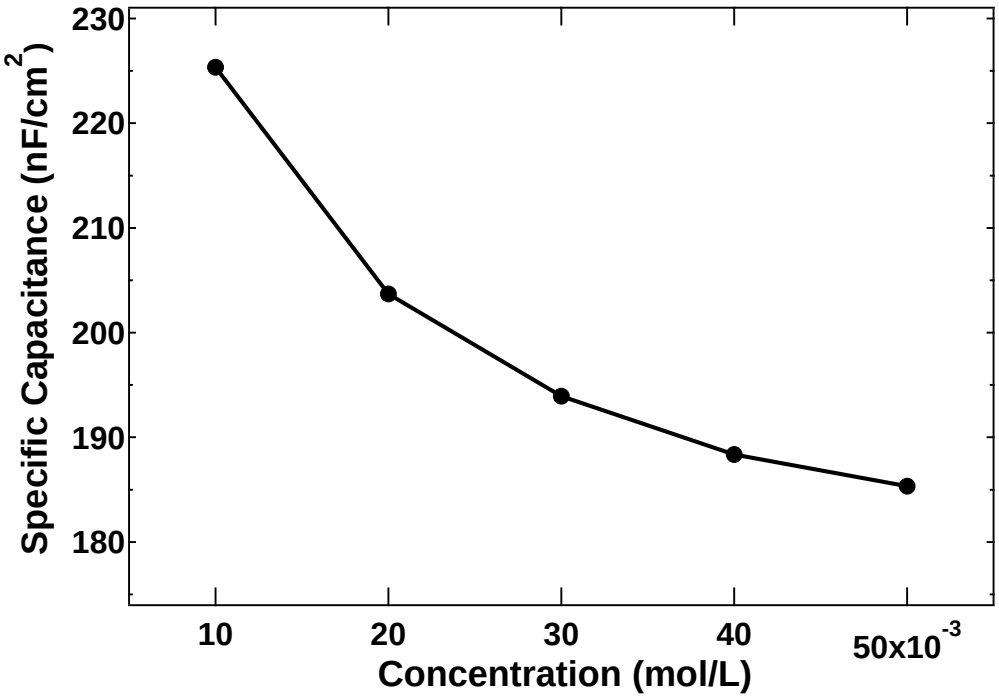

Figure A.15. Specific capacitance at different concentration of electrolyte in ethylene glycol

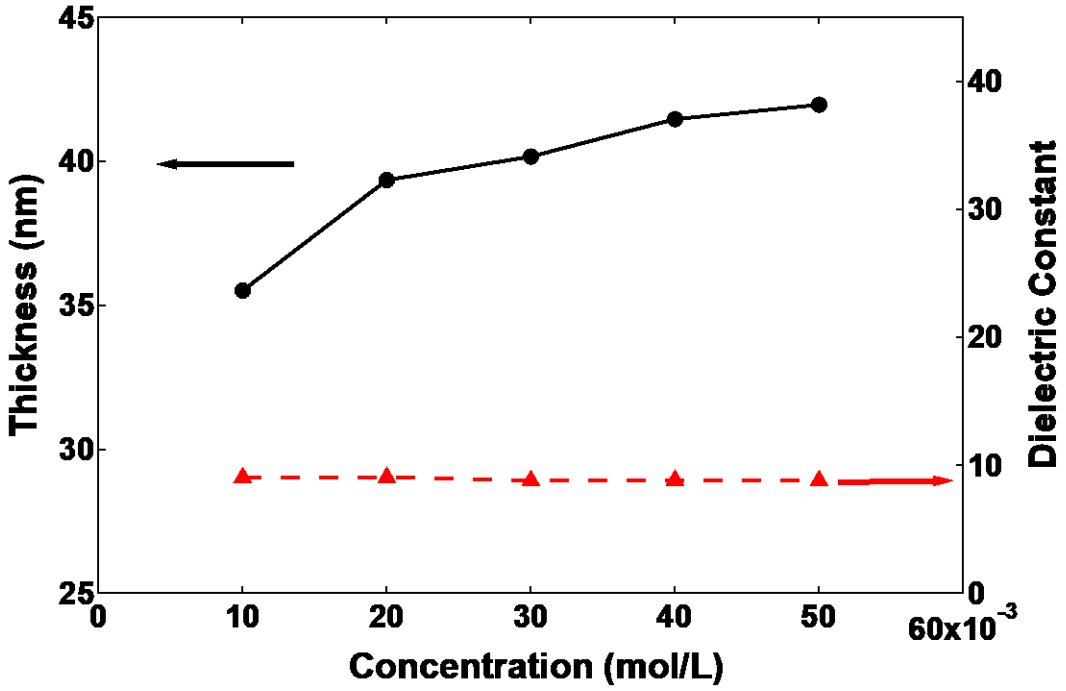

Figure A.16. Thickness and dielectric constant of the AAO film anodized at different concentration in ethylene glycol

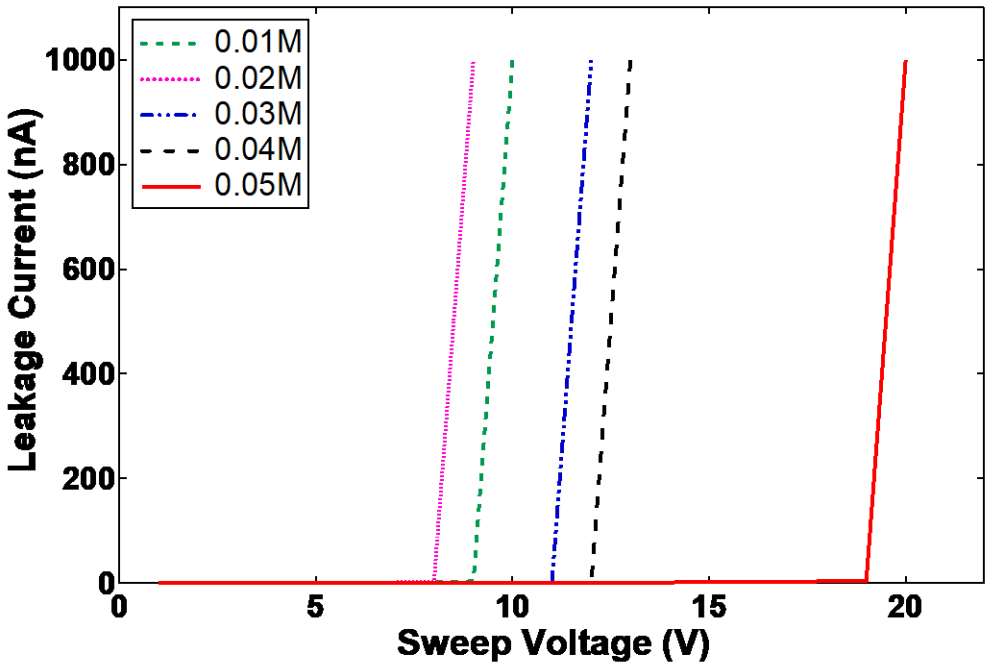

Figure A.17. Leakage current for capacitors fabricated in ethylene glycol at different concentration of electrolyte

Electron Conduction Mechanism: The electron conduction mechanism within AAO was expected to follow Schottky type emission [171,173,175], as expressed by the Richardson equation shown in Equation 2 [173].

$$J = AT^2 \exp\left[\frac{q\{\varphi_b + (\frac{qE}{4\pi\varepsilon_0\varepsilon_r})^{1/2}\}}{k_B T}\right] \quad (2)$$

In Eq. 2, J is the leakage current density (A/cm^2), A is the Richardson constant, T is the absolute temperature, q is the electron charge, φ_b is the barrier height, E is the electric field strength, ε_0 is the vacuum permittivity, ε_r is the dielectric constant of the barrier film, and k_b is the Boltzmann constant. Figure A.18 shows the linear relationship between log current vs square root of the electric field for AAO films formed in ethylene glycol at (a) 0.03 M APO at room temperature for 60 min., (b) 0.05 M APO at room temperature for 60 min., (c) 0.05 M APO at 5°C for 60 min., and (d) 0.05 M APO at room temperature for five minutes, where all of them match the Schottky conduction mechanism.

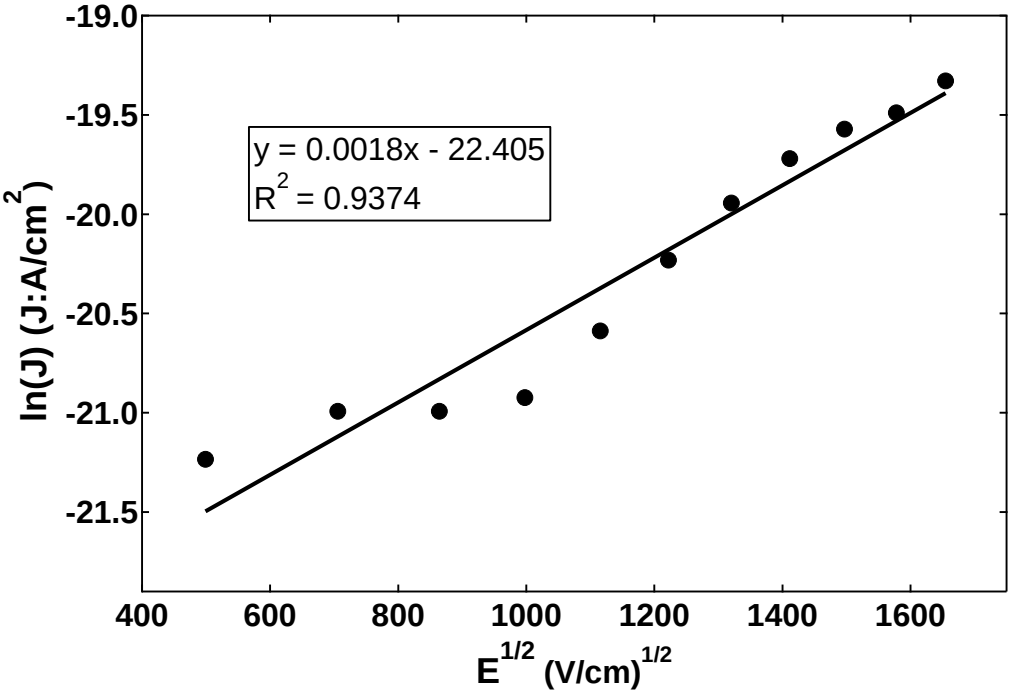

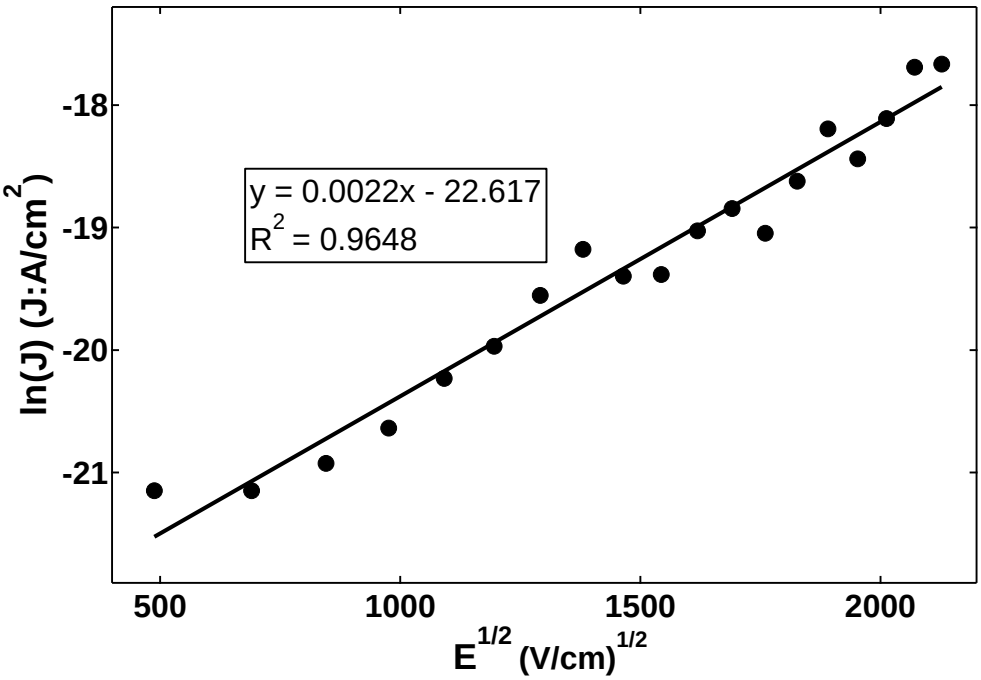
y = 0.0022x - 22.617
R2 = 0.9648
-18
-19
-20
-21
500
1000
1500
2000
ln(J) (J:A/cm2)
E1/2 (V/cm)1/2

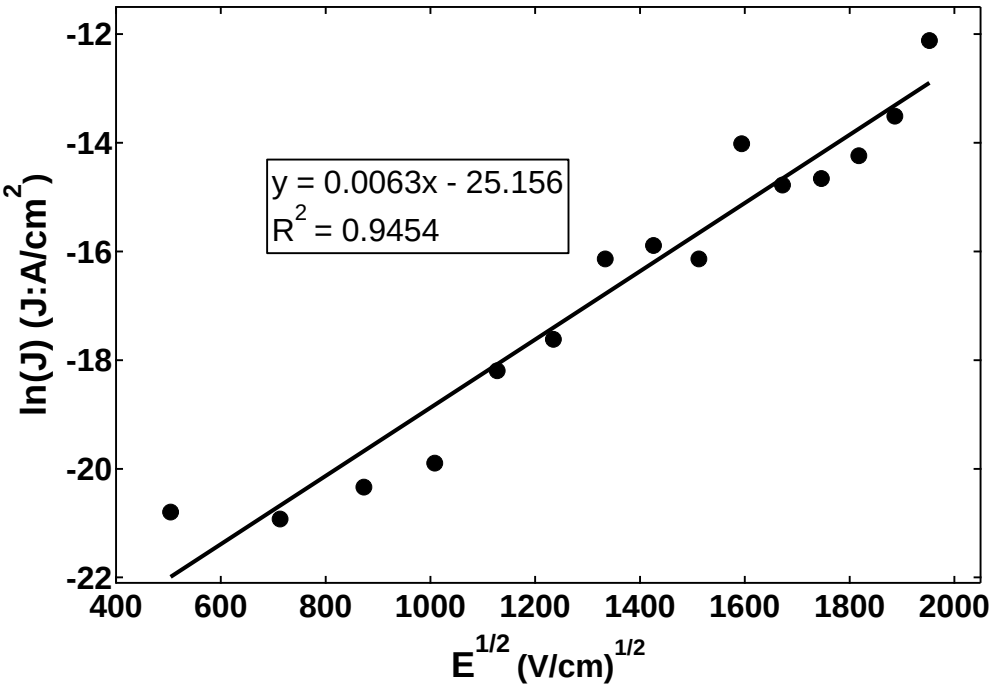
y = 0.0063x - 25.156
R2 = 0.9454
ln(J) (J:A/cm2)
E1/2 (V/cm)1/2
-12
-14
-16
-18
-20
-22
400
600
800
1000
1200
1400
1600
1800
2000

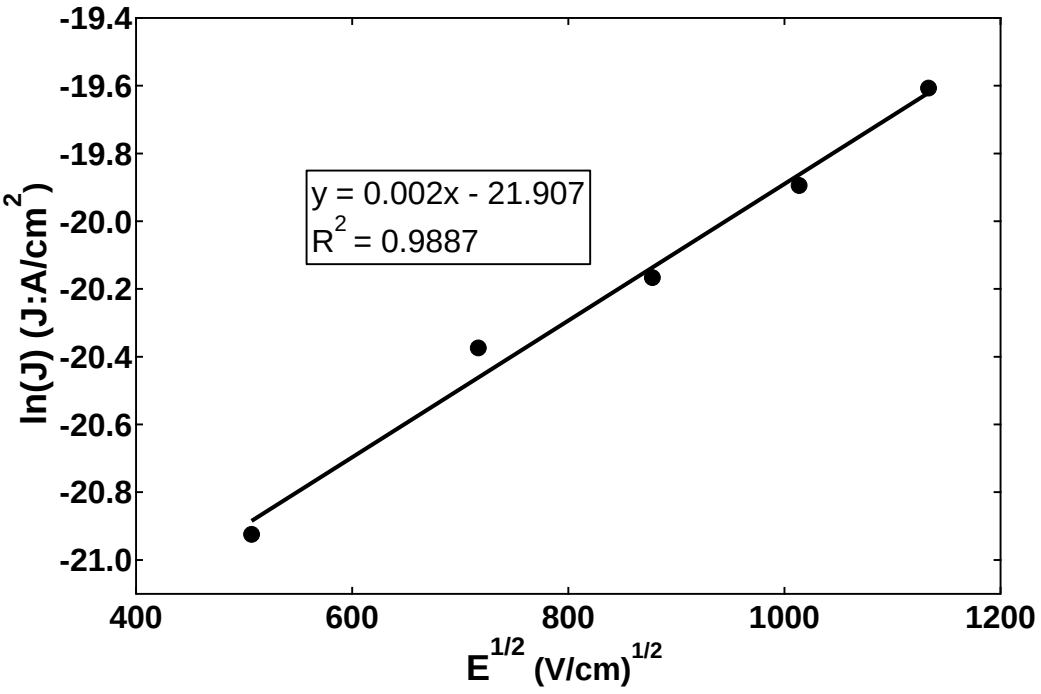

Figure A.18. Schottky plot of leakage current density for capacitors fabricated at (a) 0.03 M APO at room temperature for 60 mins, (b) 0.05 M APO at room temperature for 60 mins, (c) 0.05 M APO at 5 °C for 60 mins, (d) 0.05 M APO at room temperature for 5 mins

Linearity of capacitance with voltage: The linearity of capacitance with voltage was investigated for AAO films made in DI water and ethylene glycol at three different voltages. The International Technology Roadmap for Semiconductor states specific goals for leakage current and linearity: leakage current less than 10 nA/cm^2 and non-linearity coefficient (quadratic term in a relationship between capacitance and applied voltage) less

than 100 ppm/V^2 [166]. The non-linearity coefficient of the capacitors fabricated in both DI waterand ethylene glycol was determined by use of Equation 3 [176,177]

$$C(V) = C_0(\alpha V^2 + \beta V + 1) \qquad (3)$$

In Eq. 3, C is capacitance as a function of voltage, C_0 is the capacitance at zero bias, and α and β are the quadratic and linear voltage coefficients, respectively. Ideally, the capacitance should change linearly with the applied bias and have a non-ideal factor α of zero. Figure A.19 shows the relationship between relative capacitance and applied voltage for AAO films formed in ethylene glycol and DI water. The non-ideality factor α is tabulated in Table A.2. The non-ideality quadratic coefficients were relatively small for the AAO films formed in ethylene glycol. However, the values for AAO films formed in DI water were in excess of the ITRS goal of <100 ppm/V^2, making ethylene glycol the better choice as the solvent for fabrication of the capacitor.

Table B.2. Non-linearity quadratic term comparison between ethylene glycol and DI water.

Anodization Voltage (V)	Non-linearity quadratic term in Ethylene Glycol (ppm/V^2)	Non-linearity quadratic term in DI water(ppm/V^2)
25	-30	100
20	-50	200
15	6	300

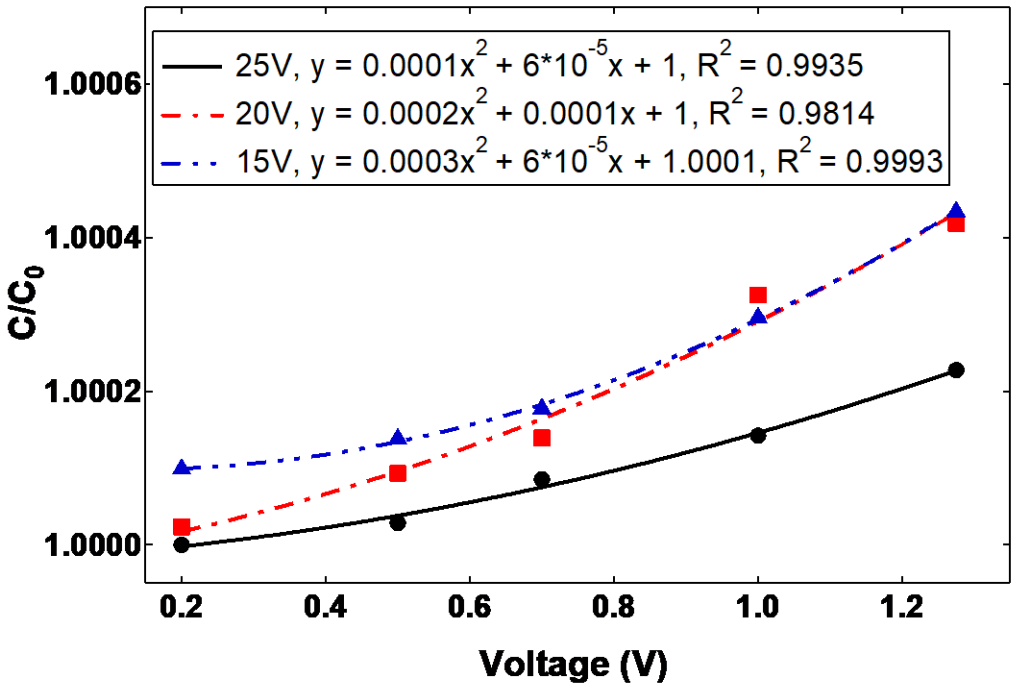
25V, y = 0.0001x2 + 6*10-5x + 1, R2 = 0.9935
20V, y = 0.0002x2 + 0.0001x + 1, R2 = 0.9814
15V, y = 0.0003x2 + 6*10-5x + 1.0001, R2 = 0.9993
1.0006
1.0004
1.0002
1.0000
C/C0
0.2
0.4
0.6
0.8
1.0
1.2
Voltage (V)

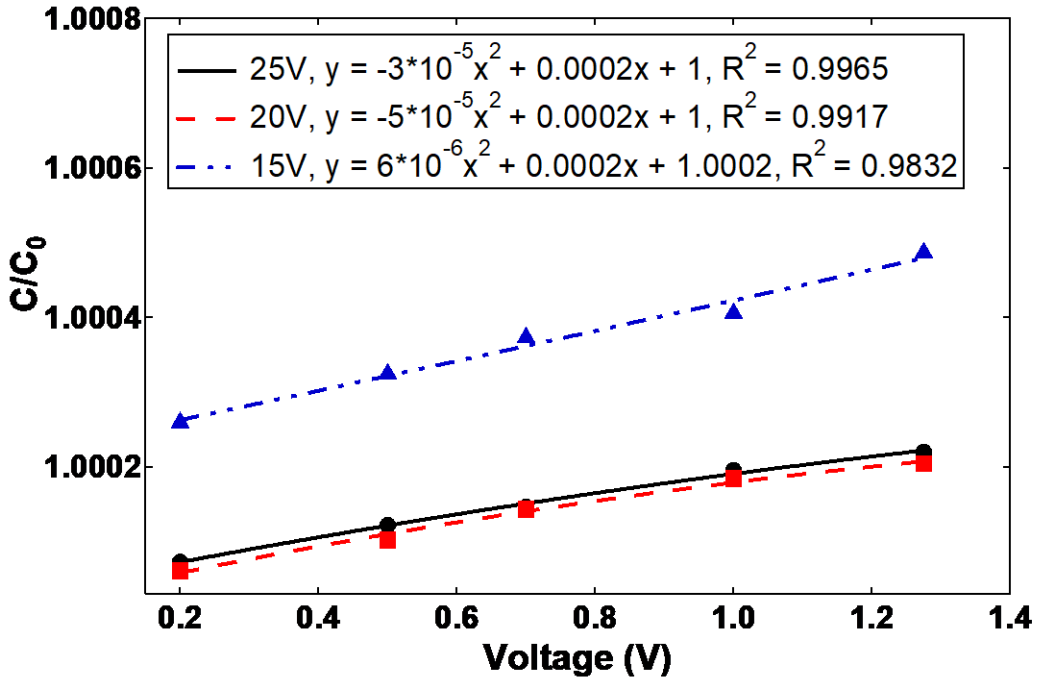

Figure A.19. Non-linear fitting of the normalized capacitance of capacitors fabricated in (a) DI water, (b) ethylene glycol

A.4 Conclusion

APO was selected as the electrolyte for potentiostatic anodization of aluminum to form barrier type dielectric films because of the stability and quality of the resulting oxide. The effect of solvent, anodization voltage, time, temperature, and electrolyte concentration in the formation of AAO were studied. Ethylene glycol solvent produced higher specific capacitance and quality AAO films compared to DI water. The linear growth relationship of thickness vs. the anodization voltage made it possible to control the capacitance of the capacitor. Increasing anodization time resulted in better quality and higher breakdown

voltage AAO films. The ethylene glycol electrolyte was not sensitive to temperature in terms specific capacitance, and room temperature yield the best AAO quality. By increasing the concentration of the electrolyte, the specific capacitance and the breakdown strength of the fabricated capacitors were improved. Linear fitting based on Richardson equation confirmed the conduction mechanism in AAO film was based on the Schottky emission mechanism, which agreed well with other literature studies of anodized aluminum capacitors. Lastly, the quadratic voltage coefficient of the capacitors fabricated in ethylene glycol and DI water was determined. The values showed that the capacitors fabricated in ethylene glycol behaved more ideally and the quadratic voltage coefficient met ITRS specifications, less than 100 ppm/V^2.

APPENDIX B.

TRANSIENT ENERGY HARVESTER AND SENSORS BASED ON TRIBOELECTRIC NANOGENERATOR USING ACID-SENSITIVE POLY(PHTHALALDEHYDE)

B.1 Sample Preparation

Without silver nanowires (AgNW)

PPHA films were formulated in a clean scintillation vial by dissolving all solid contents (i.e., PPHA, PAG, anthracene) and liquid contents (BMP TFSI) in THF. Weight ratio of 12:1 for THF and PPHA were used for all formulations in order to obtain the right viscosity to spread and cover the PTFE petri dishes for drying. All polymer formulation was prepared containing 10 part per hundred resin (pphr) PAG, 2.1 pphr anthracene, and 100 pphr BMP TFSI, with all weight fraction reference to the weight of PPHA added into the formulation. The sample was dried in a nitrogen-rich, pressurized chamber at 15 psig for 18 hrs, followed by slow bleeding of THF out of chamber for 3 hrs. Samples were then taken out of the pressurized chamber and peeled off the substrate. All samples were then flattened and allowed further drying for 3 days before taken to test. All dried samples have average thickness of 100 μm.

With AgNW

AgNW is poured and coated onto a glass substrate and dried in ambient until the coating is conductive. Nylon strips were used as fences to create enclosed area on glass substrates to control the surface area and thickness of the casted PPHA films. PPHA films

were formulated as described above and uniformly poured into the prepared glass substrates. All films were allowed to dry following the same procedure as described above. The pressure-dried films were allowed for further drying for 24 hrs in a dark ambient environment. A razor blade was then used to lift off a corner of the film from the glass substrate. Films were then submerged into a room-temperature water bath for 15 mins, followed by peeling off the entire film from each glass substrate.

B.2 Thermal/Mechanical Properties of Ag-Nanowires Covered Film

Mechanical properties of PPHA film with and without AgNW on the surface were characterized using dynamic mechanical analyzer (DMA) using TA Instrument Q800 Dynamic Mechanical Analyzer. Samples had dimension of 11 mm * 7 mm * 0.1 mm (length * width * thickness). Stress-strain curve of samples were measured at 23 °C with a preload force of 0.015 N and were elongated with a constant force ramp rate of 1 N/min until sample-failure occurred. Young's modulus [MPa], strain to break value [%], and yield stress [MPa] were extracted from the stress-strain curve. The ability of a material to absorb energy without fracturing is represented by modulus of resilience [J/m^3] and was calculated using equation below. Result is shown in Figure B.1. Summary of mechanical properties is shown in Table B.1.

$$Modulus\ of\ Resilience = \frac{Yield\ Stress^2}{2 * (Young's\ Modulus)}$$

Thermogravimatric analysis (TGA) was performed using a TA Instrument Q50 under inert nitrogen condition with a constant flow rate of 40 ml/min. Weight of 6.112 mg PPHA film containing 10 pphr PAG, 2.1 pphr anthracene, 100 pphr BMP TFSI, and Ag

NW covered surface was loaded into TGA and investigated for its thermal stability. Furnace temperature was ramped at 5 °C/min to 250 °C. Figure B.2 shows the weight fraction change of the loaded film with the ramping of temperature. The onset decomposition of the film is around 113 °C. About 50% residual weight was leftover, due to the Ag NW and non-volatile BMP TFSI.

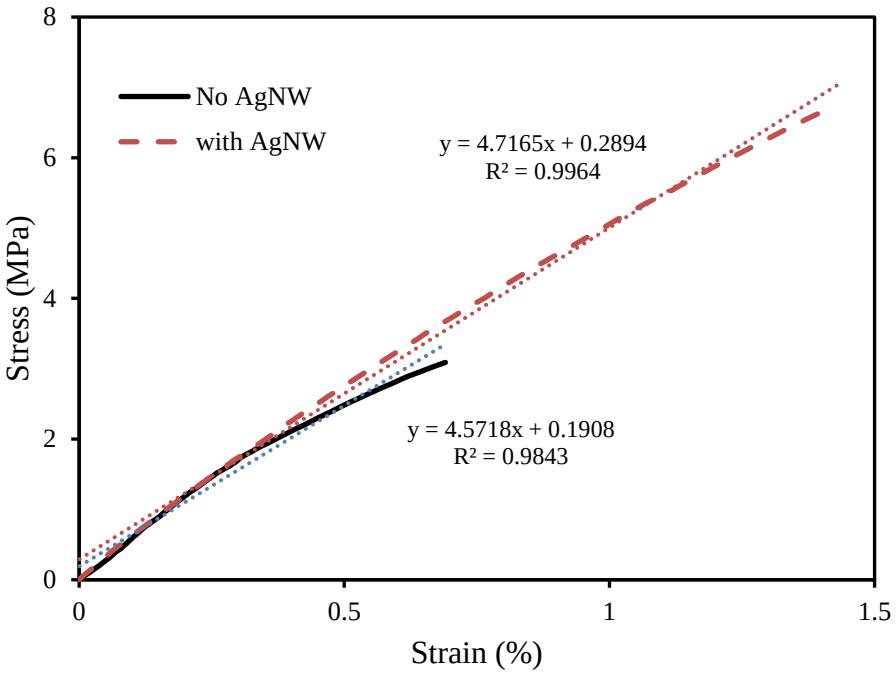

Figure B.1. Stress-strain curve of PPHA with/without AgNW coating on the surface

Table B.1. Summarized mechanical properties data.

	Young's Modulus	Strain to Break	Yield Stress (MPa)	Toughness (J/m^3)
No AgNW	457	0.69%	3.09	0.0104
With AgNW	472	1.43%	6.75	0.0483

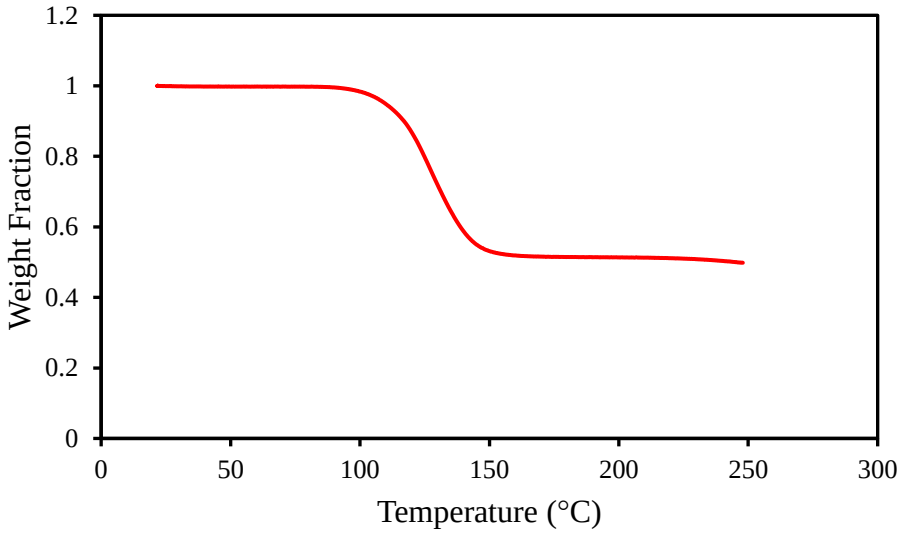

Figure B.2. TGA of AgNW coated PPHA film.

B.3 Photoinduced Degradation

The degradation of a 100 µm PPHA film was characterized by Nicolet iS50 FT-IR instrument. Attenuated total reflectance (ATR) mode was used and total scans of 32 were performed for each sample. Samples were exposed using a portable B-100 series ultraviolet lamp with an intensity of 4 mW/cm^2 at 365 nm. Data were collected after samples were exposed for 0 s, 10 s, 60 s, and 90 s. The formation of carbonyl peak at 1680 cm^{-1} were

compared to the monomer ortho-phthalaldehyde for indication of the extent of polymer degradation. Figure B.3 shows the FTIR of exposed PPHA film with different amount of dose.

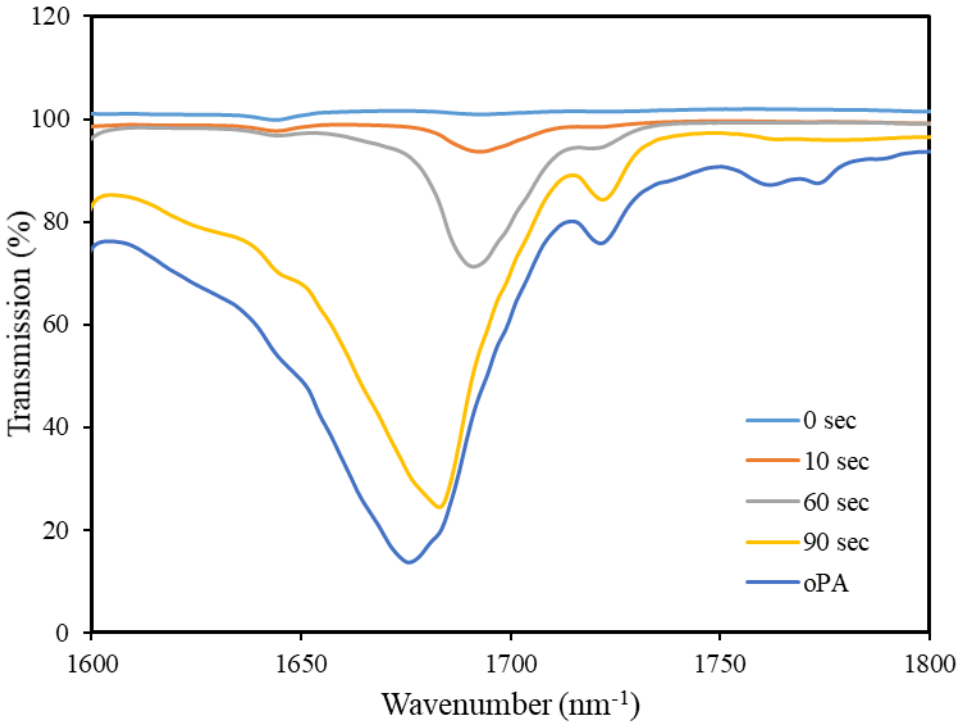

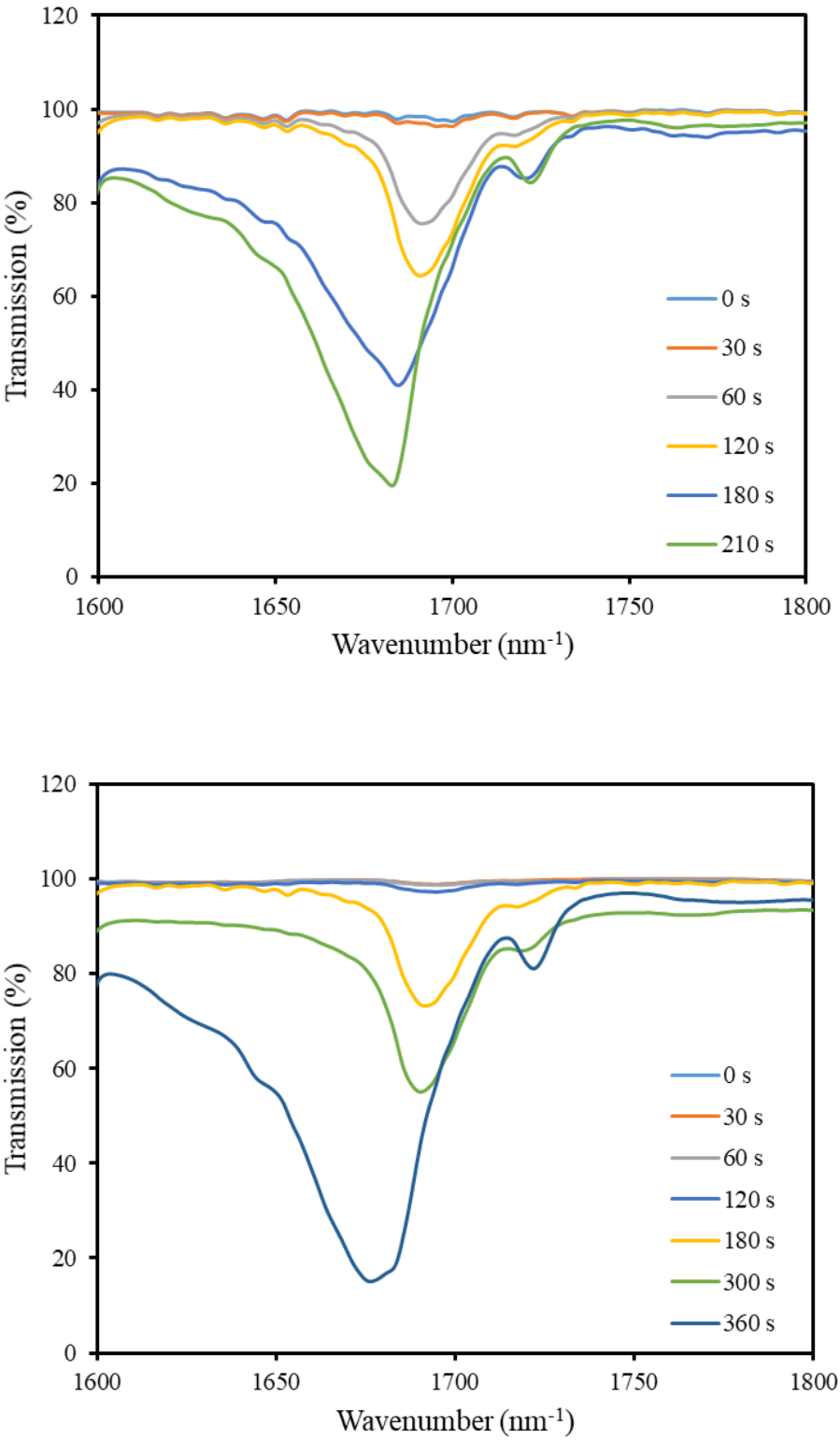

Figure B.3. FTIR of exposed PPHA film. a) 10% PAG, b) 5% PAG, c) 1% PAG

B.4 Demo Pictures – Transient Energy Harvester/Touch Sensor

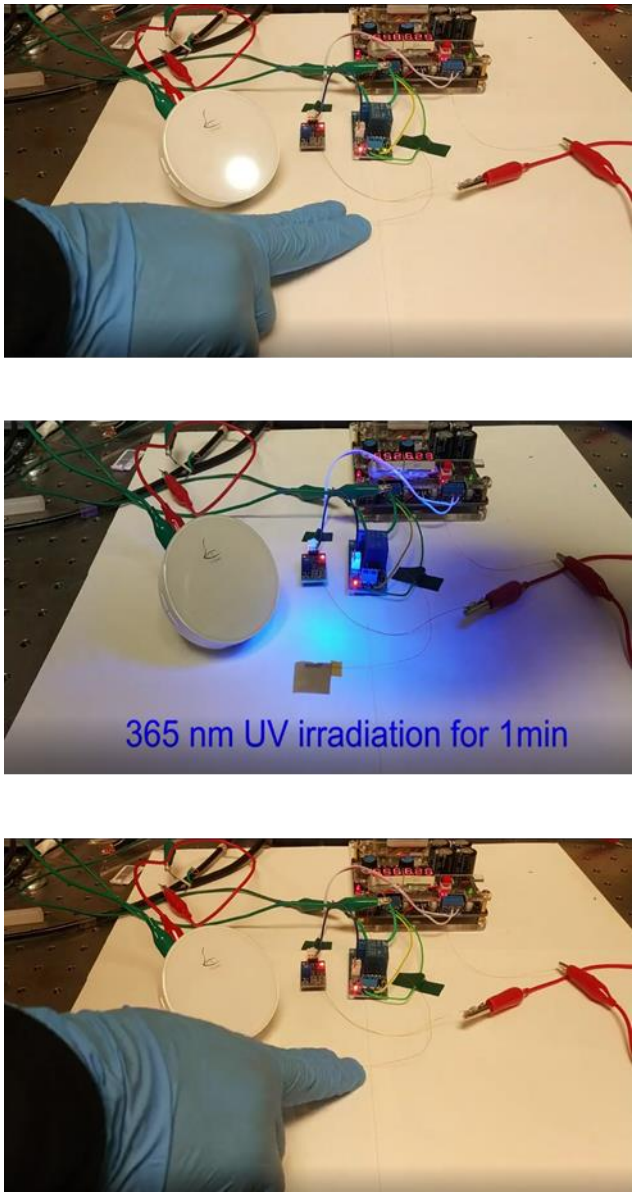

Figure B.4. Transient touch sensor to ring the bell (This picture was a collaboration with Changsheng Wu.)

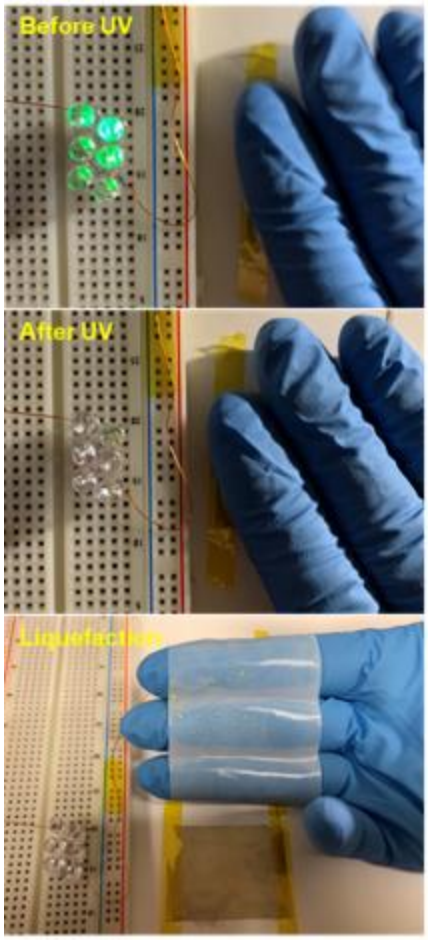

Figure B.5. Transient energy harvester to light up six green LEDs connected in series (This picture was a collaboration with Changsheng Wu.)

APPENDIX C.

COEFFICIENT OF THERMAL EXPANSION MEASUREMENT DATA FOR CALCULATION OF RESIDUAL STRESS OF POROUS EPOXY FILM

C.1 Nanoindentation Depth and Film Thickness Measurement

Nanoindentation measurement details to support the claim in the manuscript that all nanoindentation was measured with the indentation depth less than 10% thickness of the thin epoxy film.

Table C.1. Nanoindentation depth for measurement of reduced modulus for films using SMA2000 as crosslinker

Indentation Force (μN)	**Indentation Depth Using SMA2000 (nm)**					
	0% porosity	10% porosity	15% porosity	20% porosity	25% porosity	30% porosity
100	63.6	62.4	63.2	55.1	58.6	78.6
150	86.9	83.2	84.7	91.4	77.9	73.3
200	105.8	109.6	112.7	99.6	99.6	103.9
250	123.9	126.9	113.8	112.7	105.9	108.7

Table C.2. Nanoindentation depth for measurement of reduced modulus for films using SMA4000 as crosslinker

Indentation Force (μN)	Indentation Depth Using SMA4000 (nm)					
	0% porosity	10% porosity	15% porosity	20% porosity	25% porosity	30% porosity
100	61.7	72.2	65.3	68.7	70.5	93.2
150	93.5	96.6	96.9	99.1	102.0	126.0
200	123.3	125.2	121.7	126.3	127.8	168.9
250	143.7	140.5	141.2	148.6	155.5	207.4

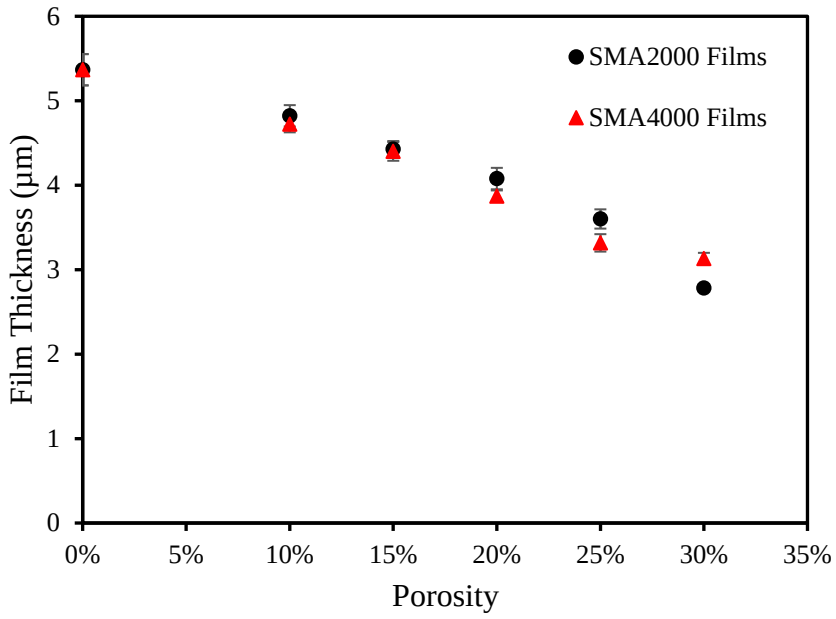

Figure C.1. Porous epoxy film thickness for various porosity used for dielectric constant calculation and mechanical property measurement

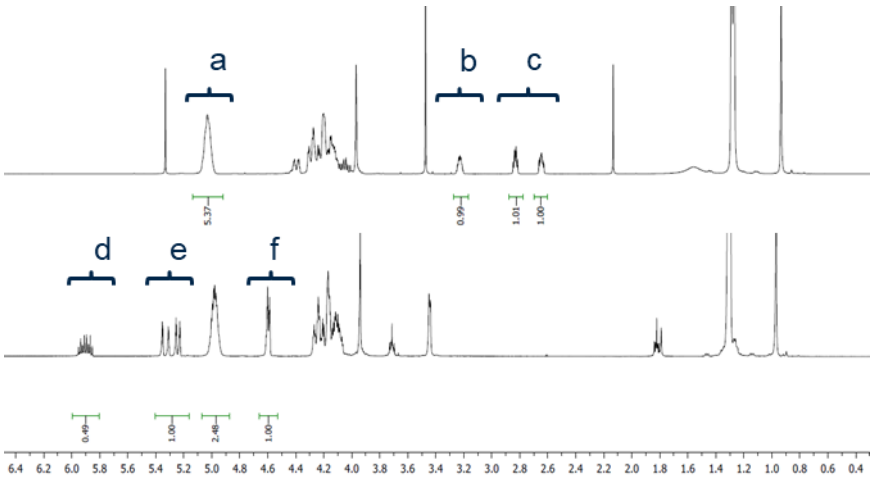

Figure C.2. NMR of epoxide functionalized poly(propylene carbonate) used in porous epoxy formulation.

C.2 All Film Parameters Needed for Residual Stress Calculation

Radius of curvatures used to calculate for coefficient of thermal expansion were obtained from BowOptic 208 tool.

Table C.3. Parameter used for calculation CTE values for films using SMA2000 as crosslinker

Sample (SMA2000)	Temperature (°C)	R_1 (m)	R_2 (m)	t_s (mm)	t_f (mm)
0% porosity	120	323.355	109.270	0.983	0.002884
	130		106.737		
	140		105.821		
	150		102.415		
	160		100.607		
20% porosity	120	379.454	373.791	0.983	0.002779
	130		351.284		
	140		326.257		
	150		310.425		
	160		282.225		

	120		-198.153		
	130		-213.246		
30% porosity	140	-173.623	-222.345	0.984	0.001527
	150		-223.044		
	160		-239.526		

Table C.4. Parameter used for calculation CTE values for films using SMA4000 as crosslinker

Sample (SMA4000)	**Temperature (ºC)**	**R_1 (m)**	**R_2 (m)**	**t_s (mm)**	**t_f (mm)**
	120		334.518		
	130		319.937		
0% porosity	140	385.717	310.153	0.982	0.003031
	150		293.399		
	160		267.788		
	120	-230.210	-248.463	0.990	0.002891

20% porosity	130		-258.710		
	140		-272.072		
	150		-302.702		
	160		-317.213		
30% porosity	120		262.623		
	130		239.308		
	140	351.482	233.637	0.983	0.003014
	150		202.871		
	160		193.880		

APPENDIX D.

POLY(PHTHALALDEHYDE) FILM FORMULATION TESTING

D.1 Summary of Characteristic Photospeed, Transient Properties of Poly(phthalaldehyde) Formulation

Table D.1. Summary of characteristic films tested for sunlight exposure

Polymer		Plasticizer		Ionic Liquid	Fiber		Time	Test Temp	Freezing Point
PPHA : BA 1:1	PPHA Only	PEO	BEHP	BMP	Glass	Acrylic			
X			3%	30%	20%		2 min @ 10:14am (26 min at dawn)	42 F	Crystallize Immediately
X			3%	30%	20%		50 sec @ 1:48pm (21 min at dawn)	62 F	Liquid outside
X			5%	30%	20%		2 min @ 10:14am (26 min at dawn)	42 F	Crystallize Immediately
X			5%	30%	20%		50 sec @ 1:48pm (21 min at dawn)	62 F	Stay liquid outside
X			7%	30%	20%		2 min @ 10:14am (26 min at dawn)	42 F	Crystallize Immediately
X			7%	30%	20%		50 sec @ 1:48pm (21 min at dawn)	62 F	Stay liquid outside
X		5%		20%	20%		20 min @ 9:38am (79 min at dawn)	37 F	Crystallize Immediately
X		5%		20%	20%		2 min @ 1:22pm (32 min at dawn)	46 F	Liquid state for 2 mins
X		5%		30%	20%		13 min @ 9:38am (63 min at dawn)	37 F	Crystallize Immediately
X		5%		30%	20%		2 min @ 1:22pm (32 min at dawn)	46 F	Crystallize Immediately
X		5%		40%	20%		19 min @ 9:38am (76 min at dawn)	37 F	Crystallize Immediately
X		5%		40%	20%		2 min @ 1:22pm (26 min at dawn)	46 F	Stay liquid outside
X		10%		20%	20%		20 mins at 9:38am (79 min at dawn)	37 F	Crystallize Immediately
X		10%		20%	20%		2.5 min @ 1:22pm (35 min at dawn)	46 F	Crystallize Immediately
X		10%		30%	20%		24 min @ 9:38am (87 min at dawn)	37 F	Liquid state for 1 min
X		10%		30%	20%		3.5 min @ 1:22pm (26 min at dawn)	46 F	Liquid state for 3 mins
X		10%		40%	20%		24 min @ 9:38am (87 min at dawn)	37 F	Liquid state for 1 min
X		10%		40%	20%		7 min @ 1:22pm (57 min at dawn)	46 F	Liquid at 46F
	X		0%	50%	20%		1.5 mins at 9:35am (21 min at dawn)	50 F	Liquid at 50 F Liquid at 39 F Solid at 25 F
	X		2%	50%	20%		2.5 mins at 9:35am (27 min at dawn)	50 F	Liquid at 50 F Liquid at 39 F Solid at 25 F
	X		3%	50%	20%		2.5 mins at 9:35am (27 min at dawn)	50 F	Liquid at 50 F Liquid at 39 F Solid at 25 F

	X		5%	50%	20%		2.5 mins at 9:35am (27 min at dawn)	50 F	Liquid at 50 F Liquid at 39 F Liquid at 25 F
	X			60%	20%				Liquid at 50 F Liquid at 39 F Solid at 25 F
	X			70%	20%				Liquid at 50 F Liquid at 39 F Solid at 25 F
	X			70%	30%				Liquid at 50 F Liquid at 39 F Liquid at 25 F

D.2 Additional Plasticizers Tested for Poly(phthalaldehyde) Films

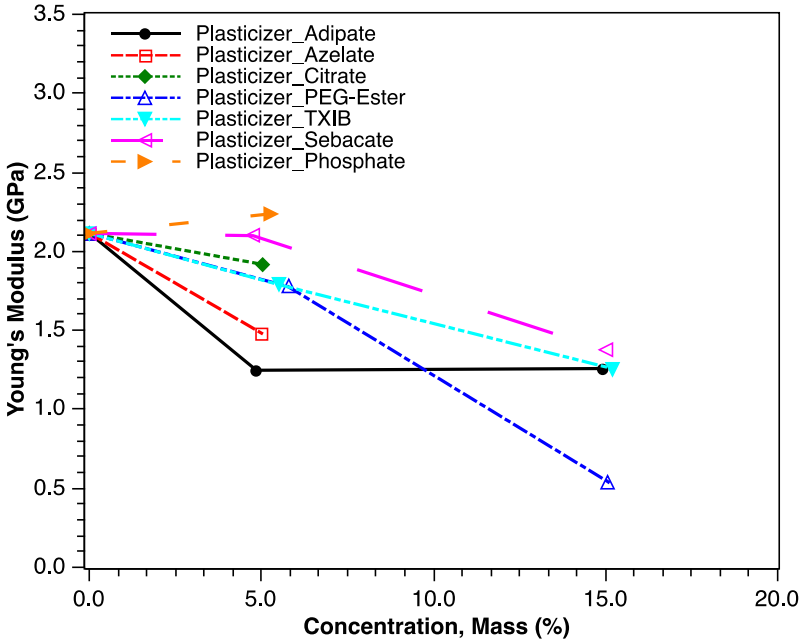

Figure D.1. Young's modulus of PPHA films using different plasticizers with various loadings

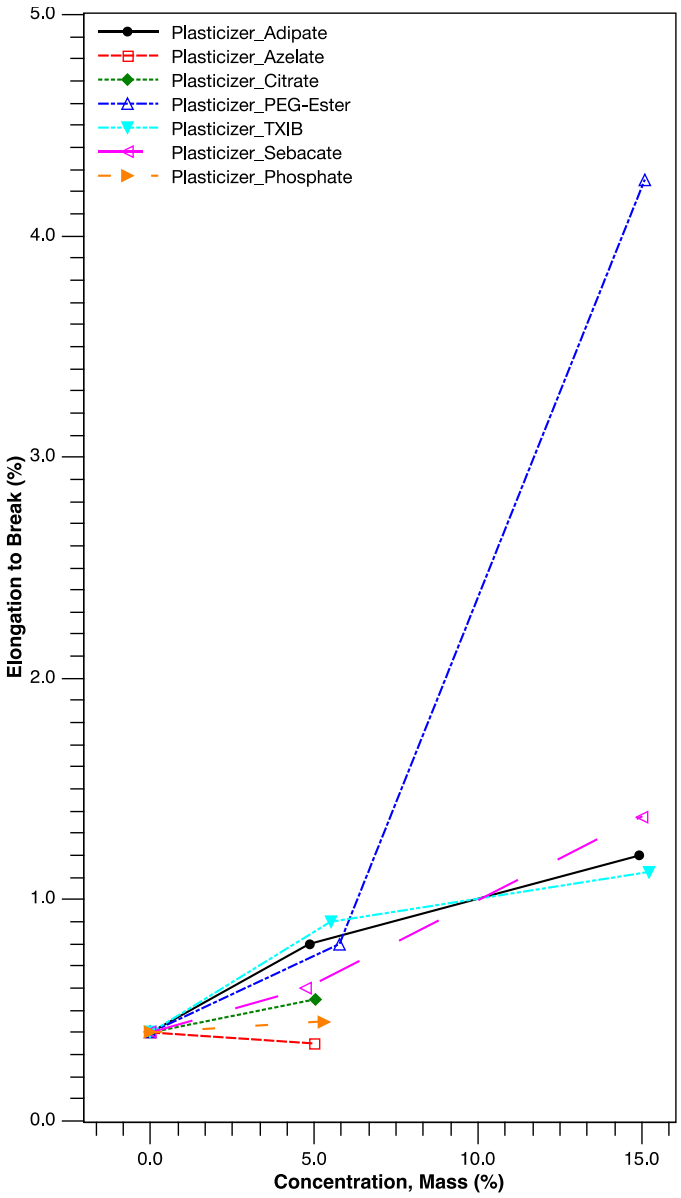

Figure D.2. Elongation to break of PPHA films using different plasticizers with various loadings

Table D.2. Summary of modulus and elongation to break for various plasticizers

Plasticizer ID	Wt%	Modulus	% Elongation
Bis(2-ethylhexyl) adipate	4.85	1.247	0.80
Diethyl azelate	5.00	1.482	0.35
Butyryl-n-trihexylcitrate	5.04	1.917	0.55
Poly(ethylene glycol) bis(2-ethylhexanoate)	5.77	1.777	0.80
2,2,4-trimethyl-1,3-pentanediol diisobutyrate (TXIB)	5.49	1.790	0.90
Bis(2-ethylhexyl) sebacate	4.75	2.099	0.60
Tributyl phosphate	5.28	2.238	0.45

Plasticizer ID	Wt%	Modulus	% Elongation
Bis(2-ethylhexyl) adipate	14.93	1.258	1.2
Poly(ethylene glycol) bis(2-ethylhexanoate)	15.08	0.540	4.25
2,2,4-trimethyl-1,3-pentanediol diisobutyrate (TXIB)	15.21	1.790	0.75
Bis(2-ethylhexyl) sebacate	14.99	1.373	1.38

REFERENCES

[1] F. Niklaus, G. Stemme, J.Q. Lu, R.J. Gutmann, Adhesive wafer bonding, J. Appl. Phys. 99 (2006) 031101 (1-28). doi:10.1063/1.2168512.

[2] K.K. Fu, Z. Wang, J. Dai, M. Carter, L. Hu, Transient Electronics : Materials and Devices, Chem. Mater. 28 (2016) 3527–3539. doi:10.1021/acs.chemmater.5b04931.

[3] E. Uzunlar, J. Schwartz, O. Phillips, P.A. Kohl, Decomposable and Template Polymers: Fundamentals and Applications, J. Electron. Packag. 138 (2016) 020802 (1-15). doi:10.1115/1.4033000.

[4] E. Uzunlar, P.A. Kohl, Size-Compatible, Polymer-Based Air-Gap Formation Processes, and Polymer Residue Analysis for Wafer-Level MEMS Packaging Applications, J. Electron. Packag. 137 (2015) 041001. doi:10.1115/1.4030952.

[5] J.M. Schwartz, O. Phillips, A. Engler, A. Sutlief, J. Lee, P.A. Kohl, Stable, High-Molecular-Weight Poly(phthalaldehyde), J. Polym. Sci. Part A Polym. Chem. 55 (2017) 1166–1172. doi:10.1002/pola.28473.

[6] G.A. Luinstra, Poly(propylene carbonate), old copolymers of propylene oxide and carbon dioxide with new interests: Catalysis and material properties, Polym. Rev. 48 (2008) 192–219. doi:10.1080/15583720701834240.

[7] M.D. Wedlake, P.A. Kohl, Thermal decomposition kinetics of functionalized polynorbornene, J. Mater. Res. 17 (2002) 632–640. doi:10.1557/JMR.2002.0090.

[8] M.R. Kember, A. Buchard, C.K. Williams, Catalysts for CO2/epoxide copolymerisation, Chem. Commun. 47 (2011) 141–163. doi:10.1039/C0CC02207A.

[9] O. Phillips, J.M. Schwartz, P.A. Kohl, Thermal decomposition of poly(propylene carbonate): End-capping, additives, and solvent effects, Polym. Degrad. Stab. 125 (2016) 129–139. doi:10.1016/j.polymdegradstab.2016.01.004.

[10] T. Sasaki, T. Yoneyama, S. Hashimoto, S. Takemura, Y. Naka, Photoinduced depolymerization of poly(olefin sulfone)s possessing photobase generator side-chains: Effect of spacer-chain length, J. Polym. Sci. Part A Polym. Chem. 51 (2013) 3873–3880. doi:10.1002/pola.26787.

[11] R. Gronheid, I. Blakey, A.K. Whittaker, I. Pollentier, M.J. Leeson, J. Blinco, T.R. Younkin, K. Lawrie, K. Jack, Extreme ultraviolet (EUV) degradation of poly(olefin sulfone)s: Towards applications as EUV photoresists, Radiat. Phys. Chem. 80 (2010) 236–241. doi:10.1016/j.radphyschem.2010.07.038.

[12] M.J. Bowden, L.F. Thompson, Electron Irradiation of Poly(olefin Sulfones) Application to Electron Beam Resists, J. Appl. Polym. Sci. 17 (1973) 3211–3221.

[13] L.F. Thompson, M.J. Bowden, A New Family of Positive Electron Beam Resists—Poly(Olefin Sulfones), J. Electrochem. Soc. 120 (1973) 1722. doi:10.1149/1.2403352.

[14] A. Sagi, R. Weinstain, N. Karton, D. Shabat, Self-immolative polymers, Angew. Chemie - Int. Ed. 47 (2008) 5434–5435. doi:10.1002/anie.200802474.

[15] K.J. Ivin, Thermodynamics of addition polymerization, J. Polym. Sci. Part A Polym. Chem. 38 (2000) 2137–2146. doi:10.1002/(SICI)1099-0518(20000615)38:12<2137::AID-POLA20>3.0.CO;2-D.

[16] J.M. Schwartz, A. Engler, O. Phillips, J. Lee, P.A. Kohl, Determination of Ceiling Temperature and Thermodynamic Properties of Low Ceiling Temperature Polyaldehydes, J. Polym. Sci. Part A Polym. Chem. 56 (2018) 221–228. doi:10.1002/pola.28888.

[17] M.J. Bowden, L.F. Thompson, Effect of olefin structure on the vapor-development of poly (olefin sulfones) under electron irradiation, Polym. Eng. Sci. 17 (1977) 269–273. doi:10.1002/pen.760170411.

[18] J.S. Robbins, K.M. Schmid, S.T. Phillips, Effects of electronics, aromaticity, and solvent polarity on the rate of azaquinone-methide-mediated depolymerization of aromatic carbamate oligomers, J. Org. Chem. 78 (2013) 3159–3169. doi:10.1021/jo400105m.

[19] R.A. McBride, E.R. Gillies, Kinetics of self-immolative degradation in a linear polymeric system: Demonstrating the effect of chain length, Macromolecules. 46 (2013) 5157–5166. doi:10.1021/ma4009753.

[20] J. De Winter, A.P. Dove, A. Knoll, P. Gerbaux, P. Dubois, O. Coulembier, Control over molar mass, dispersity, end-groups and kinetics in cyclopolymerization of ortho-phthalaldehyde: Adapted choice of a phosphazene organocatalyst, Polym. Chem. 5 (2014) 706–711. doi:10.1039/c3py01307c.

[21] A.M. Dilauro, G.G. Lewis, S.T. Phillips, Self-Immolative Poly(4,5-dichlorophthalaldehyde) and its Applications in Multi-Stimuli-Responsive Macroscopic Plastics, Angew. Chemie - Int. Ed. 54 (2015) 6200–6205. doi:10.1002/anie.201501320.

[22] A.M. Dilauro, S.T. Phillips, End-capped poly(4,5-dichlorophthalaldehyde): A stable self-immolative poly(aldehyde) for translating specific inputs into amplified outputs, both in solution and the solid state, Polym. Chem. 6 (2015) 3252–3258. doi:10.1039/c5py00190k.

[23] A.M. Dilauro, J.S. Robbins, S.T. Phillips, Reproducible and Scalable Synthesis of End-Cap-Functionalized Depolymerizable Poly(phthalaldehydes), Macromolecules. 46 (2013) 2963–2968. doi:10.1021/ma4001594.

[24] J.A. Kaitz, S. Moore, Copolymerization of o-Phthalaldehyde and Ethyl Glyoxylate: Cyclic Macromolecules with Alternating Sequence and Tunable Thermal Properties, Macromolecules. 47 (2014) 5509–5513. doi:10.1021/ma5013557.

[25] J.A. Kaitz, C.E. Diesendruck, J.S. Moore, Divergent macrocyclization mechanisms in the cationic initiated polymerization of ethyl glyoxylate, Macromolecules. 47 (2014) 3603–3607. doi:10.1021/ma500674c.

[26] B. Belloncle, F. Burel, H. Oulyadi, C. Bunel, Study of the in vitro degradation of poly(ethyl glyoxylate), Polym. Degrad. Stab. 93 (2008) 1151–1157. doi:10.1016/j.polymdegradstab.2008.03.004.

[27] B. Fan, J.F. Trant, A.D. Wong, E.R. Gillies, Polyglyoxylates: A versatile class of

triggerable self-immolative polymers from readily accessible monomers, J. Am. Chem. Soc. 136 (2014) 10116–10123. doi:10.1021/ja504727u.

[28] J.M. Schwartz, G. Gourdin, O. Phillips, A. Engler, J. Lee, N.R. Abdulkadir, R.C. Miller, A. Sutlief, P.A. Kohl, Cationic polymerization of high-molecular-weight phthalaldehyde-butanal copolymer, J. Appl. Polym. Sci. 136 (2019) 1–7. doi:10.1002/app.46921.

[29] J.A. Kaitz, S. Moore, Functional Phthalaldehyde Polymers by Copolymerization with Substituted Benzaldehydes, Macromolecules. 46 (2013) 608–612. doi:10.1021/ma302575s.

[30] P. Liu, J. Wang, L. Tong, Y. Tao, Advances in the Fabrication Processes and Applications of Wafer Level Packaging, J. Electron. Packag. 136 (2014) 024002. doi:10.1115/1.4027397.

[31] M. Esashi, Wafer level packaging of MEMS, J. Micromechanics Microengineering. 18 (2008) 1–13. doi:10.1109/SENSOR.2009.5285574.

[32] P. Monajemi, P.J. Joseph, P.A. Kohl, F. Ayazi, Wafer-level MEMS packaging via thermally released metal-organic membranes, J. Micromechanics Microengineering. 16 (2006) 742–750. doi:10.1088/0960-1317/16/4/010.

[33] Y.C. Chen, P.A. Kohl, Photosensitive sacrificial polymer with low residue, Microelectron. Eng. 88 (2011) 3087–3093. doi:10.1016/j.mee.2011.05.034.

[34] A.M. Padovani, L. Riester, L. Rhodes, S.A. Bidstrup Allen, P. a. Kohl, Chemically

Bonded Porogens in Methylsilsesquioxane, J. Electrochem. Soc. 149 (2002) F161–F170. doi:10.1149/1.1515282.

[35] C. V Nguyen, K.R. Carter, C.J. Hawker, J.L. Hedrick, R.L. Jaffe, R.D. Miller, J.F. Remenar, H.-W. Rhee, P.M. Rice, M.F. Toney, M. Trollsås, D.Y. Yoon, Low-Dielectric, Nanoporous Organosilicate Films Prepared via Inorganic/Organic Polymer Hybrid Templates, Chem. Mater. 11 (1999) 3080–3085. doi:10.1021/cm990114d.

[36] J. Li, Z. Du, H. Li, C. Zhang, Chemically induced phase separation in the preparation of porous epoxy monolith, J. Polym. Sci. Part B Polym. Phys. 48 (2010) 2140–2147. doi:10.1002/polb.22095.

[37] N. Fritz, H. Dao, S. Ann, B. Allen, P.A. Kohl, Polycarbonates as temporary adhesives, Int. J. Adhes. Adhes. 38 (2012) 45–49.

[38] X. Xue, S. Yang, Z. Wang, Heat-Depolymerizable Polypropylene Carbonate as a Temporary Bonding Adhesive for Fabrication of Flexible Silicon Sensor Chips, IEEE Trans. Components, Packag. Manuf. Technol. 7 (2017) 1751–1758. doi:10.1109/TCPMT.2017.2742554.

[39] F. Niklaus, P. Enoksson, K. Edvard, G. Stemme, Low-temperature full wafer adhesive bonding, J. Micromechanics Microengineering. 11 (2001) 100–107.

[40] S. Schlautmann, G.A.J. Besselink, R.B.M. Schasfoort, Fabrication of a microfluidic chip by UV bonding at room temperature for integration of temperature-sensitive layers, J. Micromechanics Microengineering. 13 (2003) 81–84.

[41] S.-W. Hwang, C.H. Lee, H. Cheng, J.-W. Jeong, S.-K. Kang, J.-H. Kim, J. Shin, J. Yang, Z. Liu, G.A. Ameer, Y. Huang, J.A. Rogers, Biodegradable Elastomers and Silicon Nanomembranes/Nanoribbons for Stretchable, Transient Electronics, and Biosensors, Nano Lett. 15 (2015) 2801–2808. doi:10.1021/nl503997m.

[42] S. Hwang, J. Song, X. Huang, H. Cheng, S. Kang, B.H. Kim, J. Kim, S. Yu, Y. Huang, J.A. Rogers, High-Performance Biodegradable/Transient Electronics on Biodegradable Polymers, Adv. Mater. 26 (2014) 3905–3911. doi:10.1002/adma.201306050.

[43] S.H. Jin, J. Shin, I. Cho, S.Y. Han, D.J. Lee, C.H. Lee, J. Lee, J.A. Rogers, Solution-processed single-walled carbon nanotube field effect transistors and bootstrapped inverters for disintegratable, transient electronics, Appl. Phys. Lett. 105 (2014) 013506-1-013506-4. doi:10.1063/1.4885761.

[44] O.P. Lee, H.L. Hernandez, S. Moore, Tunable Thermal Degradation of Poly(vinyl butyl carbonate sulfone)s via Side-Chain Branching, ACS Macro Lett. 4 (2015) 665–668. doi:10.1021/acsmacrolett.5b00234.

[45] M. Tsuda, M. Hata, R.I.E. Nishida, S. Oikawa, Acid-Catalyzed Degradation Mechanism of Poly(phthalaldehyde): Unzipping Reaction of Chemical, J. Polym. Sci. Part A Polym. Chem. 35 (1997) 77–89.

[46] H. Ito, C.G. Willson, Chemical Amplification in the Design of Dry Developing Resist Materials, Polym. Eng. Sci. 23 (1983) 1012–1018.

[47] O. Phillips, A. Engler, J.M. Schwartz, J. Jiang, C. Tobin, Y. Guta, P.A. Kohl,

Sunlight Photo-depolymerization of Transient Polymers, J. Appl. Polym. Sci. (2019) 47141 (1-12).

[48] K.M. Lee, O. Phillips, A. Engler, P.A. Kohl, B.P. Rand, Phototriggered Depolymerization of Flexible Poly(phthalaldehyde) Substrates by Integrated Organic Light-Emitting Diodes, ACS Appl. Mater. Interfaces. 10 (2018) 28062–28068. doi:10.1021/acsami.8b08181.

[49] H.L. Hernandez, S. Kang, O.P. Lee, S. Hwang, J.A. Kaitz, B. Inci, C.W. Park, S. Chung, N.R. Sottos, J.S. Moore, J.A. Rogers, S.R. White, Triggered Transience of Metastable Poly (phthalaldehyde) for Transient Electronics, Adv. Mater. 26 (2014) 7637–7642. doi:10.1002/adma.201403045.

[50] T.J. Spencer, P.A. Kohl, Decomposition of poly(propylene carbonate) with UV sensitive iodonium salts, Polym. Degrad. Stab. 96 (2011) 686–702. doi:10.1016/j.polymdegradstab.2010.12.003.

[51] O. Phillips, J.M. Schwartz, A. Engler, G. Gourdin, P.A. Kohl, Phototriggerable Transient Electronics : Materials and Concepts, in: IEEE 67th Electron. Components Technol. Conf., 2017: pp. 772–779. doi:10.1109/ECTC.2017.174.

[52] S. Peng, Y. An, C. Chen, B. Fei, Y. Zhuang, L. Dong, Thermal degradation kinetics of uncapped and end-capped poly(propylene carbonate), Polym. Degrad. Stab. 80 (2003) 141–147. doi:10.1016/S0141-3910(02)00395-6.

[53] Jayachandran, Joseph Paul, Reed, Hollie A., Zhen, Hongshi, Rhodes, Larry F., Henderson, Clifford L., Allen, Sue Ann Bidstrup, P.A. Kohl, Air-channel fabrication

for microelectromechanical systems via sacrificial photosensitive polycarbonates, J. Microelectromechanical Syst. 12 (2003) 147–159. doi:10.1109/jmems.2003.809963.

[54] A.M. Feinberg, H.L. Hernandez, C.L. Plantz, E.B. Mejia, N.R. Sottos, S.R. White, J.S. Moore, Cyclic Poly(phthalaldehyde): Thermoforming a Bulk Transient Material, ACS Macro Lett. 7 (2018) 47–52. doi:10.1021/acsmacrolett.7b00769.

[55] C.E. Diesendruck, G.I. Peterson, H.J. Kulik, J.A. Kaitz, B.D. Mar, P.A. May, S.R. White, T.J. Martínez, A.J. Boydston, J.S. Moore, Mechanically triggered heterolytic unzipping of a low-ceiling-temperature polymer., Nat. Chem. 6 (2014) 623–8. doi:10.1038/nchem.1938.

[56] F. Jin, X. Li, S. Park, Synthesis and application of epoxy resins : A review, J. Ind. Eng. Chem. 29 (2015) 1–11. doi:10.1016/j.jiec.2015.03.026.

[57] C.C. Chiu, C.C. Lee, T.L. Chou, C.C. Hsia, K.N. Chiang, Analysis of Cu/Low-k structure under back end of line process, Microelectron. Eng. 85 (2008) 2150–2154. doi:10.1016/j.mee.2008.04.007.

[58] M. Vilmay, D. Roy, F. Volpi, J.M. Chaix, Characterization of low-k SiOCH dielectric for 45 nm technology and link between the dominant leakage path and the breakdown localization, Microelectron. Eng. 85 (2008) 2075–2078. doi:10.1016/j.mee.2008.04.045.

[59] L. Broussous, W. Puyrenier, D. Rebiscoul, V. Rouessac, A. Ayral, Porosity and structure evolution of a SiOCH low k material during post-etch cleaning process,

Microelectron. Eng. 84 (2007) 2600–2605. doi:10.1016/j.mee.2007.07.001.

[60] W. Volksen, R.D. Miller, G. Dubois, Low Dielectric Constant Materials, Chem. Rev. 110 (2010) 56–110.

[61] G. Maier, Low dielectric constant polymers for microelectronics, Prog. Polym. Sci. 26 (2001) 3–65. doi:10.1016/S0079-6700(00)00043-5.

[62] P.A. Kohl, Low – Dielectric Constant Insulators for Future Integrated Circuits and Packages, Annu. Rev. Chem. Biomol. Eng. 2 (2011) 379–401. doi:10.1146/annurev-chembioeng-061010-114137.

[63] B. De, N. Karak, Ultralow dielectric, high performing hyperbranched epoxy thermosets: synthesis, characterization and property evaluation, RSC Adv. 5 (2015) 35080–35088. doi:10.1039/C5RA04248H.

[64] J. Jiao, L. Wang, P. Lv, Y. Cui, J. Miao, Improved dielectric and mechanical properties of silica / epoxy resin nanocomposites prepared with a novel organic – inorganic hybrid mesoporous silica : POSS – MPS, Mater. Lett. 129 (2014) 16–19. doi:10.1016/j.matlet.2014.05.010.

[65] M. Pan, C. Zhang, B. Liu, J. Mu, Dielectric and Thermal Properties of Epoxy Resin Nanocomposites Containing Polyhedral Oligomeric Silsesquioxane, J. Mater. Sci. Res. 2 (2013) 153–162. doi:10.5539/jmsr.v2n1p153.

[66] S. Sasaki, N.T.T. Electrical, C. Laboratories, Dielectric Properties of Cured Epoxy Resins Containing the Perfluorobutenyloxy Group, J. Polym. Sci. Part C Polym.

Lett. 24 (1986) 249–252.

[67] D. Miller, V. Kumar, Microcellular and nanocellular solid-state polyetherimide (PEI) foams using sub-critical carbon dioxide II. Tensile and impact properties, Polymer (Guildf). 52 (2011) 2910–2919. doi:10.1016/j.polymer.2011.04.049.

[68] J. Wang, Z. Du, H. Li, A. Xiang, C. Zhang, Interconnected porous epoxy monoliths prepared by concentrated emulsion templating, J. Colloid Interface Sci. 338 (2009) 145–150. doi:10.1016/j.jcis.2009.06.013.

[69] D.R.L. H. Matsuyama, S. Berghmans, Formation of anisotropic membranes via thermally induced phase separation, Polymer (Guildf). 40 (1999) 2289–2301. http://search.proquest.com/docview/304539067?accountid=62373.

[70] J. Kiefer, R. Porouchani, D. Mendels, J.B. Ferrer, C. Fond, J.L. Hedrick, H.H. Kausch, J.G. Hilborn, Macroporous thermosets via chemically induced phase separation, Microporous Macroporous Mater. 431 (1996) 527–532.

[71] J. Li, Z. Du, H. Li, C. Zhang, Porous epoxy monolith prepared via chemically induced phase separation, Polymer (Guildf). 50 (2009) 1526–1532. doi:10.1016/j.polymer.2009.01.049.

[72] Q.R. Huang, C.W. Frank, D. Mecerreyes, W. Volksen, R.D. Miller, Phase separation behavior of poly(methyl methacrylate-co-dimethylaminoethyl methacrylate)/methyl silsesquioxane hybrid nanocomposites studied by dansyl fluorescence, Chem. Mater. 17 (2005) 1521–1528. doi:10.1021/cm048774s.

[73] K.R. Carter, R.A. DiPietro, M.I. Sanchez, T.P. Russell, P. Lakshmanan, J.E. McGrath, Polyimide nanofoams based on ordered polyimides derived from poly(amic alkyl esters): PMDA/4-BDAF, Chem. Mater. 9 (1997) 105–118. doi:Doi 10.1021/Cm960242r.

[74] J.L. Hedrick, K.R. Carter, R. Richter, R.D. Miller, T.P. Russell, V. Flores, D. Meccereyes, P. Dubois, R. Jerome, Polyimide nanofoams from aliphatic polyester-based copolymers, Chem. Mater. 10 (1998) 39–49. doi:Doi 10.1021/Cm960523z.

[75] K.R. Carter, R.A. DiPietro, M.I. Sanchez, S.A. Swanson, Nanoporous polyimides derived from highly fluorinated polyimide/poly(propylene oxide) copolymers, Chem. Mater. 13 (2001) 213–221. doi:10.1021/cm990707o.

[76] S. Yang, P.A. Mirau, C.S. Pai, O. Naiamasu, E. Reichmanis, E.K. Lin, H.J. Lee, D.W. Gidley, J. Sun, Molecular templating of nanoporous ultralow dielectric constant (≈1.5) organosilicates by tailoring the microphase separation of triblock copolymers, Chem. Mater. 13 (2001) 2762–2764. doi:10.1021/cm0102786.

[77] E.F. Connor, V.Y. Lee, T. Magbitang, C.J. Hawker, W. Volksen, R. Siemens, R.A. DiPietro, J.C. Hedrick, H.C. Kim, R.D. Miller, J.L. Hedrick, First example of a nanoporous high-temperature polymer thermoset: Eluding transition-time-temperature constraints associated with organic thermosets, Adv. Mater. 16 (2004) 1525–1529. doi:10.1002/adma.200306321.

[78] H. Lee, E.K. Lin, H. Wang, W. Wu, W. Chen, E.S. Moyer, Structural Comparison of Hydrogen Silsesquioxane Based Porous Low- k Thin Films Prepared with

Varying Process Conditions, Chem. Mater. 14 (2002) 1845–1852. doi:10.1021/cm011569h.

[79] B.J. Cha, S. Kim, K. Char, J.K. Lee, D.Y. Yoon, H.W. Rhee, Nanoporous organosilicate thin films prepared with covalently bonded adamantylphenol pore generators, Chem. Mater. 18 (2006) 378–385. doi:10.1021/cm051916d.

[80] S. Oh, J.K. Lee, P. Theato, K. Char, Nanoporous thin films based on polylactide-grafted norbornene copolymers, Chem. Mater. 20 (2008) 6974–6984. doi:10.1021/cm801421w.

[81] W.C. Wang, R.H. Vora, E.T. Kang, K.G. Neoh, C.K. Ong, L.F. Chen, Nanoporous Ultra-Low-k Films Prepared from Fluorinated Polyimide with Grafted Poly(acrylic acid) Side Chains, Adv. Mater. 16 (2004) 54–57. doi:10.1002/adma.200305185.

[82] F. Tikart, K.-H. Leis, Epoxy Resin, Styrene-Maleic Anhydride Copolymer and Co-crosslinking Agent, United States Patent, No. 6,509,414. (2003). doi:10.1016/j.(73).

[83] W.H. Park, J.K. Lee, K.J. Kwon, Cure Behavior of an Epoxy-Anhydride-Imidazole System, Polym. J. 28 (1996) 407–411. doi:10.1295/polymj.28.407.

[84] L. Bouledjnib, S. Sahli, Investigation Of Pores Influence on Dielectric Constant Value in Low k Materials Using Monte Carlo Method, Mj Condens. Matter. 12 (2010) 199–203. http://www.fsr.ac.ma/MJCM/sup_pdf/pdf_vol12/vol12-art36.pdf.

[85] X. Zhao, H. Liu, Review of polymer materials with low dielectric constant, Polym. Int. 59 (2010) 597–606. doi:10.1002/pi.2809.

[86] S.K. Bhattacharya, R.R. Tummala, Epoxy Nanocomposite Capacitors for Application as MCM-L Compatible Integral Passives, J. Electron. Packag. 124 (2002) 1. doi:10.1115/1.1400751.

[87] Junfeng Zhang, Cheng Qiang Cui, Thiam Beng Lim, E.T. Kang, Koon Gee Neoh, Adhesion improvement of a poly(tetrafluoroethylene)- copper laminate by thermal graft copolymerization, J. Adhes. Sci. Technol. 12 (1998) 1205–1218. doi:10.1163/156856198X00399.

[88] C. Yuan, J. Wang, K. Jin, S. Diao, J. Sun, J. Tong, Q. Fang, Postpolymerization of functional organosiloxanes: An Efficient strategy for preparation of low-k material with enhanced thermostability and mechanical properties, Macromolecules. 47 (2014) 6311–6315. doi:10.1021/ma501263c.

[89] L. Fan, C.P. Wong, Adhesion evaluation on low-cost alternatives to thermosetting epoxy encapsulants, IEEE Trans. Electron. Packag. Manuf. 26 (2003) 173–178. doi:10.1109/TEPM.2003.817716.

[90] J. Balde, G. Messner, Low Dielectric Constant — The Substrate of the Future, Circuit World. 14 (1987) 11–14.

[91] M. Morgen, J.-H. Zhao, C. Hu, T. Cho, P.S. Ho, E. Todd, Low dielectric constant materials for advanced interconnects, Jom. 51 (1999) 37–40. doi:10.1007/s11837-999-0158-8.

[92] M.R. Baklanov, K. Maex, Porous low dielectric constant materials for microelectronics, J. Appl. Phys. 93 (2003) 8793–8841. doi:10.1098/rsta.2005.1679.

[93] D. Shamiryan, T. Abell, F. Iacopi, K. Maex, Low-k dielectric materials, Mater. Today. 7 (2004) 34–39. doi:10.1016/s1369-7021(04)00053-7.

[94] J. Jiao, Y. Shao, F. Huang, J. Wang, Z. Wu, Toughening of POSS–MPS composites with low dielectric constant prepared with structure controllable micro/mesoporous nanoparticles, RSC Adv. 8 (2018) 40836–40845. doi:10.1039/c8ra07430e.

[95] J.H. Wang, G.Z. Liang, H.X. Yan, S.B. He, Mechanical and dielectric properties of epoxy/dicyclopentadiene bisphenol cyanate ester/glass fabric composites, Express Polym. Lett. 2 (2008) 118–125. doi:10.3144/expresspolymlett.2008.16.

[96] T. Na, H. Jiang, L. Zhao, C. Zhao, Preparation and characterization of novel naphthyl epoxy resin containing 4-fluorobenzoyl side chains for low-k dielectrics application, RSC Adv. 7 (2017) 53970–53976. doi:10.1039/c7ra09941j.

[97] Z. Tao, S. Yang, J. Chen, L. Fan, Synthesis and characterization of imide ring and siloxane-containing cycloaliphatic epoxy resins, Eur. Polym. J. 43 (2007) 1470–1479. doi:10.1016/j.eurpolymj.2007.01.039.

[98] J. Jiang, O. Phillips, L. Keller, P.A. Kohl, Grafted Epoxide Functionalized Polypropylene Carbonate Porogen for Low Dielectric Constant Epoxy Films, ECS J. Solid State Sci. Technol. 6 (2017) N163–N170. doi:10.1149/2.0281709jss.

[99] F. Tikart, K.-H. Leis, W. Kopp, Epoxy Resin, Styrene-Maleic Anhydride Copolymer and Crosslinking Agent, United States Patent, No. 8,022,140 B2. (2011). doi:10.1038/incomms1464.

[100] J.L. Salas-Vernis, J.P. Jayachandran, S. Park, H.A. Kelleher, S.A.B. Allen, P.A. Kohl, Hydrophobic/hydrophilic surface modification within buried air channels, J. Vac. Sci. Technol. B. 22 (2004) 953–960. doi:10.1116/1.1715084.

[101] M. Poletto, Effect of styrene maleic anhydride on physical and mechanical properties of recycled polystyrene wood flour composites, Maderas. Cienc. y Tecnol. 18 (2016) 533–542. doi:10.4067/s0718-221x2016005000046.

[102] B. Kim, J. Choi, S. Yang, S. Yu, M. Cho, Influence of crosslink density on the interfacial characteristics of epoxy nanocomposites, Polymer (Guildf). 60 (2015) 186–197. doi:10.1016/j.polymer.2015.01.043.

[103] J.W. Yu, J. Jung, Y.M. Choi, J.H. Choi, J. Yu, J.K. Lee, N.H. You, M. Goh, Enhancement of the crosslink density, glass transition temperature, and strength of epoxy resin by using functionalized graphene oxide co-curing agents, Polym. Chem. 7 (2016) 36–43. doi:10.1039/c5py01483b.

[104] J.A. Kaitz, O.P. Lee, J.S. Moore, Depolymerizable polymers: preparation, applications, and future outlook, MRS Commun. 5 (2018) 191–204. doi:10.1557/mrc.2015.28.

[105] J.A. Kaitz, C.E. Diesendruck, S. Moore, End Group Characterization of Poly(phthalaldehyde): Surprising Discovery of a Reversible, Cationic Macrocyclization Mechanism, J. Am. Chem. Soc. 135 (2013) 12755–12761. doi:10.1021/ja405628g.

[106] S.T. Phillips, J.S. Robbins, A.M. Dilauro, M.G. Olah, Amplified Responses in

Materials Using Linear Polymers that Depolymerize from End-to-End When Exposed to Specific Stimuli, J. Appl. Polym. Sci. 40992 (2014) 1–12. doi:10.1002/app.40992.

[107] C.W. Park, S. Kang, H.L. Hernandez, J.A. Kaitz, D.S. Wie, J. Shin, O.P. Lee, N.R. Sottos, J.S. Moore, J.A. Rogers, S.R. White, Thermally Triggered Degradation of Transient Electronic Devices, Adv. Mater. 27 (2015) 3783–3788. doi:10.1002/adma.201501180.

[108] H.L. Hernandez, O.P. Lee, C.M.P. Casey, J.A. Kaitz, C.W. Park, C.L. Plantz, J.S. Moore, S.R. White, Accelerated Thermal Depolymerization of Cyclic Polyphthalaldehyde with a Polymeric Thermoacid Generator, Macromol. Rapid Commun. 39 (2018) 1800046 (1-5). doi:10.1002/marc.201800046.

[109] J.M. Schwartz, ADVANCES IN LOW-K AND TRANSIENT POLYMERS, Georgia Institute of Technology, 2017.

[110] M. Rahman, C.S. Brazel, Ionic liquids: New generation stable plasticizers for poly(vinyl chloride), Polym. Degrad. Stab. 91 (2006) 3371–3382. doi:10.1016/j.polymdegradstab.2006.05.012.

[111] M.P. Scott, M. Rahman, C.S. Brazel, Application of ionic liquids as low-volatility plasticizers for PMMA, Eur. Polym. J. 39 (2003) 1947–1953. doi:10.1016/S0014-3057(03)00129-0.

[112] A. Sankri, A. Arhaliass, I. Dez, A.C. Gaumont, Y. Grohens, D. Lourdin, I. Pillin, A. Rolland-Sabaté, E. Leroy, Thermoplastic starch plasticized by an ionic liquid,

Carbohydr. Polym. 82 (2010) 256–263. doi:10.1016/j.carbpol.2010.04.032.

[113] M.P. Scott, C.S. Brazel, M.G. Benton, J.W. Mays, D. Holbrey, R.D. Rogers, Application of ionic liquids as plasticizers for poly (methyl methacrylate), Chem. Commun. (2002) 1370–1371. doi:10.1039/b204319j.4.

[114] G. Wypych, Handbook of Plasticizers, Elsevier Ltd, 2012. doi:10.1016/B978-1-895198-50-8.50015-1.

[115] S. Berdzinski, J. Horst, P. Straßburg, V. Strehmel, Recombination of lophyl radicals in pyrrolidinium-based ionic liquids, ChemPhysChem. 14 (2013) 1899–1908. doi:10.1002/cphc.201300098.

[116] V. Strehmel, S. Berdzinski, H. Rexhausen, Interactions between ionic liquids and radicals, J. Mol. Liq. 192 (2014) 153–170. doi:10.1016/j.molliq.2013.12.007.

[117] A. Selmi, Effect of Glass Fiber Content on the Flexural Modulus of Elasticity of Glass-Epoxy Sandwich Composites, in: Emerg. Trends Eng. Technol., 2014: pp. 187–191.

[118] L. Yin, H. Cheng, S. Mao, R. Haasch, Y. Liu, X. Xie, S. Hwang, J.A. Rogers, Dissolvable Metals for Transient Electronics, Adv. Funct. Mater. 24 (2014) 645–658. doi:10.1002/adfm.201301847.

[119] H. Acar, S. Çınar, M. Thunga, M.R. Kessler, N. Hashemi, Study of Physically Transient Insulating Materials as a Potential Platform for Transient Electronics and Bioelectronics, Adv. Funct. Mater. 24 (2014) 4135–4143.

doi:10.1002/adfm.201304186.

[120] A.M. Dilauro, H. Zhang, M.S. Baker, F. Wong, A. Sen, S.T. Phillips, Accessibility of Responsive End-Caps in Films Composed of Stimuli-Responsive, Depolymerizable Poly(phthalaldehydes), Macromolecules. 46 (2013) 7257–7265. doi:10.1021/ma401463e.

[121] S. Tang, L. Tang, X. Lu, H. Liu, Programmable Payload Release from Transient Polymer Microcapsules Triggered by a Specific Ion Coactivation Effect, J. Am. Chem. Soc. 140 (2018) 94–97. doi:10.1021/jacs.7b11022.

[122] J. Jiang, O. Phillips, A. Engler, M.H. Vong, P.A. Kohl, Photodegradable Transient Bilayered Poly(phthalaldehyde) with Improved Shelf-life, Polym. Adv. Technol. (2019) 1–7. doi:10.1002/pat.4552.

[123] J. Jiang, M. Warner, O. Phillips, A. Engler, P.A. Kohl, Tunable Transient and Mechanical Properties of Photodegradable Poly(phthalaldehyde), (2018).

[124] V. Gold, D. Bethell, Advances in Physical Organic Chemistry APL, Academic Press Inc., New York, NY, 1975.

[125] K. Rad-moghadam, S. Ali, R. Mousazadeh, S.T. Roudsari, N -methyl-2-pyrrolidonium chlorosulfonate : An efficient ionic-liquid catalyst and mild sulfonating agent for one-pot synthesis of δ-sultones, J. Mol. Liq. 218 (2016) 275–280. doi:10.1016/j.molliq.2016.02.082.

[126] M. Lequestel, J.Y.; Laurence, C.; Lachkar, A.; Helbert, M.; Berthelot, Hydrogen-

Bond Basicity of Secondary and Tertiary Amides, Carbamates, Ureas and Lactams, J. Chem. Soc. Trans. 2. (1992) 2091–2094.

[127] I.M. El Nahhal, S.M. Zourab, F.S. Kodeh, A.I. Qudaih, Thin film optical BTB pH sensors using sol–gel method in presence of surfactants, Int. Nano Lett. 2 (2012) 1–9.

[128] S.W. Hwang, H. Tao, D.H. Kim, H. Cheng, J.K. Song, B. Rill E; Brenckle, M A; Panilaitis, S.M. Won, Y.S. Kim, Y.M. Song, K.J. Yu, A. Ameen, R. Li, Y. Su, M. Yang, D. Kaplan, M.R. Zakin, M.J. Slepian, Y. Huang, F.G. Omenetoo, J.A. Rogers, A Physically Transient Form of Silicon Electronics, Science (80-.). 337 (2012) 1640–1644. doi:10.1126/science.1245938.

[129] J.A. Kaitz, C.E. Diesendruck, J.S. Moore, Dynamic covalent macrocyclic poly(phthalaldehyde)s: Scrambling cyclic homopolymer mixtures produces multi-block and random cyclic copolymers, Macromolecules. 46 (2013) 8121–8128. doi:10.1021/ma401744k.

[130] G.I. Peterson, A.J. Boydston, Kinetic analysis of mechanochemical chain scission of linear poly(phthalaldehyde), Macromol. Rapid Commun. 35 (2014) 1611–1614. doi:10.1002/marc.201400271.

[131] W.E. Mcewen, J.W. Demassa, Acid Generation in the Thermal Decomposition of Diaryl iodonium Salts, Heteroat. Chem. 7 (1996) 349–354.

[132] S. Kang, W.L. Wu, K.W. Choi, A. De Silva, C.K. Ober, V.M. Prabhu, Characterization of the photoacid diffusion length and reaction kinetics in EUV

photoresists with IR spectroscopy, Macromolecules. 43 (2010) 4275–4286. doi:10.1021/ma902548a.

[133] R. Li, H. Cheng, Y. Su, S.W. Hwang, L. Yin, H. Tao, M.A. Brenckle, D.H. Kim, F.G. Omenetto, J.A. Rogers, Y. Huang, An analytical model of reactive diffusion for transient electronics, Adv. Funct. Mater. 23 (2013) 3106–3114. doi:10.1002/adfm.201203088.

[134] S. V. Postnikov, M.D. Stewart, H.V. Tran, M. a. Nierode, D.R. Medeiros, T. Cao, J. Byers, S.E. Webber, C.G. Wilson, Study of resolution limits due to intrinsic bias in chemically amplified photoresists, J. Vac. Sci. Technol. B Microelectron. Nanom. Struct. 17 (1999) 3335. doi:10.1116/1.591007.

[135] T. Itani, H. Yoshino, S. Hashimoto, M. Yamana, A study of acid diffusion in chemically amplified deep ultraviolet resist, 14 (1996) 4226–4228. doi:10.1116/1.588580.

[136] F.A. Houle, W.D. Hinsberg, M. Morrison, M.I. Sanchez, G. Wallraff, C. Larson, J. Hoffnagle, Determination of coupled acid catalysis-diffusion processes in a positive-tone chemically amplified photoresist, J. Vac. Sci. Technol. B Microelectron. Nanom. Struct. 18 (2000) 1874. doi:10.1116/1.1303753.

[137] L. Schlegel, T. Ueno, N. Hayashi, T. Iwayanagi, Determination of acid diffusion in chemical amplification positive deep-uv resists, Jpn. J. Appl. Phys. 30 (1991) 3132–3137. doi:10.1143/JJAP.30.3132.

[138] J. Jiang, O. Phillips, L. Keller, P.A. Kohl, Porous Epoxy Film for Low Dielectric

Constant Chip Substrates and Boards, in: Electron. Components Technol. Conf., IEEE, 2018: pp. 33–39. doi:10.1109/ECTC.2018.00013.

[139] Y. Rao, J. Yue, C.P. Wong, Material Characterization of High Dielectric Constant Polymer – Ceramic Composite for Embedded Capacitor To Rf Application, Mater. Sci. 25 (2002) 123–129. doi:10.1002/app.13690.

[140] J. Rector, J. Dougherty, V. Brown, J. Galvagni, A.V.X. Corporation, M. Beach, J. Prymak, Integrated and Integral Passive Components : A Technology Roadmap, (1997).

[141] M.A. Alam, M.H. Azarian, M. Osterman, M. Pecht, Effectiveness of embedded capacitors in reducing the number of surface mount capacitors for decoupling applications, Circuit World. 36 (2010) 22–30. doi:10.1108/03056121011015068.

[142] P. Muthana, A.E. Engin, M. Swaminathan, R. Tummala, V. Sundaram, B. Wiedenman, D. Amey, K.H. Dietz, S. Banerji, Design, modeling, and characterization of embedded capacitor networks for core decoupling in the package, IEEE Trans. Adv. Packag. 30 (2007) 809–822. doi:10.1109/TADVP.2007.901548.

[143] M.A. Alam, M.H. Azarian, M.G. Pecht, Embedded capacitors in printed wiring board: A technological review, J. Electron. Mater. 41 (2012) 2286–2303. doi:10.1007/s11664-012-2044-3.

[144] R. Ulrich, L. Schaper, D. Nelms, M. Leftwich, Comparison of Paraelectric and Ferroelectric Materials for Applications as Dielectrics in Thin Film Integrated

Capacitors, Int. J. Microcircuits Electron. Packag. 23 (2000) 172–181.

[145] J. Robertson, High density plasma enhanced chemical vapor deposition of optical thin films, Eur. Phys. J. Appl. Phys. 28 (2004) 265–291. doi:10.1051/epjap.

[146] Z. Nami, O. Misman, A. Erbil, G.S. May, Effect of growth parameters on TiO$_2$ thin films deposited using MOCVD, J. Cryst. Growth. 179 (1997) 522–538. doi:10.1016/S0022-0248(97)00144-9.

[147] D. Nelms, R. Ulrich, L. Schaper, S. Reeder, Anoaizarion lor r orming, (1998) 247–251.

[148] S.K. Bhattacharya, R.R. Tummala, Next generation integral passives: Materials, processes, and integration of resistors and capacitors on PWB substrates, J. Mater. Sci. Mater. Electron. 11 (2000) 253–268. doi:10.1023/A:1008913403211.

[149] S.K. Bhattacharya, Epoxy Nanocomposite Capacitors for Application as MCM-L Compatible Integral Passives, 124 (2002) 1–6. doi:10.1115/1.1400751.

[150] Y. Rao, S. Ogitani, P. Kohl, C.P. Wong, Novel polymer-ceramic nanocomposite based on high dielectric constant epoxy formula for embedded capacitor application, J. Appl. Polym. Sci. 83 (2002) 1084–1090. doi:10.1002/app.10082.

[151] A. Quade, H. Wulff, H. Steffen, T.M. Tun, R. Hippler, Investigation of the aluminum oxidation in an oxygen plasma excited by microwaves, Thin Solid Films. 377–378 (2000) 626–630. doi:10.1016/S0040-6090(00)01474-7.

[152] K.C. Chinnam, S. Gupta, H. Gleskova, Aluminium oxide prepared by UV / ozone

exposure for low-voltage organic thin- fi lm transistors, J. Non. Cryst. Solids. 358 (2012) 2512–2515. doi:10.1016/j.jnoncrysol.2012.01.016.

[153] S. Gupta, S. Hannah, C.P. Watson, P. Šutta, R.H. Pedersen, N. Gadegaard, H. Gleskova, Ozone oxidation methods for aluminum oxide formation : Application to low-voltage organic transistors, Org. Electron. 21 (2015) 132–137. doi:10.1016/j.orgel.2015.03.007.

[154] A. Kuznetsova, J.T. Yates, G. Zhou, J.C. Yang, X. Chen, Making a superior oxide corrosion passivation layer on aluminum using ozone, Langmuir. 17 (2001) 2146–2152. doi:10.1021/la001300x.

[155] G. Singh-Bhalla, X. Du, A.F. Hebard, Contribution of interface capacitance to the electric-field breakdown in thin-film Al-AlOx-Al capacitors, Appl. Phys. Lett. 83 (2003) 2417–2419. doi:10.1063/1.1613802.

[156] M.Y. Seo, E.N. Cho, C.E. Kim, P. Moon, I. Yun, Characterization of Al2O3 films grown by electron beam evaporator on Si substrates, Nanoelectron. Conf. (INEC), 2010 3rd Int. (2010) 1–2. doi:10.1109/INEC.2010.5424657.

[157] J. Yota, H. Shen, R. Ramanathan, Characterization of atomic layer deposition HfO2, Al2O3, and plasma-enhanced chemical vapor deposition Si3N4 as metal-insulator-metal capacitor dielectric for GaAs HBT technology, J. Vac. Sci. Technol. A Vacuum, Surfaces, Film. 31 (2013) 01A134. doi:10.1116/1.4769207.

[158] M. Esposto, S. Krishnamoorthy, D.N. Nath, S. Bajaj, T.H. Hung, S. Rajan, Electrical properties of atomic layer deposited aluminum oxide on gallium nitride, Appl. Phys.

Lett. 99 (2011) 3–6. doi:10.1063/1.3645616.

[159] D. Diesing, A.W. Hassel, M.M. Lohrengel, Aluminum oxide tunnel junctions: Influence of preparation technique, sample geometry and oxide thickness, Thin Solid Films. 342 (1999) 282–290. doi:10.1016/S0040-6090(98)01427-8.

[160] M. Kaltenbrunner, T. Sekitani, J. Reeder, T. Yokota, K. Kuribara, T. Tokuhara, M. Drack, R. Schwödiauer, I. Graz, S. Bauer-Gogonea, S. Bauer, T. Someya, An ultra-lightweight design for imperceptible plastic electronics., Nature. 499 (2013) 458–63. doi:10.1038/nature12314.

[161] M. Kaltenbrunner, P. Stadler, R. Schwödiauer, A.W. Hassel, N.S. Sariciftci, S. Bauer, Anodized aluminum oxide thin films for room-temperature-processed, flexible, low-voltage organic non-volatile memory elements with excellent charge retention, Adv. Mater. 23 (2011) 4892–4896. doi:10.1002/adma.201103189.

[162] A.I. Mardare, M. Kaltenbrunner, N.S. Sariciftci, S. Bauer, A.W. Hassel, Ultra-thin anodic alumina capacitor films for plastic electronics, Phys. Status Solidi Appl. Mater. Sci. 209 (2012) 813–818. doi:10.1002/pssa.201100785.

[163] H. Oh, C. Chi, The Electrochemical Behaviors of Barrier-Type Anodic Films on Aluminum in Ammonium Adipate Solution, 21 (2000) 193–199.

[164] B.A.N. Chao-lei, H.E. Ye-dong, S. Xin, Effect of citric acid on microstructure and electrochemical characteristics of high voltage anodized alumina film formed on etched Al Foils, Trans. Nonferrous Met. Soc. China. 21 (2010) 133–138. doi:10.1016/S1003-6326(11)60689-4.

[165] J.R. Dickey, Improved Dielectric Properties for Anodic Aluminum Oxide Films by Soft/Hard Two-Step Electrolytic Anodization, J. Electrochem. Soc. 136 (1989) 1772. doi:10.1149/1.2097010.

[166] E. Hourdakis, A.G. Nassiopoulou, High performance MIM capacitor using anodic alumina dielectric, Microelectron. Eng. 90 (2012) 12–14. doi:10.1016/j.mee.2011.03.020.

[167] C.N. Ajit, S.R. Jawalekar, THIN FILM AI20 a CAPACITORS, 37 (1976) 85–89.

[168] M.K. Rao, S.R. Jawalekar, Improved thin film Al2O3 capacitors, Thin Solid Films. 51 (1978) 185–188. doi:10.1016/0040-6090(78)90352-8.

[169] D. Kannadassan, R. Karthik, P.S. Mallick, M.S. Baghini, Temperature and stress dependent properties of barrier type anodic Al 2O3 MIM capacitor, 2012 Int. Conf. Emerg. Electron. ICEE 2012. 63 (2012) 1–4. doi:10.1109/ICEmElec.2012.6636238.

[170] W. Lee, S.-J.S.S. Park, Porous anodic aluminum oxide: anodization and templated synthesis of functional nanostructures, Chem. Rev. 114 (2014) 7487–7556. doi:10.1021/cr500002z.

[171] J. Chen, M. Yao, X. Yao, Electromechanical Breakdown of Barrier-Type Anodized Aluminum Oxide Thin Films Under High Electric Field Conditions, J. Electron. Mater. 45 (2016) 892–898. doi:10.1007/s11664-015-4195-5.

[172] J.-K. Chang, C.-M. Liao, C.-H. Chen, W.-T. Tsai, Microstructure and Electrochemical Characteristics of Aluminum Anodized Film Formed in

Ammonium Adipate Solution, J. Electrochem. Soc. 150 (2003) B266. doi:10.1149/1.1570822.

[173] N. Mikuni, T. Shibata, S. Shinkai, K. Sasaki, H. Yanagisawa, M. Yamane, Y. Abe, Preparation of Thin-Film Capacitor with High Reliability by Anodization of Zr–Al Alloy Film, Jpn. J. Appl. Phys. 46 (2007) 5249–5253. doi:10.1143/JJAP.46.5249.

[174] Y. Ma, X. Zhou, Y. Liao, X. Chen, C. Zhang, H. Wu, Z. Wang, W. Huang, Effect of Anodizing Parameters on Film Morphology and Corrosion Resistance of AA2099 Aluminum-Lithium Alloy, J. Electrochem. Soc. 163 (2016) C369–C376. doi:10.1149/2.1081607jes.

[175] S. Ikonopisov, N. Elenkov, Field and temperature dependence of the electronic conduction from electrolytes through the barrier anodic film on niobium, J. Electroanal. Chem. 88 (1978) 417–420.

[176] R.K. Hester, K.S. Tan, M. De Wit, J.W. Fattaruso, S. Kiriaki, J.R. Hellums, Fully Differential ADC with Rail-to-Rail Common-Mode Range and Nonlinear Capacitor Compensation, IEEE J. Solid-State Circuits. 25 (1990) 173–183. doi:10.1109/4.50301.

[177] S.K. Lee, K.S. Kim, S. Kim, D.J. Lee, S.J. Park, S. Kim, Characterizing Voltage Linearity and Leakage Current of High Density Al 2 O 3 / HfO 2 / Al 2 O 3, Ieee Electron Device Lett. 32 (2011) 384–386. doi:10.1109/LED.2010.2099200.